

A NUMERICAL HOMOGENIZATION APPROACH TO CHARACTERIZE IN-PLANE
ANISOTROPIC HYPERELASTIC RESPONSES OF A NON-METALLIC
HONEYCOMB CORE

A Dissertation by

Hooman Shahverdi Moghaddam

Master of Science, Azad University, 2010

Bachelor of Engineering, Azad University, 2007

Submitted to the Department of Aerospace Engineering
and the faculty of the Graduate School of
Wichita State University
in partial fulfillment of
the requirements for the degree of
Doctor of Philosophy

May 2020

© Copyright 2020 by Hooman Shahverdi Moghaddam

All Rights Reserved

A NUMERICAL HOMOGENIZATION APPROACH TO CHARACTERIZE IN-PLANE
ANISOTROPIC HYPERELASTIC RESPONSES OF A NON-METALLIC
HONEYCOMB CORE

The following faculty members have examined the final copy of this dissertation for form and content, and recommend that it be accepted in partial fulfillment of the requirement for the degree of Doctor of Philosophy, with a major in Aerospace Engineering.

Suresh Keshavanarayana, Committee Chair

Charles Yang, Committee Member

Nicholas. A. Smith, Committee Member

Klaus A. Hoffmann, Committee Member

Hamid M. Lankarani, Committee Member

Accepted for the College of Engineering

Dennis Livesay, Dean

Accepted for the Graduate School

Coleen Pugh, Dean

DEDICATION

To my parents and my wife

Innovation is the courage to explore the path no one else dares to.

ACKNOWLEDGEMENTS

I would like to thank my thoughtful advisor, Dr. Suresh Keshavanarayana, for his unconditional support, patience, wisdom, and guidance. I would also like to express my gratitude to my committee members, Dr. Charles Yang, Dr. Nicholas. A. Smith, Dr. Klaus A. Hoffmann and Dr. Hamid M. Lankarani for their useful suggestions, comments and patience at all stages of this project.

I appreciate my fellow Dmitrii Ivanov for his unconditional help and excellent performance in providing me with experimental results.

I am grateful to my parents for supporting me in everything- I cannot thank you enough for encouraging me throughout my Ph.D. studies.

Lastly, the most special thanks go to my wife for being the emotional support I needed to accomplish this task and all the sacrifices she has made for me.

ABSTRACT

In this research, a numerical homogenization approach to predict the experimentally observed nonlinear elastic, orthotropic and asymmetric responses of non-metallic honeycomb cores under large in-plane deformations is presented. A pragmatic approach to simulate the general in-plane and/or flexural loading of the bulk core is to homogenize the core behavior using a nonlinear equivalent-continuum (effective) constitutive model. To accomplish this, an anisotropic hyperelastic constitutive model was developed to capture the effective constitutive relations of the bulk honeycomb core. The hyperelastic constitutive model was assembled using data obtained from an experimentally validated Finite Element model of the Representative Volume Element or unit cell of the honeycomb core microstructure using curve-fitting methods. The hyperelastic material model was first evaluated using a single element model, which represented the unit cell of the honeycomb core, in a commercial nonlinear finite element program on which simple states of loading such as uniaxial tension and compression were imposed. After validation of the model using elementary simulations, it was employed for nonlinear finite element simulations of the bulk honeycomb core using simple continuum elements, subjected to complex loading and boundary conditions such as simulations of in-plane flexure and picture-frame pure shear tests. In this research, a commercial HRP-fiberglass/phenolic hexagonal cell honeycomb core was employed to generate benchmark data required to support and validate numerical models. Good agreement was observed between the model predictions and test data.

TABLE OF CONTENTS

Chapter	Page
1 INTRODUCTION	1
2 LITERATURE REVIEW	13
2.1 Linear Effective Constitutive Models.....	14
2.1.1 Mathematical Models.....	16
2.1.2 Numerical Models.....	26
2.2 Nonlinear Effective Constitutive Models	31
2.2.1 Mathematical Models.....	34
2.2.2 Hyperelastic Models	37
3 MOTIVATION, OBJECTIVES, AND METHODOLOGY.....	41
3.1 Motivation.....	41
3.2 Objectives	42
3.3 Methodology	43
4 EXPERIMENTS AND OBSERVATIONS.....	46
4.1 Honeycomb Core Cell Geometry Features and Material Properties	47
4.2 In-Plane Uniaxial Testing of Bulk Honeycomb Core.....	49
4.2.1 Result and Discussion	50
4.3 In-Plane Pure Shear Testing of Bulk Honeycomb Core	52
4.3.1 Digital Image Correlation (DIC) Measurements	55
4.3.2 Result and Discussion	59
4.4 In-Plane Off-Axis Pure Shear Testing of Bulk Honeycomb Core.....	69
4.4.1 Result and Discussion.....	70
4.5 In-Plane Flexure Testing of Bulk Honeycomb Core	76
4.5.1 Result and Discussion.....	78
5 FINITE ELEMENT MODEL OF HEXAGONAL HONEYCOMB CORE WITH DETAILED MICROSTRUCTURE	83
5.1 Finite Element Modeling of Core Unit Cell	83
5.2 Loading and Boundary Conditions	86
5.2.1 Uniaxial Simulations.....	87
5.2.2 Pure Shear Simulations	88
5.2.3 Multi-Axial Simulations	89
5.3 Result and Discussion.....	91
5.3.1 FEA Predictions of In-Plane Response.....	91
5.3.2 FEA Predictions of Out-of-Plane Reponse.....	97

TABLE OF CONTENTS (continued)

Chapter	Page
5.3.3	FEA Predictions of Multi-Axial Reponse..... 101
6	EFFECTIVE CONSTITUTIVE MODELLING OF FINITE STRAIN IN-PLANE RESPONSES OF HEXAGONAL HONEYCOMB CORE..... 103
6.1	Hyperelasticity : Preliminaries..... 106
6.2	Orthotropic Strain Energy Density Functions..... 108
6.3	Hyperelastic Constitutive Modelling of Hexagonal Honeycomb Core 116
6.3.1	Generalized Structural Tensor 116
6.3.2	Hyperelastic Constitutive Model for In-Plane Loading..... 122
6.3.3	Identification of Material Parameters for Hyperelastic Model 124
6.4	Implementation of Hyperelastic Material Model in FEA Program 128
6.5	Result and Discussion 133
6.5.1	Single Element Finite Element Analysis 133
6.5.2	Full Scale Honeycomb Core Finite Element Analysis 136
6.5.2.1	FEA Simulations of Picture-Frame Pure Shear Tests..... 136
6.5.2.2	FEA Simulations of In-Plane Flexure Tests 145
	SUMMARY, CONCLUSIONS AND FUTURE WORK 154
	REFERENCES 159
	APPENDIX..... 168
A.	User Subroutine Codes for Implementation of the Hyperelastic Constitutive Model in MSC Marc FEA Program..... 169

LIST OF TABLES

Table	Page
4-1 Mechanical Properties of the Constituents of Fiberglass/Phenolic Honeycomb Core [13, 15]	48
5-1 Boundary and Symmetry Constraints Used for Uniaxial FEA.....	87
5-2 Boundary and Symmetry Constraints Used for Pure Shear FEA.....	88
5-3 Boundary and Symmetry Constraints Used for Multi-Axial FEA	89
6-1 Material Parameters of Hyperelastic Constitutive Model for In-Plane Uniaxial Response of Fiberglass/Phenolic Honeycomb.....	126

LIST OF FIGURES

Figure	Page
1.1 Basic schematic of honeycomb sandwich panel [1].	1
1.2 Different honeycomb core cell configurations [1].	2
1.3 Principal material directions of honeycomb cores.	3
1.4 Different manufacturing methods of adhesively bonded commercial honeycomb cores [1].	4
1.5 Details of a commercial core cell along with its idealization.	4
1.6 The concept of homogenization and RVE.	5
1-7 In-plane nonlinear elastic responses of (a) HRP-fiberglass/phenolic [15] and (b) Nomex [12] hexagonal honeycomb cores under large compressive and tensile loadings.	7
1.8 Schematic of core-forming process alongside illustration of core cell deformations on convex and concave sides of core in (L-W) plane with its dominant failure modes [18, 19].	9
1.9 Schematics of flexural testing for studying the in-plane behavior of honeycomb core under complex loading scenarios.	10
2-1 Widely analyzed cellular structures in literature: (a) Auxetic and (b) Hexagonal honeycomb core [33].	13
2-2 Schematic of (a) uniaxial and (b) shear tests to determine the nine orthotropic effective elastic constants using the RVE of honeycomb core.	15
2-3 Ashby and Gibson’s analytical model for calculation of all nine orthotropic effective elastic constants of hexagonal honeycomb core [3, 36].	17
2-4 Summary of Masters and Evans model [7, 36].	18
2-5 Summary of Becker model [37].	19
2-6 Summary of Burton and Noor model [6].	20

LIST OF FIGURES (continued)

Figure	Page
2-7 Summary of Balawi and Abot model for commercial hexagonal honeycomb [5].	21
2-8 Summary of Malek and Gibson model for hexagonal honeycomb core to account for nodes at cell wall intersections [39].	22
2-9 Summary of Mukhopadhyay and Adhikari [8] model for irregular hexagonal honeycomb core with spatially random variations in cell angles.	23
2-10 Summary of model reported in [40] for honeycomb cores with curved cell walls.	24
2-11 Summary of model reported in [10] for commercial adhesively bonded hexagonal honeycomb core.	25
2-12 FEM of 1/8 segment of unit cell used by Penado [9].	26
2-13 FEM of sandwich panels used by Kayran and Aydincaak [42].	27
2-14 FEM of core cell: (a) 3D view, and (b) 1/4 symmetry [13].	28
2-15 FEA simulations of a bulk honeycomb core using a homogenized model for (a) a small strain and (b) a large strain analysis with respective constitutive models.	30
2-16 Effective shear stress-strain curves of (a) the regular hexagonal and (b) the auxetic hexagonal honeycomb cores under simple shear deformation [30].	33
2-17 Comparison between the nonlinear homogenized in-plane shear stress-strain response predicted by Lan and Fu [24] and linear model predicted by Ashby and Gibson [3].	35
3-1 Schematic of the numerical homogenization approach procedure.	45
4-1 Detailed geometry and dimensions of the HRP-honeycomb core cell [13, 15].	47
4-2 Schematic of uniaxial in-plane test apparatus and setup: (a) tension and (b) compression [13, 15].	49
4-3 Process of calculation of the homogenized quantities at each load step.	50

LIST OF FIGURES (continued)

Figure	Page
4-4 (a) Homogenized engineering stress-strain curves; (b) transverse strains versus longitudinal strains for in-plane tensile and compressive loads along L- and W-directions [13].	51
4-5 Geometry and dimensions of test specimen along with test apparatus for in-plane pure shear testing.	52
4-6 Schematic of the shear test fixture subjected to the applied tensile load along with the state of forces acting on the honeycomb core in (L-W) plane and its deformation [57].	53
4-7 View of test arrangement for in-plane pure shear testing of honeycomb core.	55
4-8 ARAMIS adjustable 6M, 3D DIC system set up.....	56
4-9 A speckle pattern created on the target (top) surface of the honeycomb core specimen for DIC measurments.	57
4-10 Facet size (comparable with the honeycomb core unit cell size), and overlap used for DIC computations.	57
4-11 DIC calculation of the homogenized local shear angle of the honeycomb core.	58
4-12 Axial force – crosshead displacement curve resulting from pure shear test along with the photo sequence of the test until the core collapse.	59
4-13 The distribution of <i>Green-Lagrange</i> strains calculated by ARAMIS DIC system at honeycomb core failure.....	61
4-14 Illustration of ribbon and transverse predefined paths for calculation of strains across the honeycomb core specimen in ARAMIS professional software	61
4-15 In-plane strain profiles along the two predefined paths across the honeycomb core measured by ARAMIS at four different axial force levels	62
4-16 Corner-pin locations for finite element stress analysis [59]	63

LIST OF FIGURES (continued)

Figure	Page
4-17 Average shear stress-shear angle curve for fiberglass/phenolic honeycomb core resulting from shear test data	64
4-18 Local shear angle (γ_{LW} [deg]) contours measured by ARAMIS DIC system at different stages of axial force on the picture-frame cross-head.	66
4-19 Max., Min. and Avg. values of the local shear angle and normal strains over the central area of the core specimen calculated by ARAMIS DIC system for each frame.	67
4-20 Schematic of off-axis pure shear testing conducted on HRP-fiberglass/phenolic honeycomb core along with the state of stresses acting on the core specimen in (L-W) plane.....	69
4-21 Geometry and dimensions of the off-axis honeycomb core specimen along with the final fabricated core for mounting in the picture-frame fixture and DIC analysis.	70
4-22 Axial force - displacement curve resulting from off-axis pure shear test along with the photo sequence of the test until the core collapse.	71
4-23 The distribution of <i>Green-Lagrange</i> strains calculated by ARAMIS DIC system at the honeycomb core failure.....	72
4-24 In-plane strain distributions along the sketched ribbon and transverse paths across the honeycomb core measured by ARAMIS at four different axial force levels.....	73
4-25 Average values of strains in principal directions (L-W) over the central part of the core specimen calculated by ARAMIS DIC system for each frame.....	74
4-26 Average shear stress-shear angle diagram for the HRP- honeycomb core obtained from off-axis (X-Y) pure shear test and comparison with the test data for the pure shear in (L-W) plane.	75
4-27 Geometry and dimensions of honeycomb beam specimens together with their respective orientations for cantilever bending tests.	76
4-28 Honeycomb core specimen in the deformed state under flexural loading.	77

LIST OF FIGURES (continued)

Figure	Page
4-29 Load-Displacement plots from in-plane flexure tests in (L-W) and (W-L) planes.	78
4-30 The contours of <i>Green-Lagrange</i> strains calculated by ARAMIS DIC system at failure load.	79
4-31 Profiles of in-plane <i>Green-Lagrange</i> strains across the width of the (a) long and (b) short honeycomb beams with L (X)-W(Y) orientation.....	80
4-32 Profiles of in-plane <i>Green-Lagrange</i> strains across the width of the (a) long and (b) short honeycomb beams with W (X)-L(Y) orientation.....	81
5-1 (a) A unit cell (RVE) of hexagonal honeycomb core; (b) 1/2 symmetry unit cell with half-thickness; (c) an elemental strip of the half symmetry unit cell used in FEA.....	84
5-2 Constitutive modelling of the cell wall of HRP-fiberglass/phenolic core in FEM [13]....	85
5-3 Identification of boundary edges (E) and surfaces (S) to define symmetry and boundary conditions.....	86
5-4 3D views of FEMs of honeycomb core with and without adhesive layer and fillets.	90
5-5 Effective engineering stress-strain curves obtained from FEA and comparison with test data [13, 15] for in-plane (L-W) uniaxial loadings.	91
5-6 FEA predictions of Poisson’s effects for uniaxial tests along ribbon (L) and transverse (W) directions and comparison with test data [13, 15].	93
5-7 FEA predictions using the half thickness RVE and comparison with FEA results predicted by an elemental strip RVE.	94
5-8 Effective engineering stress-strain curves for pure shear loading in (L-W) plane.	95
5-9 In-plane (L-W) deformed configuration of honeycomb core cell walls under uniaxial and pure shear loadings.....	95

LIST OF FIGURES (continued)

Figure	Page
5-10 Comparison of FEA predictions with previous linear models reported in literature.....	96
5-11 FEA predictions for uniaxial tests in thickness (T) direction.....	97
5-12 Effective engineering stress-strain curves for pure shear loading in (L-T) and (W-T) planes	99
5-13 Out-of-plane deformed configuration of honeycomb core cell walls under different loading cases.	100
5-14 Equi-biaxial tension and compression curves obtained from FEA.	101
5-15 FEA prediction of HRP-fiberglass/phenolic honeycomb core under hydrostatic compression.	102
6-1 Change in volume of HRP- honeycomb under uniaxial in-plane loadings [13].	105
6-2 Physical interpretation of invariants $tr(CN_i)$ and $tr(CN_iCN_j)$ in principle plane (1-2).....	110
6-3 Representations of reference and actual configuration and corresponding geometric mappings [69].	111
6-4 Illustrations of one-dimensional convex , strictly convex and non-convex functions from Ebbing [69].....	112
6-5 Example of an unstable hyperelastic material model.	113
6-6 General fiber-reinforced material [64].	117
6-7 Schematic of principal material directions and secondary fiber directions for hexagonal honeycomb core in the (L-W) plane.....	119
6-8 Least-squares fit of polyconvex orthotropic SEDF using data from FEM of RVE of HRP- fiberglass/phenolic honeycomb core.	127

LIST OF FIGURES (continued)

Figure	Page
6-9	Schematic model of the homogenized unit cell of hexagonal honeycomb core along with boundary conditions used in FEA for elementary axial simulations. 128
6-10	Definition of structural tensors for characterizing the principal material directions of hexagonal honeycomb cores oriented at an angle α to the X direction. 130
6-11	Summary of finite element analysis using hyperelastic constitutive model implemented by means of user-subroutine in MSC Marc program. 132
6-12	(a) Engineering stress-strain curves, (b) Poisson’s effects, and (c) strain energy densities predicted by FEM using hyperelastic material model and comparison with test data and FEM using orthotropic material model. 134
6-13	Equi-biaxial tension and compression predicted by FEM using hyperelastic material model and comparison with FEM of core RVE. 135
6-14	Geometry and boundary conditions along with the material orientations setup used for FEA simulations of in-plane (L-W) and off-axis (X-Y) pure shear tests. 137
6-15	Global load-displacement diagrams predicted by FEMs and comparison with test data for pure shear deformation in (L-W) plane. 139
6-16	In-plane <i>Green-Lagrange</i> strains contours predicted by the FEM. 139
6-17	Shear strain profiles along the two predefined paths obtained from FEM at different load stages and comparison with test data (DIC). 140
6-18	Global load-displacement diagrams predicted by FEMs and comparison with test data for pure shear deformation in (X-Y) plane. 141
6-19	In-plane <i>Green-Lagrange</i> strains contours predicted by the FEM. 142
6-20	Longitudinal strains profiles along the two predefined paths obtained from FEM at different load stages and comparison with test data (DIC). 143
6-21	FEA predictions with constant and variable shear modulus and comparison with test data for HRP-honeycomb core. 144

LIST OF FIGURES (continued)

Figure	Page
6-22	Finite element models of the in-plane cantilever-honeycomb beam tests..... 145
6-23	Deformed configuration of the honeycomb core beams under flexure in (L-W) plane with different cell orientation vectors for ribbon (L) and transverse (W) directions..... 146
6-24	Principal material (L, W) orientations for the initial and deformed configurations of cantilever honeycomb beams..... 147
6-25	Comparison of load-displacement curves predicted by FEMs of cantilever HRP-fiberglass/phenolic honeycomb beam with test data. 148
6-26	Profiles of in-plane strains across the width of the long honeycomb beam with (L (X)-W(Y)) orientation. 149
6-27	Profiles of in-plane strains across the width of the short honeycomb beam with (L (X)-W(Y)) orientation. 150
6-28	Profiles of in-plane strains across the width of the long honeycomb beam with (W (X)-L(Y)) orientation. 151
6-29	Profiles of in-plane strains across the width of the short honeycomb beam with (W (X)-L(Y)) orientation. 152

LIST OF ABBREVIATIONS

RVE	Representative Volume Element
SEDF	Strain Energy Density Function
FEA	Finite Element Analysis
FEM	Finite Element Model
DIC	Digital Image Correlation
HRP	Heat-Resistant Phenolic Resin
Det ()	Determinant of ()
Cof ()	Co-factor of ()
Tr ()	Trace of ()
J	Jacobian

LIST OF SYMBOLS

L	Ribbon Direction
W	Transverse Direction
T	Through Thickness Direction
σ_{ij}	Engineering Stress Tensor
S_{ij}	Second Piola - Kirchhoff Stress Tensor
ε_{ij}	Engineering Strain Tensor
E_{ij}	Green - Lagrange strain tensor
γ_{ij}	Engineering Shear Strains
D_{ijkl}	Fourth - Order Stiffness Tensor
E_{ii}	Young's Moduli
G_{ij}	Lame's Shear Moduli
ν_{ij}	Poisson's Ratios
C_{ij}	Right Cauchy–Green Deformation Tensor
F_{ij}	Deformation Gradient Tensor
I_{ij}	Second - Order Identity Tensor

LIST OF SYMBOLS (continued)

N_{ij}	Second - Order Structural Tensor
R_{ij}	Second - Order Orthogonal Tensor
λ_i	Stretch Ratios

CHAPTER 1

INTRODUCTION

Honeycomb cores are discrete and anisotropic materials which are extensively used in weight sensitive structural applications, such as in aerospace, automotive and marine industries because of their high through-thickness stiffness-to-weight ratios [1]. These materials are commonly used in sandwich panels, consisting of two relatively thin, high density and high stiffness face sheets, adhesively bonded to a soft, relatively thicker and low density core, as illustrated in Figure 1.1. In general, the core carries transverse shear load and separates the face sheets, while face sheets carry in plane loads and bending moments [2]. High flexural stiffness resulting in enhanced stability, excellent fatigue resistance, noise abatement, are some of the features of honeycomb sandwich panels [1].

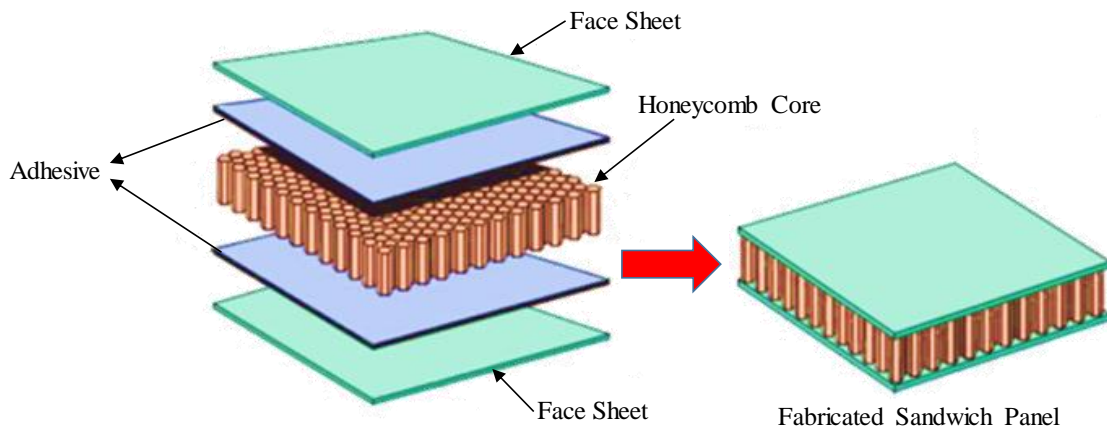


Figure 1.1. Basic schematic of honeycomb sandwich panel [1].

The honeycomb cores are available in a multitude of cell geometries and cell wall materials which offer unique advantages in terms of weight savings, sandwich panel manufacturability, sandwich stiffness and strength, etc. [1]. The honeycomb cores are made from different metallic or non-metallic web (thin flat sheet) materials including aluminium, stainless steel, fiberglass,

Nomex, Kraft paper, etc. [1, 3]. Figure 1.2 shows the common cell shapes of honeycomb cores which include hexagon and their variants, square, and flex-core [1, 4]. The hexagonal cells are the most common geometric configuration owing to the advantages they offer in manufacturing. Other cell geometries are essentially variants of the hexagonal shape to achieve specific properties for the bulk core.

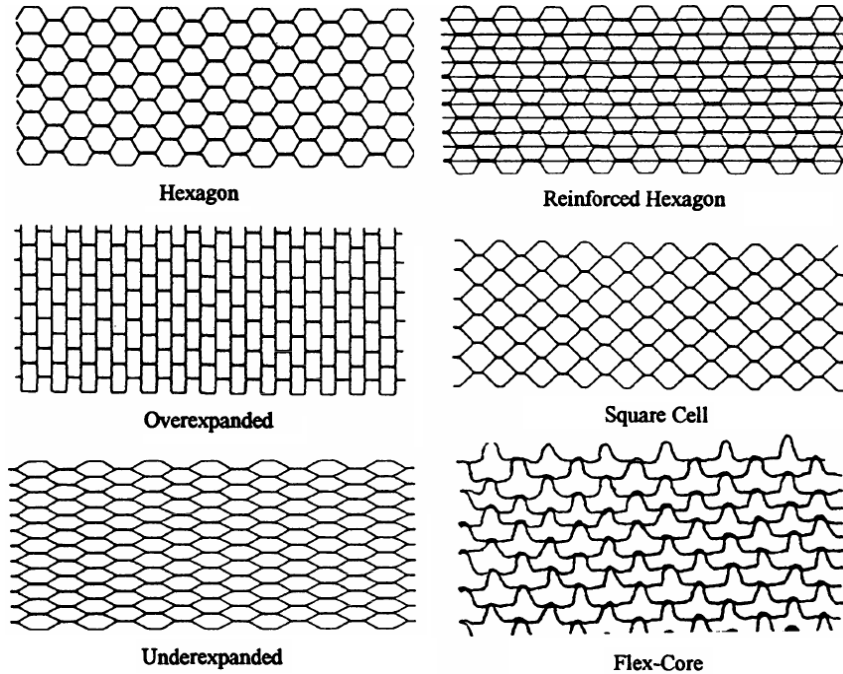


Figure 1.2. Different honeycomb core cell configurations [1].

The mechanical properties for honeycomb cores are often reported along the three principal material directions denoted by ribbon (L), transverse (W) and through thickness (T) directions, as illustrated in Figure 1.3. The honeycomb core properties which are commonly published by the core manufacturers are the following: the nominal core density and core cell size, compressive (and crush) strength and modulus in (T) direction, shear strengths and moduli in the (L-T) and (W-T) planes [4]. The in-plane (L-W) moduli and strengths of the honeycomb cores are seldom reported as they are considerably low and deemed inconsequential in the stress analysis of sandwich structures where the high-modulus face sheets dominate the load carrying process.

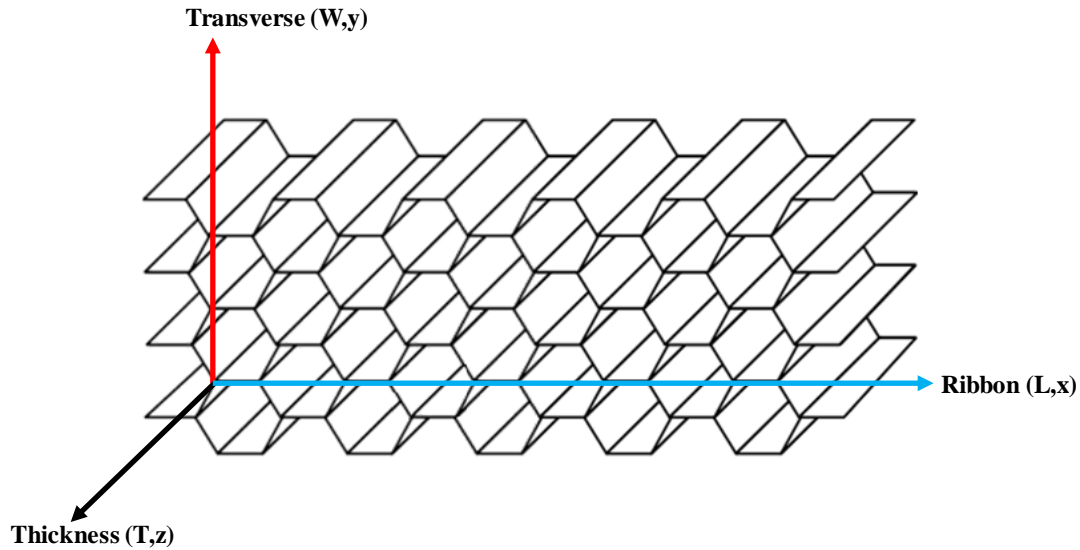


Figure 1.3. Principal material directions of honeycomb cores.

There are several widely used methods to make honeycomb cores which include adhesive bonding, resistance welding, brazing, diffusion bonding and thermal fusion [1]. However, adhesive bonding is the most common manufacturing method. In this method, adhesive node lines are printed on sheet material, and then one of two different techniques is used to convert a sheet material into honeycomb core: the expansion process and corrugation process, both of which are illustrated in Figure 1.4. It should be noted that the node adhesive in corrugated cores can be 10% of the total honeycomb weight, while it is only about 1% or less in expanded cores [1]. The typical core cell geometry of adhesively bonded honeycomb cores is composed of double cell walls corresponding to the adjacent ribbons being bonded together, single or inclined cell walls, cell wall curvatures, adhesive layers, and adhesive fillets at the node intersections. These features are shown schematically in Figure 1.5. The geometry of an idealized core cell, which is mostly used in the numerical and analytical analyses reported in literature, is also shown in the same figure.

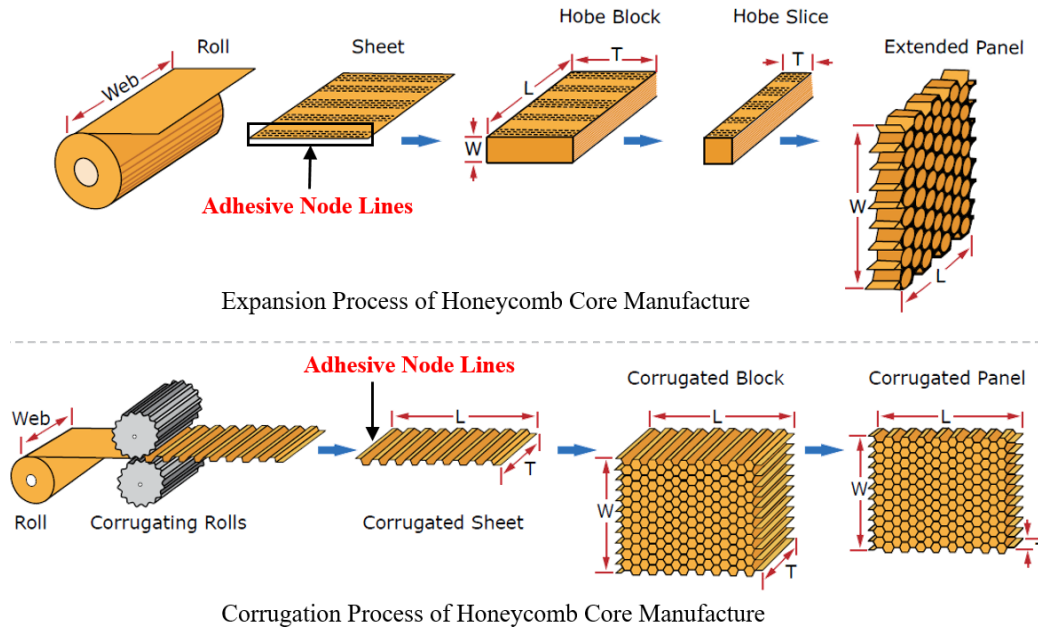


Figure 1.4. Different manufacturing methods of adhesively bonded commercial honeycomb cores [1].

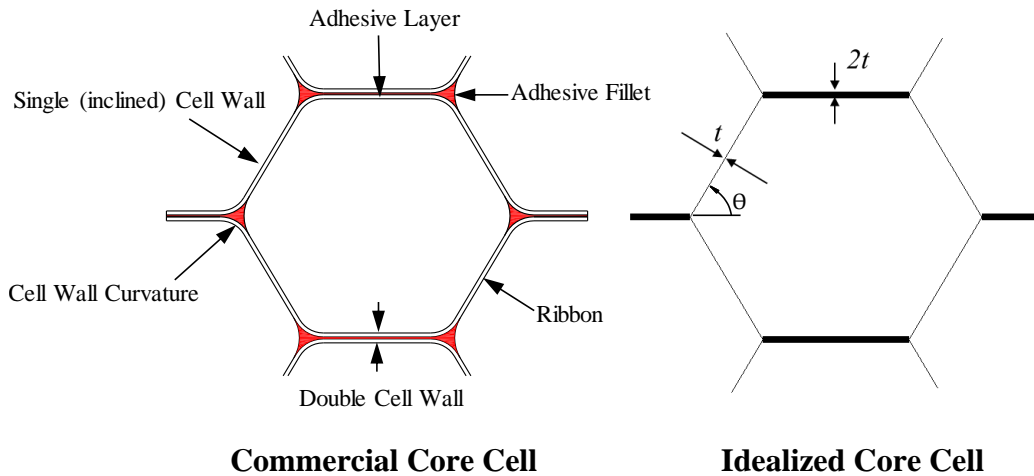


Figure 1.5. Details of a commercial core cell along with its idealization.

Due to complexity associated with the geometry of honeycomb core structures, to analyze large-scale honeycomb core sandwich structures, it is computationally more efficient to model the core as a homogenized solid with equivalent mechanical properties rather than considering the detailed cellular structure. As illustrated in Figure 1.6, for the homogenization analysis, a honeycomb core material which occupies a domain Ω with an external boundary $\partial\Omega$ has to be

replaced by a similar body Ω^* with the same shape and an external boundary $\partial\Omega^*$. Both bodies have to be subjected to the same external loads (t_i, f_i) and displacements (u_i), as illustrated in the same figure. The body Ω^* is supposed to consist of the homogeneous effective medium with yet unknown properties. Because of the periodic and regular microstructural pattern associated with the cellular material such as hexagonal honeycomb core, homogenized mechanical properties of the core can be obtained by considering a representative volume element (RVE) or unit cell of the body Ω with the given microstructure and a corresponding RVE* of the homogenized body Ω^* , instead of considering the full core, as shown in Figure 1.6. The properties of the RVE must be determined in such a way that the mechanical behavior of both volumes are identical at the macroscopic level. This can be accomplished by proper selection of boundary and loadings conditions.

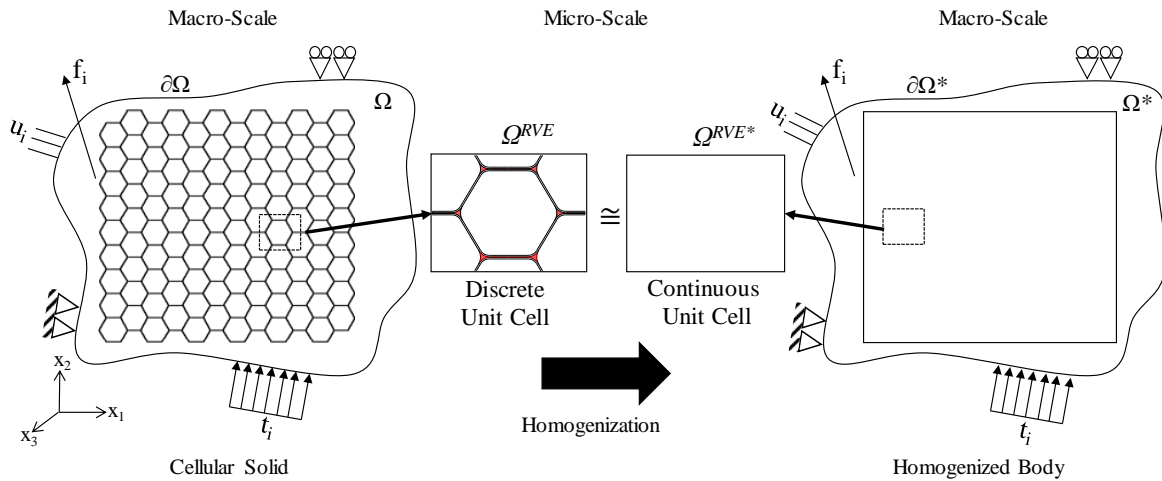


Figure 1.6. The concept of homogenization and RVE.

Depending on the type of analysis, linear or nonlinear orthotropic effective constitutive models¹ must be employed to capture the mechanical behavior of the core under different loading and boundary conditions.

¹ Effective constitutive models refer to homogenized equivalent-continuum constitutive models.

In the analysis of sandwich structures that employ high modulus facesheets, the magnitude of core deformations are constrained by the facesheets, thus facilitating the use of homogenized core properties based on a small strain assumption. A linear orthotropic effective constitutive law can be used to describe the homogenized behavior of the core in the small strain regime. The homogenization of the honeycomb core and determination of the nine orthotropic effective elastic constants of the honeycomb core have been extensively investigated by several researchers, and reviews of previous studies have also been documented [3, 5-11]. Among the models developed to predict the mechanical properties of the honeycomb cores, almost all of them are only applicable to ideal cores. In other words, perfect bonding is assumed between the adjacent ribbons and a detailed geometric treatment of the fillet region, as shown in Figure 1.5, are ignored in the analyses.

To study the mechanical responses of honeycomb cores under large deformations, it is useful to distinguish between in-plane (L-W) and out-of-plane (T-L or T-W) responses of the cores. The in-plane deformation analysis is referred to as cellular deformation analysis and is ascribed to the mechanism(s) by which the honeycomb core cell walls deform [3]. For composite or non-metallic honeycombs, in general, at room temperature, the in-plane mechanical responses of the bulk material are nonlinear, asymmetric, anisotropic, and fully recoverable (elastic) in the finite strain regime [12-14]. This is attributed to the geometric non-linearity (small strain, large rotation) associated with flexural deformations of the inclined cell walls. Moreover, as deformations increase, two geometric phenomena including densification (at which point the cell walls start closing up within their longitudinal direction) under tensile-dominated loads and shear instability (at which point the double-thickness cell walls rotate in the opposite direction) under compressive-dominated loads may result in stiffening and softening responses, respectively, of the honeycomb core, thereby resulting in the observed asymmetric behavior.

These phenomena are depicted in Figure 1-7 for two widely used composite hexagonal honeycombs in the aerospace industry [12, 15].

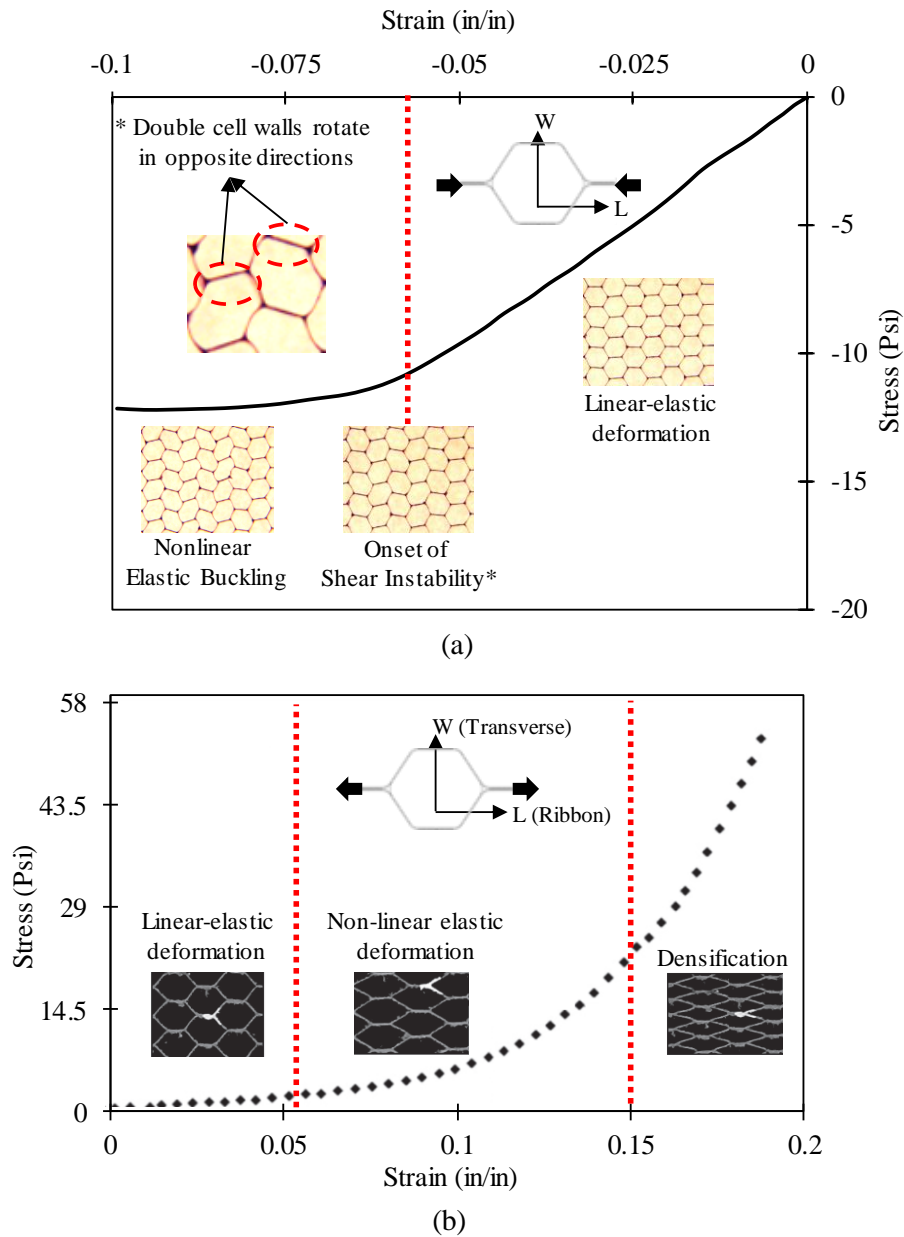


Figure 1-7. In-plane nonlinear elastic responses of (a) HRP-fiberglass/phenolic [15] and (b) Nomex [12] hexagonal honeycomb cores under large compressive and tensile loadings.

It is evident from that the linear-elastic constitutive laws can only be adopted to capture the behavior of the cores at the small strain levels, up to which point the classical *Bernoulli-Euler* beam theory [3] can be used to analyze the bending deformation of the inclined cell walls.

On the other hand, out-of-plane properties are mainly required for design of honeycomb cores in sandwich panels and dominated by the mechanical properties of the cell materials and not the cellular deformation [3]. Furthermore, under in-plane loadings, out-of-plane (W-T, W-L) Poisson's contraction effects are almost zero [3]. This unique behavior can be advantageous for decoupling the in-plane and out-of-plane effective constitutive models for the loading scenarios wherein the in-plane deformations dominate the overall deformation of the honeycomb cores.

Forming and shaping of the flat honeycomb cores for use in high-performance structural applications, such as airframe structural sandwich panels with complex curvatures, is one of the important processing operations in the fabrication of composite honeycomb structures. The forming of polymer matrix-based cores is performed at elevated temperatures, wherein the honeycomb core cells experience large in-plane deformations (L-W plane) owing to flexure resulting from out-of-plane loading. The inelastic strains accumulated at elevated temperatures due to creep/relaxation of the material help preserve most of the imposed deformation. The deformed core is then bonded to the facesheets using a co-cure co-bond process [16, 17]. This process is shown schematically in Figure 1.8. During the core-forming process, node bond failures [18, 19] due to separation of the adjacent ribbons are the dominant failure mode of the core.

Numerical simulations of the core forming processes would be desirable to minimize the hitherto trial and error approach used to achieve complex shaped cores without node bond failures. To accomplish this, the bulk honeycomb core behavior has to be modelled with the required orthotropy and nonlinearity observed under large deformations.

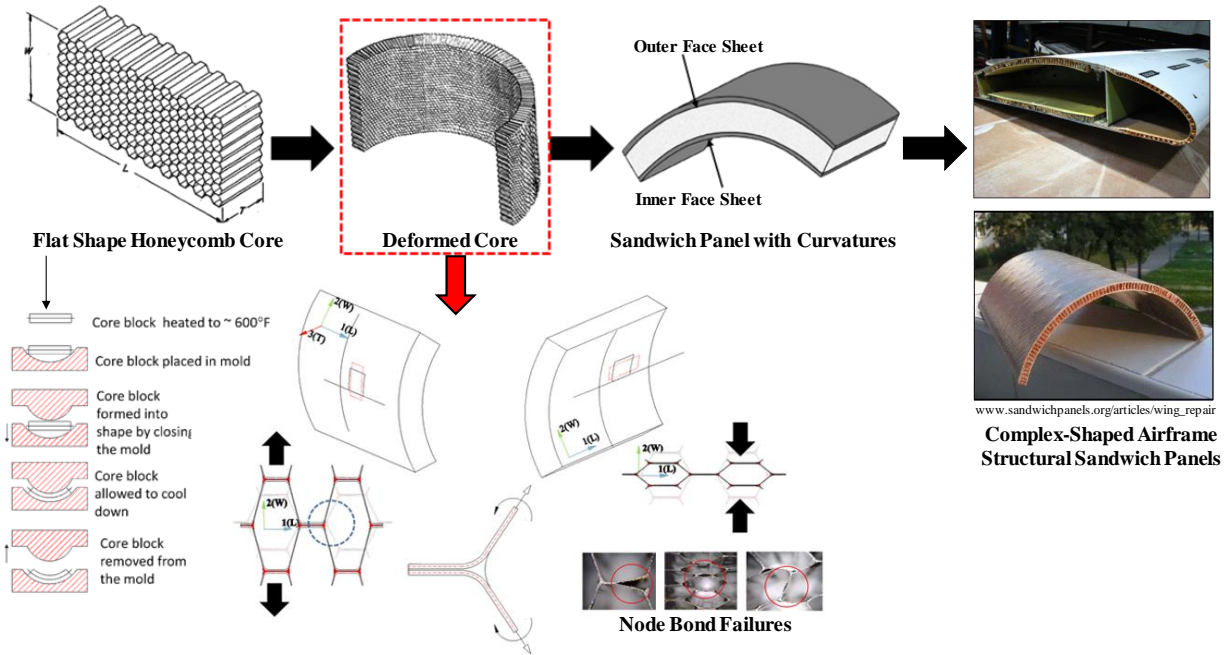


Figure 1.8. Schematic of core-forming process alongside illustration of core cell deformations on convex and concave sides of core in (L-W) plane with its dominant failure modes [18, 19].

There are several analytical studies published in open literature [20-24] that develop nonlinear constitutive relations based on the large deflection beam theory [25] for capturing the in-plane deformations of hexagonal honeycomb cores with an idealized cell geometry shown in Figure 1.5. These methods are based on solving a set of nonlinear governing differential equations resulting from the inclusion of the large rotation effects, as well as the elastic buckling, in derivation of the governing equations for bending analysis of the cell walls. However, these models cannot be used to capture the behavior of the commercial honeycomb cores due to ignoring of the inclusion of node bond adhesive fillets. As reported in [13], increased node bond adhesive fillet size significantly stiffens the mechanical responses of honeycomb core under large uniaxial in-plane deformation. Moreover, it is almost infeasible to employ these models as effective constitutive models of the core in finite element software. The limitations are due to the complexity associated

with the mathematical derivations and the fact that the analytical models may only be used for analysing the honeycomb cores under simple load cases such as uniaxial and shear deformations.

Owing to the physical dimensions of the bulk core involved in the forming process, detailed modelling of the core cells would be computationally prohibitive. A pragmatic approach to simulate the general in-plane and/or flexural loading of the bulk core is to homogenize the core behavior using a suitable constitutive model. To the best of the author's knowledge, no publication is available in open-literature which specifically discusses the simulations of commercial honeycomb cores subjected to the complex in-plane/out-of-plane loading scenarios such as bending simulations, as shown in Figure 1.9. Since the out-of-plane moduli of the core are orders of magnitude higher than the in-plane moduli, the flexural behavior of core will be dominated by the large-in plane deformations of the cells.

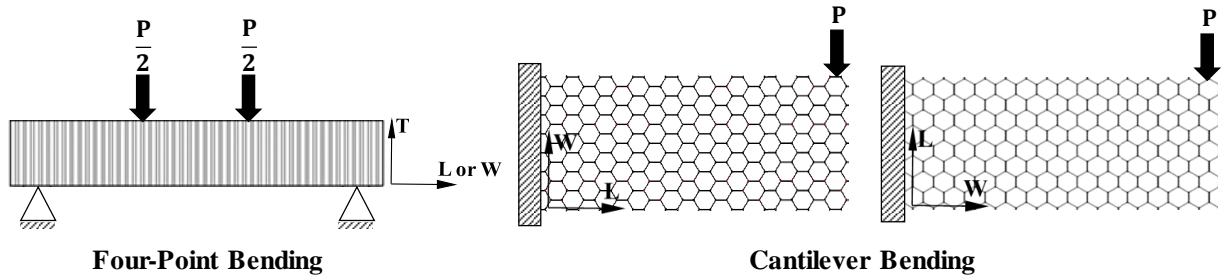


Figure 1.9. Schematics of flexural testing for studying the in-plane behavior of honeycomb core under complex loading scenarios.

The direction-dependent, asymmetric, and nonlinear-elastic responses of non-metallic honeycomb cores point toward the suitability of a hyperelastic material formulation for use in homogenized models of the honeycomb cores. Furthermore, it has been shown [13] that honeycomb cores must be considered as compressible materials in the homogenization process, particularly under large deformations.

The formulation of a hyperelastic behavior law lies on the proposition of a Strain Energy Density Function (SEDF)². The inherent behavior of materials such as anisotropy, compressibility, etc., must be captured by the respective SEDF [26].

There are only a few studies [27-30] that employ hyperelastic constitutive models to predict the in-plane nonlinear effective stress-strain curves of idealized cellular materials at finite strains. The findings of this study highlight the nonlinear core behavior, which is restricted to a specific loading scenario, but cannot provide a complete picture of the nonlinear anisotropic deformations of the honeycomb

In this research development of a nonlinear effective constitutive model for capturing the in-plane, asymmetric (tension/compression), nonlinear elastic responses of commercial non-metallic hexagonal honeycomb cores in the finite strain regime is presented. The main goal of the present research was to employ an appropriate hyperelastic constitutive model to simulate the bulk core behavior using simple continuum elements in a finite element program subjected to complex loading scenarios, such as in-plane and transverse flexure shown in Figure 1.9. To accomplish this, an orthotropic compressible hyperelastic constitutive model, using a polyconvex strain energy density function (SEDF) was employed for modelling the in-plane behavior of commercial hexagonal honeycomb cores. The hyperelastic constitutive model was assembled by nonlinear curve fitting of effective engineering stress-strain curves obtained from an experimentally validated finite element model of the representative unit cell of a commercial adhesively bonded HRP-fiberglass/phenolic hexagonal honeycomb core under large in-plane uniaxial and pure shear loadings. The hyperelastic model was then implemented in a commercial finite element program (MSC Marc [31]) employing user-subroutines. The hyperelastic constitutive model was evaluated

² The strain-energy density of a material is defined as the strain energy per unit volume.

under simple states of loading using a single element finite element analysis. The predictions of the model including the stress-strain behavior, Poisson effects, and the strain energy densities were compared with test data for the in-plane uniaxial tension/compression as well as the pure shear responses of the HRP-honeycomb core. Good agreement was observed between the model predictions and test data.

After validation of the hyperplastic model using the elementary simulations, it was used for nonlinear FEA simulations of the bulk HRP-honeycomb core subjected to complex loading and boundary conditions including the simulations of picture-frame pure shear and in-plane flexure tests. There was a reasonable agreement between the FEA with hyperelastic material model predictions and experimental results for the HRP-honeycomb core.

In this research ARAMIS DIC system [32] was also used to measure homogenized surface strain and displacement fields in the core specimen during the deformation process to validate FEA simulations of the bulk honeycomb core.

The proposed homogenization approach can be employed for nonlinear FEA simulations of honeycomb core forming processes to provide design guidelines and forming process limits to prevent node bond failures during the manufacturing of complex-shaped sandwich panels.

CHAPTER 2

LITERATURE REVIEW

The homogenization of the honeycomb cores and development of the effective constitutive models, have been investigated by several researches. Several types of honeycomb cores have been considered in the literature, including hexagonal, rectangular, triangular, re-entrant and etc. However, hexagonal honeycomb cores and recently, re-entrant or auxetic honeycomb cores (see Figure 2-1) [33], those which have negative Poisson's ratio, have been the most commonly analyzed core.

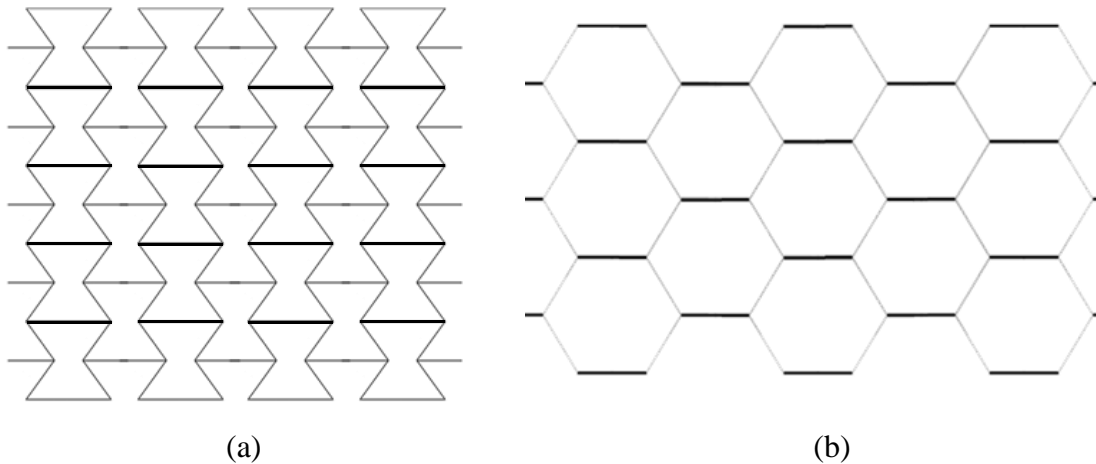


Figure 2-1. Widely analyzed cellular structures in literature: (a) Auxetic and (b) Hexagonal honeycomb core [33].

Mechanical characterization of honeycomb cores and development of the effective constitutive relations to describe the homogenized behavior of the cores can be investigated analytically, numerically or through experiments. Based on previous experimental data and theory [12], in general, honeycomb cores can be classified as orthotropic materials with three principal material directions due to their inherent cellular structure, as depicted in Figure 1.3. Under this assumption, an orthotropic effective constitutive law must be used to describe the homogenized

mechanical responses of the core. However, depending on the homogenized core responses which can be linear or nonlinear, a compliant constitutive model must be employed.

The intent of the article review in this section rest on the following purposes: first, to provide the deep insight into understanding the mechanics of deformation of the honeycomb cores; second, to understand the homogenization of the cores and determination of the effective continuum constitutive relations (linear and nonlinear) and finally to highlight the shortcomings of the proposed constitutive models discussed in open literature.

The review presented herein considers key publications whose findings are pertinent to this investigation which are the homogenized constitutive models proposed by different authors for in-plane and out-of-plane mechanical properties of honeycomb cores. However, emphasis is on constitutive models employed to characterize the in-plane mechanical responses of the cores. To facilitate the understanding of the proposed constitutive models, the review of publications is divided into two major areas which include the linear and nonlinear effective continuum constitutive models.

2.1 Linear Effective Constitutive Models

To describe the mechanical behavior of continuum honeycomb cores under small deformations, a linear effective constitutive law must be employed. The honeycomb core conforms to generalized Hooke's law for a specially orthotropic material [34] which is expressed as

$$\begin{bmatrix} \bar{\sigma}_{11} \\ \bar{\sigma}_{22} \\ \bar{\sigma}_{33} \\ \bar{\sigma}_{23} \\ \bar{\sigma}_{13} \\ \bar{\sigma}_{12} \end{bmatrix} = \begin{bmatrix} \bar{D}_{11} & \bar{D}_{12} & \bar{D}_{13} & 0 & 0 & 0 \\ \bar{D}_{12} & \bar{D}_{22} & \bar{D}_{23} & 0 & 0 & 0 \\ \bar{D}_{13} & \bar{D}_{23} & \bar{D}_{33} & 0 & 0 & 0 \\ 0 & 0 & 0 & \bar{D}_{44} & 0 & 0 \\ 0 & 0 & 0 & 0 & \bar{D}_{55} & 0 \\ 0 & 0 & 0 & 0 & 0 & \bar{D}_{66} \end{bmatrix} \begin{bmatrix} \bar{\epsilon}_{11} \\ \bar{\epsilon}_{22} \\ \bar{\epsilon}_{33} \\ 2\bar{\epsilon}_{23} \\ 2\bar{\epsilon}_{13} \\ 2\bar{\epsilon}_{12} \end{bmatrix} \quad (2.1)$$

where $\bar{\sigma}$, $\bar{\varepsilon}$ and \bar{D} are respectively the homogenized stress, strain and stiffness tensors for a homogenized RVE of the core. The components of the symmetric stiffness tensor are expressed as

$$\begin{aligned} \bar{D}_{ii} &= \bar{E}_i \frac{1 - \bar{\nu}_{jk} \bar{\nu}_{kj}}{\Delta}, \quad \bar{D}_{ij} = \bar{D}_{ji} = \bar{E}_i \frac{\bar{\nu}_{ij} + \bar{\nu}_{kj} \bar{\nu}_{ik}}{\Delta}, \quad i \neq j \neq k \neq i, \quad i, j = 1, 2, 3 \\ \Delta &= 1 - \bar{\nu}_{12} \bar{\nu}_{21} - \bar{\nu}_{13} \bar{\nu}_{31} - \bar{\nu}_{23} \bar{\nu}_{32} - 2 \bar{\nu}_{21} \bar{\nu}_{13} \bar{\nu}_{32} \\ \bar{D}_{44} &= \bar{G}_{23}, \quad \bar{D}_{55} = \bar{G}_{13}, \quad \bar{D}_{66} = \bar{G}_{12} \end{aligned} \quad (2.2)$$

where \bar{E}_i ($i = 1, 2, 3$), $\bar{G}_{ij} = \bar{G}_{ji}$ and $\bar{\nu}_{ij} = (\bar{E}_i / \bar{E}_j) \bar{\nu}_{ji}$ ($i \neq j = 1, 2, 3$) which respectively denote the Young's moduli, Lamé's shear moduli and Poisson's ratios, are the orthotropic effective elastic constants for the whole geometry of the RVE of honeycomb core.

To determine all the nine orthotropic effective elastic constants and assemble the stiffness matrix, six elementary boundary conditions are needed to be applied on the RVE, which refer to three uniaxial extensions and three shear deformations. This process is illustrated schematically in Figure 2-2.

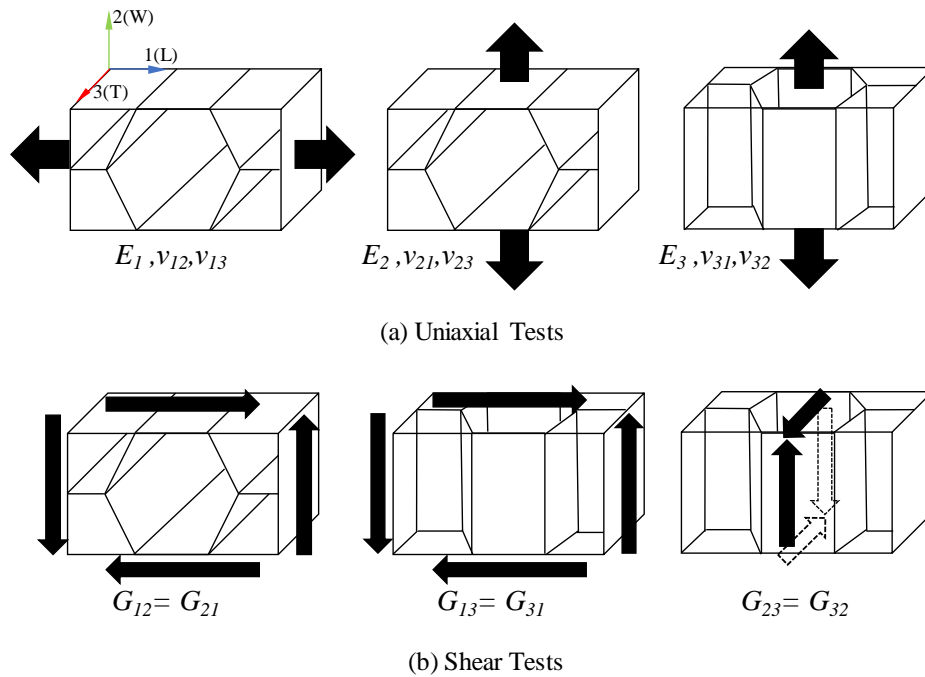


Figure 2-2. Schematic of (a) uniaxial and (b) shear tests to determine the nine orthotropic effective elastic constants using the RVE of honeycomb core.

2.1.1 Mathematical Models

The mathematical models developed by several researchers to determine the orthotropic effective elastic constants of honeycomb cores are summarized in this section.

Gibson and Ashby [3] presented the earliest and most widely referenced analytical model to determine the nine engineering effective elastic constants of the low density hexagonal honeycomb cores. Figure 2-3 shows the geometric parameters of the honeycomb core unit cell used in their analysis. The model was developed for idealized low density core ($(t/l) \ll 1$) and the presence of double cell walls, node bond adhesive and its fillet region as well as the cell wall curvatures were not considered in the analysis. The primary model for predicting the in-plane moduli and Poisson's ratios was developed by modelling the inclined cell walls as cantilever beams fixed at the one end and guided at the other end, as shown in Figure 2-3. The classical (Euler-Bernoulli) beam theory [35] without considering transverse shear effects was used to determine the in-plane effective elastic constants of the honeycomb core. The axial deformations of the cell walls were also ignored in the analysis.

All nine orthotropic effective elastic constants obtained by their analytical analysis for irregular hexagonal honeycomb core are shown in Figure 2-3. As is illustrated in the figure, the expression for effective elastic constants are presented in terms of elastic properties of the cell walls (E_s, ν_s and G_s) and geometric parameters defining the core cell. Note that regular hexagonal honeycombs have equal sides and the internal angles are all 120° ; besides the cell walls are all of the same thickness. Therefore, six planes of symmetry (in-plane) can be identified and material exhibit transversely isotropic properties. The in-plane properties of regular hexagonal honeycomb cores can be characterized by only two elastic constants (E and ν). As shown in Figure 2-3, the

prediction of out-of-plane moduli are greater than in-plane moduli by a factor of $(t/l)^2$. Furthermore, upper and lower bounds for the out-of-plane shear moduli were obtained.

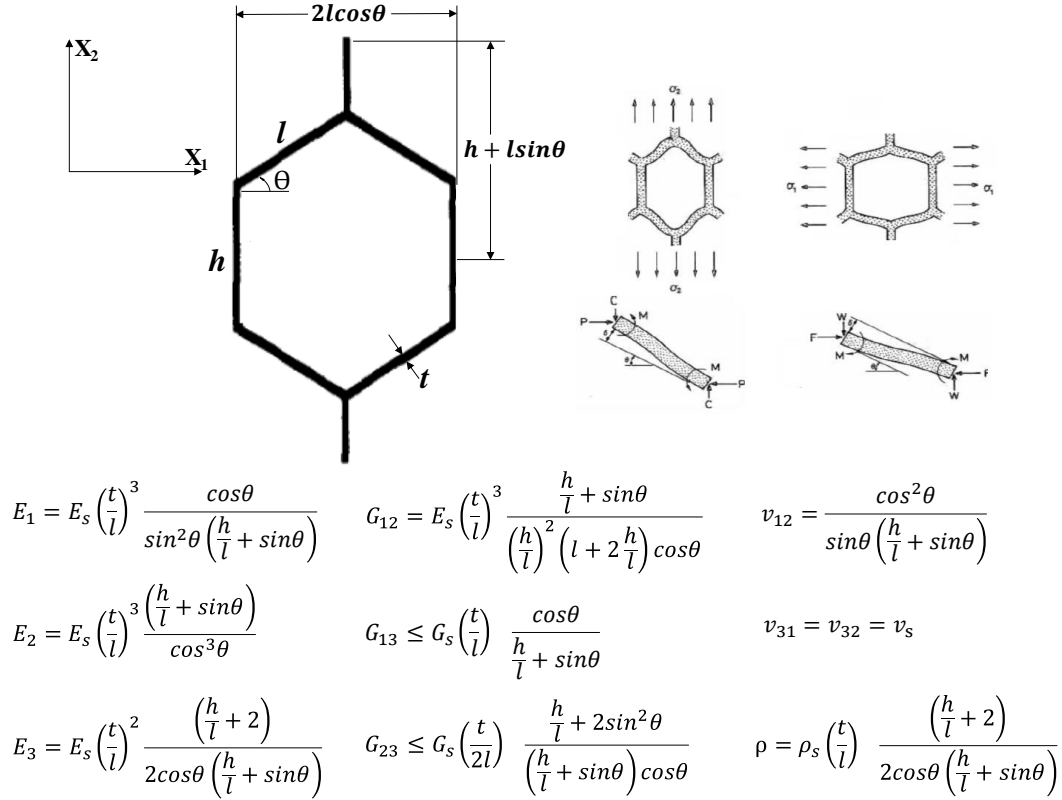


Figure 2-3. Ashby and Gibson's analytical model for calculation of all nine orthotropic effective elastic constants of hexagonal honeycomb core [3, 36].

Masters and Evans [7] modified the Gibson and Ashby [3] model by incorporating the three mechanisms of flexing, hinging, and stretching in their model, in order to address the bending, shear, and axial deformations of the cell walls for more accurate prediction of the effective in-plane elastic constants. Three deformation mechanisms were captured in terms of force constants K_f , K_s and K_h as described in Figure 2-4.

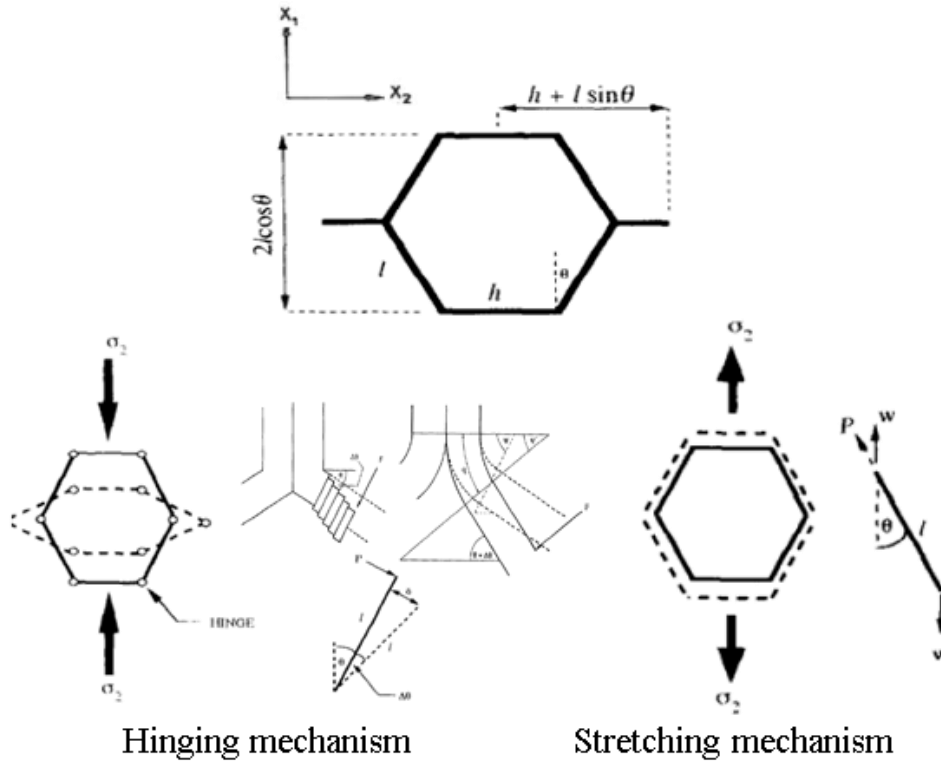
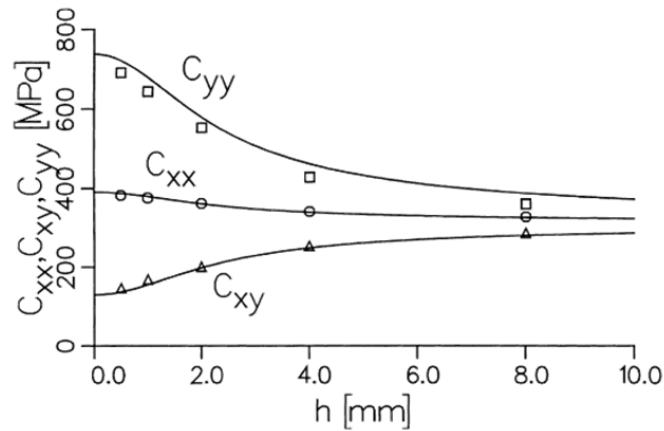
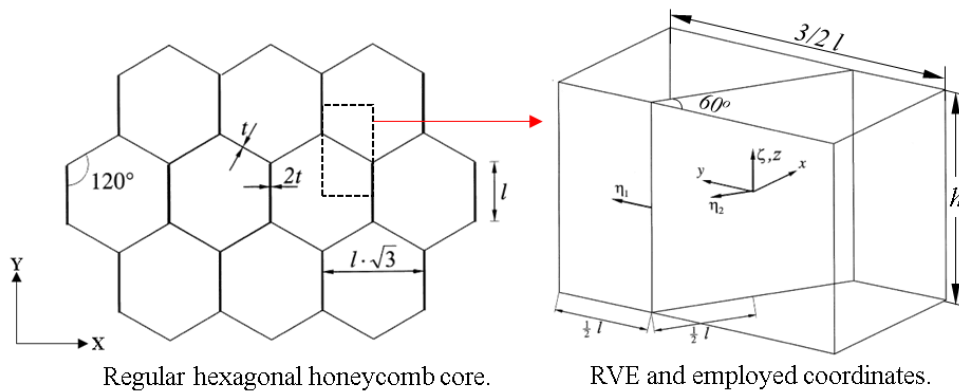


Figure 2-4. Summary of Masters and Evans model [7, 36].

For thin cell walls, the flexure mode dominates and reduces to that of Gibson and Ashby [3]. The stretching mode was used to account for the axial stiffness and associated deformations of the cell walls. The curvature at the cell wall intersection was considered in hinging mechanism but only for the shear modulus prediction. The curvature was not considered to calculate the bending or axial stiffness of the honeycomb core unit cell. Masters and Evans [7] model were developed to determine the in-plane effective elastic constants of idealized honeycomb core and hence the effect of node bond adhesive and its fillet region were neglected. Although, the effect of cell wall curvatures were captured in hinging model, it only used for shear deformation mode. The out-of-plane constants were not determined and also no double thickness cell walls were considered in the analysis.

Becker [37] derived a closed-form description of the effective in-plane core stiffness of regular hexagonal honeycomb core, including thickness effect using strain energy based approach. The core discretization and expression for in-plane stiffness is shown in Figure 2-5. The model correlated very well with finite element simulations as shown in the same figure. The analysis is however limited to idealized core unit cell and does not address the node bond adhesive, cell wall curvature and the presence of double cell walls.

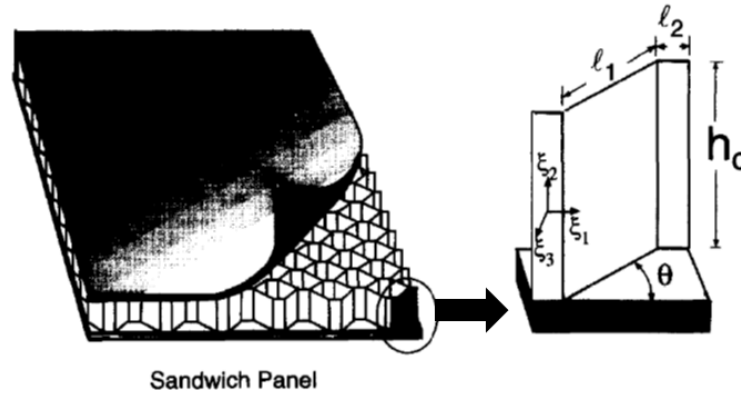


Effective core stiffness C_{xx} , C_{yy} and C_{xy} as functions of the core thickness h .

Figure 2-5. Summary of Becker model [37].

Honeycomb core properties with double cell wall thickness along the ribbon direction (as a result of expansion or corrugation manufacturing process), have been a topic of interest among several studies.

Burton and Noor [6] derived analytical equations by using models similar to the Gibson and Ashby models [3] and incorporating the effect of double-thickness in their analysis. The better predictions of nine elastic constants of hexagonal honeycomb core were obtained. However, the model predictions are only valid for idealized honeycomb core unit cell in a small strain regime. The summary of the model and sample expression for in-plane modulus are shown in Figure 2-6.



$$\frac{\rho}{\rho_s} = \frac{(1 + \eta)}{(\eta + \cos \theta) \sin \theta} \left(\frac{t_c}{l_1} \right)$$

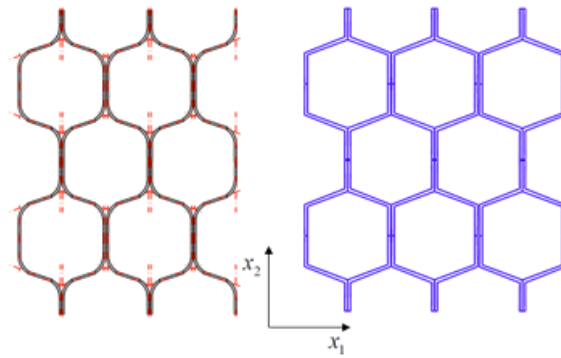
$$E_1 = E_s \left\{ \frac{1}{(\sin \theta) (\lambda \sin^2 \theta / (\eta + \cos \theta) (t_c / l_1)^3 + (\eta + \cos^2 \theta) / (\eta + \sin \theta) (t_c / l_1))} \right\}$$

$$\eta = 2l_2 / l_1, \lambda = 1, t_c = \text{cell wall thickness}, E_s = \text{cell wall Young's modulus}$$

Figure 2-6. Summary of Burton and Noor model [6].

Balawi and Abot [5, 38] developed a refined analytical model for commercial regular hexagonal honeycomb cores with double-thickness cell walls that include the cell wall curvatures in the vicinity of the intersection points of hexagon. The proposed RVE included the one-fourth segment of the core unit cell which was divided into curved and straight regions. The three mechanisms of bending, shear and axial deformations were considered in the analytical analysis. It was shown that effective moduli in both transverse and ribbon directions for curved cell walls are very sensitive to the radius of curvature. Furthermore, anisotropic behavior of the core was

ascribed to the cell wall curvature and double thickness cell wall effect particularly for honeycombs with higher relative density. The predictions of the model were conformed to that predicted by Master and Evans [7] for regular honeycomb core with straight cell wall ($R=0$). The model predictions were validated by experimental data and good agreements were found. The summary of the model and the sample complicated equation for effective elastic constants are summarized in Figure 2-7. The effect of node bond adhesive and its fillet region are also neglected in this model.



Regular hexagonal honeycomb core with (a) curved and (b) straight cell walls at the intersection points.

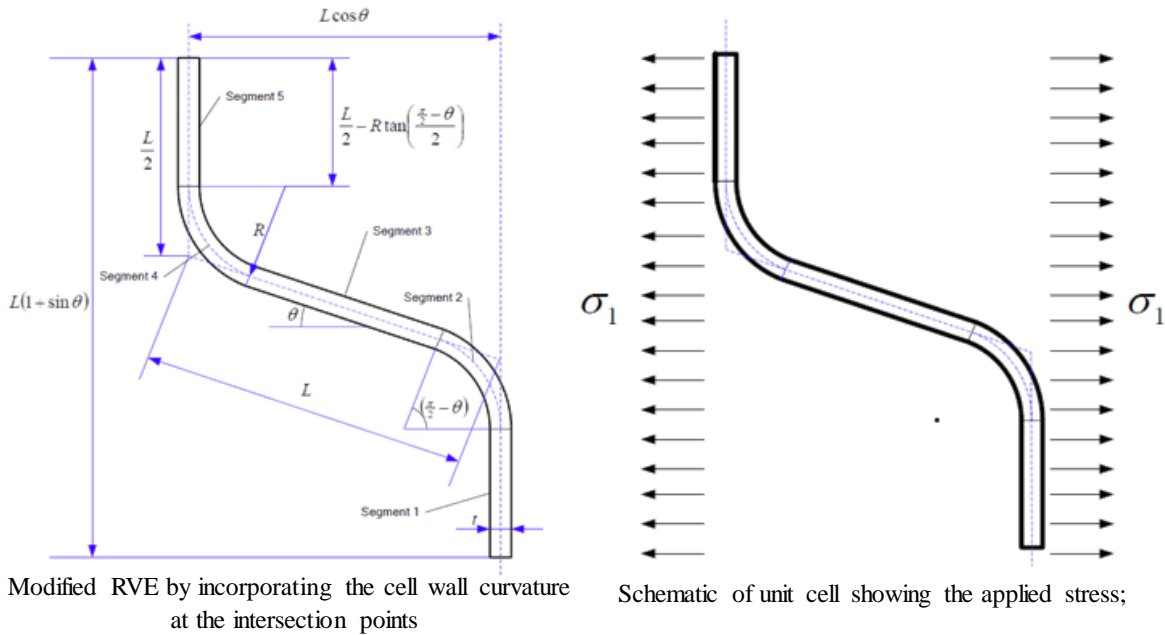
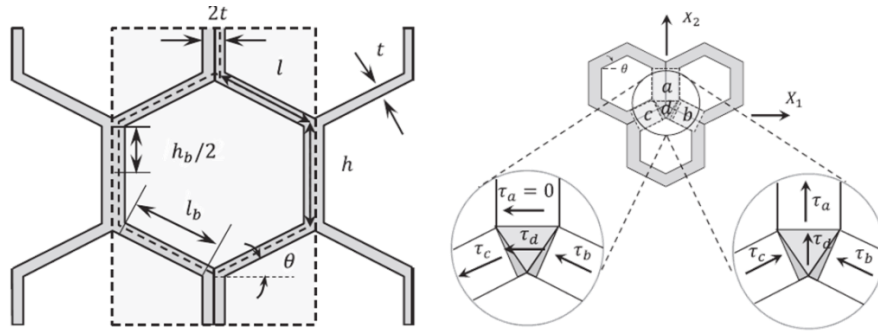


Figure 2-7. Summary of Balawi and Abot model for commercial hexagonal honeycomb [5].

Malek and Gibson [39] developed an analytical model for the nine effective elastic constants of periodic hexagonal honeycombs with uniform and double-thickness cell walls by modifying the analysis of Gibson and Ashby [3] to account for nodes at the intersection of the vertical and inclined members. It was observed that the effect of the nodes on effective elastic constants is negligible for low relative density honeycomb cores and it can be more significant at higher relative densities; unlike the upper and lower bounds for out-of-plane shear moduli predictions in Gibson and Ashby [3] model, closed-formed equations were obtained in the analysis. The summary of the model and samples of effective elastic moduli are shown in Figure 2-8.



$$\left(\frac{\rho^*}{\rho_s}\right) = \left(1 - \frac{l \cos \theta (h_b + l \sin \theta)}{(l \cos \theta + t)(h + l \sin \theta)}\right)$$

$$E_1^* = E_s \left(\frac{t}{l}\right)^3 \times \frac{\cos \theta}{(h/l + \sin \theta) \sin^2 \theta} \left[\frac{1}{1 + (2.4 + 1.5\nu_s + \cot^2 \theta) \left(\frac{t}{l}\right)^2} \right]$$

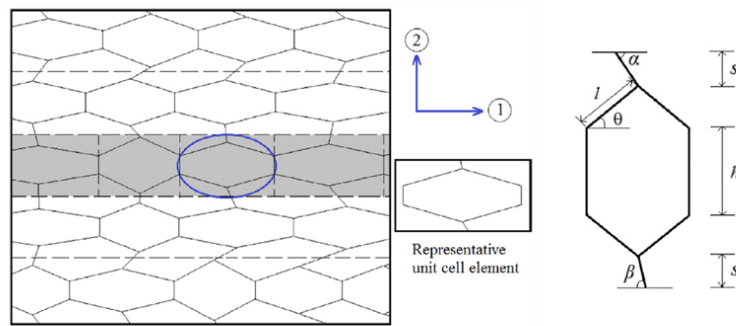
$$G_{13}^* = G_s \left(\frac{t/l}{(h/l + \sin \theta)(\cos \theta + t/l)}\right) \left[\cos^2 \theta \left(\frac{l_b}{l}\right) + 2 \left(\frac{t}{l}\right) \tan \left(\frac{\pi}{4} - \frac{\theta}{2}\right) \right]$$

Figure 2-8. Summary of Malek and Gibson model for hexagonal honeycomb core to account for nodes at cell wall intersections [39].

The model predictions were compared with numerical results as well as the prediction of Gibson and Ashby [3] analysis. The predictions of the model were very close to the previous ones given in Gibson and Ashby [3] for low relative density honeycombs. However, at higher relative densities, the discrepancy between the model predictions and Gibson and Ashby [3] were slightly higher especially for effective shear moduli. The analytical results were in good agreement with

numerical model predictions and test data at higher relative densities. However, the elastic constants were developed for idealized core without considering the effect of node bond adhesive material and its geometrical features.

Mukhopadhyay and Adhikari [8] developed an analytical formulation for predicting the closed-form expressions of equivalent elastic properties of irregular honeycombs with spatially random variations in cell angles due to manufacturing uncertainty, structural defects, and etc. using unit cell based approaches. The model was compared with FEA results and some findings from available literature such as Gibson and Ashby model [3]. The summary of the model is shown in Figure 2-9.



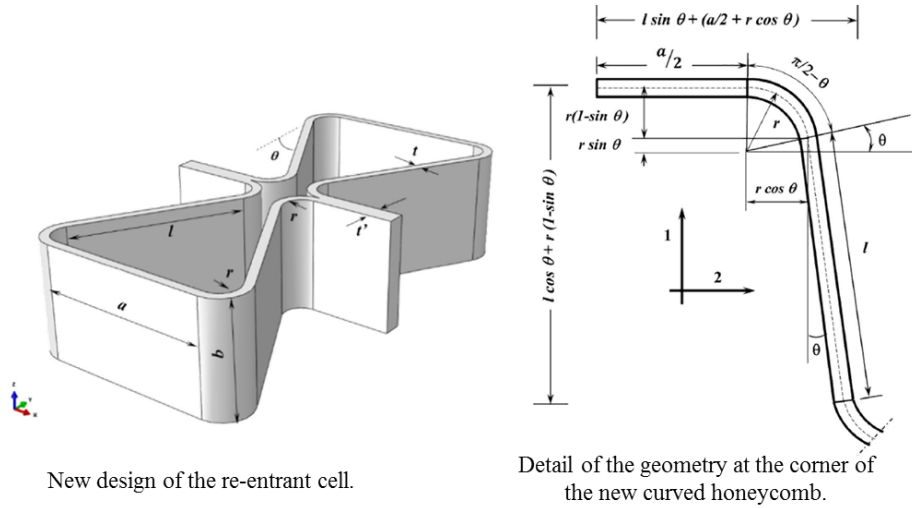
$$E_{1U} = E_s \left(\frac{t}{l}\right)^3 \frac{\cos \theta}{\left(\frac{h}{l} + \sin \theta\right) \sin^2 \theta}$$

$$E_{2U} = E_s \left(\frac{t}{l}\right)^3 \frac{\left(\frac{h}{l} + 2\frac{s}{l} + 2 \sin \theta\right)}{\cos \theta \left(2 \cos^2 \theta + 8\left(\frac{s}{l}\right)^3 \left(\frac{\cos^2 \alpha}{\sin^3 \alpha} + \frac{\cos^2 \beta}{\sin^3 \beta}\right) + 2\left(\frac{s}{l}\right)^2 (\cot^2 \alpha + \cot^2 \beta)\right)}$$

Figure 2-9. Summary of Mukhopadhyay and Adhikari [8] model for irregular hexagonal honeycomb core with spatially random variations in cell angles.

It was shown that the variations in cell angle have significant effect on in-plane effective elastic constants particularly E_2 and ν_{21} . This uncertainty in the elastic moduli of honeycombs owing to random variations in cell angle would have significant influence on the subsequent analysis and design process which should be taken into account. The presence of the node bond adhesive, however, was not addressed in the model.

An analytical model based on energy method (Castigliano's theorem) [40] was developed to investigate the effect of curvature of cell walls on the in-plane uniaxial elastic properties of hexagonal honeycomb cores with round corners. The honeycomb can also provide auxetic (in-plane Poisson's ratio) deformations with internal negative cell angles as illustrated in Figure 2-10. It was shown that while higher curvatures provide a decrease in the magnitude of the Poisson's ratio for positive internal cell angle, the magnitude of the negative Poisson's ratio is increased in re-entrant or auxetic configurations. The presence of curvatures also tends to shift toward negative cell angles the peak of in-plane uniaxial anisotropy and the switch between the negative and positive Poisson's ratio zones. The core relative density and a sample of elastic constant derived in this study are shown in the same figure. The equations obtained in this research are only applicable for idealized core without modelling the node bond adhesive region.



$$\frac{\rho}{\rho_s} = \frac{1}{2} t \frac{(a + 2l - 2r\theta + \pi r)}{(a + 2r \cos\theta + l \sin\theta)(2r + l \cos\theta - 2r \sin\theta)}$$

$$\frac{E_1}{E_s} = \gamma^3 \frac{\cos\theta}{(\beta + \sin\theta)\sin^2\theta} \left(\frac{1}{1 + \gamma^2(\cot^2\theta + \frac{12}{5}(\nu + 1))} \right)$$

Figure 2-10. Summary of model reported in [40] for honeycomb cores with curved cell walls.

Recently a new analytical model [10] was developed for predicting the in-plane effective elastic constants of commercial adhesively bonded hexagonal honeycomb cores made of isotropic materials in which more attention is paid to account for the radius of curvature of the inclined walls and the adhesive layer thickness between adjacent ribbons in double thickness cell walls, as depicted in Figure 2-11. The deformation mechanisms of the honeycomb cells included flexure, stretching, shearing and hinging. The FEM of a RVE was used for model calibration and validation considering different relative densities of real honeycombs. Although the model predictions provide new insight into understanding the mechanics of commercial hexagonal honeycombs, the inclusion of the node bond adhesive fillets were neglected in the analysis while the increased node bond fillet significantly increases the stiffness of the core at infinitesimal strain, as reported in [13].

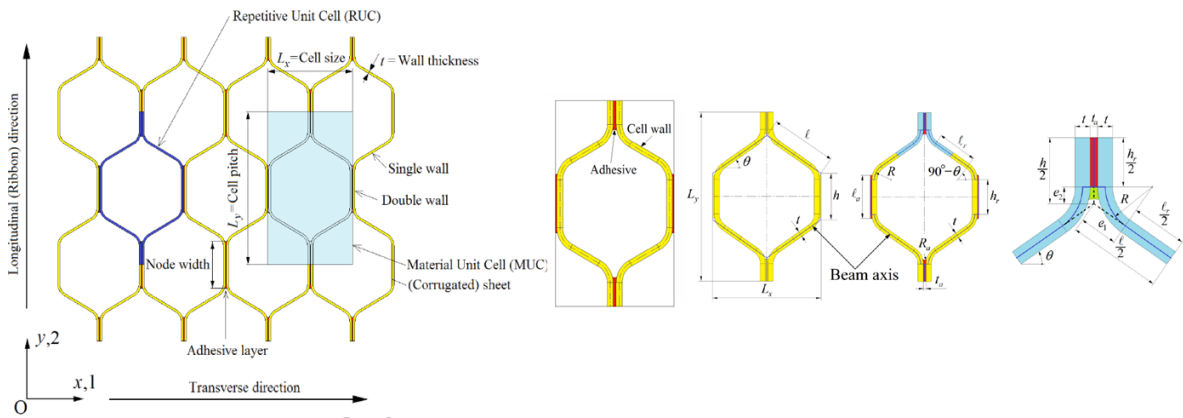


Figure 2-11. Summary of model reported in [10] for commercial adhesively bonded hexagonal honeycomb core.

Almost all previously discussed mathematical models are only suitable for applications involving idealized (perfect bonding between ribbons) honeycomb cores; therefore, the adhesive layer and fillet region are most often ignored in the analyses; moreover, mathematical models are only limited to the honeycomb cores made of homogenous isotropic materials and modeling the composite honeycomb cores requires more complex derivation for the effective elastic constants

of the core. The predictions of these models are also suitable for applications where the core's in-plane deformations are restricted to a small strain regime.

To overcome the above-mentioned shortcomings of analytical models, numerical analysis has proven to be a convincing and powerful approach if they are validated by experimental data. Several researches have employed numerical models to characterize the in-plane behavior of the honeycomb cores which are reviewed in a following section.

2.1.2 Numerical Models

Penado [9] used the three dimensional (3D) FEM of a one-eighth segment of a unit cell in order to replicate the behavior of the overall core by employing shell elements as illustrated in Figure 2-12. The model was validated using experimental and published data for aluminum foil cores. The model was used for estimating the 3D elastic constants for core cell walls made of composite materials of various layups. However, the idealized honeycomb core geometry was employed in the FEM.

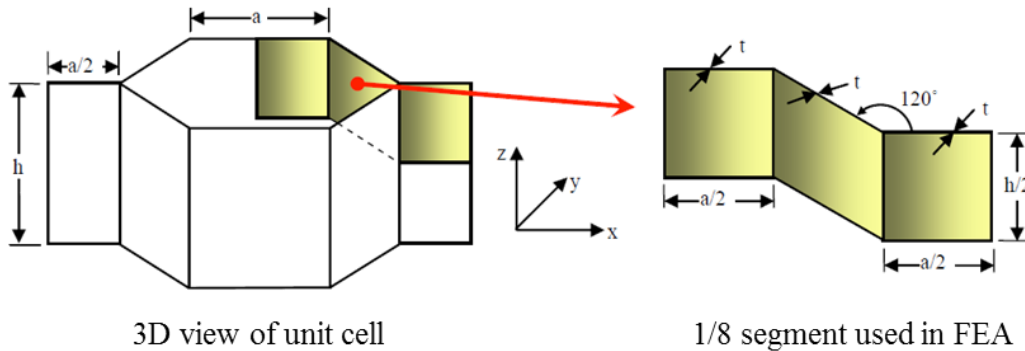


Figure 2-12. FEM of 1/8 segment of unit cell used by Penado [9].

Grediac [41] used a FEM of a representative unit cell of an idealized core to study the transverse (thickness direction (T)) shear in honeycomb core. The effect of the core thickness on the shear modulus G_{xz} was investigated. The results of the FEMs were then compared to those of test data and analytic expressions for the transverse shear stiffness.

Kayran and Aydincak [42] evaluated the elastic properties predicted by different analytical models discussed previously by employing a 3D FEM of sandwich panels with the idealized honeycomb core geometry modeled based on the existing continuum models of the honeycomb core, as shown in Figure 2-13. Based on their FEA, they concluded that the in-plane properties predicted by Masters and Evans [7], in combination with the transverse out-of-plane shear properties predicted by Grediac [41], gave the best results when modeling the core in a sandwich panel.

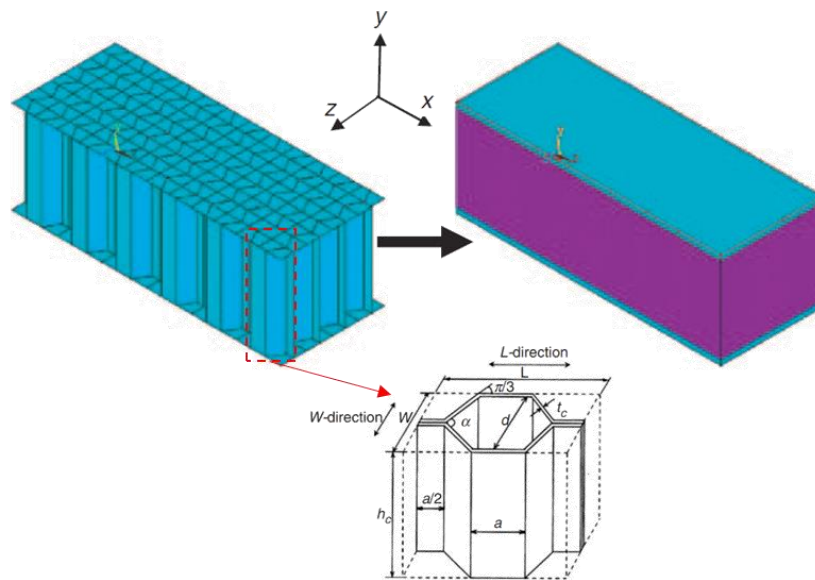


Figure 2-13. FEM of sandwich panels used by Kayran and Aydincak [42].

Catapano and Montemurro [43] conducted a 3D numerical study to predict all elastic constants for generally orthotropic honeycombs with double-thickness cell walls using a FEM of the repetitive unit cell using solid elements and compared them with analytical models discussed previously. The predictions of out-of-plane modulus agreed with those of the other investigators. However, the in-plane elastic properties, especially for cores with thick walls, differed by 8% to 23% when compared with the existing models. The authors attributed this difference to the

inability of shell-based models to accurately capture the geometry of the unit cell and thus cannot take into account the 3D state of stress which is prevalent in honeycomb cores.

A numerical approach based on equality of the strain energy of a representative volume element (RVE) cell and a corresponding homogeneous solid was developed by Qiu et al. [44] to determine the nine orthotropic effective components of stiffness matrix for an idealized hexagonal honeycomb core. They showed a good agreement between their numerical predictions and experimental results for in-plane moduli.

Although there are no limitations for numerical modeling of honeycomb cores, the simple geometry of the idealized core cell is employed in most of the above mentioned numerical models and the geometric features as well as the material properties of the node bond adhesive layers and its fillet regions are mostly neglected.

Recently, a 3D FEM of representative unit cell [13] was introduced in which all the detailed geometric features of a commercial HRP-fiberglass/phenolic hexagonal honeycomb core made using the corrugation manufacturing process are captured, as shown in Figure 2-14.

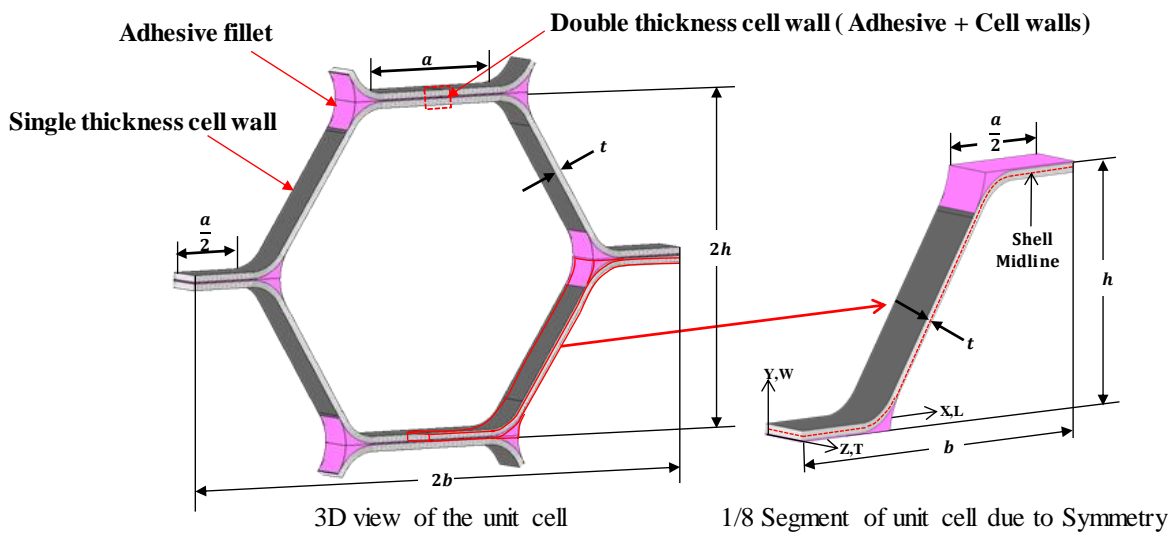


Figure 2-14. FEM of core cell: (a) 3D view, and (b) 1/4 symmetry [13].

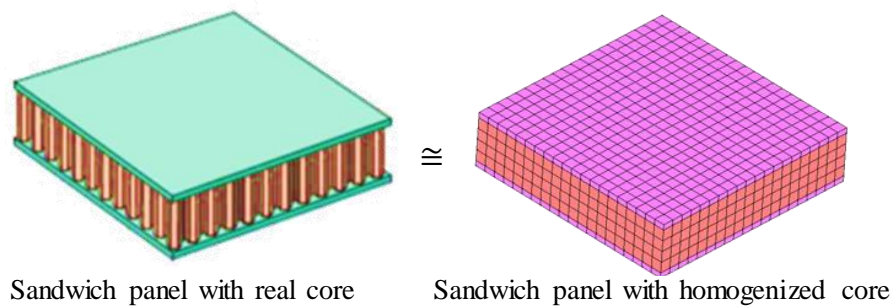
The model was used to conduct a parametric study on the effects of the adhesive fillet and its geometry on uniaxial in-plane mechanical responses of the core under large deformation; the effective elastic constants of the core were predicted by the FEM at infinitesimal strain and compared with the predictions of some of the above discussed analytical models. It was shown that, increased node bond adhesive fillet size significantly increases the effective in-plane elastic constants of the core in a small strain regime and excluding it from the analysis (predictions of the analytical models) resulting in inaccurate calculation of the effective quantities of the honeycomb core. The FEA results were validated by experimental data.

The linear effective constitutive relations for describing the mechanical behavior of honeycomb cores are suitable for applications where the core in-plane deformations are restricted to a small strain regime. In sandwich structures wherein high modulus facesheets are employed, the core deformations are constrained by the facesheets, thus facilitating the use of homogenized core properties based on small strain assumption. Figure 2-15 (a) shows the homogenized modeling of a sandwich panel in a FEA program wherein a honeycomb core is modeled using simple solid elements and the linear orthotropic effective constitutive law can be employed for material modeling of the continuum core model.

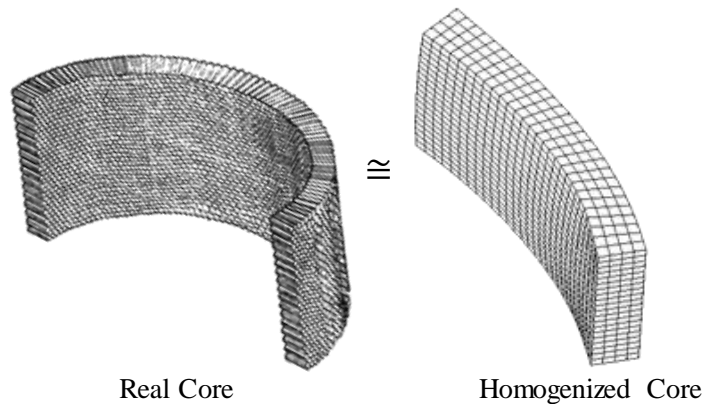
However, the linear constitutive models may not be suitable for applications involving large deformations such as those occurring during thermoforming of honeycomb cores to be used in curved sandwich structures or analyzing the honeycomb core under in-plane and traverse flexure, as illustrated in Figure 2-15 (b). Chen [45] conclusively showed that the in-plane moduli obtained from RVE analysis cannot be used to analyze the bending behavior of honeycomb cores; the Gibson & Ashby [3] models for in-plane deformations of core predict in-plane Poisson ratios equal to unity. This creates problems when computing the bending stiffness of equivalent

homogenous cores. This work further suggests the asymmetric behavior of the core owing to the dependence of core properties on the geometry of the cell. Under flexure, the cells on the tension and compression sides deform differently and thus possess different elastic properties. In such a scenario, the deformation dependent elastic properties must be employed to capture the flexure behavior accurately.

In general, for the loading scenarios wherein the in-plane deformations dominate the overall deformation of the honeycomb cores, the bulk honeycomb core behavior must be modeled with the required orthotropy and nonlinearity observed under large deformations and therefore the nonlinear effective constitutive models must be employed.



(a) Linear Constitutive Model



(b) Non-Linear Constitutive Model

Figure 2-15. FEA simulations of a bulk honeycomb core using a homogenized model for (a) a small strain and (b) a large strain analysis with respective constitutive models.

2.2 Nonlinear Effective Constitutive Models

As discussed previously, in-plane deformations of honeycomb cores under small deformations can be described by three mechanisms of flexing, stretching and hinging. However, flexure mode dominates the overall deformation of the honeycomb core and hinging and stretching modes can be considered to be negligible particularly for low relative density cores; consequently, elastic bending theory without considering the large rotation effect is regularly employed to derive a closed form solution for the prediction of effective elastic properties of homogenized honeycomb cores leading to development of the linear orthotropic effective constitutive models.

The in-plane mechanical responses of honeycomb cores in the finite strain regime are primarily different from the analogous behaviors of the core under small deformation due to the significant changes in geometry which cannot be captured in the small strain analysis. Under large deformations, in general, honeycomb cores undergo both material and geometric nonlinearities associated with large bending induced deflection and rotation of the inclined cell walls, elastic buckling, and plastic deformation depending on microstructures and macroscopic loading directions [30]. Moreover for non-metallic honeycombs, as deformations increase, two geometric phenomena including densification (at which point the cell walls start closing up within their longitudinal direction) under tensile-dominated loads and shear instability (at which point the double-thickness cell walls rotate in the opposite direction) under compressive-dominated loads may respectively result in nonlinear stiffening and softening responses of the honeycomb cores, referred to as asymmetric behavior, as illustrated in Figure 1-7.

In-plane mechanical responses of honeycomb cores under large deformations have been investigated by a few number of researchers.

Numerical, analytical and experimental studies [13, 15, 46] were carried out on HRP-fiberglass/phenolic hexagonal cell honeycomb core to investigate the uniaxial in-plane mechanical responses of the core under large deformation. It was shown that the homogenized in-plane stress-strain responses of the core are nonlinear, asymmetric and anisotropic. The predictions of the finite element analysis and analytical model were also consistent with test data. Similarly, the nonlinear uniaxial response of Nomex honeycomb core was observed through experimental study performed by Karakoc and Freund [12] at high strain condition, as illustrated in Figure 1-7 (b).

There are several studies in which the mechanical response of honeycomb cores under high-strain compression have been investigated; the reviews of previous studies are also documented [15, 20-22]. It has been shown that under high-compressive strain particularly along the ribbon (L) direction, not only the elastic buckling of the cell walls magnifies the deformation, but also the rotation of the adjacent double thickness cell walls in opposite directions, which is called shear instability, leads to nonlinear elastic softening response (fully recoverable) until the failure of the core. This behavior is shown Figure 1-7 (a) for a commercial HRP-fiberglass/phenolic honeycomb core.

Mechanical responses of hexagonal and auxetic honeycomb cores made of Polycarbonate under simple shear deformation [30] were investigated through experimental and numerical studies. Nonlinear effective shear stress-strain curves were obtained from the experiments particularly for the auxetic honeycomb core as illustrated in Figure 2-16. The effects of core microstructures on the homogenized shear responses were also investigated using FEA.

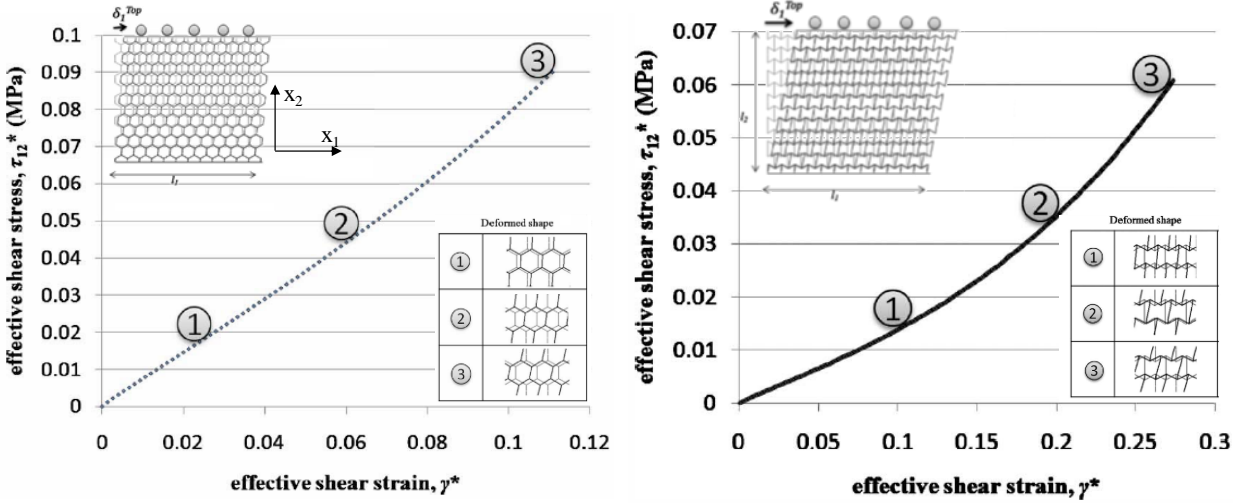


Figure 2-16. Effective shear stress-strain curves of (a) the regular hexagonal and (b) the auxetic hexagonal honeycomb cores under simple shear deformation [30].

Małgorzata [14] performed a numerical study on the in-plane mechanical responses of auxetic honeycomb cores under tension and compression loadings. It was shown that the behavior of materials with the auxetic beam microstructure is significantly nonlinear. The paths of material characteristics were dependent on the tension-compression direction and on the material and geometric microstructural parameters [14].

Effective mechanical behaviors of hexagonal honeycombs made of hyperelastic solid foam at finite strain were investigated using numerical based homogenization approach [47, 48]. The nonlinear anisotropic effective stress-strain responses were predicted under uniaxial and biaxial tensile and compressive loadings as well as the pure shear deformation. The influence of the microstructural parameters on the effective stress-strain behavior was also studied.

In order to analyze the in-plane homogenized mechanical responses of honeycomb core in the finite strain regime, it is essential to develop a nonlinear effective constitutive model. Here, it should be noted that, the main focus of this research is to investigate the nonlinear constitutive relations developed over a constituent material's elastic range; in other words, material nonlinearity is not considered in the development of the constitutive relations. In fact, the nonlinear

behavior of the honeycomb core is attributed to the inherent nature of the cellular structures resulting from the influence of microstructural deformation mechanisms under macroscopic loadings in the finite strain regime.

The nonlinear effective constitutive models for characterizing the in-plane mechanical responses of honeycomb cores can be developed using two different approaches which include:

1. Mathematical derivation of the effective constitutive relations (stress-strain relationships) using the classical bending theory with considering the influence of large rotation in the governing equations.
2. Development of nonlinear effective constitutive models using hyperelastic strain energy density functions (SEDF).

The literature addressing the details of the aforementioned approaches are summarized in the following paragraphs.

2.2.1 Mathematical Models

Zhu and Mills [22] investigated the in-plane behavior of regular hexagonal honeycombs core under compressive loading by performing a theoretical analysis. Both geometric and material nonlinearities were considered in the analysis. It was shown that the mechanical response of the core is nonlinear under a high compressive strain condition in both ribbon and transverse directions resulting from elastic buckling of the inclined cell walls as well as the rotation of the double thickness cell walls which lead to nonlinear softening response of the core. The analytical results were validated by experimental data.

Lan and Fu [24] performed a mathematical analysis based on the elastic bending theory of beams in large deflection, in order to investigate mechanical responses of regular hexagonal honeycomb core subjected to large in-plane shear and uniaxial deformations. The method was

based on solving a set of nonlinear governing differential equations resulting from including the large rotation effect in derivation of the governing equations for bending analysis of the cell wall. Nonlinear homogenized stress-strain relations (effective constitutive model) were obtained from the analysis. The nonlinear prediction of the model under shear loading was compared with the linear prediction of Gibson and Ashby [3] model. The prediction of the nonlinear model coincided with the linear one at infinitesimal strain, as illustrated in Figure 2-17. Moreover, the modified factors were produced and incorporated into the linear effective elastic constants predicted by Ashby and Gibson [3] in order to update the elastic constants and consequently constitutive relations at incremental analysis (applying the total load in small increments), based on the updated geometry.

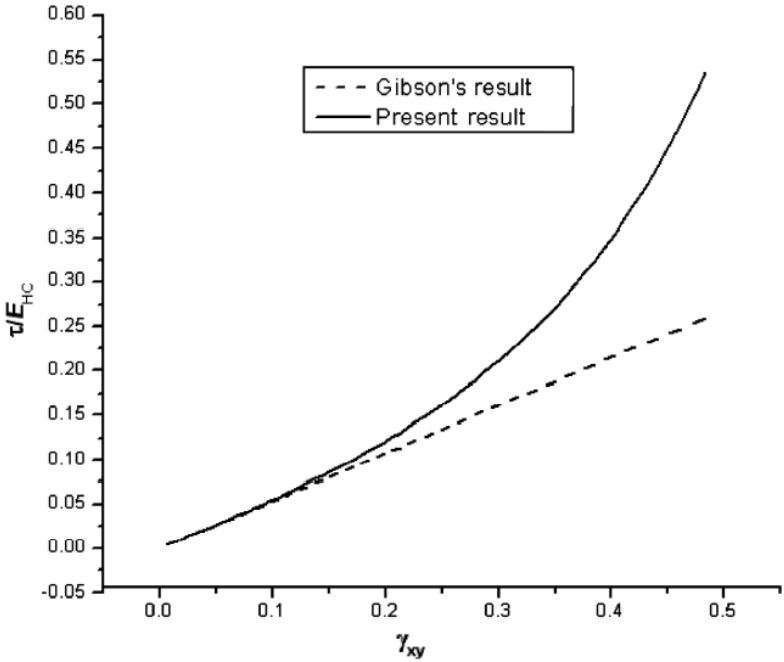


Figure 2-17. Comparison between the nonlinear homogenized in-plane shear stress-strain response predicted by Lan and Fu [24] and linear model predicted by Ashby and Gibson [3].

The nonlinear elastic response of honeycombs under in-plane shear was also explored in [23] by analysing the large deflection of cell walls in a unit cell. The effect of double thickness cell walls was investigated in the analyses and it was found that doubling the thickness of cell walls of honeycombs increases their shear strengths particularly along the transverse direction and does not affect the core stiffness.

Recently, a new analytical model was derived [46, 49] to investigate the in-plane homogenized stress-strain relationship of an adhesively bonded commercial hexagonal honeycomb core under large deformation. The model incorporates some advanced features of the core cell such as cell wall curvatures, node bond adhesive layers, and adhesive fillets at the cell wall intersections in the analysis. The analytical model was derived based on solving a set of linear and nonlinear governing differential equations using numerical integration method. The model is also able to predict the normal (peel) stress distribution along the node bond adhesive layer within the double wall and the fillet region. Nonlinear homogenized results of the fiberglass/phenolic honeycomb core predicted by the analytical model were compared with test data [15] as well as predictions from FEMs of both real and idealized (without modeling the node bond adhesive) core cells [13] to investigate the effects of the node bond adhesive. Predictions of the analytical model were in good agreement with the test data and predictions of the FEM of the real core cell.

Although the analytical models, which are based on large deflection cell wall bending analysis, capture the nonlinear mechanical responses of the core very well and provide a better understanding of the influence of the honeycomb core microstructures on nonlinear behavior of the bulk core under large deformation, implementation of these models requires solving of a series of nonlinear partial equations using complex elliptical integral forms [24, 30]. Development of the mathematical models for complex core cell structure such as commercial honeycomb core cell

which includes single cell wall, cell wall curvature, node bond adhesive layer and its fillet region will induce more complexity in the governing equations [46]; besides, they are only applicable to honeycomb cores made of homogeneous isotropic materials except the recent model reported in [46, 49] wherein both flexural and in-plane stiffness of the cell wall material are captured. Moreover, it is almost infeasible to employ these models as effective constitutive models of the core in finite element software. The infeasibility is due to complexity associated with the mathematical derivations and also the fact that the analytical models may only be used for analysing the honeycomb cores under simple load cases such as uniaxial and shear deformations.

2.2.2 Hyperelastic Models

The direction-dependent, asymmetric, and nonlinear-elastic responses of non-metallic honeycomb cores [13] point toward the suitability of a hyperelastic material formulation for use in homogenized models of the honeycomb cores. Furthermore, it has been shown [13] that honeycomb cores must be considered as compressible materials in the homogenization process, particularly under large deformations.

The constitutive theory which describes the mechanical behavior of elastic solids with the use of (only) one material function is called hyperelasticity. The hyperelastic materials are truly elastic in the sense that if a load is applied to such a material and then removed, the material returns to its original shape without any dissipation of energy in the process [50]. The formulation of a hyperelastic behavior law relies on the proposition of a strain energy density function (SEDF) from which the constitutive relations are derived. The inherent behavior of a hyperelastic materials such as anisotropy and compressibility must be captured by the proposed SEDF.

Several studies [27-29, 47, 48] have been undertaken wherein hyperelastic constitutive models were developed to predict the in-plane nonlinear effective stress-strain curves of idealized

cellular materials at finite strains. These models can only be used for prediction of the mechanical responses of honeycomb cores under simple loading scenarios such as uniaxial, and shear deformations. The proposed models cannot be used as an effective constitutive model of a bulk honeycomb core for FEA simulations of the core under complex loading scenarios such as in-plane bending simulations wherein the constitutive model must capture the behavior of the core under multi-axial states of stress.

The hyperelastic constitutive modeling of hexagonal and auxetic polycarbonate honeycomb cores under in-plane simple shear loading was investigated by Ju and Summers [30]. They employed three prevalent compressible, isotropic hyperelastic material models to find the best-fitted model conforming to the effective stress-strain responses of the cores under simple shear loading. The findings of this study highlight the nonlinear core behavior, which is restricted to a specific loading scenario, but cannot provide a complete picture of the nonlinear anisotropic deformations of the honeycombs.

As discussed in this section, to generate the homogenized effective stress-strain curves of a honeycomb core and investigate the effect of core microstructures on the stress-strain relations, in the first place, an appropriate RVE is required in which all the artefacts of the honeycomb core cell are captured. Under large strain conditions, each component of the honeycomb core RVE such as node bond fillet, cell wall curvature and etc. might have a significant effect on the nonlinear macroscopic behavior of the core and induce more nonlinearity associated with the significant changes in geometry. For commercial hexagonal honeycomb cores, the 3D FEM of representative unit cell introduced in [13] is the most effective one which has been validated by experimental results. The effect of geometrical features on the homogenized mechanical responses of the cores can be easily investigated in FEA simulations by employing the introduced RVE.

The orthotropic homogenized behavior of honeycomb cores in a small strain regime can be easily captured using the linear orthotropic effective constitutive law given in equation (2.1); considering the fact that the use of the closed form analytical equations for prediction of the elastic constants which are mainly derived for idealized hexagonal honeycomb cores result in inaccurate predictions for the homogenized responses of commercial hexagonal honeycomb cores.

The choice of an appropriate RVE similar to the proposed RVE in [13, 46] developed for commercial hexagonal honeycombs and employing the finite element or analytical model developed in [13, 46, 49] would be more reliable than traditional models for calculating the effective elastic constants of commercial hexagonal honeycombs under small strain deformations.

Relying on available models discussed for describing the nonlinear effective constitutive relations of honeycomb cores at finite strain, implementing the mathematical models is much more complicated than hyperelastic constitutive models. Furthermore they are mostly developed for idealized core cell due to complexity of including the geometric features of the core cell in the governing equations. However, the hyperelastic constitutive models are mainly developed for the prediction of effective stress-strain responses of honeycomb cores under simple loading scenarios.

To the best of the authors' knowledge, no publication that is available in the open literature specifically discusses the simulations of commercial honeycomb cores subjected to in-plane or out-of-plane flexure. Since the out-of-plane moduli of the core are orders of magnitude higher than the in-plane moduli, the flexural behavior of the core will be dominated by the large-in plane deformations of the cells. For these loading scenarios, full honeycomb cores must be analyzed, and modeling a very large number of cells individually is not feasible. Therefore, a pragmatic approach to simulate the general in-plane and/or flexural loading of the bulk core would be to

homogenize the core behavior using the suitable constitutive model which captures the asymmetric, orthotropic and nonlinear elastic responses of the core under large deformations.

In the present research, development of a compressible anisotropic hyperelastic constitutive model for prediction of the experimentally observed in-plane, orthotropic, asymmetric and nonlinear elastic responses of commercial nonmetallic hexagonal honeycomb cores is presented. The constitutive model was implemented in a commercial finite element software as the effective material modeling of a homogenized core to investigate the in-plane mechanical responses of the core under large deformations using several loading scenarios. The finite element results were validated by test data for a commercial adhesively bonded HRP-fiberglass/phenolic honeycomb core.

CHAPTER 3

MOTIVATION, OBJECTIVES, AND METHODOLOGY

3.1 Motivation

As discussed in the previous chapters, for composite or non-metallic honeycombs, in general, at room temperature, the in-plane mechanical responses of the bulk material are nonlinear, asymmetric, anisotropic, and fully recoverable (elastic) in the finite strain regime. This is attributed to the geometric nonlinearity (small strain, large rotation) associated with flexural deformations of the inclined cell walls. Therefore, to capture the finite strain in-plane responses of the honeycomb cores using a homogenized equivalent-continuum model (effective) of the core, a nonlinear effective constitutive model must be employed.

A review of the different databases and published researches shows that the available nonlinear effective constitutive models for non-metallic honeycombs are either too complex to perform and limited to the geometry of the idealized core cell such as mathematical models or can not provide the complete picture of the nonlinear anisotropic deformations of the honeycombs, such as hyperelastic models; on top of that, they are only applied on constitutive modeling of the honeycomb cores subjected to simple loading and boundary conditions such as in-plane uniaxial and shear deformations. For these loading scenarios, the RVE of honeycomb core microstructure would be sufficient to capture the in-plane behavior of the core and it is not necessary to analyze the bulk honeycomb core.

When it comes to constitutive modeling of the commercial honeycomb cores under flexural loading conditions such as FEA simulations of honeycomb core forming manufacturing processes shown in Figure 1.8, in which honeycomb core cells experience the large in-plane (L-W plane) deformations owing to flexure resulting from out-of-plane loading, a full scale honeycomb core

must be analyzed and modeling a very large number of cells individually is not feasible. However, none of the existing models can be used for this purpose.

Having a comprehensive and straightforward effective constitutive model for capturing the in-plane, orthotropic, asymmetric and nonlinear-elastic responses of the honeycomb cores in the finite strain regime can be valuable and beneficial for a wide range of applications, e.g., nonlinear FEA simulations of honeycomb core forming processes using simple continuum elements to determine the formability of honeycomb core to different curvatures and provide the design guidelines and forming process limits to prevent node bond failures which has been hitherto done by trial and error process resulting in loss of materials, labor and high production costs.

3.2 Objectives

The purpose of this research was twofold: firstly, to develop an appropriate and straightforward nonlinear effective constitutive model to characterize the in-plane orthotropic hyperelastic responses of composite or non-metallic honeycomb cores, in-general, in the finite strain regime. The model was then employed as an effective material model of a bulk honeycomb core in a finite element software using simple continuum elements for the nonlinear FEA simulations of the bulk core subjected to complex loading scenarios.

Secondly, validation of the model using different experiments such as in-plane uniaxial, bending, and shear tests, wherein the in-plane deformations dominate the overall deformation of the honeycomb core. This was the convincing way to examine the developed material model.

3.3 Methodology

In this study, an orthotropic compressible hyperelastic constitutive model, using a polyconvex strain energy density function (SEDF) for modelling the in-plane behavior of commercial non-metallic hexagonal honeycomb cores was developed. The constitutive model was formulated such that the in-plane and out-of-plane responses of the honeycomb cores were considered to be decoupled.

In order to perform the finite element based homogenization approach using the developed hyperelastic constitutive model, the following steps were carried out:

- a) Identifying the core of interest which included the core material, core cell shape and size.
- b) Experimental characterization of the mechanical properties of the constituents of the honeycomb core for providing the input data for FEM of the RVE of the core.
- c) Development of the finite element model (FEM) of the core RVE to generate the homogenized stress-strain curves for different loading cases such as uniaxial, pure shear and biaxial. The FEM of the core RVE was also used to investigate the effects of microstructure on homogenized mechanical responses of the core.
- d) Assembly of the hyperelastic constitutive model by nonlinear curve fitting of the effective engineering stress-strain curves obtained from the experimentally validated finite element model of the core RVE.
- e) Evaluating the hyperelastic constitutive model using a single element FEM on which simple states of loading (uniaxial, biaxial and pure shear) were imposed and comparison of predicted stress-strain curves with test data. Note that, the hyperelastic model was implemented in a commercial finite element program (MSC Marc [31]) employing user subroutines.

- f) Nonlinear FEA simulations of the bulk honeycomb core using simple continuum elements with the hyperelastic material model, subjected to complex loading and boundary conditions, such as simulations of honeycomb in-plane cantilever bending test and comparison with test data.

The above mentioned procedure is shown schematically in Figure 3-1. In current study, the numerical homogenization approach and experimental works were performed on a commercial HRP-fiberglass/phenolic hexagonal cell honeycomb core which is one of the most widely used composite honeycomb cores in aerospace industry.

It should be noted that, in this research all the simulations were conducted using 2D elements under plane strain condition owing to the type of the tests conducted on the core. 3D elements could have been utilized, too, because under in-plane loadings, out-of-plane properties of the core are not affected and therefore it is assumed that the in-plane and out-of-plane constitutive models are decoupled. The more details will be discussed in the following chapters.

The developed methodology in this research can be used for any non-metallic honeycombs irrespective of their cell size and geometry.

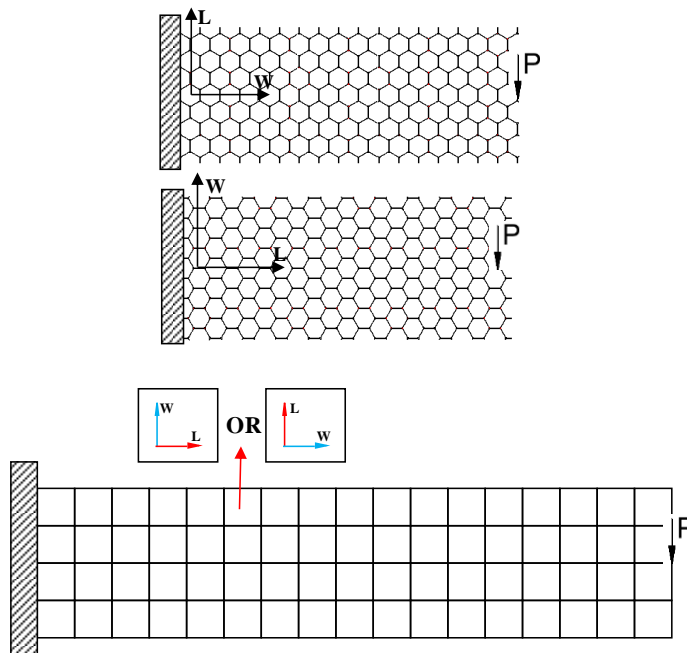
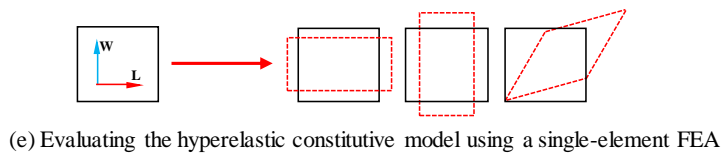
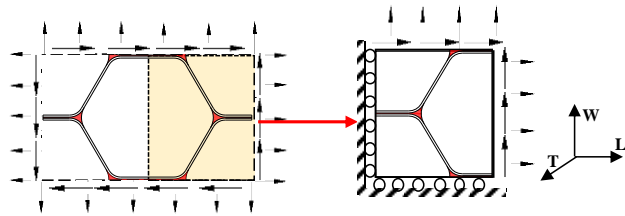
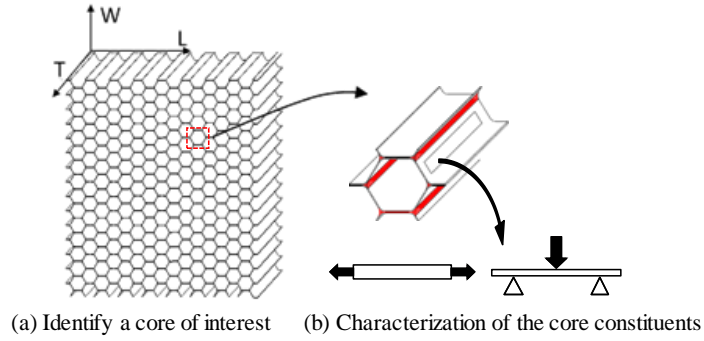


Figure 3-1. Schematic of the numerical homogenization approach procedure.

CHAPTER 4

EXPERIMENTS AND OBSERVATIONS

In this study to support and validate the development of the numerical homogenization approach shown in Figure 3-1, a comprehensive experimental study was conducted on a specific honeycomb core of interest. It should be emphasized that all the experiments were conducted as a part of a larger research program [51], and in the current study, only the experimental results were employed for conducting data analysis and validation of the numerical models.

The honeycomb core was characterized experimentally to generate basic material properties and bench mark data required to support and validate the FEM of the RVE of the core microstructure as well as the FEM of the homogenized core with developed hyperelastic constitutive model. The experimental studies were carried out at different levels which contain the following steps:

- Characterization of the honeycomb core microstructure including the core cell geometry and material constitutions to facilitate the development of the FEM of the core RVE.
- Characterization of the bulk core to obtain the homogenized material properties including the homogenized stress-strain behaviors of the core under in-plane uniaxial tensile and compressive loadings as well as the pure shear loading to evaluate the finite element predictions of the core RVE and also to assemble and validate the hyperelastic constitutive model.
- Characterization of the bulk core under complex loading scenarios such as in-plane cantilever bending tests and bi-axial test using picture-frame shear fixture to evaluate the FEA simulations of the homogenized core using the hyperelastic material model.

The details of the experiments and key observations are enumerated in the following sections.

4.1 Honeycomb Core Cell Geometry Features and Material Properties

In the present study, the geometry of a unit cell of commercial Hexcel HRP-3/8-4.5 hexagonal cell fiberglass/phenolic honeycomb core [4] made using a corrugation manufacturing process was employed. The core has a nominal density of 4.5 lb/ft³, cell size of 0.375 inches, and thickness of 2.4 in. Figure 4-1 shows the detailed geometry of the honeycomb core unit cell characterized using image analysis. A representative cell constructed using mid-line dimensions based on average values (~30 measurements) is illustrated in the same figure. As is shown in Figure 4-1, the measured dimensions indicate that the geometry of the representative cell which includes cell walls, cell wall curvatures at intersections, node bond adhesive layers and fillets does not conform to that of a regular hexagon (idealized core) shown in Figure 1.5 (b)

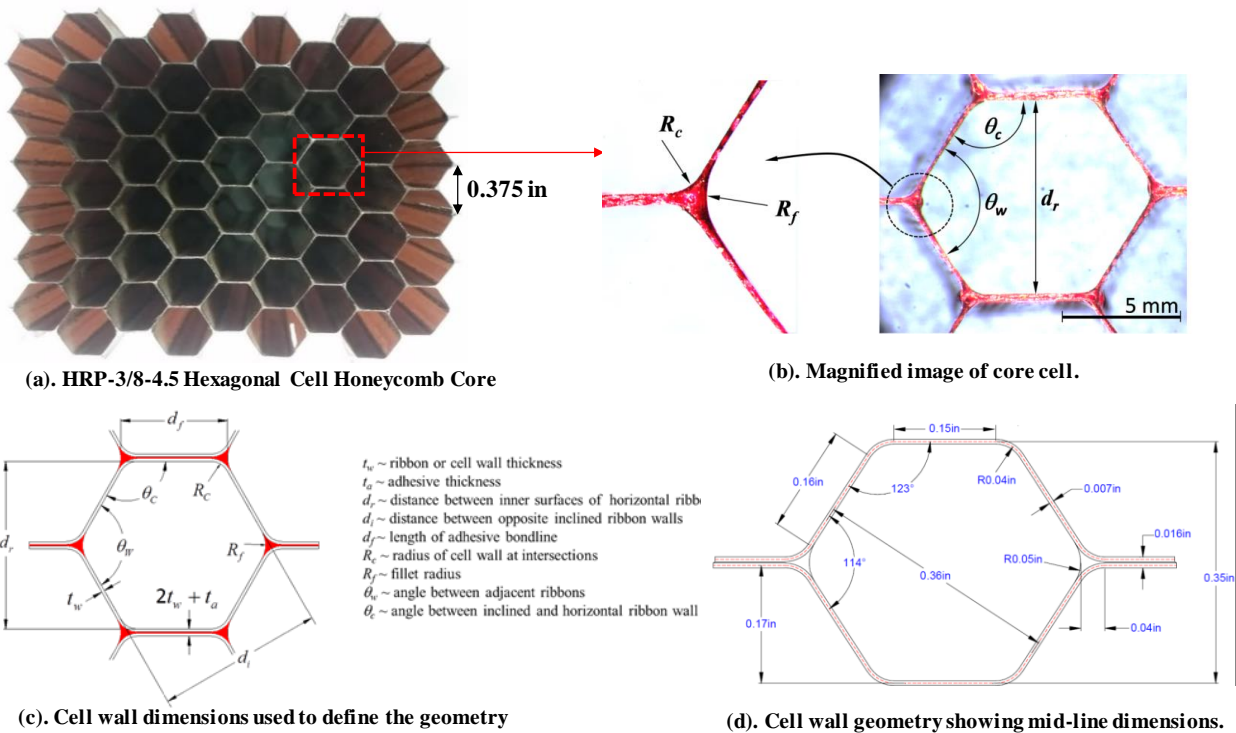


Figure 4-1. Detailed geometry and dimensions of the HRP-honeycomb core cell [13, 15].

Honeycomb cores are manufactured by different manufacturers and core suppliers typically provide homogenized properties of the whole honeycomb structures in the thickness direction and transverse planes [52]. Thus, raw material data of the constituents of the cell wall and node bond adhesive are seldom available in the public domain. In the present study, to facilitate the finite element modeling of the representative unit cell (RVE) of the core microstructure, it was necessary to know the mechanical properties of the cell wall and node bond adhesive. The material properties of the honeycomb core cell including the ribbon material, made of plain weave fiberglass fabric dipped in a heat-resistant phenolic resin to achieve the final nominal density [4], and node bond adhesive, made of phenolic resin, are summarized in TABLE 4-1. The ribbon material properties were determined by conducting the in-plane tension and three-point flexure tests on the cell walls samples of the honeycomb core to determine the both axial and flexural stiffness of the ribbon material due to the heterogeneity associated with a single fabric ply which results in obtaining of different in-plane and flexural moduli [53]; the details of the tests have been reported in [13, 15].

However, the material properties used for the phenolic resin node bond adhesive were extracted from literature [54, 55] because it would be impractical to fabricate cast resin samples using the same processing parameters experienced by the adhesive during honeycomb manufacturing process.

TABLE 4-1

MECHANICAL PROPERTIES OF THE CONSTITUENTS OF FIBERGLASS/PHENOLIC HONEYCOMB CORE [13, 15]

Ribbon Tensile Modulus (MSI)	Ribbon Flexural Modulus (MSI)	Ribbon Poisson's Ratio	Adhesive Tensile Modulus (MSI)	Adhesive Poisson's Ratio
1.90	1.25	0.17	0.533	0.33

4.2 In-Plane Uniaxial Testing of Bulk Honeycomb Core

In order to characterize the uniaxial in-plane mechanical responses of the HRP-fiberglass/phenolic honeycomb core subjected to large deformations, a series of quasi-static, uniaxial tension and compression tests were conducted along the ribbon (L) and transverse (W) directions using a custom built test fixture, as shown in Figure 4-2. The details of the experiments have been reported in author's other publications [13, 15].

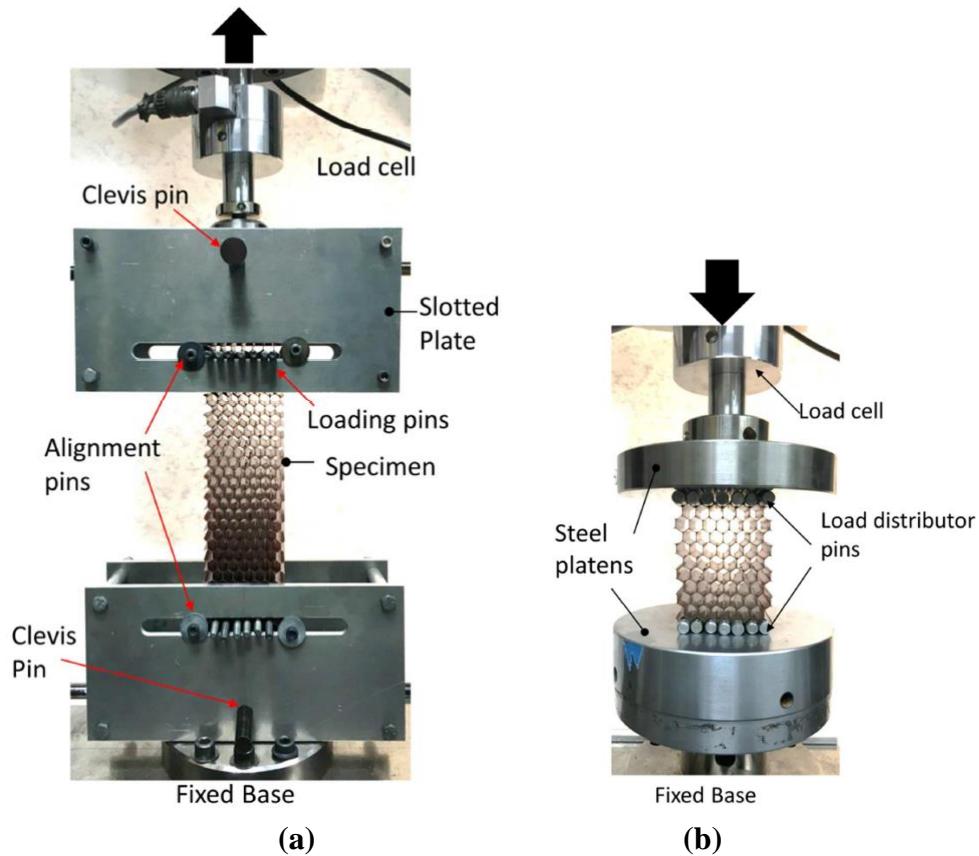
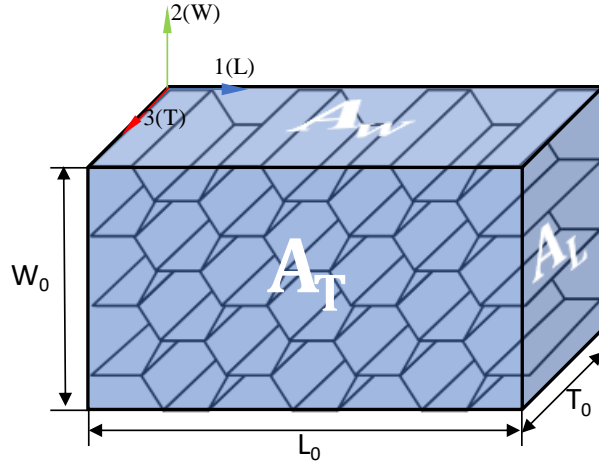


Figure 4-2. Schematic of uniaxial in-plane test apparatus and setup: (a) tension and (b) compression [13, 15].

The load-displacement curves obtained from the test data were used to calculate homogenized engineering stress, strain and engineering constants (tangent moduli) at each load step, as illustrated in Figure 4-3.



$$\sigma_i^n = \frac{F_i^n}{A_i} \quad i, j = 1(L), 2(W) \text{ or } 3(T) \text{ directions}$$

$$\varepsilon_i^n = \frac{u_i^n}{L_i} \quad n = \text{step number}$$

$$E_i^n = \frac{\sigma_i^{n+1} - \sigma_i^n}{\varepsilon_i^{n+1} - \varepsilon_i^n} \quad L_i = \text{length of core in } i\text{-direction}$$

$$v_{ij}^n = \frac{\varepsilon_j^{n+1} - \varepsilon_j^n}{\varepsilon_i^{n+1} - \varepsilon_i^n} \quad A_i = \text{projected area of core on a plane perpendicular to } i\text{-, } j\text{-direction}$$

F_i = total force in i -direction
 u_i = total displacement in i -direction
 σ_i = normal engineering stress in i -direction
 ε_i = normal engineering strain in i -direction
 E_i = extension modulus in i -direction
 ν_{ij}^n = Poisson's ratio

Figure 4-3. Process of calculation of the homogenized quantities at each load step.

4.2.1 Result and Discussion

The homogenized engineering stress-strain diagram for loading along the ribbon and transverse directions with the embedded typical images of the deformed core cells as well as the Poisson effects under tension and compression loading are shown in Figure 4-4.

As indicated by test results in Figure 4-4 (a), the homogenized stress-strain behavior of the honeycomb core are markedly nonlinear and anisotropic. Under tensile loading, the core exhibits a stiffening behavior with loading due to the stabilizing nature of the tensile load which tends to align the inclined cell walls along the loading direction (densification) while the softening

responses are observed under compressive loading which is attributed to cell wall buckling as well as the shear instability where the cell walls rotate in opposite direction. The nonlinear Poisson contraction is also observed from test data which is close to unity at low strain levels, as presented in Figure 4-4 (b).

The homogenized stress-strain curves obtained from test data will be used to assemble the hyperelastic SEDF and evaluate the results predicted by the FEM of the core RVE besides the FEM of the homogenized core using the hyperelastic constitutive model.

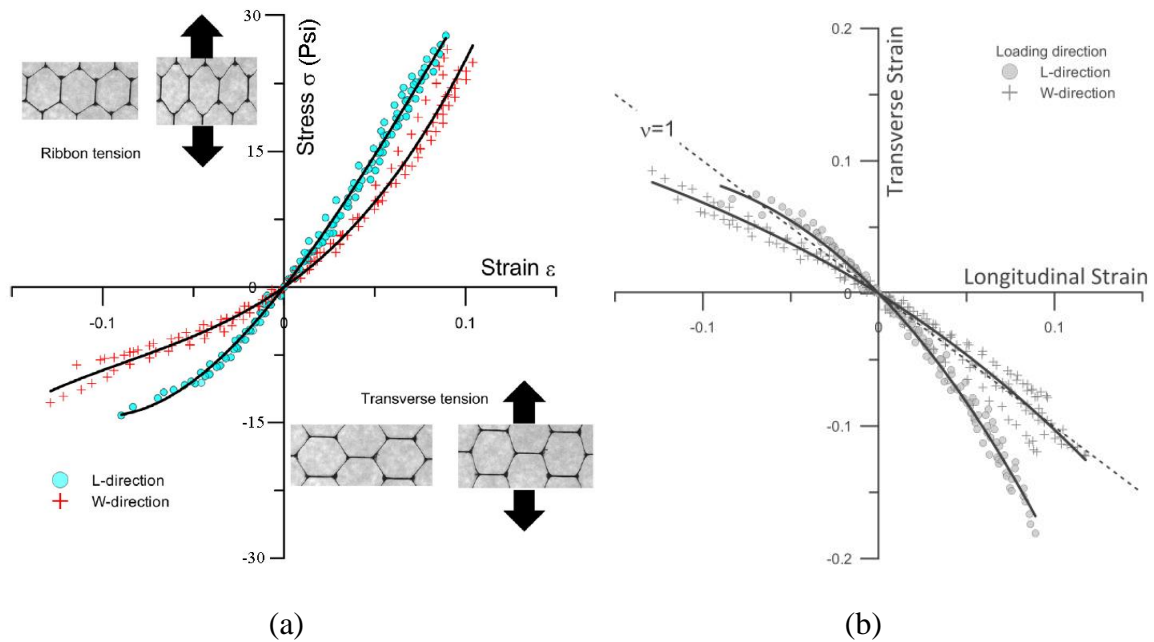
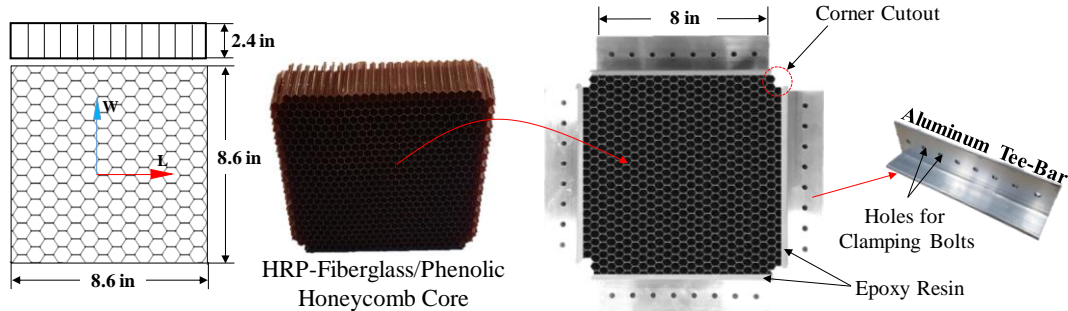


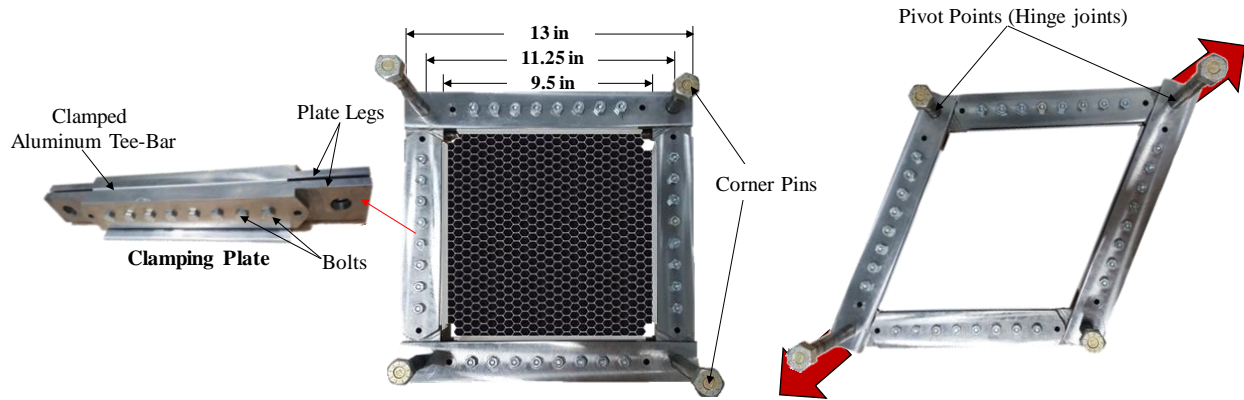
Figure 4-4. (a) Homogenized engineering stress-strain curves; (b) transverse strains versus longitudinal strains for in-plane tensile and compressive loads along L- and W-directions [13].

4.3 In-Plane Pure Shear Testing of Bulk Honeycomb Core

In order to investigate the in-plane mechanical response of the HRP-fiberglass/phenolic honeycomb core subjected to large in-plane shear deformation and assess the effectiveness of the numerical models, a quasi-static pure shear test was conducted using a custom-built picture-frame shear-test fixture, as illustrated in Figure 4-5.



(a) Geometry and dimensions of test specimen and its preparation procedure.



(b) Steel picture-frame shear-test fixture and its deformed configuration.

Figure 4-5. Geometry and dimensions of test specimen along with test apparatus for in-plane pure shear testing.

As is shown in Figure 4-5, a square plate HRP-honeycomb core specimen, having dimensions of $8.6 \times 8.6 \times 2.4$ in, is cast and epoxy bonded to the flanges of Aluminum Tee-bars; four corner cutouts are also made on the honeycomb core specimen to accommodate the shearing of the test section and prevent the immediate buckling of the core cell walls. The webs of the Tee-bars are then clamped into an articulated heavy steel frame made up of four clamping plates, each

consisting of two very stiff steel plate legs, through uniformly distributed high strength bolts. Finally, each pair of clamping plates are connected at the corners using high-strength steel pins (hinge joints) to allow rotation. To avoid bearing of the steel plate legs on the pins at the corners, holes of the steel plate were machined slightly larger than the pin diameter. The deformed configuration of the fixture which results in “ideal pure -shear deformation” is also shown in Figure 4-5.

To simulate the applied pure shear stresses which act on the honeycomb core in the principal plane (L-W), the picture-frame shear-test fixture is rotated 45° and subjected to external diagonal tensile load [56], as schematically shown in Figure 4-6. The applied tensile load to the rigid steel frame induced equivalent shear forces along the edges of the honeycomb core specimen through uniformly distributed bolts and Aluminum T-bars.

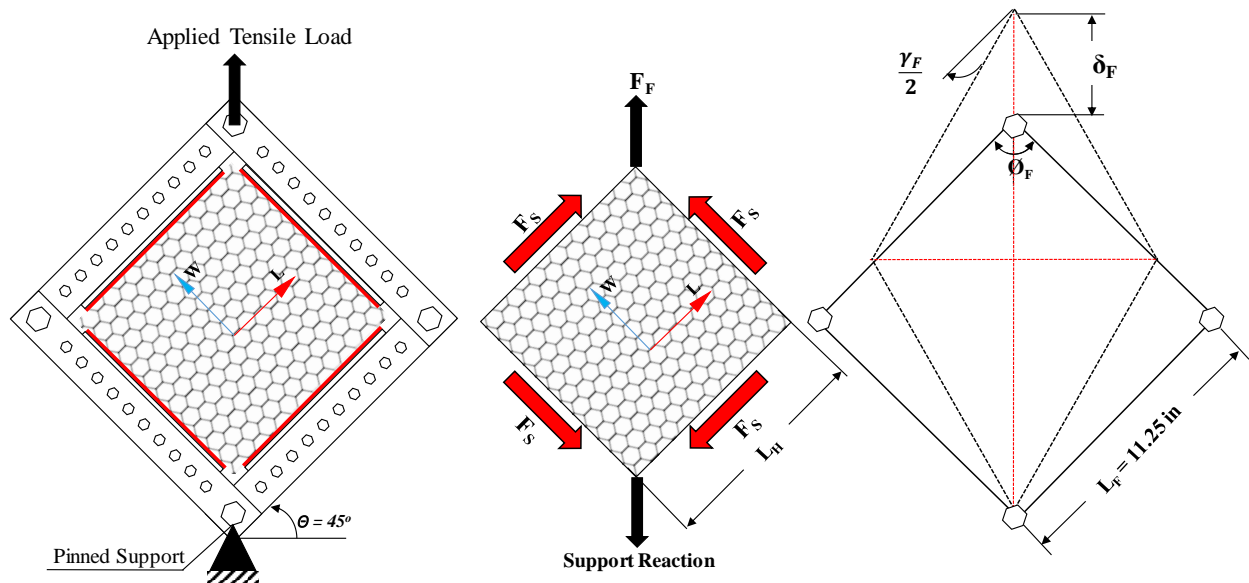


Figure 4-6. Schematic of the shear test fixture subjected to the applied tensile load along with the state of forces acting on the honeycomb core in (L-W) plane and its deformation [57].

As illustrated in Figure 4-6, by simple kinematic analysis of the picture frame, frame shear angle γ_F or average in-plane shear angle ($\bar{\gamma}_{LW}$), frame angle θ_F which is initially 90° and the shear forces

F_S acting on the frame legs can be given as a function of frame displacement δ_F and the frame resistance force (the force measured by the load cell in the crosshead) F_F , by equation (4.1):

$$\begin{aligned}\phi_F &= 2 \cos^{-1} \left[\frac{1}{\sqrt{2}} + \frac{\delta_F}{2L_F} \right] \\ \gamma_F = \bar{\gamma}_{LW} &= \frac{\pi}{2} - \phi_F = \frac{\pi}{2} - 2 \cos^{-1} \left[\frac{1}{\sqrt{2}} + \frac{\delta_F}{2L_F} \right] \\ F_S &= \frac{F_F}{2 \cos(\frac{\phi_F}{2})} = \frac{F_F}{2 \left[\frac{1}{\sqrt{2}} + \frac{\delta_F}{2L_F} \right]}\end{aligned}\quad (4.1)$$

where L_F is the side length (the length between the center of the corner pins at the end of one side) of the picture frame.

The average in-plane engineering shear stress acting on the honeycomb core specimen, can be simply calculated by:

$$\bar{\tau}_{LW} = \frac{F_S}{L_H t_H} \quad (4.2)$$

where L_H and t_H are the length and thickness of the honeycomb core specimen shown in Figure 4-5 (a). The core thickness was assumed constant during the test due to the high out-of-plane stiffness of the core.

In this study, the tensile load was applied to the picture-frame shear-test fixture using an electromechanical universal testing machine (Sintech 5/G, MTS). The force measurement was made using a 5000 lbf capacity load cell and the test was conducted under displacement control mode at a nominal crosshead displacement rate of 0.05 in/minute. The force and displacement data were recorded at a rate of 1/10 Hz during the test until the failure of the honeycomb core. View of the in-plane pure shear test setup is shown in Figure 4-7.

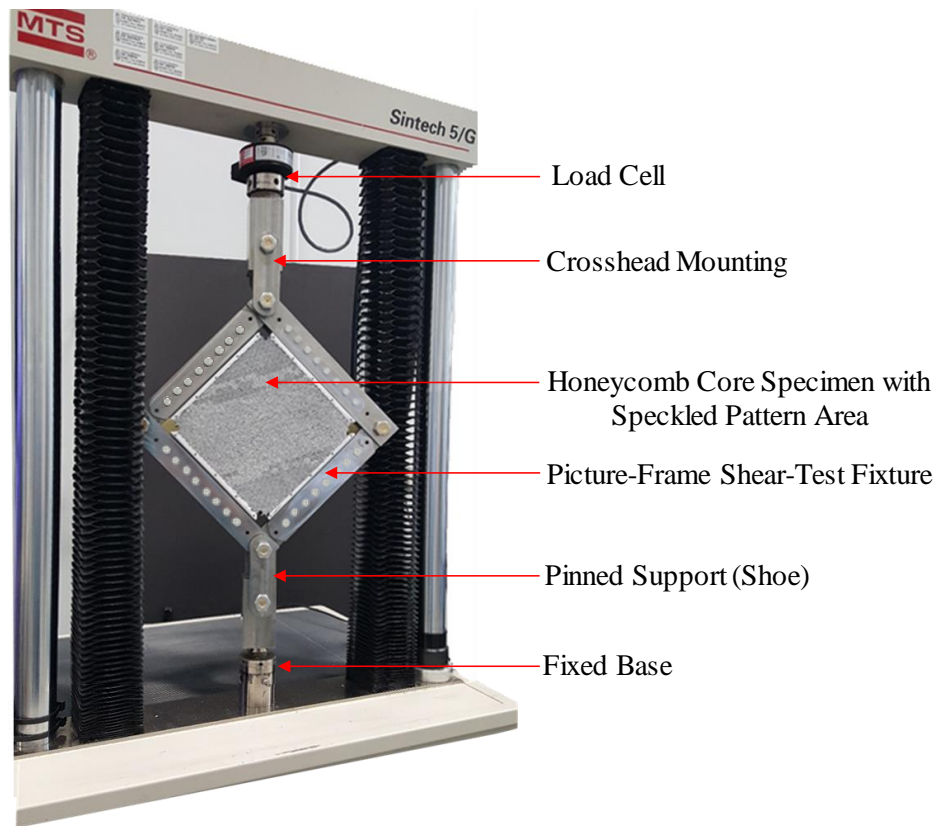


Figure 4-7. View of test arrangement for in-plane pure shear testing of honeycomb core.

4.3.1 Digital Image Correlation (DIC) Measurements

As illustrated in Figure 4-8, ARAMIS adjustable 6M system [32] which is a non-contact and material-independent measuring system based on digital image correlation (DIC) was used to measure strain and displacement components throughout the core specimen during the deformation process. The ARAMIS DIC system (operating in both 2D and 3D events) uses a series of sequential digital images using a 6-megapixel stereo camera system to determine the surface deformation and surface strain of objects. The systems identify features of an object and track the relative movement of those features throughout the sequential images [58].

All instrumentations (ARAMIS sensors) were connected to an electronic data acquisition system using ARAMIS Professional Software 2017 [58].

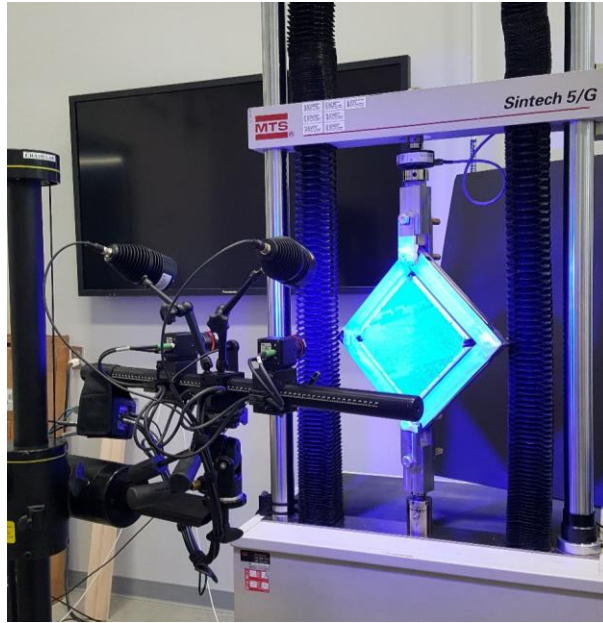
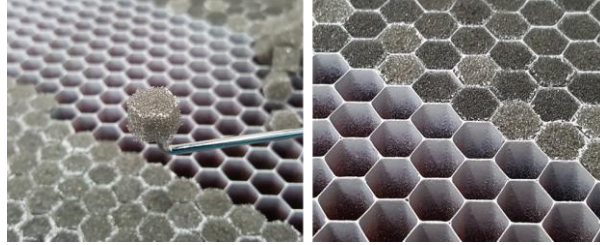


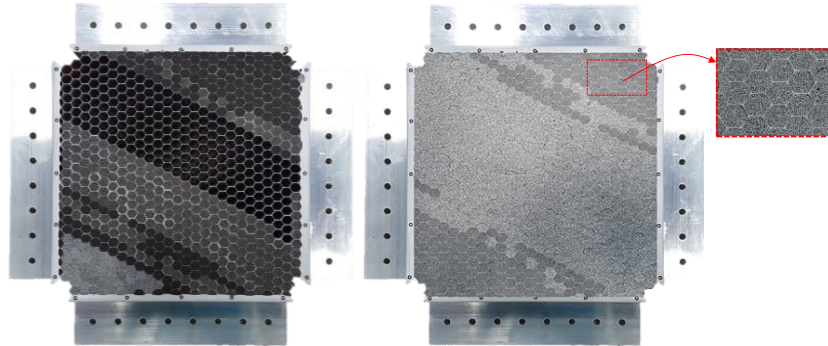
Figure 4-8. ARAMIS adjustable 6M, 3D DIC system set up.

The principle of the strain measurement in the ARAMIS DIC system is based on subset windows (or facets) that are tracked during the deformation by a correlation algorithm; the center coordinates of the facets will then be used to determine the strains [32, 58]. Unique square facets are identified by the ARAMIS system by utilizing stochastic (speckle) patterns and/or point markers applied to the surface of the target object [58]. For homogeneous and non-porous objects such as steel, this is typically achieved by spraying the surface of the material with a speckle pattern using matte spray paint.

In order to create a speckle pattern on the top (target) surface of the honeycomb core specimen, the first step is to create a fake homogeneous surface which was done by filling each cell of the core with a very low stiffness foam (sponge); a very thin layer of white matte paint was then sprayed on the foam filled surface to reduce the light reflection and exhibits sufficient contrast. It was ensured that the foam and paint did not affect the in-plane behavior of the core. A procedure for creating a speckle pattern on the honeycomb core and creating a suitable pattern color is depicted in Figure 4-9.



(I). Filling the each honeycomb core unit cell with a very low stiffness foam material to create a fake homogeneous surface.



(II). Painting the foam filled surface to create a suitable speckle pattern colour with sufficient contrast.

Figure 4-9. A speckle pattern created on the target (top) surface of the honeycomb core specimen for DIC measurements.

For the DIC computation in ARAMIS system, the facet size was carefully chosen to capture only the macroscopic deformation of the honeycomb core and not, for example, the movement of the individual cell walls. Therefore, the facet size for the honeycomb core is comparable with the unit cell size of the core which results in computation of the homogenized surface strain field throughout the core specimen as illustrated in Figure 4-10.

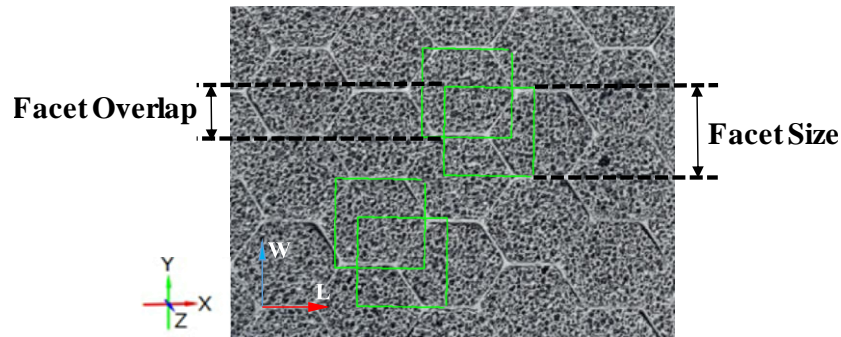


Figure 4-10. Facet size (comparable with the honeycomb core unit cell size), and overlap used for DIC computation.

It should be noted that, in the ARAMIS software, to obtain the local shear angle and strain field on the surface of the honeycomb core in (L-W) plane, coordinate system (X, Y, Z) in the initial configuration was defined along the honeycomb core principal material directions, as shown in Figure 4-10.

In order to determine the homogenized local shear angle of the honeycomb core specimen, the ARAMIS provides positions of the corners of the deforming facets which are initially square and comparable with the unit cell size, as illustrated in Figure 4-11. Based on this data, the homogenized local shear angle throughout the core specimen is calculated by:

$$\gamma_{LW} = \frac{\pi}{2} - \alpha_{LW} \quad (4.3)$$

where α_{LW} is the angle between AD and AB edges of the facet which denotes the angle between the honeycomb core L- and W- principal directions.

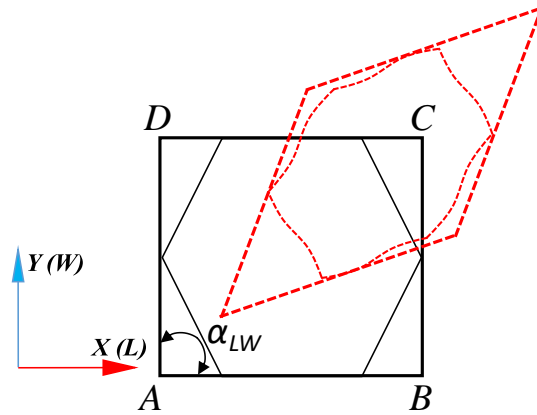


Figure 4-11. DIC calculation of the homogenized local shear angle of the honeycomb core.

Furthermore, to obtain the strain field on the honeycomb core surface in the principal plane (L-W), the ARAMIS system was used for assessment of *Green-Lagrange* (E_{ij}) strain tensor components.

4.3.2 Result and Discussion

The axial force versus crosshead displacement plot generated using the recorded data of the picture-frame fixture for in-plane pure shear testing of the HRP- fiberglass/phenolic honeycomb core as well as the deformed shapes of the honeycomb core at different load levels up to the collapse of the core are presented in Figure 4-12.

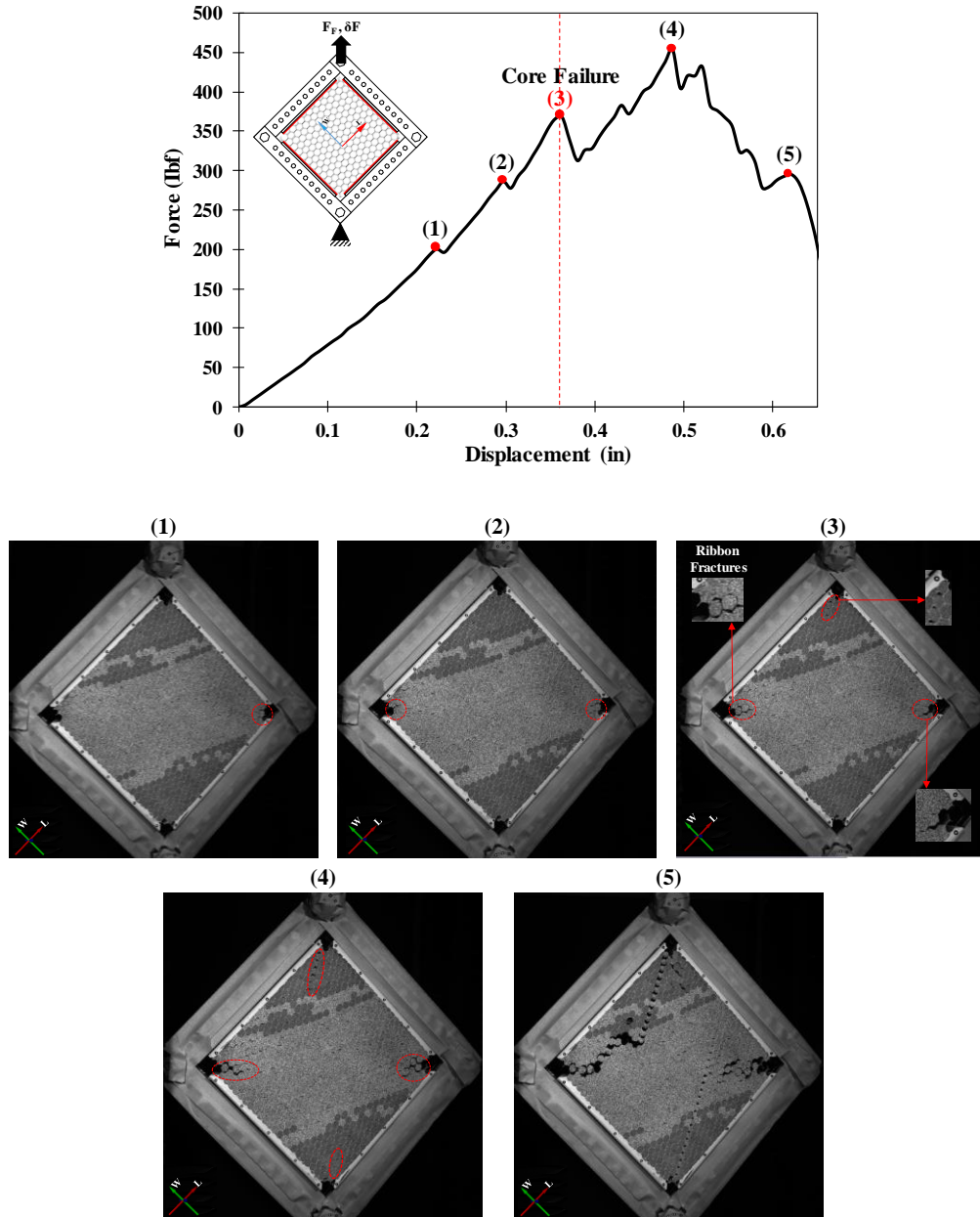


Figure 4-12. Axial force - crosshead displacement plot resulting from pure shear test along with the photo sequence of the test until the core collapse.

As can be seen in Figure 4-12, mechanical response of the honeycomb core is observed to be nonlinear up to the failure of the core. However, the nonlinearity of the test data may not be entirely attributed to the core behavior and the effect of the picture-frame fixture must be taken into account which will be discussed in the FEA of the homogenized core. Although two sudden load drops are observed during the shear deformation process due to the ribbon fractures at the honeycomb core corners, the core continues to carry additional load until the significant drop in load which occurs after an axial displacement of the fixture's top corner of 0.35 inches. This corresponds to approximately 365 lbf of axial force on the crosshead of the picture-frame fixture which is highlighted at the load level (3) in the Figure 4-12 and determined as core failure. After that, the load value continuously rises with the sequence of peaks and sub peaks because of the progressive propagation of the defects up to the load level (4) where the defects propagation, dominated by bending induced cell wall fractures, becomes unstable and core cannot carry the additional load.

As depicted in Figure 4-12, during the shear test, the failure occurs at the corners of the honeycomb core specimen, propagating from the corner cutouts towards the interior of the core until the core collapse. When tensile load is applied to the upper crosshead of the picture frame fixture, the adjacent fixture legs pivot about each other at the fixture corner pins. The kinematics of the fixture will induce in-plane compressive stresses in the diagonal upper and lower corners and in-plane tensile stresses in the other corners. The compressive stresses can cause local buckling of the honeycomb core near the corners whereas the tensile stresses can tear the honeycomb core specimen apart along the other diagonal corners or along the adhesively-bonded edge interfaces due to high bending induced deflection of the cell walls. Both of these conditions resulted in the ribbon fractures failure mode of the honeycomb core, as illustrated in Figure 4-12. It is interesting to note that, there were no failures along the adhesively bonded edges until the collapse of the core.

The in-plane *Green-Lagrange* strain-field distribution on the top (target) surface of the honeycomb core specimen calculated by ARAMIS at core failure is shown in Figure 4-13. It is evident that, the normal strain fields are approximately uniform and negligible ($\pm 1\%$) throughout the honeycomb core with the high compressive and tensile values in the vicinity of the core corner-cutouts. However, except the central part of the core, shear strain field is not uniformly distributed.

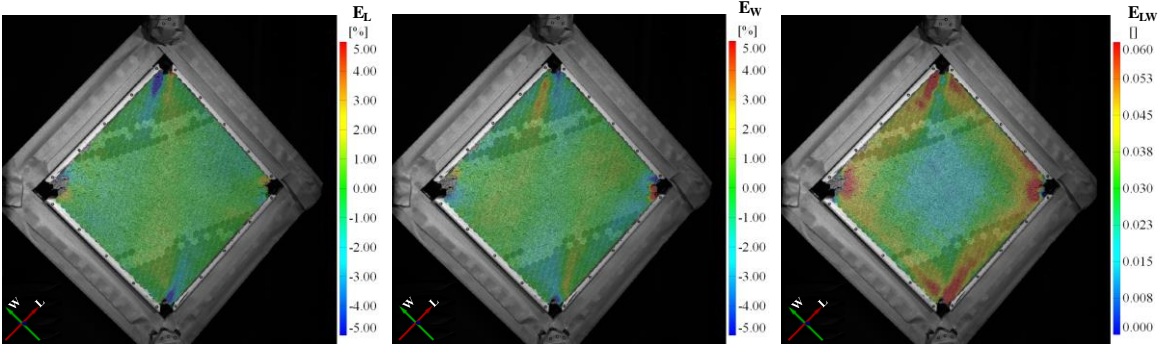


Figure 4-13. The distribution of *Green-Lagrange* strains calculated by ARAMIS DIC system at honeycomb core failure.

In order to compare the in-plane strain distributions across the honeycomb core specimen at different axial force levels, two ribbon and transverse paths were defined in the ARAMIS professional software, as illustrated in Figure 4-14.

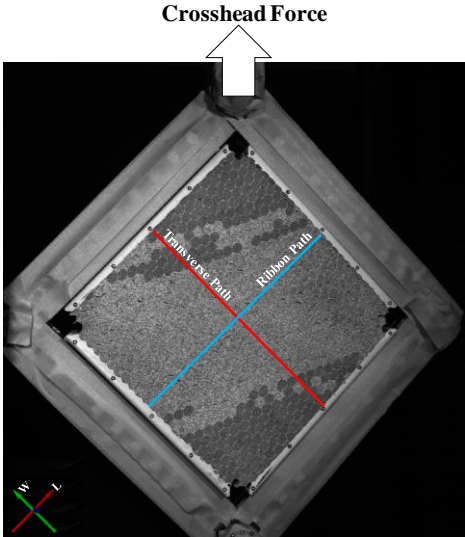


Figure 4-14. Illustration of ribbon and transverse predefined paths for calculation of strains across the honeycomb core specimen in ARAMIS professional software.

Figure 4-15 presents the in-plane strain distributions along the sketched ribbon and transverse paths, which were calculated and transformed into the predefined material coordinate system (L-W) by the software, at four different axial force stages.

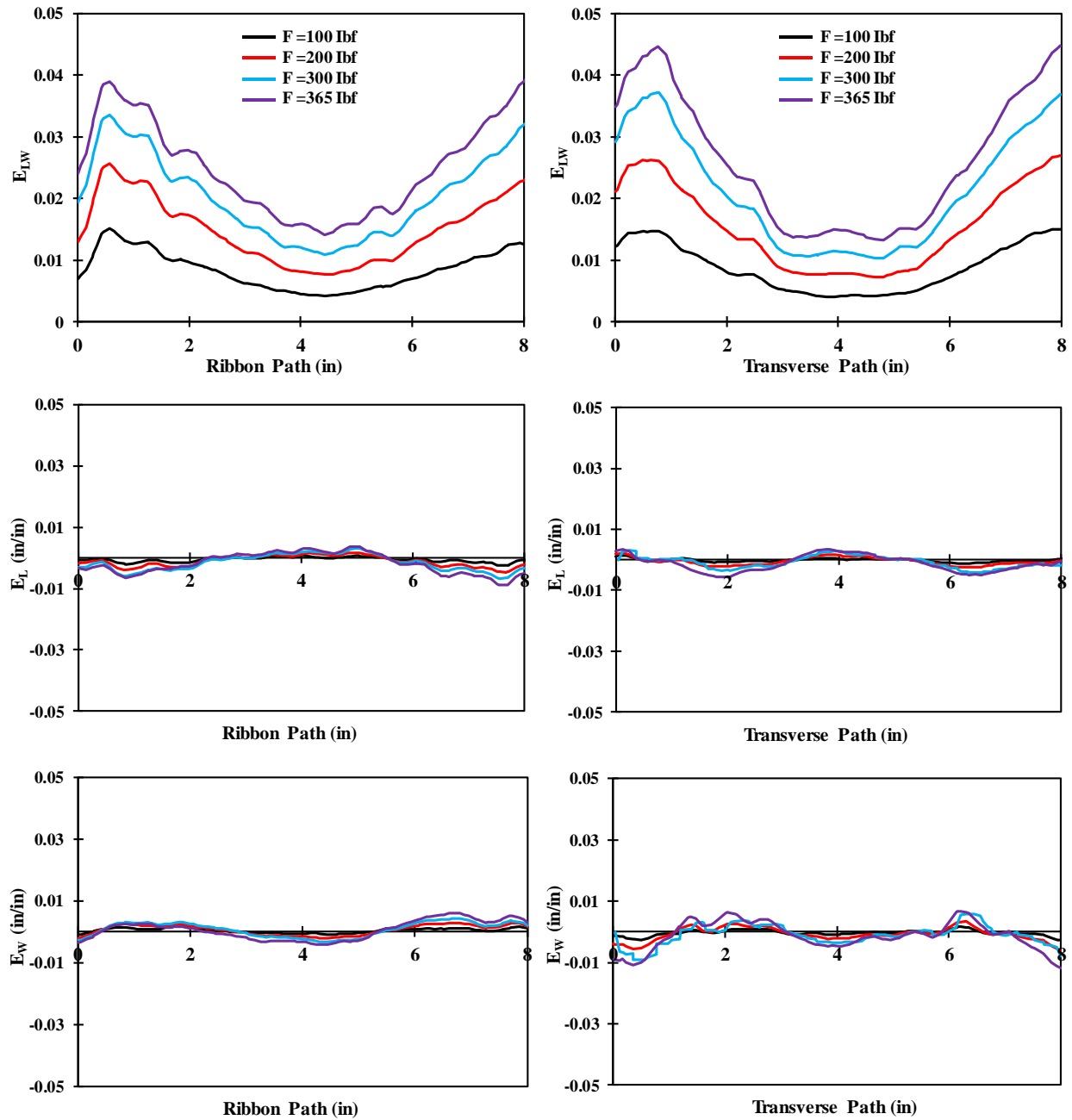


Figure 4-15. In-plane strain profiles along the two predefined paths across the honeycomb core measured by ARAMIS at four different axial force levels.

As is shown in Figure 4-15, except the central part of the honeycomb core, the shear strain distributions are not uniform along the predefined paths particularly near the glued edges. The shear strain magnitudes are almost identical along the both paths at each load level while the magnitudes of the normal strain are negligible. However, because of the biaxial state of the strain even a very small magnitude of the strains can induce significantly large stress magnitudes in the honeycomb core due to the close to unity in-plane Poisson ratios.

Ideally, the best scenario for using the picture-frame shear-fixture is to generate a uniform shear-stress (strain) distribution with no normal stresses throughout the honeycomb core specimen. However, small shear-stress gradients near the adhesively bonded edges and the corners are acceptable. Similarly, high normal stresses near the glued edges and in the corners can be acceptable, provided that the interior of the core is free of normal stresses and those induced along the adhesively bonded edges are only a few percent of the magnitude of the shear stress in the interior of the panel. Using the finite element stress analysis to aid in design and improvement of picture frame fixture efficiency, it was reported that [59], the position of the corner pins has a significant effect on the distribution of stresses throughout the sample. The best location for the pins was shown at the corners of the panel test section such that the centers of the hinges collineate with the internal edges of the frame as depicted in Figure 4-16 by position (1).

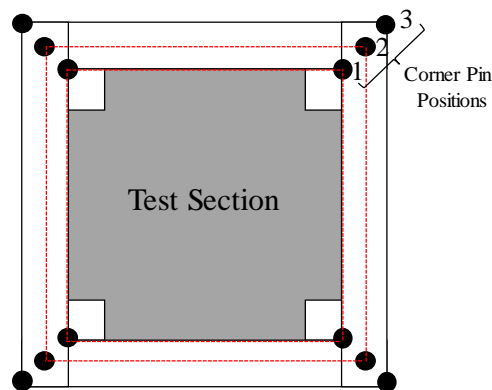


Figure 4-16. Corner-pin locations for finite element stress analysis [59].

It was shown that, when the corner pins were located at position 1, the shear stress distribution was uniform with negligible stress gradients or normal stresses. The shear stress distribution throughout the panel and the magnitude of the normal stresses in the corners changed significantly when the corner pins were moved away from the position (1) to (3). Therefore, the results shown in Figure 4-15 can be justified by the aforementioned discussion, because the corner pins of the picture-frame shear-fixture in this study were located at the position (2) in Figure 4-16 resulting in non-uniform shear field throughout the core specimen. Moreover, the facet size chosen in the ARAMIS software is another factor that requires to be explored. Particularly, near the edges, ARAMIS system was not able to capture the deformation of the unit cell due to the fixity of the honeycomb core edges and distorted unite cells, as is obvious in Figure 4-15.

In order to determine the in-plane shear rigidity modulus of the HRP-fiberglass/phenolic honeycomb core, first, the average engineering shear stress-shear angle (frame angle) diagram for the HRP-honeycomb core was generated using the axial force and crosshead displacement of the picture-frame fixture up to the core failure, as illustrated in Figure 4-17.

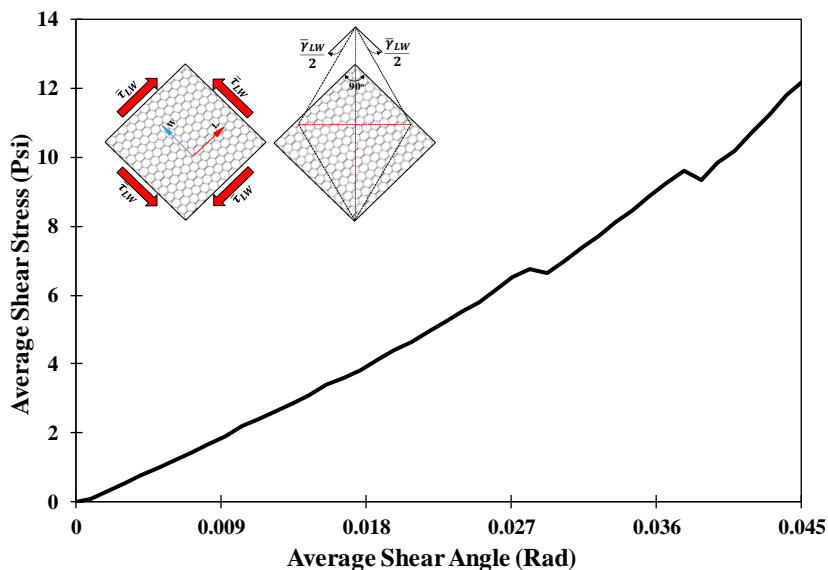


Figure 4-17. Average shear stress-shear angle curve for fiberglass/phenolic honeycomb core resulting from shear test data.

The in-plane shear modulus expression as a function of the frame shear angle in radians can be calculated from the derivative of the fitted curve of the average shear stress-shear angle of the core given in Figure 4-17 by the following simple equation

$$\bar{G}_{LW}(\bar{\gamma}_{LW}) = 3284\bar{\gamma}_{LW} + 188 \quad (4.4)$$

Using equation (4.4), a relatively high average in-plane shear modulus between 188 and 335 Psi is calculated which indicates that the HRP-honeycomb core is relatively stiff under in-plane shear deformation. However, the predicted average incremental shear modulus was obtained based on the deformation parameters of the picture frame fixture and global (macroscopic) deformation of the core specimen. This result may not necessarily represent the in-plane shear modulus of the core unless the macroscopic (average) shear angle and microscopic (local) shear angle of the honeycomb core are shown to be identical.

Figure 4-18 shows the distribution of the local shear angle given in equation (4.3) throughout the honeycomb core specimen measured by ARAMIS DIC system at different stages of axial force acting on the crosshead of the picture frame fixture. It is evident from Figure 4-18, except the central region of the core, the shear angle distribution is not uniform within the honeycomb core specimen and has a much larger magnitude near the glued edges of the core.

As discussed earlier, this can be attributed to the location of the corner pins of the picture frame fixture, kinematic of the fixture, size of the specimen, facet size in DIC and most importantly large magnitude of the normal stresses inducing in the vicinity of the adhesively bonded edges due to glued edges effect which constrained the rotation of the honeycomb core cell walls.

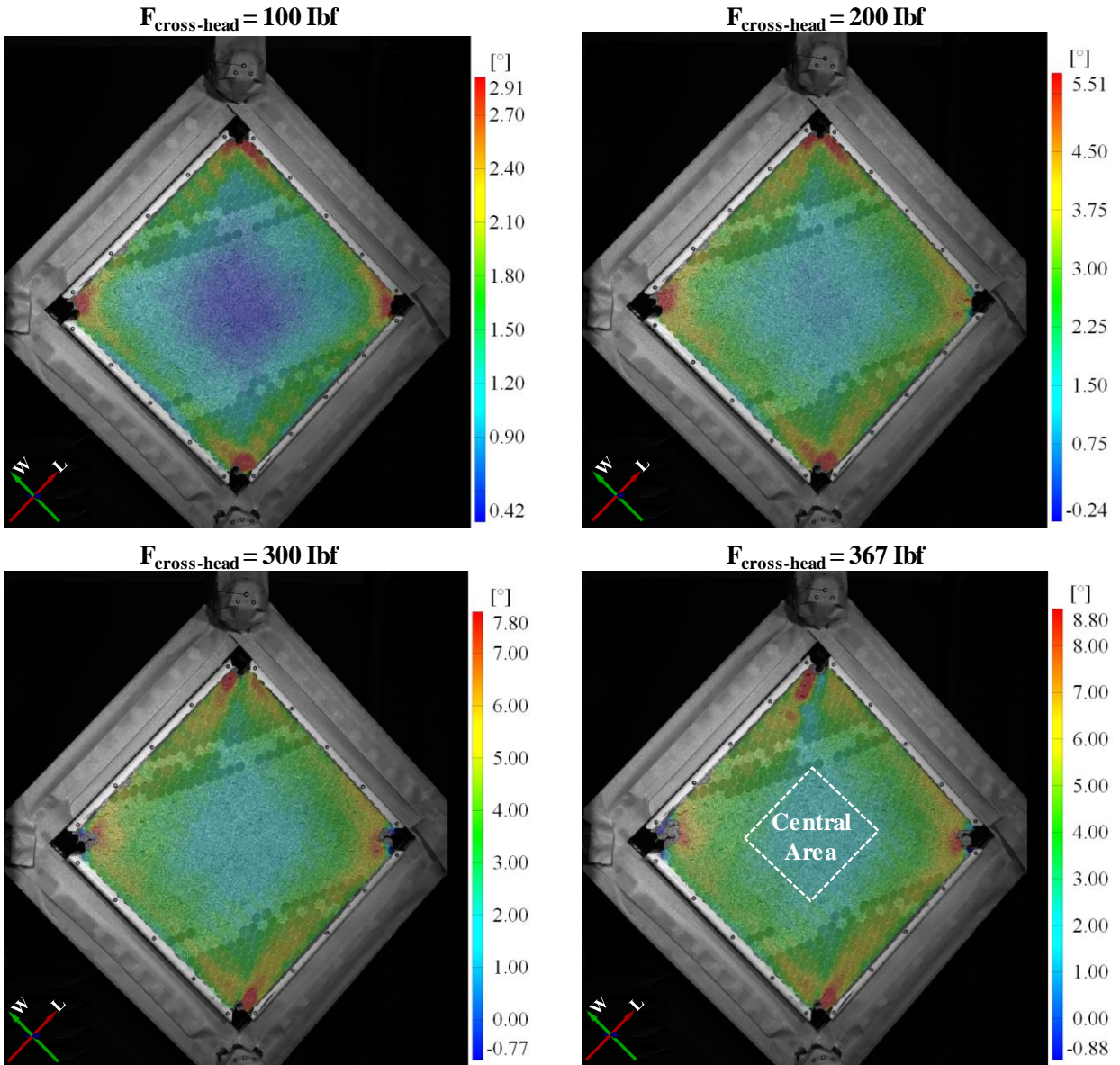


Figure 4-18. Local shear angle (γ_{LW} [deg]) contours measured by ARAMIS DIC system at different stages of axial force on the picture-frame cross-head.

The average, minimum and maximum values of the shear angle and normal strains over the central area of the honeycomb core specimen, highlighted in Figure 4-18, for each frame until the failure of the core measured by ARAMIS DIC system are plotted in Figure 4-19.

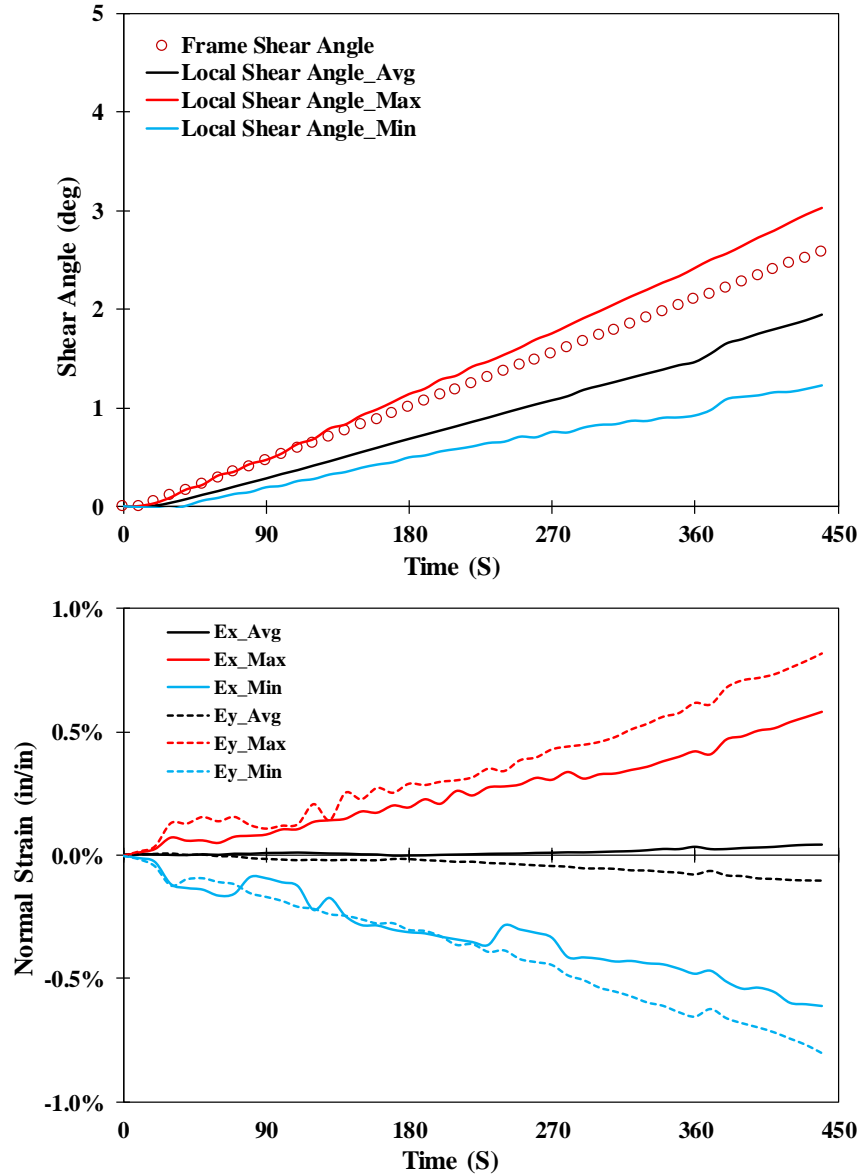


Figure 4-19. Max., Min. and Avg. values of the local shear angle and normal strains over the central area of the core specimen calculated by ARAMIS DIC system for each frame.

As is shown in Figure 4-18 and evident in Figure 4-19, the local shear-angle distribution over the central area of the honeycomb core is reasonably homogeneous and the difference between the maximum and minimum values is less than 2° even at highest angle. In addition, a relatively good agreement between the local shear angle measured by ARAMIS and frame (average) shear angle derived from the crosshead displacement is observed in Figure 4-19 particularly for the maximum

value of the local shear-angle. As can be seen in Figure 4-19, normal strains in the central part of the honeycomb core are negligible and the average values are about zero. Therefore, it can be concluded that the central area undergoes the pure shear deformation.

In conclusion, a good agreement was observed between picture-frame shear experiment and ARAMIS DIC analysis only in the central part of the honeycomb core specimen which is much smaller than the specimen size. Therefore, the nonlinear shear response of the core would not be necessarily attributed to the inherent core behavior and the effect of the fixture must be investigated.

To minimize the deviation between the frame shear-angle and the local shear-angle and having a uniform distribution of the shear angle with nearly zero normal strain distributions throughout the honeycomb core, it is first necessary to change the position of the corner pins such that the fixture corner pins coincide with the corners of the panel's test section and then find the creative way to avoid the use of adhesively bonded interface which can significantly reduce the normal strains induced along the edges or increase the size of the fixture and specimen to reduce the edge effects.

In this research, a pure shear test on the honeycomb core was considered a structural test not a material characterization test. More details about the in-plane shear behavior of the HRP-honeycomb core will be explained in finite element analysis of the core RVE to determine the effective shear stress-strain curve of the core in the next chapter. The pure shear test by modeling the specimen and the picture-frame fixture was also simulated in a finite element software to include the effect of the fixture and other factors that might contribute to the analysis for validation of the FEA simulation of the homogenized core using the developed hyperplastic constitutive model, which will be explained in chapter 6.

4.4 In-Plane Off-Axis Pure Shear Testing of Bulk Honeycomb Core

In order to investigate the mechanical behavior of the HRP-fiberglass/phenolic honeycomb core under biaxial loading along its principal directions using the picture-frame shear-test fixture, the honeycomb core was loaded in shear at $\alpha = 45^\circ$ to the principal material directions which results in equal induced tensile and compressive stresses along the ribbon and transverse directions (on the bulk core), respectively, as schematically illustrated in Figure 4-20.

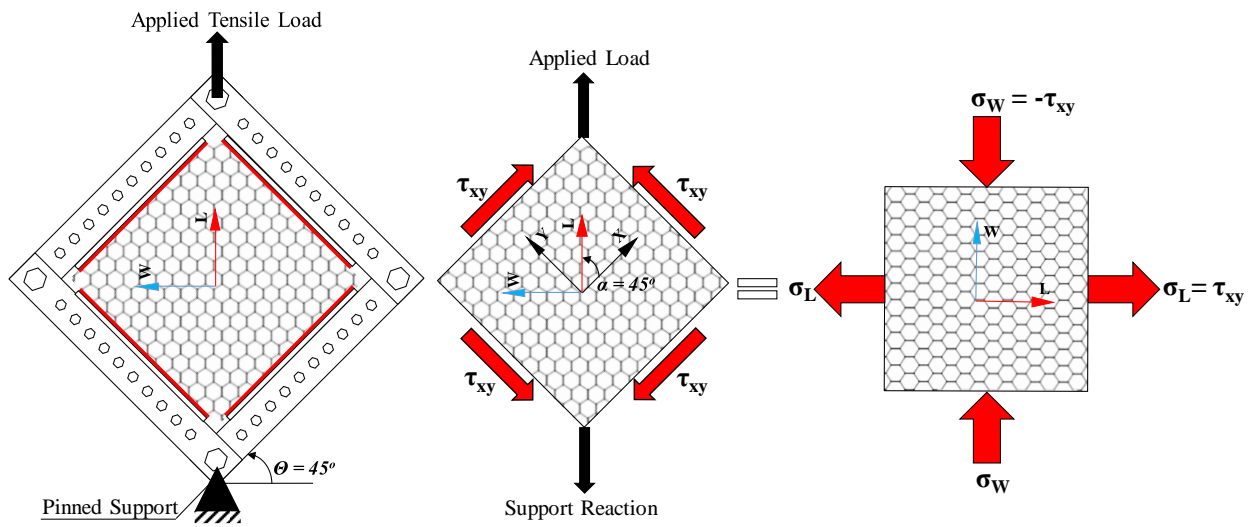


Figure 4-20. Schematic of off-axis pure shear testing conducted on HRP-fiberglass/phenolic honeycomb core along with the state of stresses acting on the core specimen in (L-W) plane.

Figure 4-21 shows the geometry and dimensions of a square plate HRP-honeycomb core specimen which was cut from the honeycomb core sheet at an angle of 45° to the principal L- and W- directions. The honeycomb core specimen, which was cast and epoxy bonded to the aluminum Tee-bars, as well as its surface preparation for DIC analysis using the ARAMIS system are also depicted in the same figure.

The same procedure and test arrangement as discussed for the in-plane-pure shear testing were replicated for the off-axis shear testing of the HRP-honeycomb core.

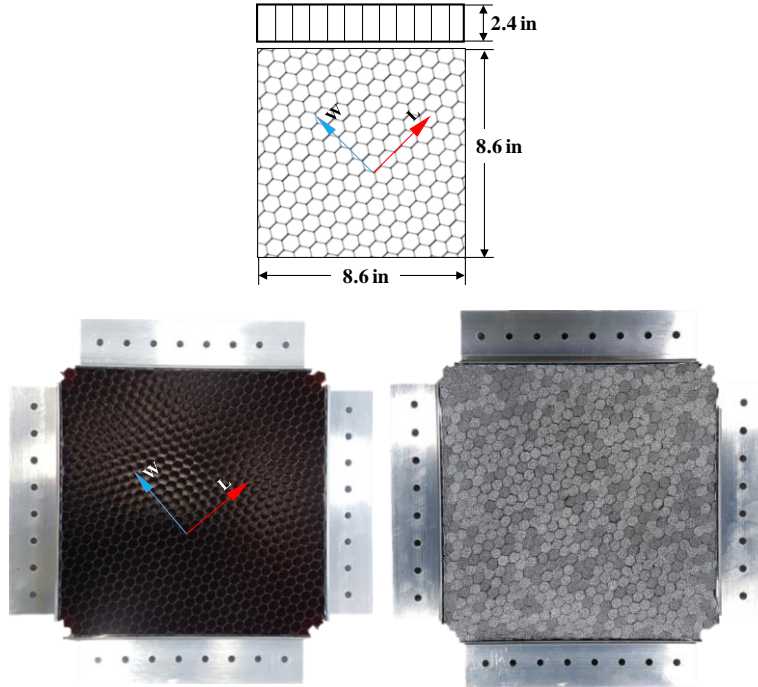


Figure 4-21. Geometry and dimensions of the off-axis honeycomb core specimen along with the final fabricated core for mounting in the picture-frame fixture and DIC analysis.

4.4.1 Result and Discussion

The crosshead force - displacement diagram generated using the recorded data of the picture-frame fixture for in-plane off-axis (X-Y) pure shear testing of the HRP- fiberglass/phenolic honeycomb core as well as the photo sequence of the test up to the collapse of the core are presented in Figure 4-22

As can be seen in Figure 4-22, the core behavior is nonlinear up to the initiation of collapse in the specimen which is indicated at load level (2) and determined as core failure. This corresponds to approximately 372 lbf of axial force acting on the crosshead of the picture-frame fixture after about 0.2 inches of crosshead axial displacement. After that, the defects are progressively propagated while the overall load remains more or less the same until the most of the cells are collapsed, which is shown in Figure 4-22 as progressive failure region.

As is evident from the photo sequence of the off axis shear test in Figure 4-22, ribbon fractures are observed to be the main cause of the core failure which are initiated in the corners of the core and propagated towards the core center.

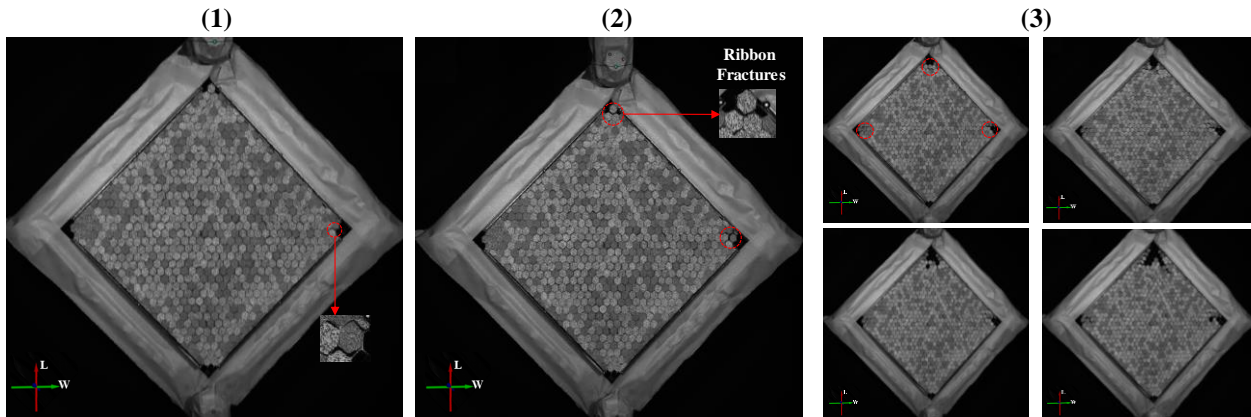
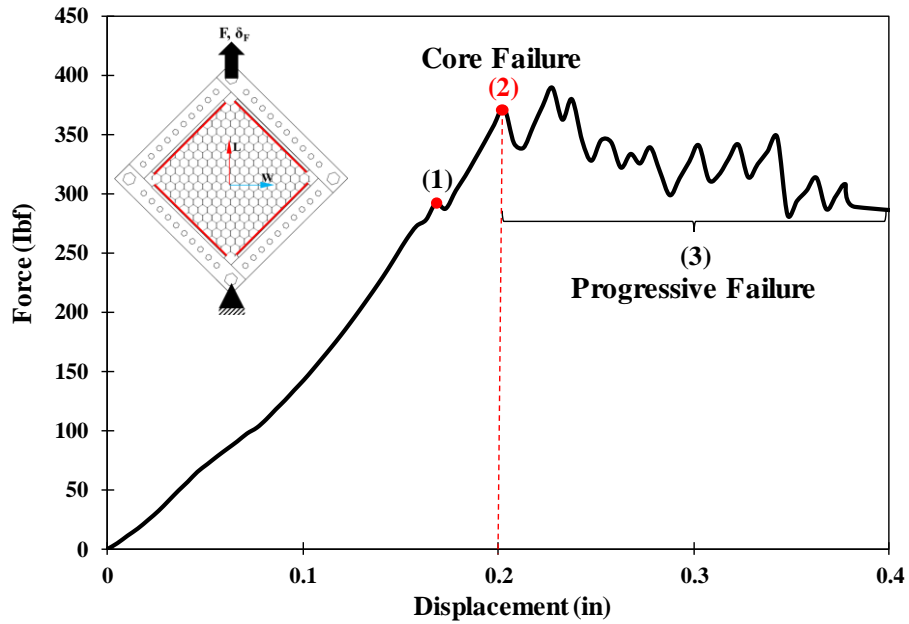


Figure 4-22. Axial force - displacement curve resulting from off-axis pure shear test along with the photo sequence of the test until the core collapse.

The in-plane *Green-Lagrange* strain measurements using ARAMIS DIC system at the core failure is shown in Figure 4-23. A uniform distribution of longitudinal strains in the central area of the core specimen can be seen. The high strain gradients are particularly observed in the vicinity of the core edges and around the core corners. The shear strain is distributed with negligible magnitude over the central part of the honeycomb core.

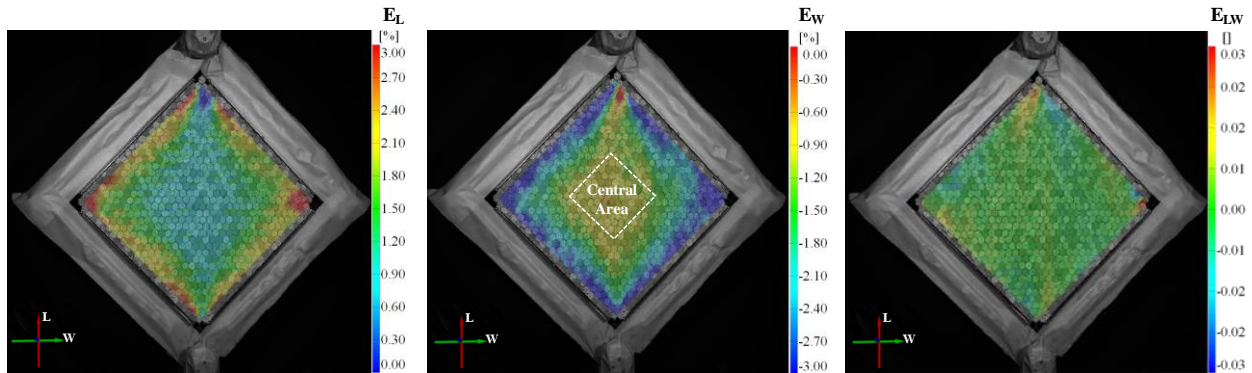


Figure 4-23. The distribution of *Green-Lagrange* strains calculated by ARAMIS DIC system at the honeycomb core failure.

The profiles of strains along the ribbon and transverse paths defined in the ARAMIS professional software across the stochastic surface of the honeycomb core specimen at different axial force levels are also presented in Figure 4-24. As illustrated in Figure 4-24, the normal strains have almost the same magnitudes and they are distributed uniformly along the central length of the sketched paths while the in-plane shear strain is observed to be negligible.

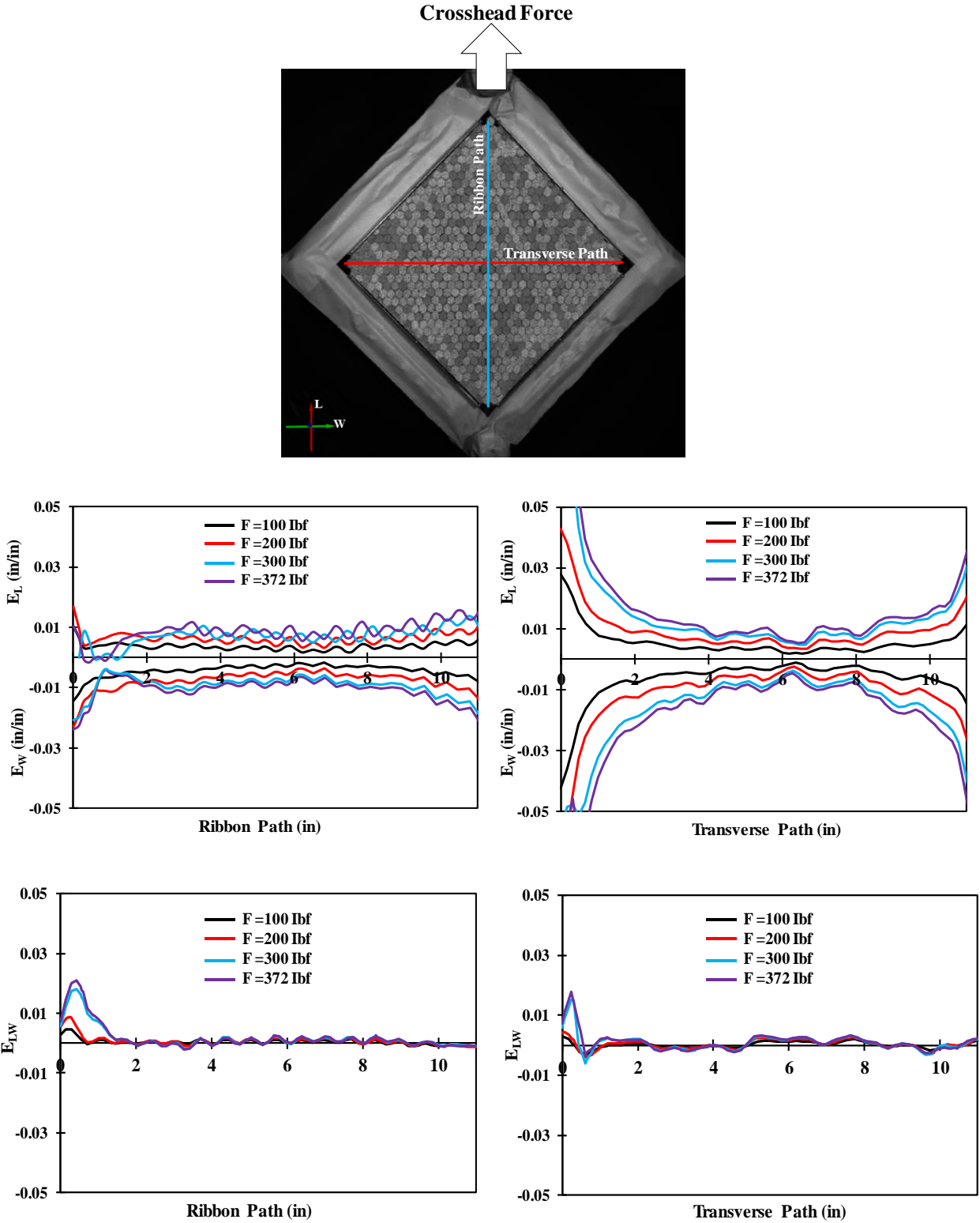


Figure 4-24. In-plane strain distributions along the sketched ribbon and transverse paths across the honeycomb core measured by ARAMIS at four different axial force levels.

The ideal scenario for using the picture-frame shear-fixture for off-axis shear testing is to generate uniform distribution of normal strains with zero shear strain throughout the honeycomb core specimen in (L-W) plane. As previously discussed, this can only happen in the central region of the core specimen.

To show the homogeneity of the strain field over the central area of the honeycomb core specimen, shown in Figure 4-23, the average strains measured by ARAMIC DIC system over the this area for each frame until the failure of the core are plotted in Figure 4-25.

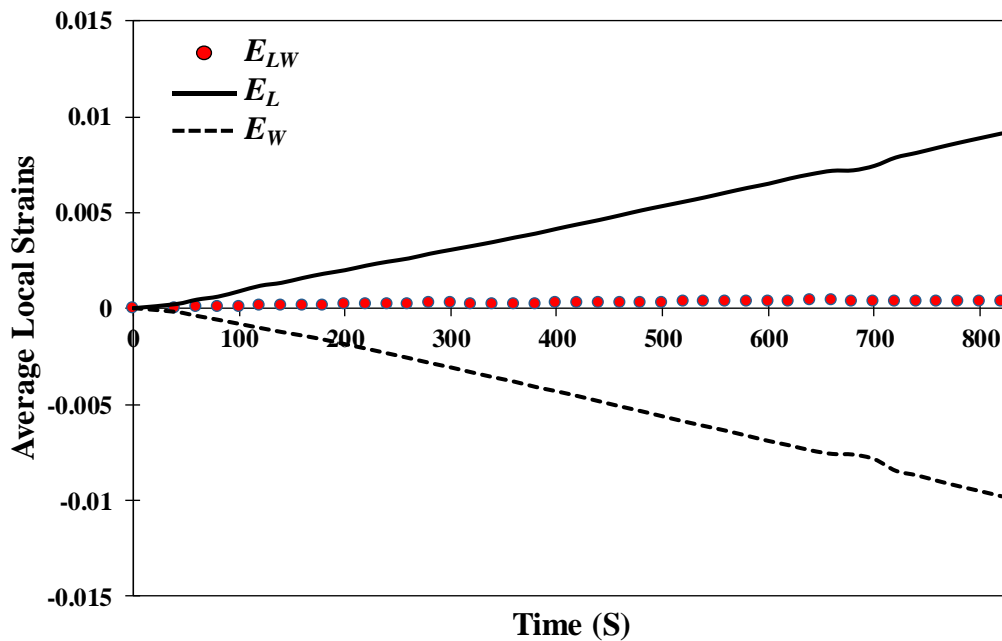


Figure 4-25. Average values of strains in principal directions (L-W) over the central part of the core specimen calculated by ARAMIS DIC system for each frame.

As can be seen in Figure 4-25, the average normal strain magnitudes are equal while the average value of the shear strain is distributed about zero.

The comparison between the average (global) engineering shear stress-shear angle (frame angle) diagrams for the HRP-honeycomb core in both (X-Y) and (L-W) planes are plotted in Figure 4-26. As is shown in the figure, the response of the core is much stiffer in the off-axis test owing to the coupling effect in (X-Y) plane [34].

It is interesting to note that, the honeycomb cores were failed at nearly the same strengths in the both tests.

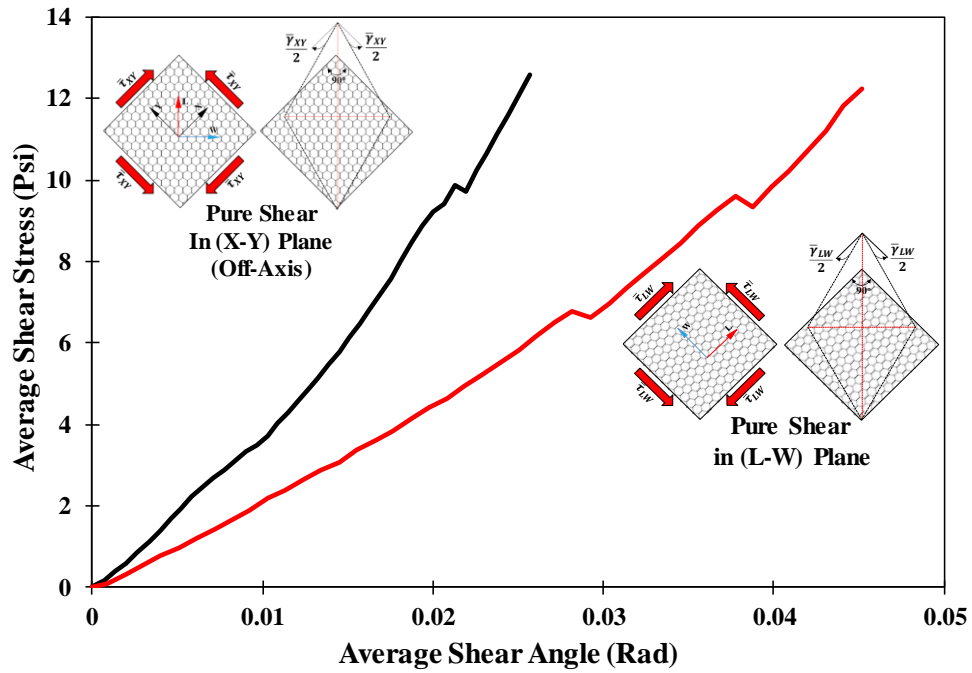


Figure 4-26. Average shear stress-shear angle diagram for the HRP- honeycomb core obtained from off-axis (X-Y) pure shear test and comparison with the test data for the pure shear in (L-W) plane.

4.5 In-Plane Flexure Testing of Bulk Honeycomb Core

In order to study the in-plane mechanical behavior of honeycomb core subjected to complex loading scenarios where in the honeycomb core cells experience multi-axial stress states during the deformation process, flexure testing using a custom-built cantilever bending fixture were conducted on HRP-fiberglass/phenolic honeycomb core beam specimens. The goals of the tests were to first, generate benchmark data to evaluate the FEA simulations of the homogenized honeycomb core beams with the hyperelastic material model (See chapter 6), second, to understand the core behavior due to combined effects of material nonlinearity, asymmetry (different tension and compression stiffness) and finally, to evaluate the in-plane shear behavior of the core.

As is shown in Figure 4-27, two sets of specimens, each consisting of a long and a short cantilever-honeycomb beam with different orientations (for each set) were considered for the flexural testing. Note that, in the figure, the number of cells for each honeycomb core is exactly equal to the real core specimen.

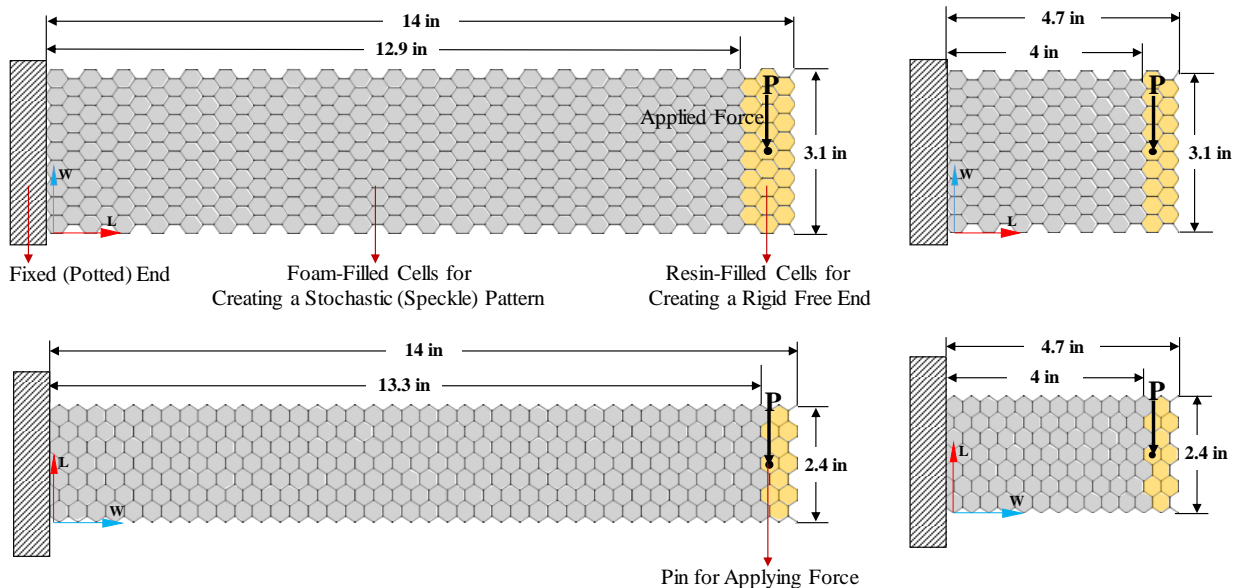


Figure 4-27. Geometry and dimensions of honeycomb beam specimens together with their respective orientations for cantilever bending tests.

As schematically presented in Figure 4-27, to create the fixed ends of the cantilevered honeycomb beams, the one ends of each specimen are potted in Aluminum C-channels of suitable dimensions using a commercial grade epoxy resin system; similarly, to create the rigid free ends for applying load, several cells of the honeycomb core specimens are filled with the epoxy resin. Loading pins are also embedded in the centers of each rigid end to facilitate the gripping and applying the load (P). As depicted in Figure 4-27, speckle patterns are also created on the honeycomb core surfaces for DIC analysis. A schematic of the deformed configuration for the honeycomb core under flexural loading is shown in Figure 4-28.

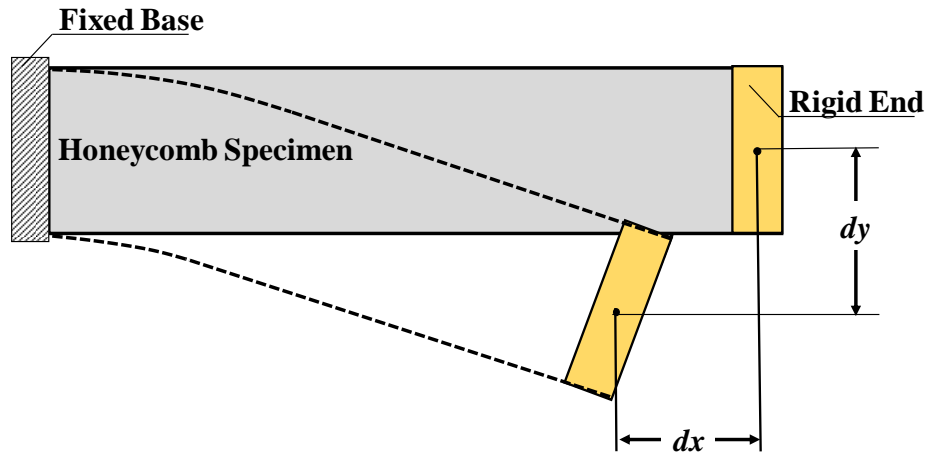


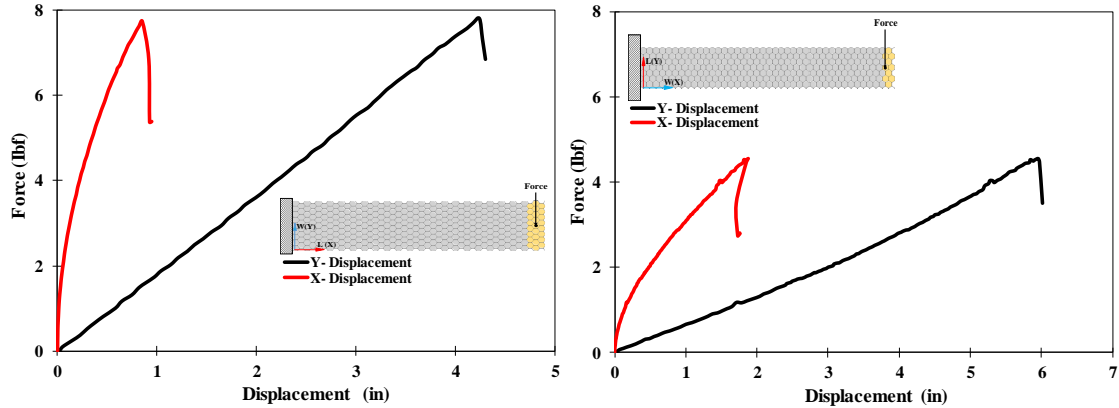
Figure 4-28. Honeycomb core specimen in the deformed state under flexural loading.

As illustrated in Figure 4-28, the large deflection of the honeycomb beam specimen is facilitated by accommodating the horizontal deflection (X-direction) of the rigid free end.

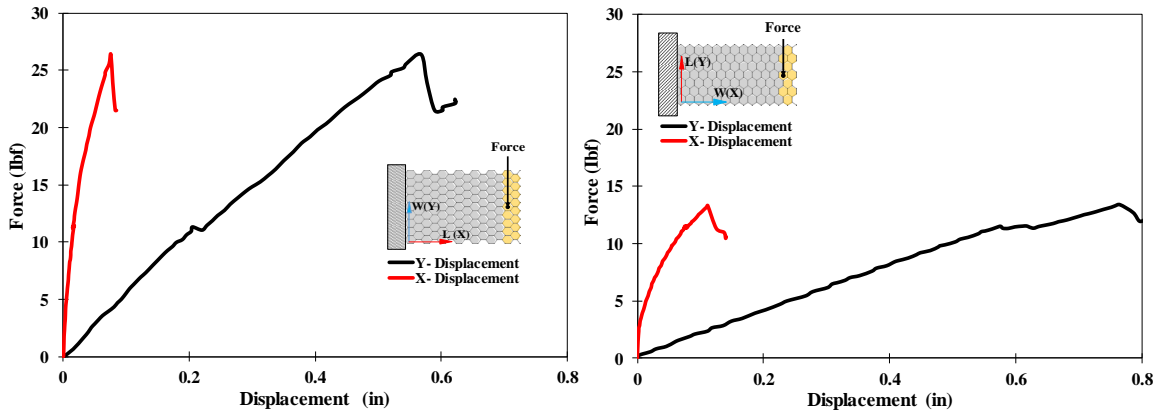
The ARAMIS DIC system was used to capture the deflections of the specimens and also to calculate the strain fields on their surfaces. The system was adjusted to capture the digital images at a frequency rate of 1/2 Hz during the deformation process.

4.5.1 Result and Discussion

The load-displacement curves for the cantilever honeycomb beam specimens are shown in Figure 4-29.



(a) Long Cantilever Honeycomb Beams.



(b) Short Cantilever Honeycomb Beams.

Figure 4-29. Load-Displacement plots from in-plane flexure tests in (L-W) and (W-L) planes.

As shown in Figure 4-29, the honeycomb core specimens exhibit higher flexural stiffness in the (L (X)-W(Y)) plane. The load-displacement responses are however nonlinear, particularly in the (W (X)-L (Y)) plane. It is evident from Figure 4-29, because of the large deflection of the beam specimens, the horizontal (X) displacements are not negligible.

To demonstrate the effectiveness of the created speckle pattern on the honeycomb core surfaces, the contours of *Green-Lagrange* strains, calculated by ARAMIS professional software, for one of the beam specimens at failure load are shown in Figure 4-30.

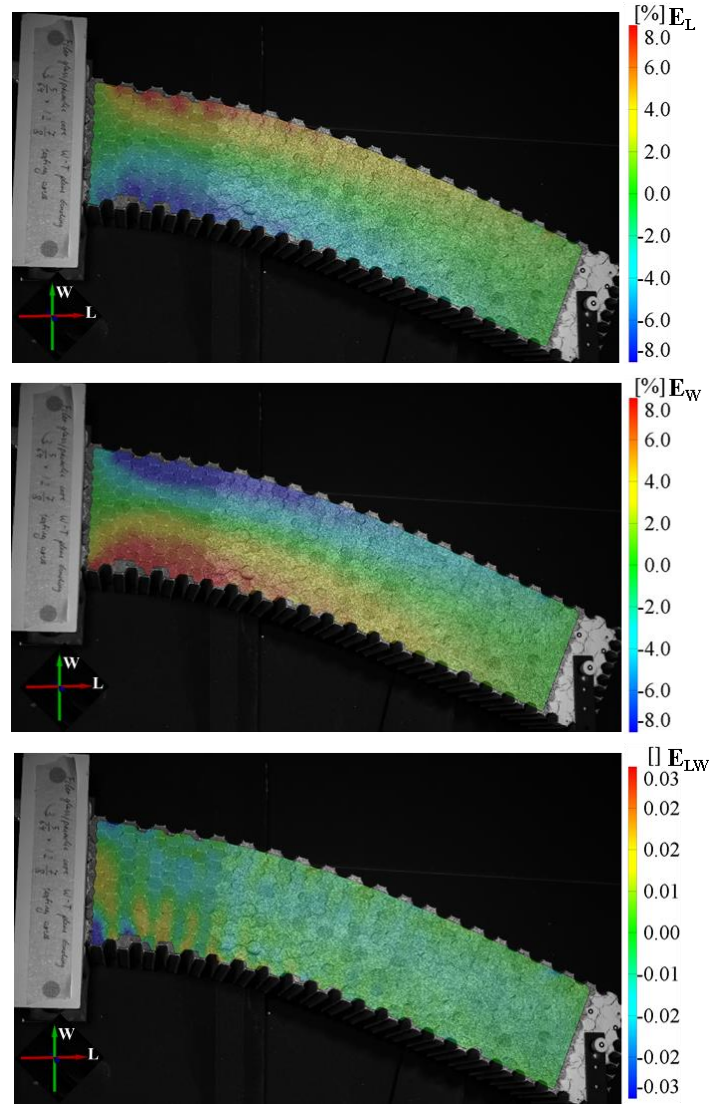


Figure 4-30. The contours of *Green-Lagrange* strains calculated by ARAMIS DIC system at failure load.

The distribution of in-plane *Green-Lagrange* strains along the predefined cross sectional (C.S) paths at three load levels for the long and short honeycomb beam specimens with (L(X)-W(Y)) orientation are shown in Figure 4-31 (a) and (b), respectively.

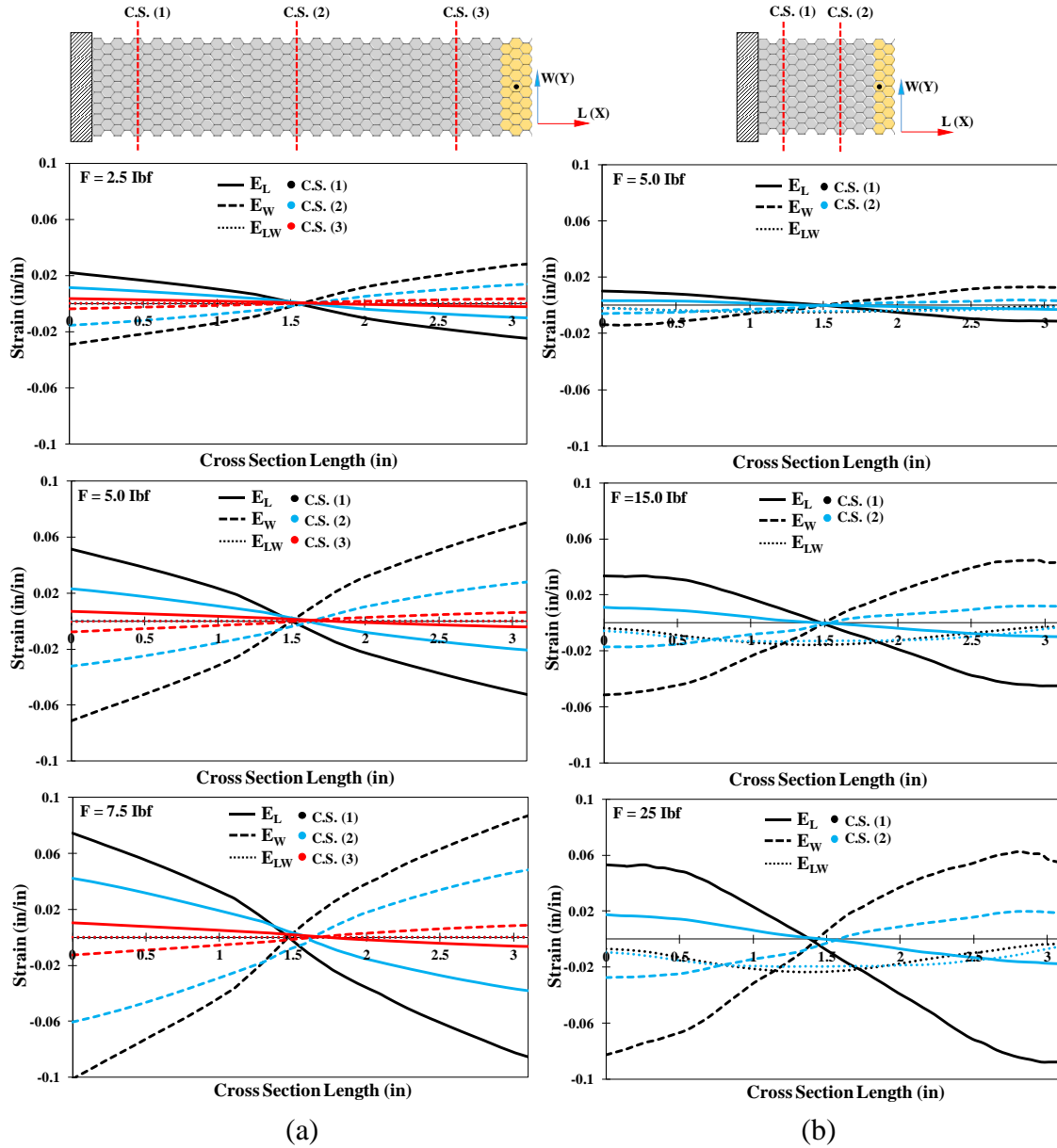


Figure 4-31. Profiles of in-plane *Green-Lagrange* strains across the width of the (a) long and (b) short honeycomb beams with L (X)-W(Y) orientation.

Similarly, the strain distributions across the width of the honeycomb cores at different locations and load levels for the long and short honeycomb beam specimens with W(X)-L(Y) orientation are respectively presented in Figure 4-32 (a) and (b).

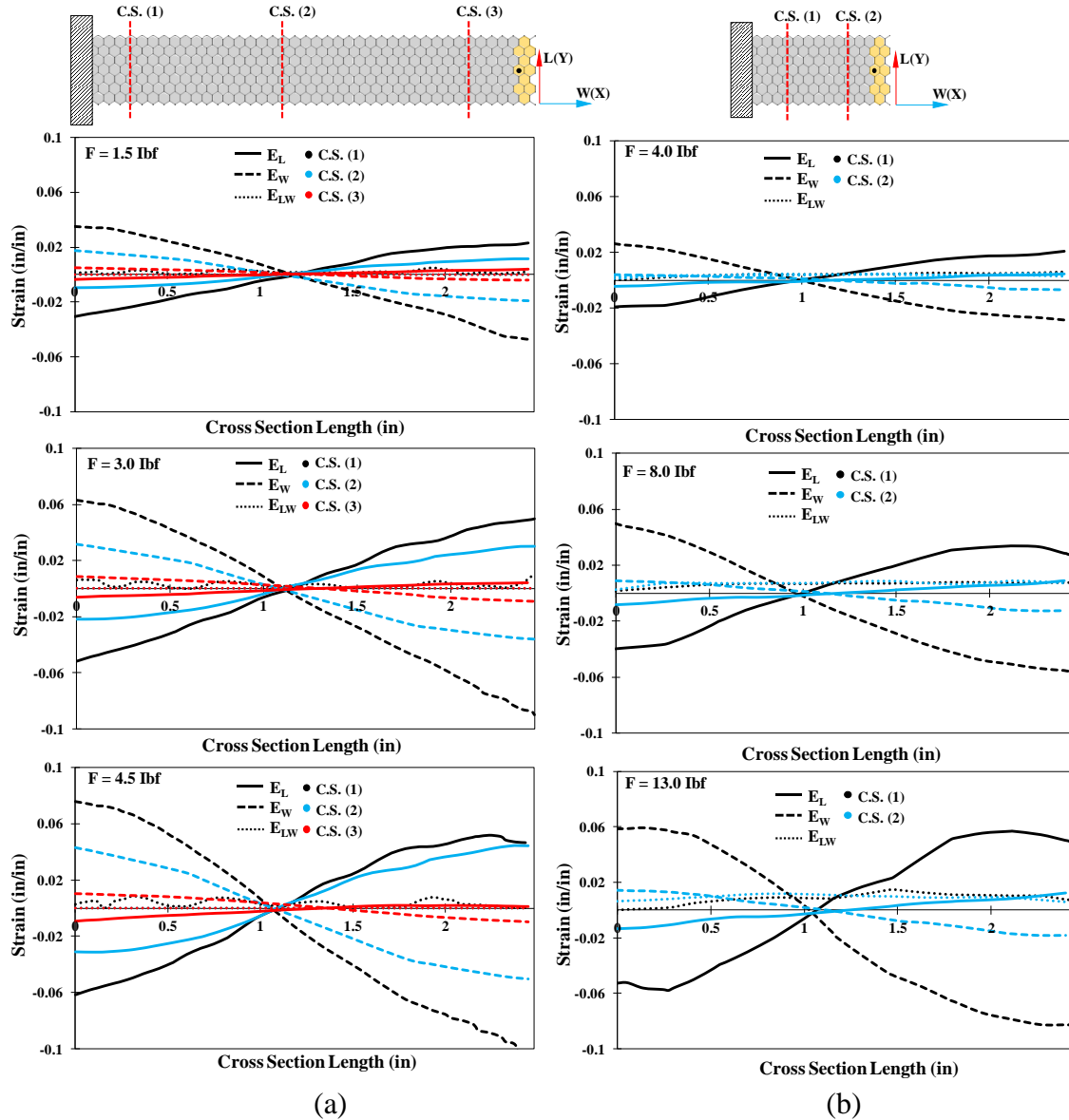


Figure 4-32. Profiles of in-plane *Green-Lagrange* strains across the width of the (a) long and (b) short honeycomb beams with $W(X)$ - $L(Y)$ orientation.

As presented in Figure 4-32, the asymmetric responses of the honeycomb cores under flexural loading are evident. For example, the normal strain in the ribbon direction E_L , on the tension side (top) of the honeycomb cores is lower than the compression side (bottom) owing to the lower stiffness under compression, E_L , as illustrated in Figure 4-31. As shown in the figures, for all the specimens (long and short beams) under flexural loading, the normal strains are the dominant strain components and the magnitudes of the shear strains are negligible even for the short beam

specimens which were expected to deform more in shear mode than the normal one. This proves the high shear rigidity of the HRP-fiberglass/phenolic honeycomb core which was also observed in the shear experiment.

The result obtained from the flexural experiments will be employed for validation of nonlinear FEA simulations of the bulk honeycomb core using simple continuum elements with the developed effective constitutive model explained in chapter 6.

CHAPTER 5

FINITE ELEMENT MODEL OF HEXAGONAL HONEYCOMB CORE WITH DETAILED MICROSTRUCTURE

In this chapter development of a finite element model of a repetitive unit cell or RVE of a commercial adhesively bonded hexagonal honeycomb core which includes all the geometric features of the commercial core cell shown in Figure 1.5 is presented. The model is used to investigate the mechanical responses of the core under different loading and boundary conditions to produce the effective stress-strain responses of the core which will then be employed to develop an effective constitutive model for the homogenized honeycomb core. Moreover, the results obtained from the FEM of the commercial core RVE are compared with a FEM of an idealized core RVE to show the importance of inclusion of the geometric features of the commercial core cell in the analysis.

5.1 Finite Element Modeling of Core Unit Cell

A 3D finite element model of a unit cell (RVE) was assembled to study the mechanical behavior of the honeycomb core. Due to symmetry within a hexagonal unit cell, only 1/2 of the cell (symmetry with respect to Y-Z (W-T) plane) was modelled based on optical measurements of the cell geometry of the commercial HRP-fiberglass/phenolic honeycomb core shown in Figure 4-1. The model incorporates all artifacts of the real honeycomb core cell, which includes single and double thickness cell walls, cell wall curvatures at intersections, the node bond adhesive layer, and its fillet to study the large deformation behavior of the honeycomb core, as shown in Figure 5-1. It is obvious in Figure 5-1(c), there is another symmetry with respect to X-Z (L-T) plane which leads to assembly of a 1/4 of the unit cell reported previously [13]; however, in current work to

better understanding of the in-plane deformations of the honeycomb core particularly under shear loading, it was decided to utilize the 1/2 symmetry unit cell.

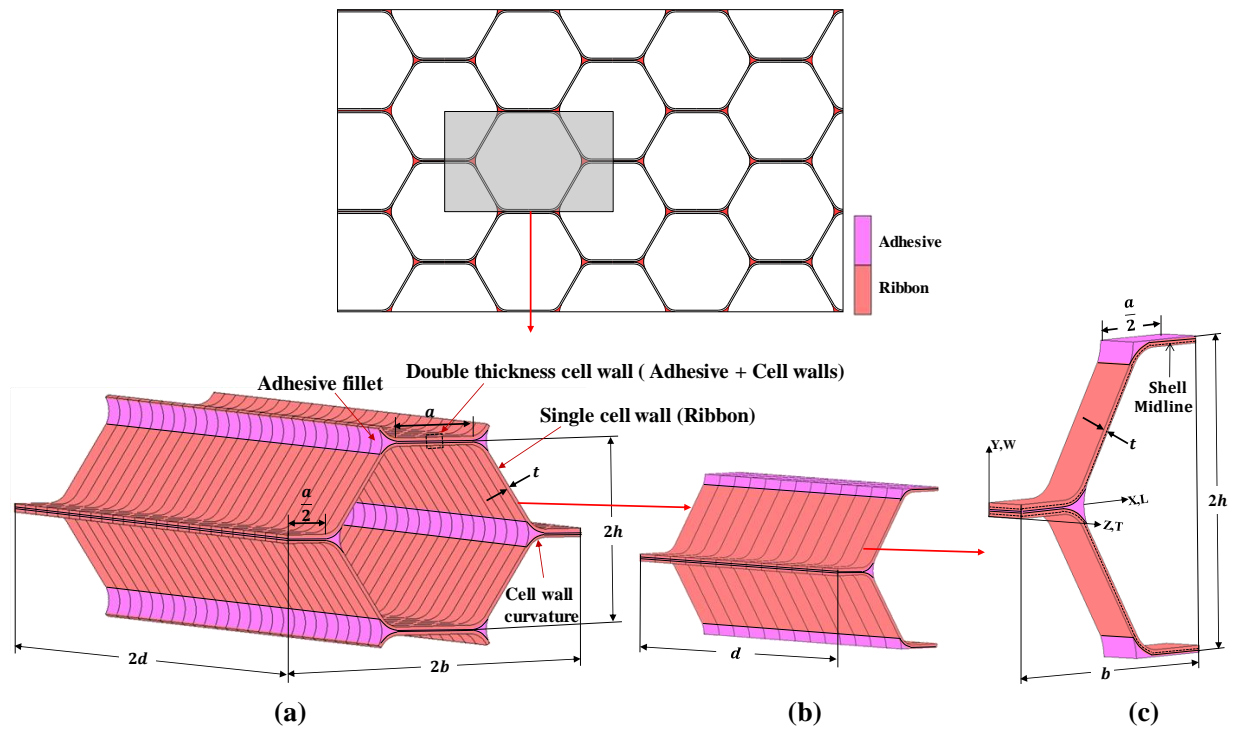


Figure 5-1.(a) A unit cell (RVE) of hexagonal honeycomb core; (b) 1/2 symmetry unit cell with half-thickness; (c) an elemental strip of the half symmetry unit cell used in FEA.

In this chapter, both in-plane and out-of-plane mechanical behaviors of the honeycomb core are investigated using the FEM of the core unit cell; however, the main focus is to characterize the in-plane behavior of the core under large deformations.

For modeling the out-of-plane (T-L and T-W) responses of the core, the 1/2 symmetry RVE with half-thickness, shown in Figure 5-1(b), was used in order to first, capture the Poisson's contraction effects and second, to demonstrate that under in-plane loadings, out-of-plane (W-T, W-L) Poisson's contraction effects are negligible [3].

Because this work is restricted to the in-plane behavior of the core without facesheets, the constraint effects on core deformation due to the stiff facesheets can be ignored [60]. As such, an

elemental strip of the unit cell shown in Figure 5-1 (c) would suffice to capture the in-plane behavior of the core.

In this research, commercial MSC Marc finite element program [31] was used to assemble and analyze the unit cell model. The cell walls were modeled using four-noded bilinear thin shell elements (Marc element 139) while isoparametric eight-noded hexahedral (Marc element 7) and six-noded pentahedral (Marc element 136) [61] were used to model the node bond adhesive and fillet regions. A segment-to-segment moment-carrying glue contact constraint [31] was used between cell wall and node bond adhesive to ensure the continuity of displacements and tractions at the interface.

To match experimentally observed flexural and in-plane moduli of the cell walls of fiberglass/phenolic honeycomb given in TABLE 4-1, the cell walls were modeled as a three-layer laminate, as shown in Figure 5-2. The effective modulus of the outer layer (skin), $E_s = 1.00 \text{ Msi}$, and the effective modulus of the inner layer (core), $E_c = 3.00 \text{ Msi}$, were calculated by employing a simple rule of mixtures [13, 15, 62]. Here, the skin and core layers represent the phenolic resin matrix and fiberglass reinforcement in FEM, respectively.

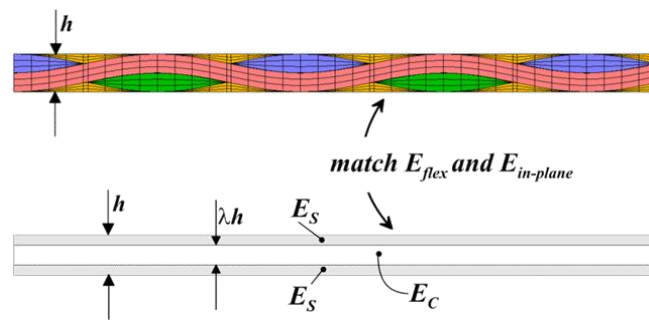


Figure 5-2. Constitutive modelling of the cell wall of HRP-fiberglass/phenolic core in FEM [13].

5.2 Loading and Boundary Conditions

To find the in-plane and out-of-plane effective stress-strain¹ responses of the honeycomb core, multiple loading cases were considered. The boundary conditions applied on the finite element models were determined based on the loading direction and symmetry conditions of the 1/2 segment of the unit cell shown in Figure 5-1 (b) and (c) for simulation of the out-of-plane and in-plane responses of the core, respectively. Depending on the loading direction, appropriate displacement boundary constraints and multi-point constraints (or tie links) were utilized. The boundary edges (for shell elements) and surfaces (for solid elements) are identified in Figure 5-3. The combination of boundary constraints and symmetry conditions are discussed in the following.

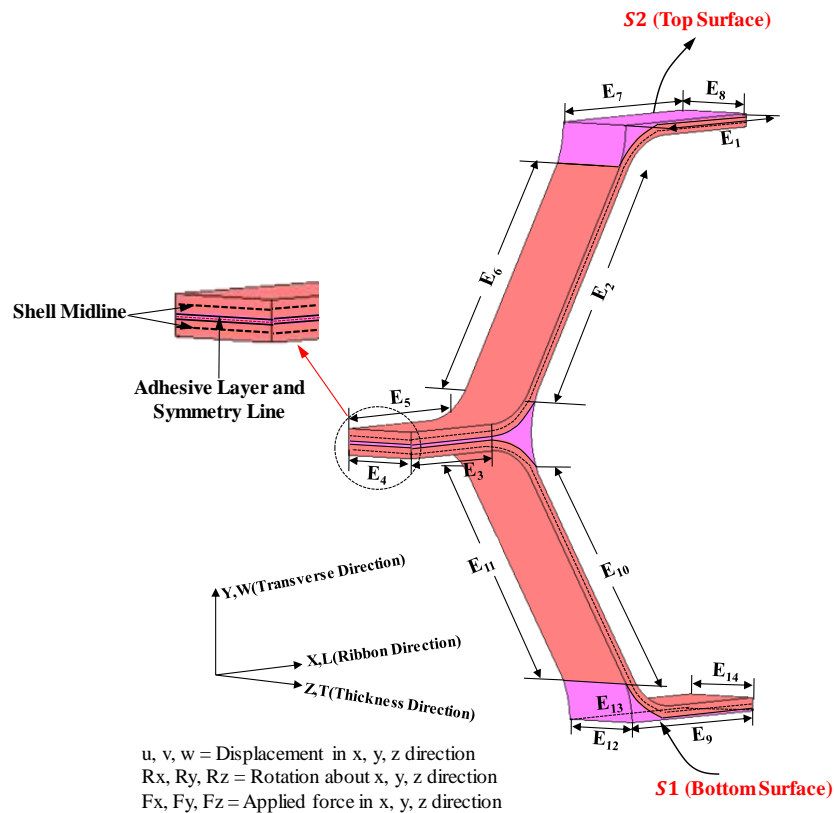


Figure 5-3. Identification of boundary edges (E) and surfaces (S) to define symmetry and boundary conditions.

¹ Effective stress-strain curves refer to homogenized equivalent-continuum curves.

5.2.1 Uniaxial Simulations

To simulate the uniaxial deformation of the core in the ribbon (L), transverse (W) and thickness (T) directions, six loading cases which included tension and compression loading along the ribbon, transverse and thickness directions were used, as summarized in TABLE 5-1. It should be noted that for modelling the out-of-plane loading cases, the boundary conditions were applied on the 1/2 symmetry RVE with half-thickness shown in Figure 5-1(b).

TABLE 5-1

BOUNDARY AND SYMMETRY CONSTRAINTS USED FOR UNIAXIAL FEA

Boundary	Uniaxial Loading Direction		
	Ribbon (L)	Transverse (W)	Thickness (T)**
E1, E2, E3, E9, E10	$w = \text{Uniform (MPC)*}$		$w = \text{Applied Displacement (MPC)}$
E4	$u = 0$ (Fixed Displacement)		
E5, E6, E7, E11, E13	$w = 0$ (Fixed Displacement)		
S1	$v = 0$ (Fixed Displacement)		
E8, E14	$u = \text{Applied Displacement (MPC)}$	$u = \text{Uniform (MPC)}$	
S2	$v = \text{Uniform (MPC)}$	$v = \text{Applied Displacement (MPC)}$	$v = \text{Uniform (MPC)}$

* MPC = Multi-Point Constraint

** Boundary conditions were applied on the 1/2 symmetry RVE with half-thickness

For example, to simulate tensile loading along the ribbon direction, the nodes on the boundary surface "S₂" and "S₁" were constrained to move the same amount along the y-direction. The nodes along the edges "E₈" and "E₁₄" alongside the solid element nodes which share the same x-coordinate were tied to a predefined master node on edge "E₈" to move the same amount along the x-direction. A prescribed displacement" was then applied to the master node. To simulate the symmetry about a vertical plane, the displacement of all nodes along the "E₄" were constrained to

be zero in x direction. In addition, the z -displacement of all along the boundary defined by $z = 0$ was also constrained.

5.2.2 Pure Shear Simulations

As is shown in TABLE 5-2 , to simulate the pure shear deformation of the core in the (L-W), (T-W) and (T-L) planes, three loading cases were employed.

TABLE 5-2

BOUNDARY AND SYMMETRY CONSTRAINTS USED FOR PURE SHEAR FEA

Boundary	Pure Shear Loading Direction within the Corresponding Plane		
	Transverse (L-W)	Transverse (T-W)**	Ribbon (T-L)**
E1, E2, E3, E9, E10	<i>Free</i>	$v =$ Applied Displacement (MPC*) $w =$ Uniform (MPC) $u = 0$ (Fixed Displacement)	$u =$ Applied Displacement (MPC) $w =$ Uniform (MPC) $v = 0$ (Fixed Displacement)
E4	$u = v = 0$ (on Adhesive Sym. Line) (Fixed Displacement)	$u = 0$ (Fixed Displacement)	$v = 0$ (Fixed Displacement)
E5, E6, E7, E11, E13	$w = 0$ (Fixed Displacement)	$u = v = w = 0$ (Fixed Displacement)	$u = v = w = 0$ (Fixed Displacement)
S1	$u, v =$ Tied to corresponding nodes on S2	$u = 0$ (Fixed Displacement)	$v = 0$ (Fixed Displacement)
E8, E14	$v =$ Applied Displacement (MPC), $u =$ Uniform (MPC) $R_z =$ Free	$u = 0$ (Fixed Displacement)	$v = 0$ (Fixed Displacement)
S2	$u, v =$ Tied to corresponding nodes on S1	$u = 0$ (Fixed Displacement)	$v = 0$ (Fixed Displacement)

* MPC = Multi-Point Constraint

** Boundary conditions were applied on the 1/2 symmetry RVE with half-thickness

For example, to simulate the in-plane (L-W) pure shear loading, the nodes on the boundary surface “S₂” were tied to corresponding nodes on the boundary surface “S₁” to share the same in-plane displacements. A prescribed displacement “ v ” was applied to a predefined master node along the edge “E₈” to which the rest of the nodes along this edge, edge “E₁₄” and solid element nodes which

share the same x -coordinate on the both edges were tied to move the same amount along y -direction while the rotation is being updated. To simulate the anti-symmetry about a vertical plane, all the nodes along the symmetry line of the adhesive elements of edge “E4” were constrained to be zero in x and y directions. In addition, the z -displacement of all along the boundary defined by $z = 0$ was also constrained.

5.2.3 Multi-Axial Simulations

To study the compressibility of the homogenized honeycomb core, hydrostatic compression loading case was simulated in the finite element software using the 1/2 symmetry RVE with half-thickness. Using the elemental strip RVE, the mechanical response of the core under in-plane equi-biaxial tension and compression were also simulated. The boundary conditions used for the implementation of these loading cases are shown in TABLE 5-3.

TABLE 5-3

BOUNDARY AND SYMMETRY CONSTRAINTS USED FOR MULTI-AXIAL FEA

Boundary	Multi-Axial Loading Direction**		
	In-Plane Equi-Biaxial Tension	In-Plane Equi-Biaxial Compression	Hydrostatic Compression
E1, E2, E3, E9, E10	$w = \text{Uniform (MPC*)}$		$w = \text{Uniform (MPC)}$ $F_z^{***} = \text{Applied Force}$
E4	$u = 0$ (Fixed Displacement)		
E5, E6, E7, E11, E13	$w = 0$ (Fixed Displacement)		
S1	$v = 0$ (Fixed Displacement)		
E8, E14	$u = \text{Uniform (MPC)}$ $F_x = \text{Applied Force}$		
S2	$v = \text{Uniform (MPC)}$ $F_y = \text{Applied Force}$		

* MPC = Multi-Point Constraint

** Boundary conditions were applied on the 1/2 symmetry RVE with half-thickness

*** Applied forces were determined such that the state of homogenized stress was equi-biaxial or hydrostatic

The strategy for modeling the equi-biaxial and hydrostatic tests was to maintain the same increment of the homogenized stresses in the ribbon, transverse and thickness (for hydrostatic loading case) directions.

Due to the large displacements involved, a nonlinear analysis using the updated *Lagrangian* framework [31] was conducted. The edge loads and displacements were applied over 100 increments to facilitate the nonlinear analysis. The results of the analysis which included applied displacements and reaction forces or applied forces and resultant displacements were used to construct effective engineering stress-strain relationships.

To show the importance of inclusion of the node bond adhesive layer and its fillet region on mechanical responses of the core, FEMs of commercial and idealized (the node bond adhesive layer and its fillet region are ignored) cores were considered, as depicted in Figure 5-4. The results obtained from the FEA of the commercial core were compared with the results of modeling the idealized core as well as the test data for uniaxial and pure shear loadings.

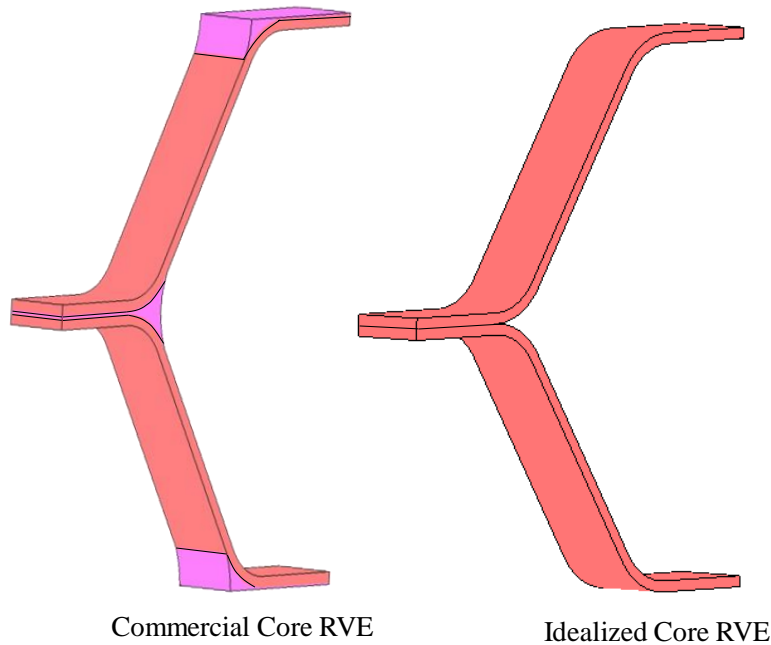
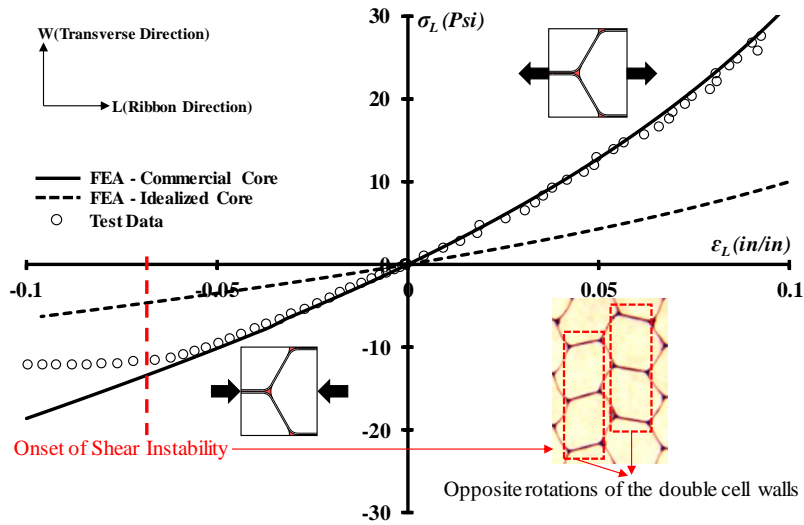


Figure 5-4. 3D views of FEMs of honeycomb cores with and without adhesive layer and fillets.

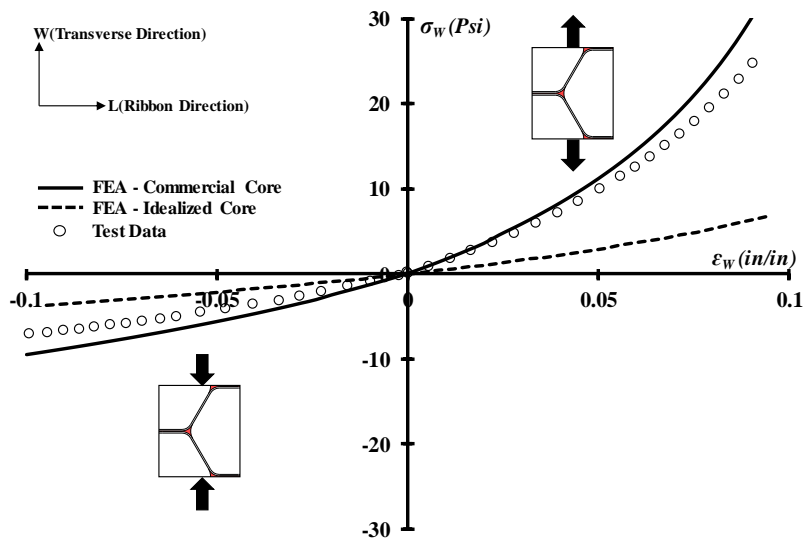
5.3 Result and Discussion

5.3.1 FEA Predictions of In-Plane Response

The effective engineering stress-strain curves predicted by the FEMs of the commercial and idealized cores for tensile and compressive loadings along the ribbon and transverse directions and comparison with the test data [13, 15] are shown in Figure 5-5.



(a) Uniaxial in ribbon direction

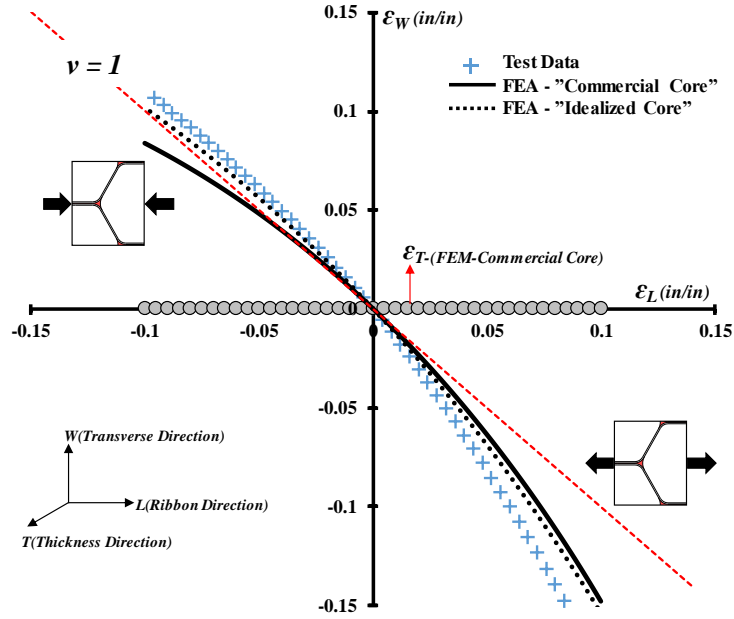


(a) Uniaxial in transverse direction

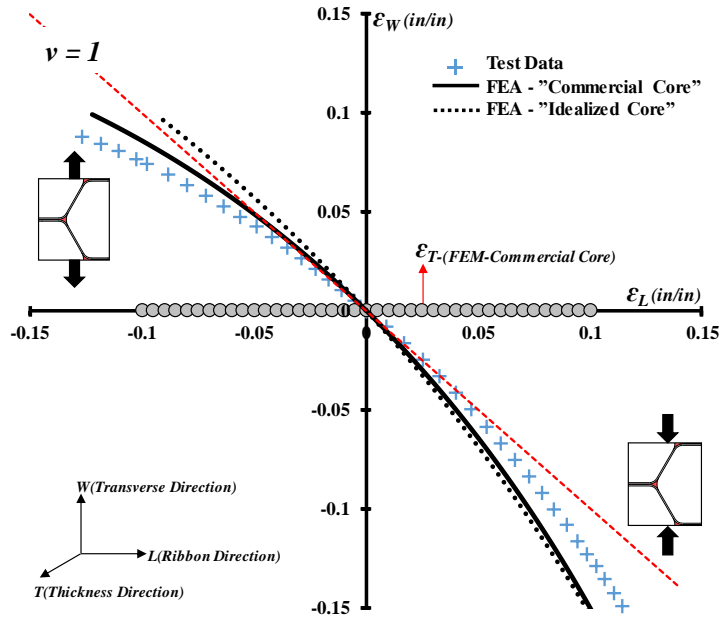
Figure 5-5. Effective engineering stress-strain curves obtained from FEA and comparison with test data [13, 15] for in-plane (L-W) uniaxial loadings.

As can be seen in Figure 5-5, the FEA predictions are nonlinear and anisotropic for uniaxial in-plane loadings along the ribbon and transverse directions, similar to that of the experimental test data; moreover, compare to results obtained from the FEM of the idealized core (no adhesive), predictions based on the real geometry of the honeycomb core are significantly stiffer, thus highlighting the importance of inclusion of the node bond adhesive layer and its fillet region. In fact, node bond adhesive fillets constrain intersections between honeycomb cell walls and induce more cell-wall-bending deformation under the same homogenized strain. It should be noted that in the compression test along the ribbon direction at higher strain, the FEA prediction (commercial RVE) is valid up to the onset of the geometric (shear) instability, whereby the double-thickness cell walls rotate in opposite directions [13, 22], as depicted in Figure 5-5 (a). The deviation between the model prediction and test data is ascribed to the symmetry boundary conditions used in the FEM. In fact, rotations of the double-thickness cell walls are restrained in the model, thereby inducing a stiffer response than in the test data. Moreover, in the compression test, any imperfections tend to be magnified, and a buckling analysis needs to be performed.

The Poisson's effects for tensile and compressive loadings along the ribbon (L) and transverse (W) directions are shown in Figure 5-6. It is evident that the relationship between the longitudinal (ϵ_L) and transverse (ϵ_W) strains is nonlinear and depends on the loading direction. Moreover, at low strain levels, the Poisson's ratio is close to unity for all loading directions. As illustrated in Figure 5-6, there are no significant deviations between results obtained from the FEMs of the commercial and idealized cores. The predictions for all models are observed to lie within the scatter band of the experimental data. Based on these observations, the effect of adhesive fillets is not a dominant factor for the Poisson's ratio.



(a) Uniaxial in ribbon direction



(b) Uniaxial in transverse direction

Figure 5-6. FEA predictions of Poisson's effects for uniaxial tests along ribbon (L) and transverse (W) directions and comparison with test data [13, 15].

As shown in Figure 5-6, under in-plane loadings, out-of-plane strains (ϵ_T) equal zero resulting in zero Poisson's ratios, ν_{LT} and ν_{WT} . However, this question might arise that the elemental strip FEM could not capture the out-of-plane (W-T, W-L) Poisson's contraction effects. In order to support this

argument that “under in-plane loadings, out-of-plane properties of the core would not be affected because the out-of-plane moduli of the core are orders of magnitude higher than the in-plane moduli and therefore, the FEM of the elemental strip RVE would suffice to predict the in-plane mechanical responses of the honeycomb core”, FEA simulations using the 1/2 symmetry unit cell with half-thickness, shown in Figure 5-1 (b), were also conducted. The effective engineering stress-strain and Poisson’s effects curves for uniaxial loadings along the ribbon and transverse directions were compared with the FEA predictions obtained from the elemental strip RVE, as illustrated in Figure 5-7. It is evident from Figure 5-7, the identical results predicted by the FEMs support the aforementioned argument.

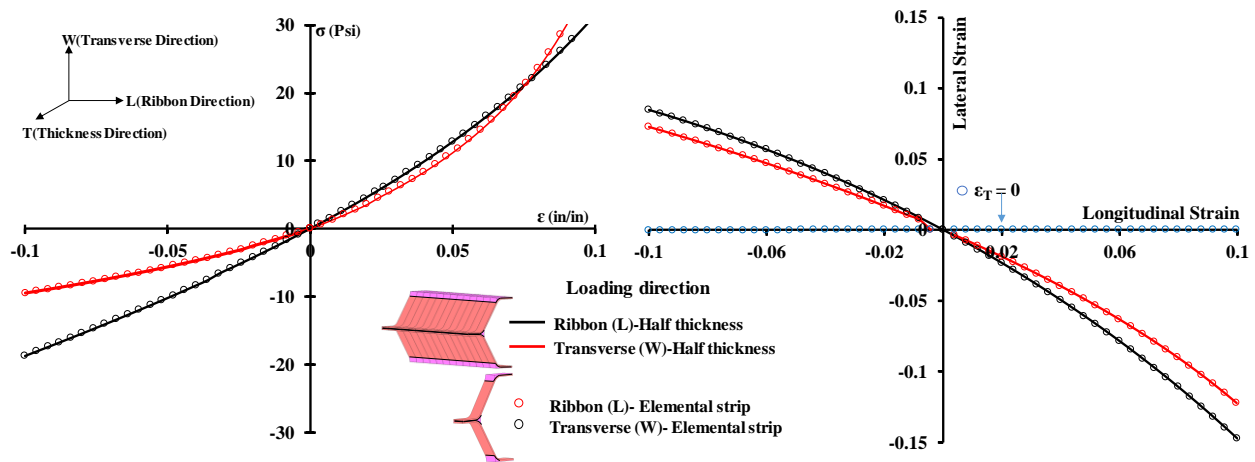


Figure 5-7 FEA predictions using the half thickness RVE and comparison with FEA results predicted by an elemental strip RVE.

Figure 5-8 shows the effective engineering shear stress-strain curves predicted by the FEMs of the commercial and idealized cores for the HRP-honeycomb core subjected to in-plane pure shear deformation. As can be seen in Figure 5-8, FEA predictions present a consistently linear stress-strain behaviors, while the test data [57] obtained from the global deformation of the picture-frame shear fixture (see chapter 4) at higher strains is observed to be nonlinear. As discussed previously, the nonlinearity of the test data may not be entirely attributed to the core behavior and the effect of the

picture frame fixture must be investigated. To produce a better comparison between the test data and FE prediction and to provide the complete picture of the stress-strain states on the honeycomb core, the full honeycomb core and the fixture details need to be modelled in FEA simulation which will be explained in the next chapter. It is evident from Figure 5-8 that the shear modulus of the honeycomb core predicted by the FEM of the real (commercial) core geometry is significantly higher than the FEM of the idealized core and slightly less than the experimental data (at small strain levels)

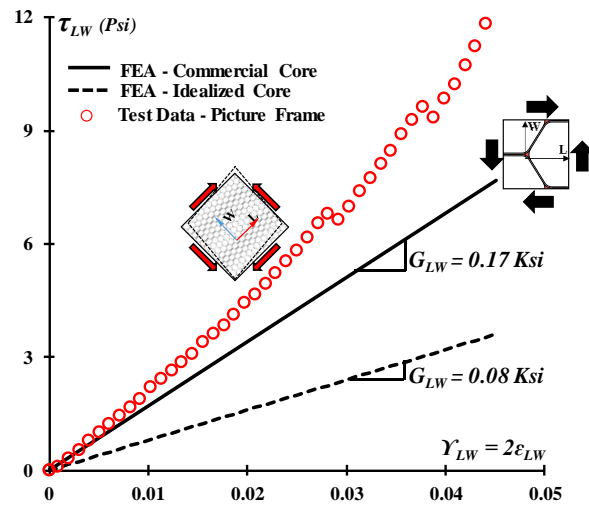


Figure 5-8. Effective engineering stress-strain curves for pure shear loading in (L-W) plane.

The deformed shapes of the honeycomb core under in-plane loadings are illustrated in Figure 5-9.

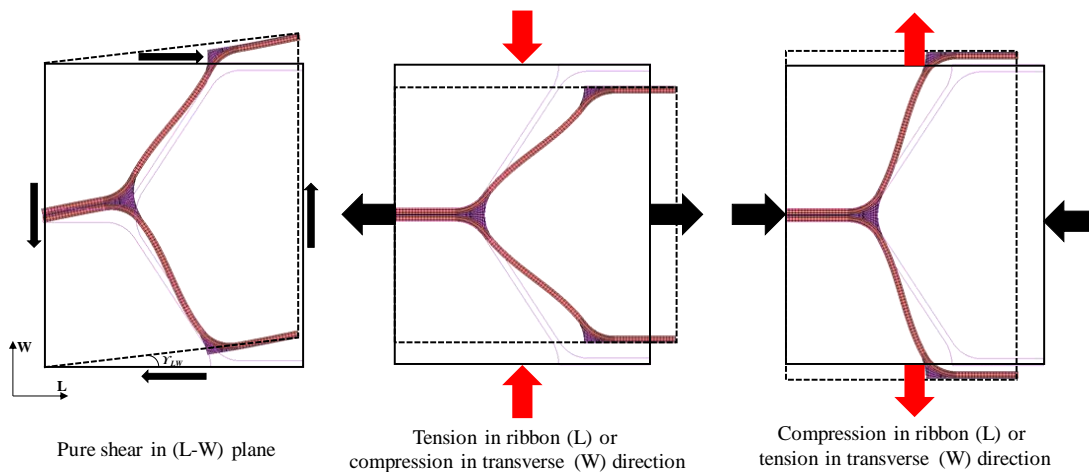


Figure 5-9. In-plane (L-W) deformed configuration of honeycomb core cell walls under uniaxial and pure shear loadings.

A comparison among the prediction of the FEMs of the commercial and idealized cores and some of the widely cited linear models is shown in Figure 5-10. As is shown in Figure 5-10, predictions by previous linear models are close to the FEM of the idealized core due to negligence of the node bond fillet, which effectively increases the length of the cell wall without adhesive support, and thus underestimates the homogenized moduli of the core. Even though good agreement is achieved between the FEM of the idealized core and previous linear models, especially the model derived by Balawi and Abot [5], the FEM of the commercial core model is much stiffer than those linear models which emphasizes the significance of the inclusion of node bond adhesive fillet in the analysis even at infinitesimal strains, as indicated in Figure 5-10.

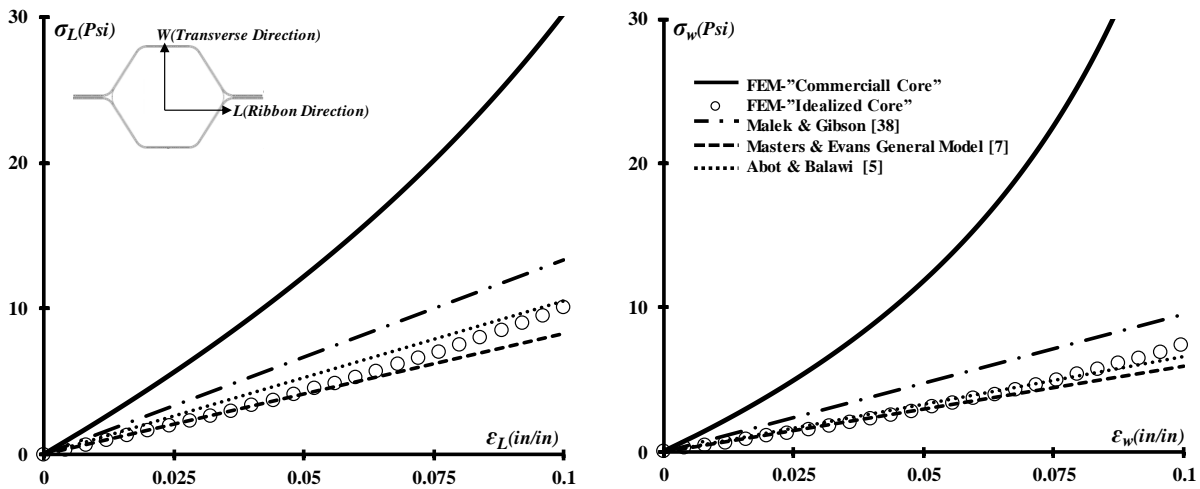
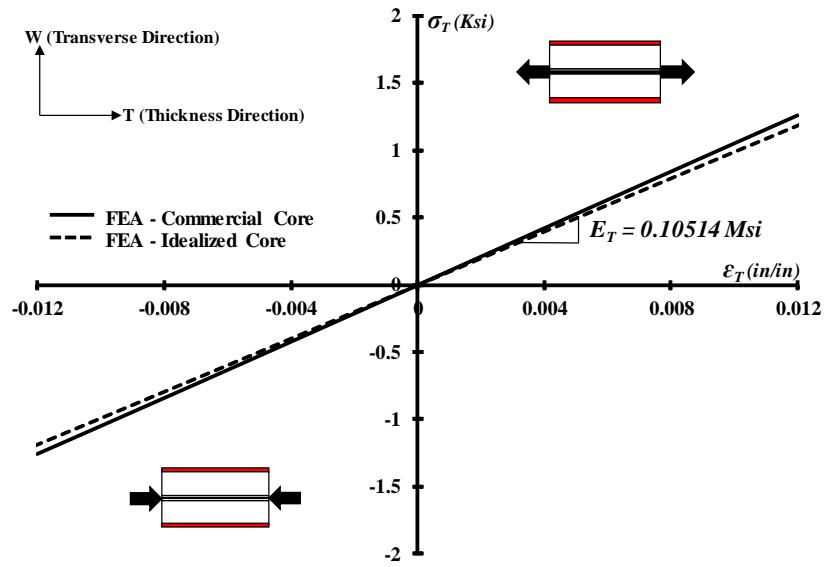


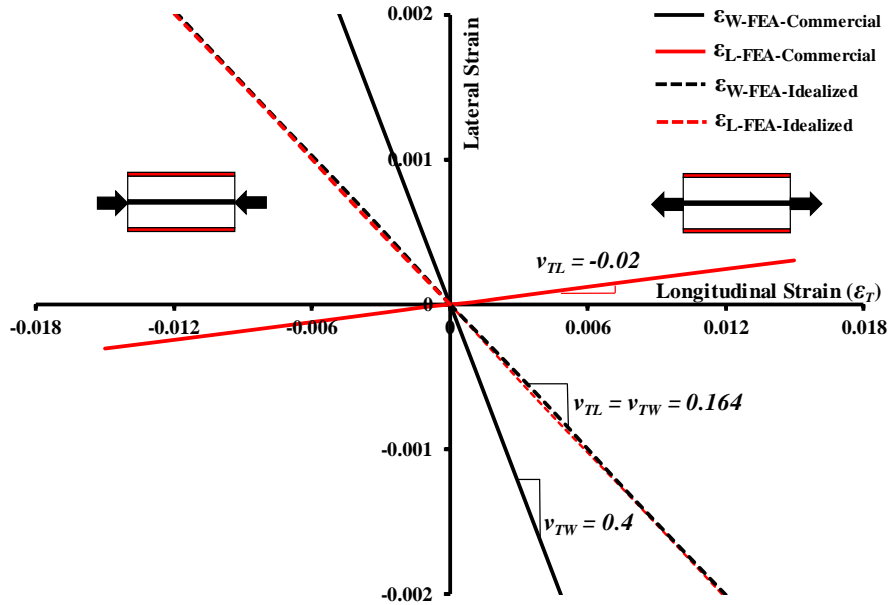
Figure 5-10 Comparison of FEA predictions with previous linear models reported in literature.

5.3.2 FEA Predictions of Out-of-Plane Reponse

The effective engineering stress-strain diagrams produced from FEA predictions of the HRP-honeycomb core RVE shown in Figure 5-1(b) as well as the Poisson's effects for uniaxial loadings along the thickness (T) direction are illustrated in Figure 5-11.



(a) Effective engineering stress-strain diagrams



(b) Poisson's effects

Figure 5-11. FEA predictions for uniaxial tests in thickness (T) direction.

As can be seen in Figure 5-11(a), the out-of-plane uniaxial behavior of the core is linear and the corresponding effective properties can be easily obtained by a rule of mixtures expression [34] consisting of the contribution of the ribbon and adhesive regions. For example, effective Young's modulus of the core, E_T , simply reflects the in-plane modulus of the ribbon and adhesive materials given in TABLE 4-1 scaled by the homogenized area of the 1/2 segment of the unit cell with half-thickness shown in Figure 5-1(b) as

$$E_T = \frac{(E_{in-ribbon}A_{cw} + E_{adhesive}A_{ad})}{A_T} = \frac{1.9 \times 0.00578 + 0.533 \times 0.00121}{0.11052} = 0.1052 \text{ Msi} \quad (5.1)$$

where $A_T = 2bh$ (refer to Figure 5-1), A_{cw} and A_{ad} are, respectively, the projected area of the half-segment of a unit cell which includes the cell wall, node bond adhesive layer, and its fillet region on the plane perpendicular to the thickness direction. A_{cw} and A_{ad} can be calculated directly using the geometry and dimensions shown in Figure 4-1. It is evident from Equation (5.1) that the out-of-plane modulus of the core is dominated by the axial stiffness of the ribbon material.

From Figure 5-11(a), it is evident that the effect of node bond adhesive layer and its fillet region on the out-of-plane stress-strain behavior of the core are negligible. However, the presence of the node bond fillet causes to obtain the anisotropic Poisson's ratios along the ribbon and transverse directions (ν_{TL} and ν_{TW}), as depicted in Figure 5-11 (b). Under uniaxial loading in thickness direction, the node bond adhesive fillet region undergoes compressive stresses and it is free to expand in ribbon direction; because of the mismatch Poisson's ratios between the ribbon and adhesive materials and the fact that the fillet region constrains the mobility of the core, the adjacent cell walls are forced to close up resulting in the elongation and contraction in ribbon and transverse directions, respectively.

Figure 5-11 (b) shows that FEA predictions of the Poisson's ratios without modeling the node bond adhesive fillet are linear and isotropic; they also reflect the Poisson's ratio of the ribbon material given in TABLE 4-1.

Figure 5-12 shows the effective engineering stress-strain curves obtained from FEA for pure shear loadings in (T-W) and (T-L) planes. As can be seen in Figure 5-12, the stress-strain behaviors predicted by the FEMs (Idealized and Commercial RVEs) are consistent and linear. It is evident that the out-of-plane shear modulus obtained from FEA for pure shear loading case in (T-L) plane is about twice the (T-W) shear modulus and they are both much higher than the in-plane (L-W) shear modulus. The results predicted by the FEMs for the out-of-plane shear moduli are also compared with those of reported in literature [4].

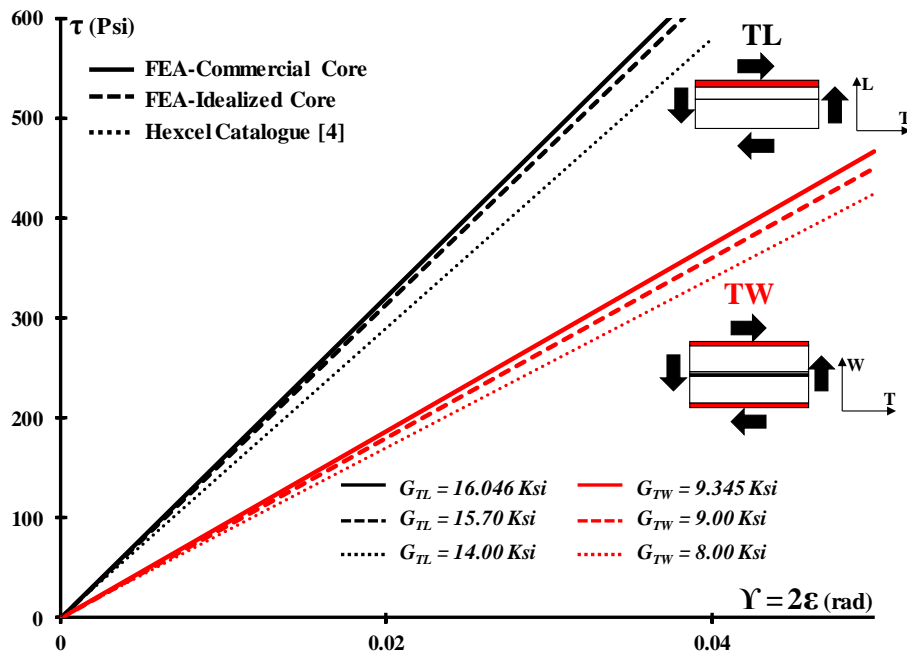


Figure 5-12. Effective engineering stress-strain curves for pure shear loading in (L-T) and (W-T) planes.

The deformed shapes of the honeycomb core under out-of-plane loadings are also illustrated in Figure 5-13.

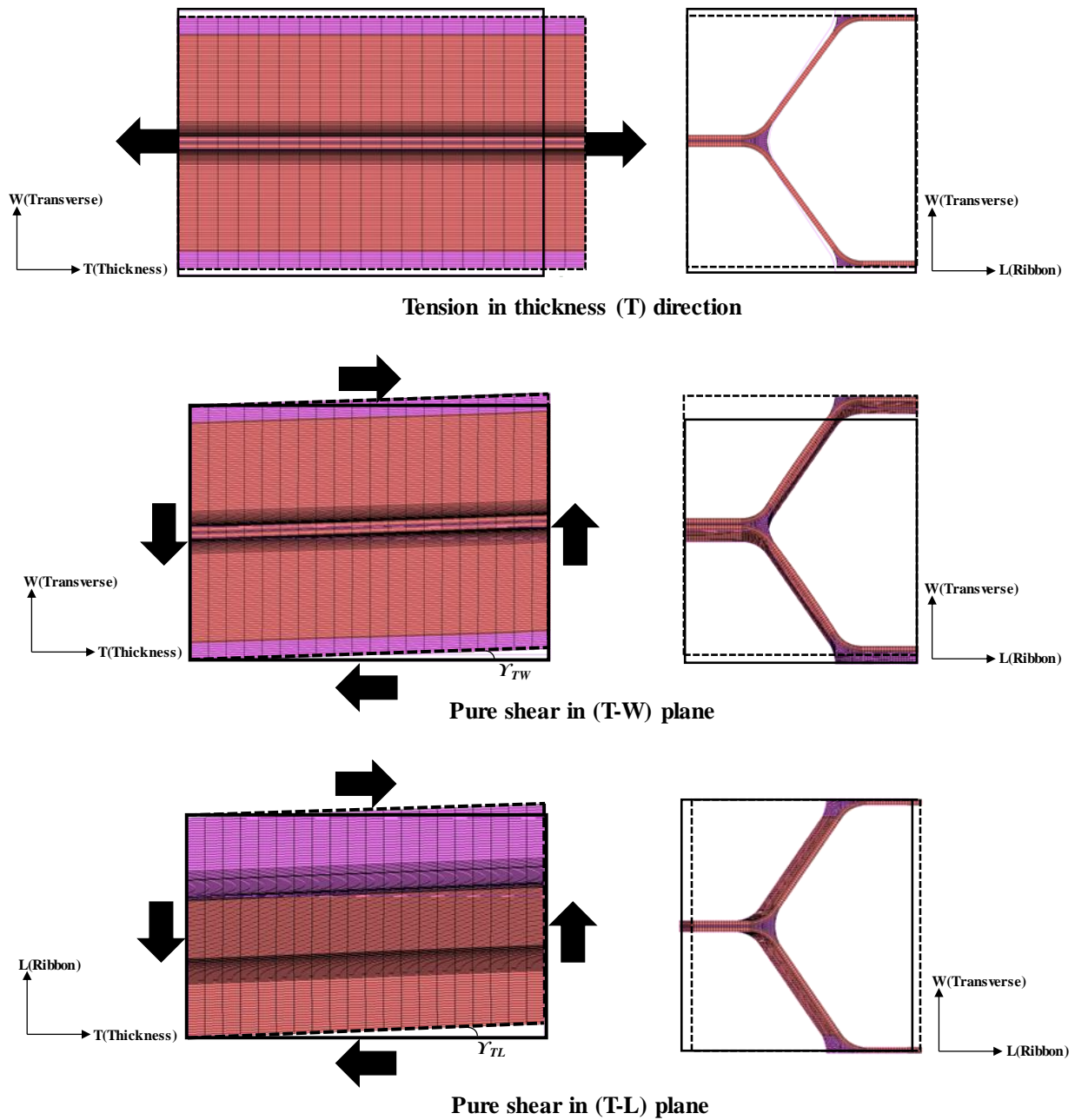


Figure 5-13. Out-of-plane deformed configuration of honeycomb core cell walls under different loading cases.

5.3.3 FEA Predictions of Multi-Axial Reponse

Figure 5-14 shows the in-plane equi-biaxial (stress) tension and compression results predicted by the finite element models. The mechanical responses of the commercial core geometry are much stiffer than those in the idealized core geometry; as indicated in the Figure 5-14. The negative strain in the ribbon direction under equi-biaxial tensile stress shows that the Poisson's effects are more significant in the ribbon direction. This can also be seen from the positive strain in the ribbon when the core is under equi-biaxial compressive stress.

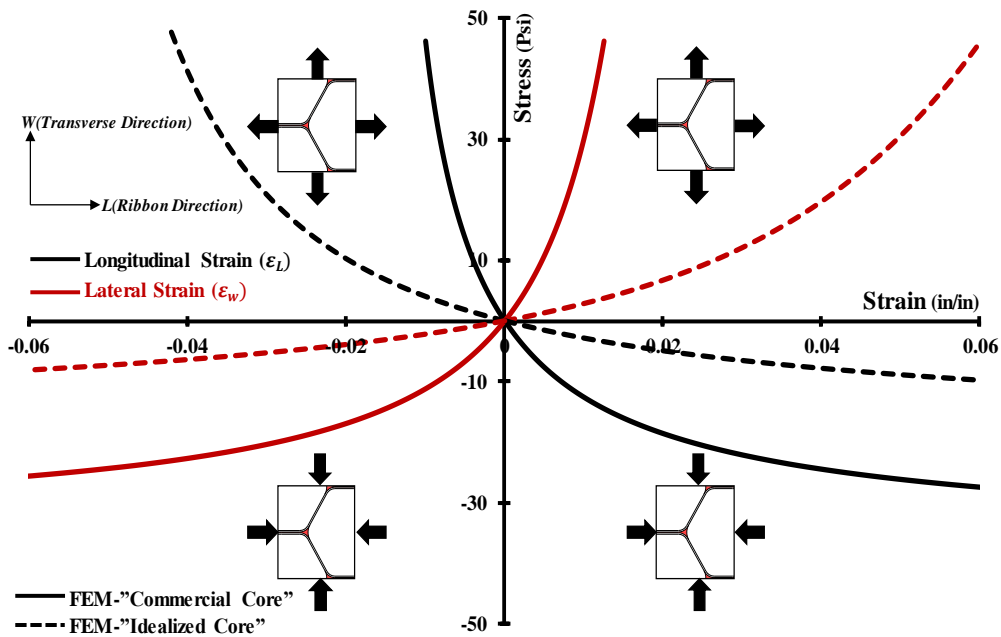


Figure 5-14. Equi-biaxial tension and compression curves obtained from FEA.

FEA prediction of the honeycomb core under hydrostatic compression to investigate the compressibility of the core is illustrated in Figure 5-15. As can be seen in the figure, the volumetric strain of the honeycomb core is not zero, and therefore, it has to be classified as a compressible material. However, as is shown Figure 5-15, the infinitesimal bulk modulus of the core is several orders of magnitude larger than the in-plane shear modulus ($K = 8 \text{ Ksi} \gg G_{LW} = 0.17 \text{ Ksi}$).

Consequently, a better approximation is to assume that the honeycomb core is a nearly incompressible material [50].

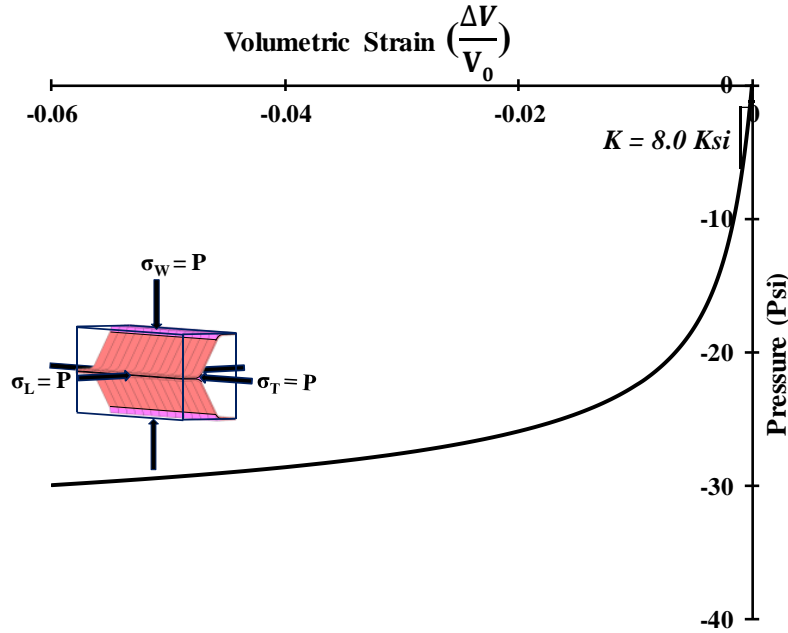


Figure 5-15. FEA prediction of HRP-fiberglass/phenolic honeycomb core under hydrostatic compression.

The results and key observations obtained from FEM of the RVE of the HRP-fiberglass/phenolic honeycomb core will be employed for developing an appropriate effective constitutive model for the homogenized HRP-honeycomb to describe the mechanical responses of the core using simple continuum elements rather than modeling the detailed microstructure in the finite element analysis, in the following chapter.

The FEM of the core RVE have been used (so far) to characterize the failure modes of the HRP-honeycomb core under different in-plane loading and boundary conditions and generate the in-plane failure envelopes [18] and also to investigate the large deformation in-plane mechanical responses of the core at elevated temperatures [19].

CHAPTER 6

EFFECTIVE CONSTITUTIVE MODELLING OF FINITE STRAIN IN-PLANE RESPONSES OF HEXAGONAL HONEYCOMB CORE

To analyze large-scale honeycomb core structures, it is computationally more efficient to model the core as a continuum solid with equivalent mechanical properties rather than considering the detailed cellular structure. In the small strain regime, such as applications of honeycomb cores in sandwich structures where in the core in-plane deformations are constrained by high modulus facesheets, the orthotropic effective Hooke's law given in equation (2.1) can be easily used to describe the effective mechanical behavior of the core under different loading and boundary conditions.

For composite or non-metallic honeycombs, in general, at room temperature, the in-plane mechanical responses of the bulk material are nonlinear, anisotropic, and fully recoverable (elastic) in the finite strain regime, as experimentally observed for the commercial HRP-fiberglass/phenolic hexagonal honeycomb core (see chapter 4). This is attributed to the geometric nonlinearity (small strain, large rotation) associated with flexural deformations of the inclined cell walls. Another unique behavior of the cores is its asymmetric response, i.e., it exhibits a stiffening response under tension-dominated loads and a softening response under compression-dominated loads. This is extremely important for the large bending analysis of honeycomb cores, such as those occurring during thermoforming of composite honeycombs. Under flexure, the cells on the tension and compression sides deform differently and thus exhibit different elastic behaviors. Therefore, the effective constitutive model must be developed such that the deformation-dependent elastic properties are captured to simulate the flexure behavior accurately. These unique responses of non-metallic honeycomb cores under large in-plane deformations point toward the

suitability of a hyperelastic material formulation for use in homogenized models of the honeycomb core.

In this research, the following assumptions have been made for developing the hyperelastic constitutive model:

- The hyperelastic constitutive model is primarily intended to capture the mechanical responses of the honeycomb core under in-plane loadings. As discussed previously and demonstrated in Figure 5-6, under in-plane loadings, the out-of-plane (W-T, L-T) Poisson's contraction effects are negligible, resulting in decoupled in-plane and out-of-plane responses.
- Generally, for using hyperelastic constitutive models, it is important to determine the compressibility conditions of hyperelastic materials for imposing the relevant conditions in the model. This can be accomplished by computing the *Jacobian* (J) of the deformation [50], which defines the volume change:

$$J = \frac{V}{V_0} = \det F \quad (6.1)$$

where $\det F$ represents the determinant of the second-order deformation gradient tensor F , and V and V_0 denote the material volume in the actual and reference configurations, respectively. The incompressibility condition requires that $J = 1$. Under uniaxial loading J can be given by

$$\begin{aligned} J &= \lambda_i \lambda_j \lambda_k, \quad i \neq j \neq k = 1, 2, 3 \\ \lambda_i &= 1 + \varepsilon_{ii} \end{aligned} \quad (6.2)$$

where λ_i and ε_{ii} represent the stretch ratios and engineering strains in each principal material direction.

For the in-plane uniaxial responses of the HRP- fiberglass/phenolic honeycomb, $\lambda_{3(T)} = 1$ and J is given by

$$J = \lambda_L \lambda_W \tag{6.3}$$

Figure 6-1 presents the volume change (J) associated with the FEA simulations of the uniaxial loading which is plotted as a function of the ratio of the elongations along the ribbon and transverse directions. As presented in Figure 6-1, under uniaxial in-plane loadings, $J \neq 1$; thus, the honeycomb core must be classified as a compressible material in the homogenization analysis, particularly under large deformations. Moreover, both test data and numerical simulations indicate that the volumetric deformation is negative for both tensile and compression loading. Under tensile loading, this implies that the volumetric strain energy is negative. This is an artifact of the core macrostructure and how the cell walls interact. The compressibility of the HRP-honeycomb core was also demonstrated in the previous chapter by the FEA simulation of the core behavior under hydrostatic pressure.

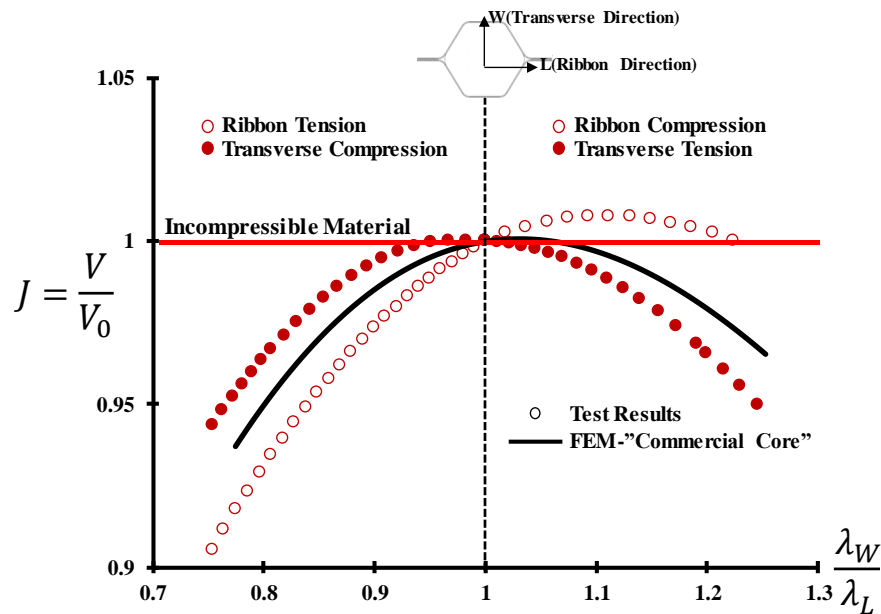


Figure 6-1. Change in volume of HRP- honeycomb under uniaxial in-plane loadings [13].

In this study, a formulation of an orthotropic compressible hyperelastic constitutive model for capturing the in-plane behavior of the HRP-fiberglass/phenolic honeycomb core is presented.

The details of the model and some important aspects of hyperelasticity are discussed in the following sections.

6.1 Hyperelasticity : Preliminaries

Hyperelastic materials are truly elastic in the sense that if a load is applied to such a material and then removed, the material returns to its original shape without any dissipation of energy in the process [31]. In other words, constitutive relations for hyperelastic materials are nonlinear and elastic at finite strains. The formulation of a hyperelastic behavior law relies on the proposition of a strain energy density function (SEDF)¹, W , expressed in terms of the deformation gradient tensor, F , from which the hyperelastic constitutive model is derived.

The SEDF must satisfy the principle of material objectivity in order to generate a frame-indifferent constitutive model. The principle of material objectivity implies that the SEDF must be independent of superimposed rigid body motions. This requirement can automatically be satisfied by defining the SEDF in terms of the right *Cauchy-Green* deformation tensor, $C = F^T F$ [63]:

¹ SEDF = Strain energy per unit reference volume

$$W = W_F(F) = W_C(C)$$

$$F_{ij} = \frac{\partial x_i}{\partial X_j} \Rightarrow [F] = \begin{bmatrix} \frac{\partial x_1}{\partial X_1} & \frac{\partial x_1}{\partial X_2} & \frac{\partial x_1}{\partial X_3} \\ \frac{\partial x_2}{\partial X_1} & \frac{\partial x_2}{\partial X_2} & \frac{\partial x_2}{\partial X_3} \\ \frac{\partial x_3}{\partial X_1} & \frac{\partial x_3}{\partial X_2} & \frac{\partial x_3}{\partial X_3} \end{bmatrix}$$

$$C_{IJ} = F^T F = \frac{\partial x_k}{\partial X_I} \frac{\partial x_k}{\partial X_J} \Rightarrow [C] = \begin{bmatrix} \frac{\partial x_k}{\partial X_1} \frac{\partial x_k}{\partial X_1} & \frac{\partial x_k}{\partial X_1} \frac{\partial x_k}{\partial X_2} & \frac{\partial x_k}{\partial X_1} \frac{\partial x_k}{\partial X_3} \\ \frac{\partial x_k}{\partial X_2} \frac{\partial x_k}{\partial X_1} & \frac{\partial x_k}{\partial X_2} \frac{\partial x_k}{\partial X_2} & \frac{\partial x_k}{\partial X_2} \frac{\partial x_k}{\partial X_3} \\ \frac{\partial x_k}{\partial X_3} \frac{\partial x_k}{\partial X_1} & \frac{\partial x_k}{\partial X_3} \frac{\partial x_k}{\partial X_2} & \frac{\partial x_k}{\partial X_3} \frac{\partial x_k}{\partial X_3} \end{bmatrix}; \quad k = 1, 2, 3 \quad (6.4)$$

$$x_i = X_I + u_i, \quad i \text{ (Deformed configuration)} = 1, 2, 3; \quad I \text{ (Initial Configuration)} = 1, 2, 3$$

The second *Piola-Kirchhoff* stress tensor S and the fourth-order tangent stiffness tensor D for an unconstrained hyperelastic material are then expressed in terms of the SEDF [50] as

$$S = 2 \frac{\partial W_C(C)}{\partial C} \quad (6.5)$$

$$D = 4 \frac{\partial^2 W_C(C)}{\partial C \partial C} \quad (6.6)$$

It should be noted that, the tangent stiffness tensor represents the elastic constants whose values depend on the level of deformation. For small deformation linear elasticity, the tangent elastic constants are equivalent to the overall elastic properties since the stress–strain curve is linear and stiffness does not change as deformation changes [50].

For constrained materials, such as an incompressible hyperelastic material, the constitutive law and the tangent stiffness tensor take the form [64]

$$\begin{aligned}
S &= 2 \frac{\partial W(C)}{\partial C} + q \frac{\partial \zeta}{\partial C} \\
D &= 4 \frac{\partial^2 W(C)}{\partial C \partial C} + 2q \frac{\partial^2 \zeta}{\partial C \partial C}
\end{aligned} \tag{6.7}$$

where q is an arbitrary scalar and $\zeta(C)$ represents the so-called constraint function accounting for kinematic constraint $\zeta(C) = 0$ [63].

6.2 Orthotropic Strain Energy Density Functions

In continuum mechanics, anisotropic properties of materials are characterized by their symmetry group. The symmetry group G of a material is the set of all orthogonal mappings Q which preserve the material symmetry. For anisotropic materials, the symmetry group can be defined with the aid of the so-called structural tensors N_i , [26] as :

$$\begin{aligned}
G &= \{Q \in orth : QN_iQ^T = N_i, i = 1, 2, \dots, n\} \\
N_i &= n_i \otimes n_i
\end{aligned} \tag{6.8}$$

where n_i is the unit base vector in the principal material directions and symbol " \otimes " denotes the second order tensor product [26].

The structural tensors are characterized by the following important properties [26]

$$\sum N_i = I, \quad N^k = N, \quad tr N_i = tr N_i^k = 1, \quad i = 1, 2, \dots, n \tag{6.9}$$

where " $tr(N_i)$ " implies a trace of the tensor N_i .

The condition of material symmetry for hyperelastic materials is written in terms of the SEDF given in equation (6.4) and the symmetry group in equation (6.8) by

$$W_C(QCQ^T) = W_C(C), \quad \forall Q \in G \tag{6.10}$$

For isotropic hyperelastic materials, equation (6.10) is satisfied for all orthogonal transformations of the reference configuration. For anisotropic hyperelastic materials, the SEDF must fulfill their material symmetries in order to capture anisotropic behavior of the materials [26].

This can be accomplished by expressing the SEDF as the isotropic function of its arguments to which the structural tensors are added [26, 65] as follows

$$W_C(QCQ^T, QN_iQ) = W_{CN}(C, N_i), \quad i = 1, 2, \dots, n, \quad \forall Q \in G \quad (6.11)$$

Orthotropic materials are characterized by symmetry with respect to three mutually orthogonal planes by reflection from which the material properties remain unchanged. The axes normal to three planes are referred to as the principal material directions $n_i, i=1,2,3$ [66].

Using the equation (6.8) and (6.9), the structural tensors for orthotropic materials can be expressed by introducing three unit vectors n_1, n_2 and n_3 as:

$$\begin{aligned} N_1 &= n_1 \otimes n_1, \quad N_2 = n_2 \otimes n_2, \quad N_3 = I - N_1 - N_2 = n_3 \otimes n_3 \\ n_i \cdot n_j &= \delta_{ij} = \begin{cases} 0, & i \neq j \\ 1, & i = j \end{cases} \end{aligned} \quad (6.12)$$

For orthotropic materials, N_i has the additional following properties

$$\begin{cases} N_i N_j = 0, & i \neq j \\ N_i N_j = N_i, & i = j \end{cases} \quad (6.13)$$

According to the classical invariant theory [26] and under consideration of equation (6.11) the general orthotropic SEDF can be represented by seven invariants as

$$W_C = \tilde{W}_{CN}(tr(CN_i), tr(C^2N_i), trC^3) = \tilde{W}_{CN}(tr(CN_i), tr(CN_iCN_j), trC^3) \quad j > i = 1, 2, 3 \quad (6.14)$$

The invariants $tr(CN_i)$ and $tr(CN_iCN_j)$ in equation (6.14) have a clear geometrical meaning. Indeed, $tr(CN_i)$ represents the square of stretch ratio (λ_i) in each principal material direction ($i = 1, 2, 3$), while $tr(CN_iCN_j)$ is related to the angle change in the principle plane ($i-j$) ($i \neq j$), as schematically presented for a (1-2) plane in Figure 6-2.

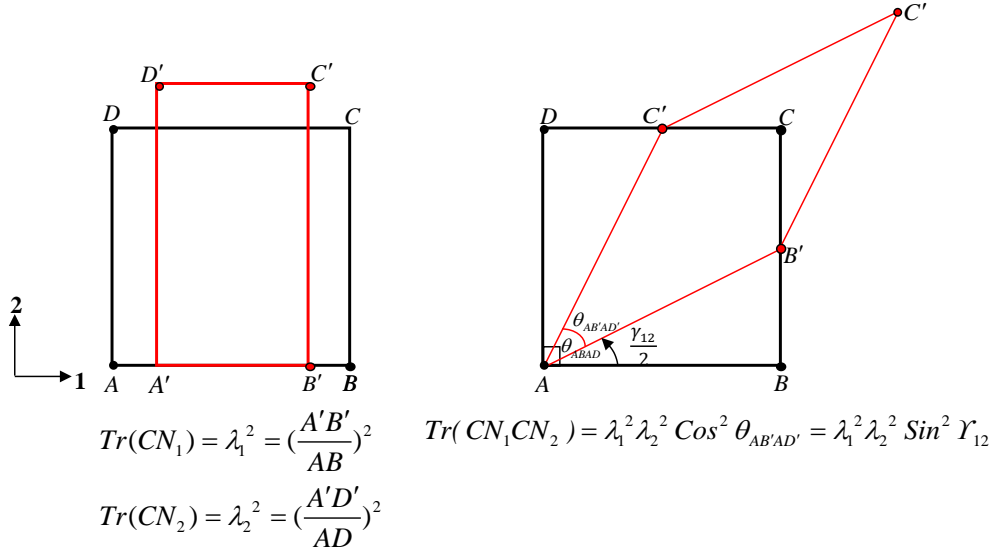


Figure 6-2. Physical interpretation of invariants $tr(CN_i)$ and $tr(CN_iCN_j)$ in principle plane (1-2).

A solution of the boundary value problem in the large strain elasticity is bound to the existence of a global minimizer of the total elastic energy of a body. To ensure this, the SEDF must be designed such that the four conditions : continuity, energy-free and stress-free natural states, polyconvexity, and coercivity are satisfied [67].

The continuity condition (at least C_2 -continuity¹) guarantees the computation of the stress and tangent stiffness tensors in equations (6.5) and (6.6).

For the natural state condition, zero SEDF and stresses are obtained in the reference (undeformed) configuration; therefore,

$$W|_{C=I} = 0, \quad S|_{C=I} = 2 \frac{\partial W}{\partial C} = 0 \quad (6.15)$$

A SEDF, is said to be polyconvex if and only if there exist the convex function \hat{W} such that [68]

$$W_F = \hat{W}_F(F, CofF, det F) \quad (6.16)$$

¹ C_2 -continuity implies that the first and second derivatives of the function are continuous.

where $\det F$ denotes the determinant of the second-order tensor F , and $\text{Cof}F = F^{-1}\det F$. The arguments F , $\text{Cof}F$, and $\det F$ describe the deformation of line, surface, and volume elements, respectively [63], as depicted in Figure 6-3.

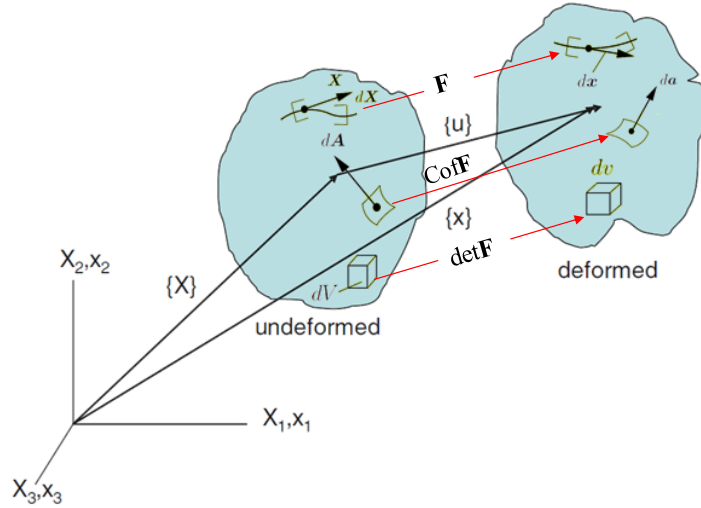


Figure 6-3. Representations of reference and actual configuration and corresponding geometric mappings [69].

In order to construct the polyconvex SEDF function, there exists a powerful tool called “additive representation” [63, 70] whereby the SEDF in equation (6.16) can be constructed as follows

$$W_F = \hat{W}_1(F) + \hat{W}_2(\text{Cof}F) + \hat{W}_3(\det F) \quad (6.17)$$

If \hat{W}_i ($i = 1, 2, 3$) are convex in the associated variable, then W_F in equation (6.17) is polyconvex; hence, construction of the polyconvex SEDF can be reduced to the formulation of convex ones. Note that the twice differentiable function of one variable $f(x)$ is said to be convex or strictly convex (have a unique (global) minimum) if and only if [69]

$$\begin{aligned} f''(x) &\geq 0 && \text{Convex function} \\ f''(x) &> 0 && \text{Strictly Convex function} \end{aligned} \quad (6.18)$$

The differences between the convex and non-convex as well as the convex and strictly-convex functions are illustrated in Figure 6-4 [69].

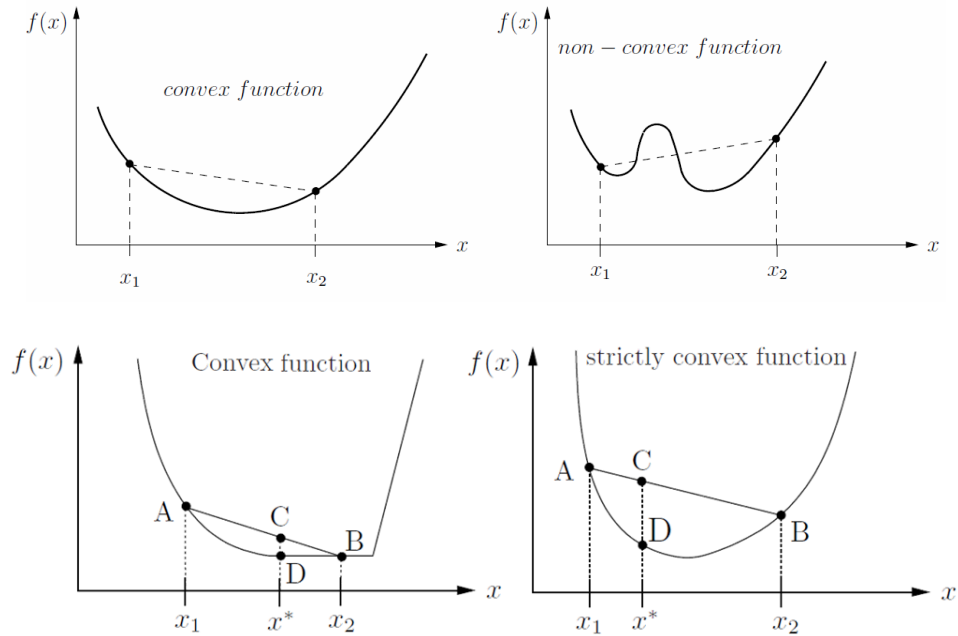


Figure 6-4. Illustrations of one-dimensional convex , strictly convex and non-convex functions from Ebbing [69].

Material stability is one of the most important issues that should be considered in the finite elasticity. It is assumed that a hyperelastic material maintains its integrity throughout the elastic deformations referred to as material stability. Therefore, the SEDF must be defined such that the predicted constitutive relations for the hyperelastic material show the stable material behavior in the large strain elasticity. The difference between the real material response and an unstable response predicted by a hyperelastic material model is shown in Figure 6-5.

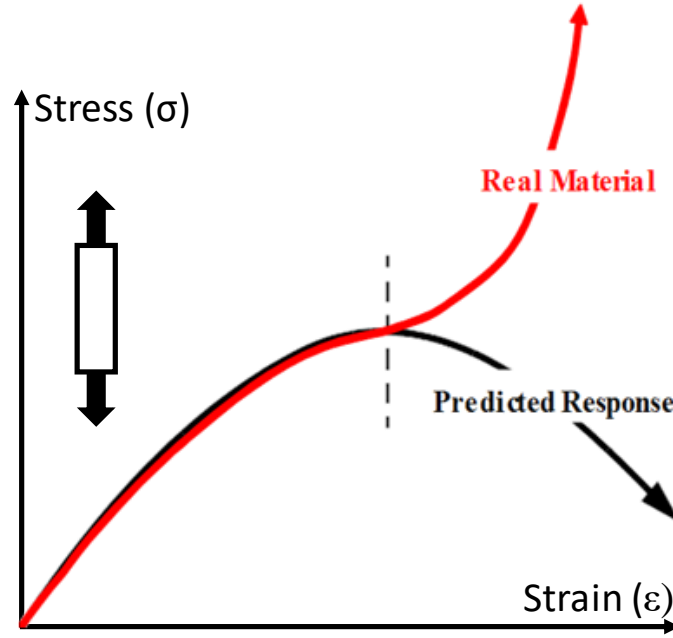


Figure 6-5. Example of an unstable hyperelastic material model.

Ellipticity condition which implicates positive definiteness of the acoustic tensor so that the speed of displacement waves is real for any direction of propagation is one of the strong criteria for ensuring a material stability. The mathematical expression and details of the ellipticity condition are documented in [64, 69]. It was proved [70, 71] that for polyconvex SEDFs, the ellipticity condition is guaranteed resulting in stable material models.

A polyconvex representation of the orthotropic SEDF in equation (6.14) is given by [63]

$$\begin{aligned}
 W_C &= \bar{W}_{CN}(I_i, J_i, III_C) \quad i = 1, 2, 3 \text{ (no summation implied)} \\
 I_i &= \text{tr}(CN_i) \\
 J_i &= \text{tr}[(\text{cof}C)N_i] \\
 III_C &= \det C
 \end{aligned} \tag{6.19}$$

where $\text{cof}C = C^{-T}\det C$. The invariants I_j , J_i , and III_C are convex with respect to F , $\text{adj}F$, and $\det F$, respectively.

It should be noted that for incompressible hyperelastic materials, the invariant, III_C representing the volume change¹ is equal to unity. Therefore, the constraint function in equation (6.7) can be given by [63]

$$\zeta(C) = III_C^{1/3} - 1 \quad (6.20)$$

For incompressible materials, the energy balance must be unaffected by the addition of a pressure; however, under hydrostatic state of stress even if $III_C = 1$, the other invariants contribute to the pressure and consequently the constitutive relation still gives a hydrostatic pressure. Therefore, when the condition $III_C = 1$ is imposed, the constitutive relation in equation (6.6) must be amended using the appropriate constraint function as shown in equation (6.7).

A growth condition referred to as coercivity implies that a continuous SEDF at large strains should reflect that infinite stress accompanied by extreme strains [69]. The details and formulation of the coercivity condition have been documented elsewhere [63, 69].

According to previous research [63, 66, 67, 69], the polyconvexity of the SEDF together with its continuity and coercivity (growth) is sufficient to satisfy the existence of a global minimizer of the total elastic energy of a body, resulting in a reasonable and physically meaningful solution for the boundary value problems.

Using the additive representation, a set of compressible, orthotropic, polyconvex and coercive SEDF can be constructed [64] as

$$W = \widehat{W}(\tilde{I}_r, \tilde{J}_r, III_C) = \frac{\mu_r}{4} \left[\sum_{r=1}^n f_r(\tilde{I}_r) + g_r(\tilde{J}_r) + h_r(\sqrt{III_C}) \right] \quad (6.21)$$

where $\mu_r \geq 0$ are material parameters with the dimension of stress and \tilde{I}_r, \tilde{J}_r are generalized invariants defined as follows:

¹ $J = \det F = \sqrt{\det C}$.

$$\begin{aligned}\tilde{I}_r &= \sum_{i=1}^3 w_i^{(r)} I_i = \text{tr}[C\tilde{N}_r], \quad r=1,2,\dots \\ \tilde{J}_r &= \sum_{i=1}^3 w_i^{(r)} J_i = \text{tr}[[\text{cof}C]\tilde{N}_r]\end{aligned}\tag{6.22}$$

where \tilde{N}_r represents the orthotropic generalized structural tensor and is given by

$$\tilde{N}_r = \sum_i^3 w_i^{(r)} N_i = w_1^{(r)} N_1 + w_2^{(r)} N_2 + w_3^{(r)} N_3\tag{6.23}$$

where $w_i^{(r)}$ denotes the weight factors of the principal or fiber directions and have the following important characteristics:

$$\sum_{i=1}^3 w_i^{(r)} = 1, \quad 0 \leq w_i^{(r)} \leq 1, \quad r = 1, 2, \dots\tag{6.24}$$

It is evident from equation (6.21), the functions f_r , g_r and h_r ¹ have to be chosen as convex and monotonous increasing functions of their invariant in order to guarantee polyconvexity and coercivity of the SEDF. It should be noted that, the conditions of the energy and stress free natural state in equation (6.15), are satisfied by the SEDF in equation (6.21) whenever [66]

$$\begin{aligned}f_r(1) &= g_r(1) = h_r(1) = 0, \quad r = 1, 2, \dots, n \\ f_r'(1) &= g_r'(1) = -\frac{1}{2} h_r'(1) = 0\end{aligned}\tag{6.25}$$

The SEDF in equation (6.21) is expressed in terms of a series with an arbitrary number of terms n ; depending on the complexity of the material behavior, an appropriate number of terms ($r=1,2,\dots,n$) may be used.

¹ h_r are convex functions with respect to $III_C^{1/2} = \det F$

6.3 Hyperelastic Constitutive Modelling of Hexagonal Honeycomb Core

The SEDF in equation (6.21) can be utilized for constitutive modelling of any hyperelastic materials irrespective of their detailed microstructural features provided that the orthotropic material symmetry is satisfied. Therefore, it can be used for characterizing the homogenized in-plane mechanical responses of honeycomb cores with any unit cell configurations due to the inherent orthotropic behavior of honeycomb core structures. However, it is possible to incorporate some of the features of honeycomb core geometry in the SEDF without influencing the orthotropic material symmetry, by means of the generalized structural tensors (N_r) in equation (6.23).

6.3.1 Generalized Structural Tensor

Before explaining the method for developing the generalized structural tensor exclusively for hexagonal honeycomb cores, it is necessary to discuss the most important feature of the generalized structural tensor for application to a general fiber-reinforced material.

First of all, it is important to know the main role of the weight factors $w_i^{(r)}$ in the expression for orthotropic generalized structural tensor in equation (6.23). In fact, $w_i^{(r)}$ represent the weight factors of the principal material directions. The weight factors take values between 0 and 1, and the higher the value of $w_i^{(r)}$, the stronger is the effect of the principal direction i on others. This feature enables to obtain the expression of directional anisotropy [67].

Now, let's define a generalized structural tensor for a general fiber-reinforced material. A schematic representation of a general fiber-reinforced material consisting of an isotropic matrix and arbitrary number (n) of fiber families is shown in Figure 6-6.

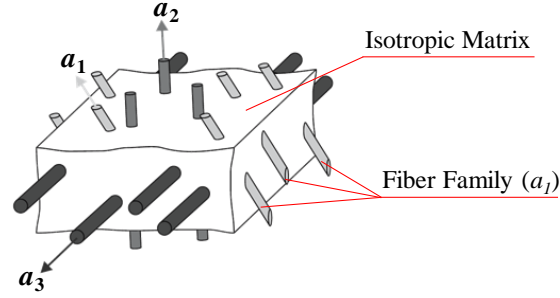


Figure 6-6. General fiber-reinforced material [64].

Using equation (6.12), the structural tensors for each fiber family are given by

$$\hat{N}_i = a_i \otimes a_i, \quad \hat{N}_0 = \frac{I}{3}, \quad i = 1, 2, \dots, n \quad (6.26)$$

where a_i denotes unit vector of each fiber family and tensor N_0 is assumed to be associated with the isotropic matrix. Note that when all $w_i^{(r)}$ take values equal to $1/3$ in equation (6.23), the material behaves as an isotropic one.

The generalized structural tensor for general fiber-reinforced material shown in Figure 6-6 can be defined by

$$\begin{aligned} \tilde{N}_r &= \sum_{i=0}^n v_i^{(r)} \hat{N}_i = v_0^{(r)} \hat{N}_0 + v_1^{(r)} \hat{N}_1 + v_2^{(r)} \hat{N}_2 + \dots + v_n^{(r)} \hat{N}_n \\ \sum_{i=0}^n v_i^{(r)} &= 1, \quad 0 \leq v_i^{(r)} \leq 1, \quad r = 1, 2, \dots, n \end{aligned} \quad (6.27)$$

where $0 \leq v_i^{(r)} \leq 1$ represent scalar weight factors and they determine the effect of the interaction between fibers.

On the basis of fiber-reinforced materials, orthotropy arises as special cases and it may be achieved by different arrangements of two or more fiber families. In these cases the generalized structural tensors in equations (6.23) and (6.27) should coincide leading to associated weight factors $w_i^{(r)}$ and $v_i^{(r)}$ [64].

For example a material with three mutually orthogonal fiber families coinciding with the principal material directions is orthotropic. In this case $n_i = a_i$. Therefore, in view of equations (6.9), (6.23), (6.26) and (6.27) one obtains [64]

$$\left\{ \begin{array}{l} \hat{N}_i(\text{Fibers}) = N_i(\text{Principal Directions}) = n_i \otimes n_i \\ \tilde{N}_0 = \frac{I}{3} = \frac{N_1 + N_2 + N_3}{3} \\ \sum_{i=0}^n v_i^{(r)} = 1 \Rightarrow v_0^{(r)} = 1 - v_1^{(r)} - v_2^{(r)} - v_3^{(r)} \\ \tilde{N}_r = \sum_{i=0}^3 v_i^{(r)} \hat{N}_i = \sum_{i=0}^3 v_i^{(r)} N_i \end{array} \right\} \Rightarrow \tilde{N}_r = \frac{1}{3} \sum_{i=1}^3 [1 - v_1^{(r)} - v_2^{(r)} - v_3^{(r)} + 3v_i^{(r)}] N_i \quad (6.28)$$

As discussed previously, under in-plane loadings, out-of-plane properties of the honeycomb cores are not affected. Therefore, it is possible to decouple the in-plane and out-of-plane SEDFs for the core. This can be accomplished by setting $w_3^{(r)} = 0$ in the generalized structural tensor in equation (6.23) resulting in

$$\begin{aligned} \tilde{N}_r &= \sum_{i=1}^2 w_i^{(r)} N_i = w_1^{(r)} N_1 + w_2^{(r)} N_2 \\ w_1^{(r)} + w_2^{(r)} &= 1, \quad 0 \leq w_1^{(r)}, w_2^{(r)} \leq 1, \quad r = 1, 2, \dots, n \end{aligned} \quad (6.29)$$

In other words, the effect of the principal direction (3 or T) is assumed to be zero for the honeycomb cores subjected to in-plane loadings.

The generalized structural tensor in equation (6.29) together with the SEDF in equation (6.21) can be easily used to describe the in-plane behavior of any kinds of honeycomb cores irrespective of their cell configurations.

In view of fiber-reinforced materials, it is possible to incorporate some of the geometric features of a honeycomb core unit cell such as the cell walls orientations into the SEDF using the generalized structural tensor. This could provide a better understanding of the developed SEDF

concerning the material constants and most importantly, the performance of the function to capture the deformations of the honeycomb core for describing the accurate constitutive relations.

Now, let us consider the in-plane view of a hexagonal honeycomb core, as illustrated in Figure 6-7.

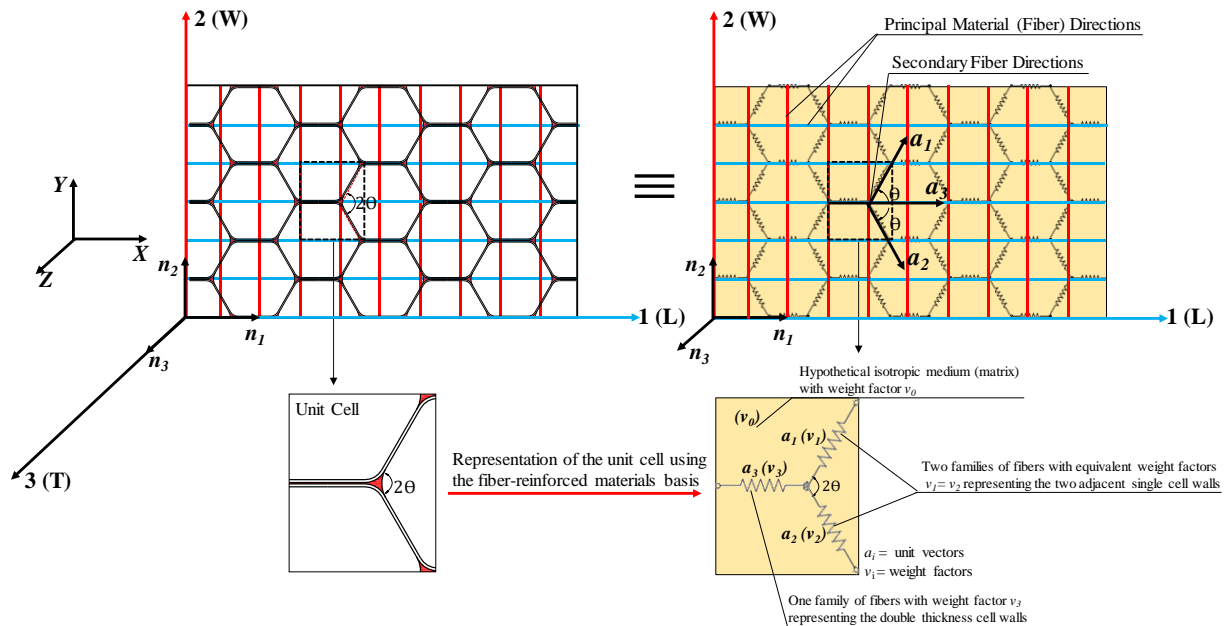


Figure 6-7. Schematic of principal material directions and secondary fiber directions for hexagonal honeycomb core in the (L-W) plane.

As can be seen in Figure 6-7, the geometry of the hexagonal honeycomb core can be constructed by repeating a representative unit cell which is composed of a double thickness cell wall, two adjacent single cell walls and angle 2θ between them, and an adhesive fillet.

A fiber-reinforced material representation of the honeycomb core unit cell is shown schematically in Figure 6-7. The unit cell can be represented by two equivalent families of fibers with associated weight factors $v_1^{(r)} = v_2^{(r)}$ which denote the effect of single cell walls and they are aligned in two directions intersecting with each other by an angle of 2θ . The effect of double thickness cell wall (2 single cell walls + adhesive layer) is also represented by one unidirectional

family of fiber with respective weight factor $v_3^{(r)}$. In Figure 6-7, the cell walls are referred to as secondary fibers and characterized by unit vectors of the secondary fiber directions, $a_i (i = 1, 2, 3)$.

The in-plane (L-W) and through thickness (T) principal material (fiber) directions are respectively given by the bisectors of the two fiber directions and the normal to the plane in which the fibers lie denoted by unit vectors $n_i (i = 1, 2, 3)$, as illustrated in Figure 6-7.

The generalized structural tensors for the fiber-reinforced representation of the honeycomb core unit cell are thus defined as in equation (6.27) by

$$\begin{aligned} \hat{N}_r &= \sum_{i=0}^3 v_i^{(r)} \hat{N}_i = v_0^{(r)} \hat{N}_0 + v_1^{(r)} \hat{N}_1 + v_2^{(r)} \hat{N}_2 + v_3^{(r)} \hat{N}_3 = v_0^{(r)} \hat{N}_0 + v_1^{(r)} (\hat{N}_1 + \hat{N}_2) + v_3^{(r)} \hat{N}_3 \\ \left\{ \begin{array}{l} \sum_{i=0}^3 v_i^{(r)} = 1 \\ v_1^{(r)} = v_2^{(r)} \end{array} \right. &\Rightarrow v_0^{(r)} + 2v_1^{(r)} + v_3^{(r)} = 1, \quad 0 \leq v_0^{(r)}, v_1^{(r)} = v_2^{(r)}, v_3^{(r)} \leq 1, \quad r = 1, 2, \dots, n \end{aligned} \quad (6.30)$$

where \hat{N}_0 and $v_0^{(r)}$, highlighted in Figure 6-7 by yellow color, denote the hypothetical isotropic medium (matrix) structural tensor and associated weight factors, respectively.

The secondary fiber directions $a_i (i = 1, 2, 3)$ can be expressed in terms of the in-plane principal material directions $n_i (i = 1, 2)$, as

$$\begin{aligned} a_1 &= n_1 \cos \theta + n_2 \sin \theta \\ a_2 &= n_1 \cos \theta - n_2 \sin \theta \\ a_3 &= n_1 \end{aligned} \quad (6.31)$$

Therefore, corresponding structural tensors $(\hat{N}_1, \hat{N}_2, \hat{N}_3)$ can be defined as in equation (6.26) by

$$\begin{aligned} \hat{N}_1 &= a_1 \otimes a_1 = \cos^2 \theta n_1 \otimes n_1 + \sin^2 \theta n_2 \otimes n_2 + \cos \theta \sin \theta (n_1 \otimes n_2 + n_2 \otimes n_1) \\ \hat{N}_2 &= a_2 \otimes a_2 = \cos^2 \theta n_1 \otimes n_1 + \sin^2 \theta n_2 \otimes n_2 - \cos \theta \sin \theta (n_1 \otimes n_2 + n_2 \otimes n_1) \\ \hat{N}_3 &= a_3 \otimes a_3 = n_1 \otimes n_1 \end{aligned} \quad (6.32)$$

Our next aim is to find the relations between the weight factors $w_i^{(r)}$ ($i = 1, 2$) associated with the principal material directions in equation (6.29) and the weight factors $v_i^{(r)}$ ($i = 0, 1, 2, 3$) related to fibers and hypothetical matrix in equation (6.30).

In view of equations (6.26) and (6.29), let's first define the isotropic structural tensor \hat{N}_0 in equation (6.30) by setting weight factors $w_1^{(r)} = w_2^{(r)} = 1/2$ as follows:

$$\hat{N}_0 = \frac{I}{2} = \frac{N_1 + N_2}{2} \quad (6.33)$$

Utilizing equations (6.32) and (6.33), the generalized structural tensors in equation (6.30) can be expressed in terms of the structural tensors $N_i = n_i \otimes n_i$ ($i = 1, 2$) assembled for the in-plane principal material directions as

$$\begin{aligned} \tilde{N}_r &= \sum_{i=0}^3 v_i^{(r)} \hat{N}_i = \left(\frac{1 + (4 \cos^2 \theta - 2)v_1^{(r)} + v_3^{(r)}}{2} \right) N_1 + \left(\frac{1 + (4 \sin^2 \theta - 2)v_1^{(r)} - v_3^{(r)}}{2} \right) N_2 \\ &\left\{ \begin{array}{l} \sum_{i=0}^3 v_i^{(r)} = 1 \\ v_1^{(r)} = v_2^{(r)} \end{array} \right. \Rightarrow v_0^{(r)} = 1 - 2v_1^{(r)} - v_3^{(r)}, \quad 0 \leq v_0^{(r)}, v_1^{(r)} = v_2^{(r)}, v_3^{(r)} \leq 1, \quad r = 1, 2, \dots, n \end{aligned} \quad (6.34)$$

Comparing equations (6.34) and (6.29), the weight factors of the in-plane principal material directions can be expressed in terms of the weight factors of the secondary fibers as follows:

$$\begin{aligned} \tilde{N}_r &= \sum_{i=1}^2 w_i^{(r)} N_i = w_1^{(r)} N_1 + w_2^{(r)} N_2 \\ w_1^{(r)} &= \left(\frac{1 + (4 \cos^2 \theta - 2)v_1^{(r)} + v_3^{(r)}}{2} \right) \\ w_2^{(r)} &= \left(\frac{1 + (4 \sin^2 \theta - 2)v_1^{(r)} - v_3^{(r)}}{2} \right) \\ &0 \leq v_1^{(r)}, v_3^{(r)} \leq 1, \quad r = 1, 2, \dots, n \end{aligned} \quad (6.35)$$

It is evident in the above equation $w_1^{(r)} + w_2^{(r)} = 1$ is automatically satisfied.

Equation (6.35) provides a better understanding of the physical interpretation of the weight factors $w_i^{(r)}$ in the SEDF for describing the in-plane constitutive behavior of hexagonal honeycomb core. For example, if the honeycomb core is subjected to tensile load in ribbon direction, as the deformation increases, tangent stiffness of the core will increase because of the densification phenomena (at which point the inclined cell walls start closing up within their longitudinal direction). As is shown in equation (6.35), this phenomenon can be captured by the weight factors $w_i^{(r)}$ which include the weigh factors of the inclined cell walls ($v_1^{(r)} = v_2^{(r)}$) and the angle between them. It should be noted that the angle Θ is the initial angle between the adjacent cell walls.

6.3.2 Hyperelastic Constitutive Model for In-Plane Loading

In this study, utilizing the equation (6.21), a set of polyconvex SEDF for orthotropic, compressible hyperelastic materials was assembled by choosing the convex and monotone increasing functions f_r , g_r and h_r of their invariants as follows [63, 69]:

$$\begin{aligned} f_r(\tilde{I}_r) &= \frac{1}{\alpha_r} (\tilde{I}_r^{\alpha_r} - 1) \\ g_r(\tilde{J}_r) &= \frac{1}{\beta_r} (\tilde{J}_r^{\beta_r} - 1) \\ h_r(\sqrt{III_C}) &= -2 \ln(\sqrt{III_C}) \end{aligned} \quad (6.36)$$

where α_r, β_r denote material constants.

Using the equation (6.18) for ensuring the convexity of the selected functions results in

$$\alpha_r \geq 1, \beta_r \geq 1 \quad (6.37)$$

Substituting the expressions for functions f_r , g_r and h_r into the SEDF in equation (6.21) leads to

$$\begin{aligned} W &= \frac{1}{4} \sum_{r=1}^n \mu_r \left[\frac{1}{\alpha_r} (\tilde{I}_r^{\alpha_r} - 1) + \frac{1}{\beta_r} (\tilde{J}_r^{\beta_r} - 1) - \ln(III_C) \right] \\ \mu_r &\geq 0 \end{aligned} \quad (6.38)$$

The SEDF in equation (6.38) satisfies the four prerequisite conditions mentioned in the previous section without further restrictions on the material coefficients. The material constants and weight factors can be identified by nonlinear curve-fitting of data obtained using experiments or numerical models of the RVE.

Based on the experimental observation for the HRP-fiberglass/phenolic honeycomb core under pure shear loading using the picture-frame shear fixture (see chapter 4), in the central region of the core (away from the edges), the longitudinal strains were weakly affected (almost zero) when the specimen loaded in shear along its principal directions. It was also shown that when the specimen loaded in shear at angle 45° to the principal directions (off-axis pure shear test), only tensile and compressive strains acted on the specimen in the principal plane and the magnitude of shear strain was negligible. Moreover, the linear stress-strain response with computation of a relatively high shear modulus was predicted from the FEM of the core RVE under in-plane, pure shear loading. Consequently, in this study, it was assumed that, the normal and shear deformations are decoupled in the material coordinate system and the SEDF in equation (6.38) was only used to capture the in-plane uniaxial responses of the HRP-fiberglass/phenolic honeycomb core.

6.3.3 Identification of Material Parameters for Hyperelastic Model

The material parameters defining the hyperelastic SEDF given in equation (6.38) were numerically identified using the in-plane, uniaxial effective stress-strain responses of the HRP-fiberglass/phenolic honeycomb core predicted by the FEM of the core RVE shown in Figure 5-5.

Under uniaxial loadings, the principal material directions and the principal axes of *right Cauchy-Green* tensor coincide. In this case, utilizing spectral decomposition [26], the *right Cauchy-Green* tensor can be expressed in a diagonal form in terms of the principal stretches as

$$C = \sum_{i=1}^3 \lambda_i^2 n_i \otimes n_i \quad (6.39)$$

Therefore, in view of equations (6.12) and (6.13), invariants I_i , J_i and III_c in equation (6.19) can be written as

$$\begin{aligned} I_i &= \lambda_i^2 \\ J_i &= \lambda_j^2 \lambda_k^2 \\ III_c &= \lambda_i^2 \lambda_j^2 \lambda_k^2, \quad i \neq j \neq k = 1(L), 2(W), 3(T) \end{aligned} \quad (6.40)$$

It should be noted that under in-plane loading, the out-of-plane (W-T, W-L) Poisson contraction effects are zero, resulting in $\lambda_3=1$. Substituting the invariants obtained in equation (6.40) into the expression for the generalized invariants in equation (6.22) and also in view of equation (6.35), the SEDF given in equation (6.38) takes the form

$$W(\lambda_1, \lambda_2) = \frac{1}{4} \sum_{r=1}^n \mu_r \left\{ \begin{array}{l} \frac{1}{\alpha_r} \left[\left(\lambda_1^2 \frac{1+(4\cos^2\theta-2)v_1^{(r)}+v_3^{(r)}}{2} + \lambda_2^2 \frac{1+(4\sin^2\theta-2)v_1^{(r)}-v_3^{(r)}}{2} \right)^{\alpha_r} - 1 \right] + \\ \frac{1}{\beta_r} \left[\left(\lambda_2^2 \frac{1+(4\cos^2\theta-2)v_1^{(r)}+v_3^{(r)}}{2} + \lambda_1^2 \frac{1+(4\sin^2\theta-2)v_1^{(r)}-v_3^{(r)}}{2} \right)^{\beta_r} - 1 \right] - \\ \ln(\lambda_1^2 \lambda_2^2) \end{array} \right\} \quad (6.41)$$

$$0 \leq v_1^{(r)}, v_3^{(r)} \leq 1, \quad \mu_r \geq 0, \alpha_r \geq 1, \beta_r \geq 1, \quad r = 1, 2, \dots, n$$

Using equations (6.5) and (6.6) the normal components of the second *Piola-Kirchhoff* stress and the tangent stiffness tensor may be obtained as

$$S_{ii} = \frac{1}{\lambda_i} \frac{\partial W}{\partial \lambda_i}, \quad i=1,2 \quad (6.42)$$

$$D_{ijij} = \frac{1}{\lambda_i \lambda_j} \frac{\partial^2 W}{\partial \lambda_i \partial \lambda_j}, \quad i, j=1,2 \quad (6.43)$$

In order to determine the material parameters included in the hyperelastic SEDF in equation (6.41), the following relations were used to convert the engineering normal stresses (σ_{ii}) and strains (ε_{ii}) to the second *Piola-Kirchhoff* stresses and stretch ratios as [50]

$$S_{ii} = \frac{\sigma_{ii}}{1 + \varepsilon_{ii}} = \frac{\sigma_{ii}}{\lambda_i}, \quad i=1,2 \text{ (no summation implied)} \quad (6.44)$$

$$\lambda_i = 1 + \varepsilon_{ii}$$

The hyperelastic SEDF was fitted to the FEA predictions of the uniaxial tension and compression behavior of the HRP-honeycomb core such that for the different combinations of stretch ratios, the stresses predicted by the model match that of the data set. To fit these relations to the FEA data, the objective function \tilde{R} in equation (6.46) was minimized with respect to the material constants μ_r , α_r , β_r , $v_1^{(r)}$, and $v_3^{(r)}$ subjected to satisfying equation (6.45), and the principal stretches λ_1 and λ_2 by means of the least-squares method. This requires that the non-zero stresses along the loading directions and traction free conditions orthogonal to it be satisfied simultaneously

$$\begin{aligned} \mu_r &\geq 0, \quad \alpha_r \geq 1, \quad \beta_r \geq 1, \\ 0 &\leq v_1^r, v_3^r \leq 1 \end{aligned} \quad (6.45)$$

$$\tilde{R} = \sqrt{\frac{1}{k} \left(\sum_{n=1}^k (\bar{S}_{11} - S_{11}(\lambda_1, \lambda_2))^2 + (\bar{S}_{22} - S_{22}(\lambda_1, \lambda_2))^2 \right)} \quad (6.46)$$

where \bar{S}_{ii} ($i = 1(L), 2(W)$) indicates the FEA predictions, and k denotes the number of data points used for approximating the stress-stretch curves obtained from the FEM of the core RVE under uniaxial loadings along the ribbon and transverse directions. Note that, the angle $\Theta = 57^\circ$, which is the initial angle between the inclined cell walls.

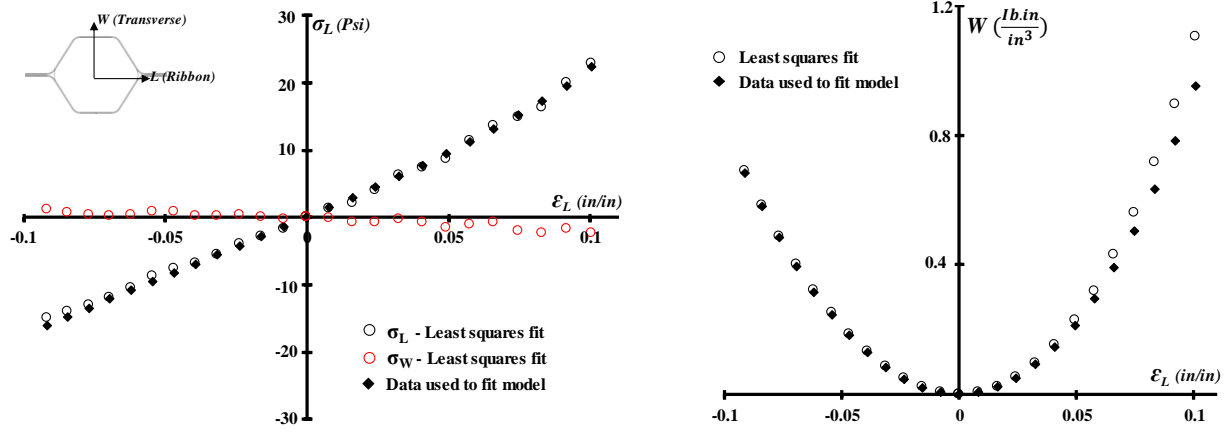
The minimization of the objective function was carried out with the aid of the generalized reduced gradient (GRG) algorithm, which is available in the Microsoft Excel solver [72]. Using trial and error, the power series in the SEDF was truncated at seven terms ($n = 7$) such that the total number of unknown material constants was 35, which satisfactorily defined the honeycomb core behavior. The values of the constants are listed in TABLE 6-1.

TABLE 6-1

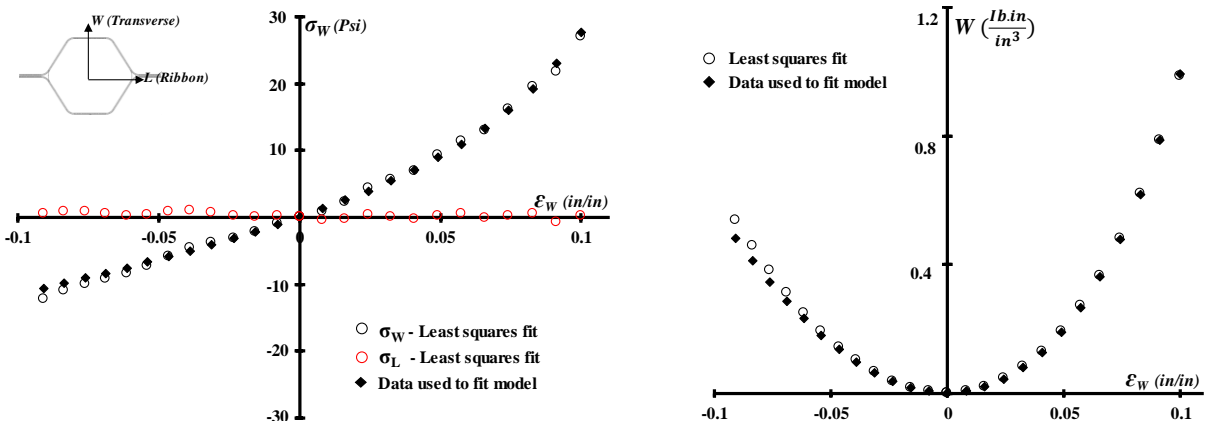
MATERIAL PARAMETERS OF HYPERELASTIC CONSTITUTIVE MODEL FOR IN-PLANE UNIAXIAL RESPONSES OF FIBERGLASS/PHENOLIC HONEYCOMB

r	1	2	3	4	5	6	7
μ_r (Psi)	60	0.7	0.55	0.0033	0.00027	5.267×10^{-7}	0.000021
α_r	805	1939	4282	1542	1204	1	940
β_r	1	1	1408	1	1.72	737	17
ν_1^r	0	0.00045	0.014	0.0081	0.098	0.0018	0
ν_3^r	0.06	0.10928	0.03	0.1535	0.000198	0.1691	0.1995

The stress-strain and strain energy density diagrams predicted by the orthotropic hyperelastic model and comparison with the FEA results are shown in Figure 6-8. It can be seen that the hyperelastic model matches the data satisfactorily. As shown in Figure 6-8, the stress-free conditions (presented by red points) are also included in the stress-strain curves. Note that the traction-free conditions are only satisfied in a least-squares sense because the computation of stresses is not based on incremental analysis. In FEA simulations, which will be presented in the next section, the traction-free conditions are automatically satisfied due to equilibrium conditions.



(a) Uniaxial in ribbon (L) direction



(b) Uniaxial in transverse (W) direction

Figure 6-8. Least-squares fit of polyconvex orthotropic SEDF using data from FEM of RVE of HRP- fiberglass/phenolic honeycomb core.

For additionally verifying the model with the experimental data, the proposed hyperelastic constitutive model was implemented in a commercial FEA software as an effective constitutive model of the homogenized HRP- fiberglass/phenolic honeycomb core. First, the elementary tests using single-element FEM were simulated for validating the model under simple states of loading and then for further validation of the model, it was employed for nonlinear FEA simulations of the bulk honeycomb core using simple continuum elements, subjected to complex loading and boundary conditions, such as in-plane flexure and picture-frame pure shear test.

6.4 Implementation of Hyperelastic Material Model in FEA Program

The hyperelastic material model was implemented using the MSC Marc finite element program [31] utilizing the *hypela2.f* user subroutine [73], which allows users to input their own material models. The evaluation of the model was first performed using a single planar element on which simple states of loading were imposed, as shown in Figure 6-9. A four-node isoparametric plane strain quadrilateral element (Marc element 115 [61]) was used for this purpose. It should be noted that, under simple states of loading, such as axial or pure shear, a single element (solid or planar) would suffice to evaluate the model of the homogenized responses of the honeycomb core under large deformations.

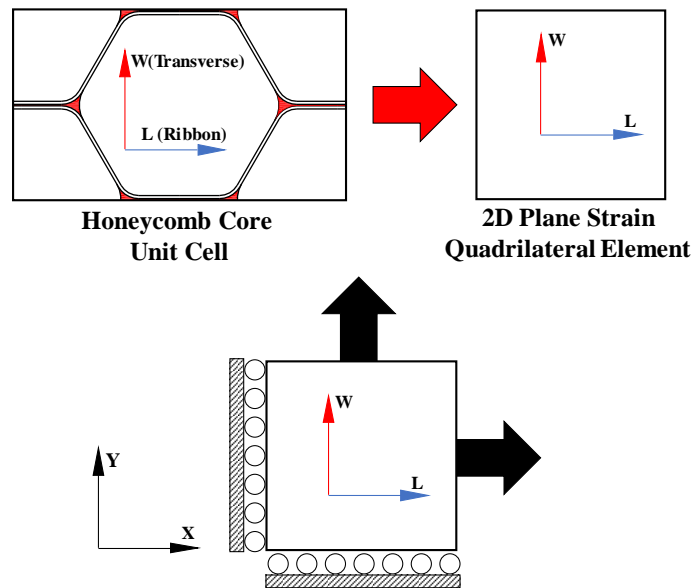


Figure 6-9. Schematic model of the homogenized unit cell of hexagonal honeycomb core along with boundary conditions used in FEA for elementary axial simulations.

Due to both geometric and material nonlinearities associated with the large deformation and hyperelastic material model, a nonlinear analysis using the large strain option based on “*Total Lagrangian*” framework [31] was used. This enables the program to compute the second *Piola-Kirchhoff* stress (S_{ij}) and *Green-Lagrange* strain (E_{ij}) tensor components, which are obtained based on the initial principal material directions defined in the reference (undeformed) configuration for

each element. The Newton-Raphson iterative solution procedure along with the Direct Multifrontal Sparse Matrix solver was chosen for the analysis [31]. Loadings (displacement control) were applied over 100 equal increments to facilitate the nonlinear analysis.

In the user subroutine, the *Green-Lagrange* strain components are the input variables that are updated internally by the MSC Marc program. The *Green-Lagrange* strain tensor components can be given in terms of the right *Cauchy-Green* deformation tensor as

$$E = \frac{1}{2}(C - I) \quad (6.47)$$

The relationship between the normal components of the *Green-Lagrange* strain tensor and the engineering strain can also be written as

$$E_{ii} = \varepsilon_{ii} + 0.5\varepsilon_{ii}^2 \quad (6.48)$$

Therefore, components of the right *Cauchy-Green* deformation tensor can be easily obtained by using equation (6.47) in the subroutine. Because the right *Cauchy-Green* deformation tensor is automatically rotated in the principal coordinate system by the program, the invariants in equation (6.19) can be computed by assigning the unit vectors $n_1 = (1,0,0)$, $n_2 = (0,1,0)$ and $n_3 = (0,0,1)$ and defining the structural tensors in equation (6.12) as

$$N_1 = n_1 \otimes n_1 = \begin{bmatrix} 1 & 0 & 0 \\ 0 & 0 & 0 \\ 0 & 0 & 0 \end{bmatrix}, \quad N_2 = n_2 \otimes n_2 = \begin{bmatrix} 0 & 0 & 0 \\ 0 & 1 & 0 \\ 0 & 0 & 0 \end{bmatrix}, \quad N_3 = n_3 \otimes n_3 = \begin{bmatrix} 0 & 0 & 0 \\ 0 & 0 & 0 \\ 0 & 0 & 1 \end{bmatrix}$$

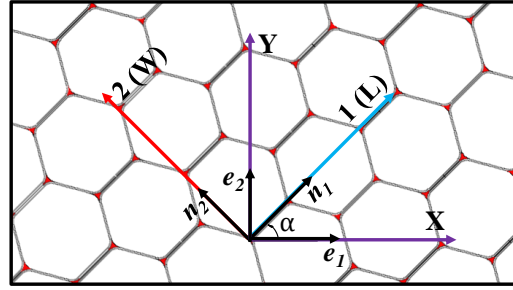
$$I_i = C_{ii} \quad (6.49)$$

$$J_i = C_{kk}C_{jj} - C_{kj}^2, \quad i \neq j \neq k = 1, 2, 3$$

$$III_C = C_{11}C_{22}C_{33} - C_{11}C_{23}^2 - C_{33}C_{12}^2 - C_{22}C_{13}^2 + 2C_{12}C_{13}C_{23}$$

To provide the better understanding of the difference between structural tensor formulations for hexagonal honeycomb cores with different cell orientations, they are also defined

for a hexagonal honeycomb core whose initial principal directions are oriented at an angle α , as illustrated in Figure 6-10.



$$\begin{aligned} n_1 &= (\cos \alpha, \sin \alpha, 0) \\ n_2 &= (-\sin \alpha, \cos \alpha, 0) \\ N_{ij} &= n_i \otimes n_j \end{aligned}$$

$$\begin{aligned} N_1 &= \begin{bmatrix} \cos^2 \alpha & \cos \alpha \sin \alpha & 0 \\ \cos \alpha \sin \alpha & \sin^2 \alpha & 0 \\ 0 & 0 & 0 \end{bmatrix} e_i \otimes e_j \\ N_2 &= \begin{bmatrix} \sin^2 \alpha & -\cos \alpha \sin \alpha & 0 \\ -\cos \alpha \sin \alpha & \cos^2 \alpha & 0 \\ 0 & 0 & 0 \end{bmatrix} e_i \otimes e_j \end{aligned}$$

Figure 6-10. Definition of structural tensors for characterizing the principal material directions of hexagonal honeycomb cores oriented at an angle α to the X direction.

As discussed previously, under in-plane loadings, out-of-plane (W-T, W-L) Poisson's contraction effects for honeycomb cores are zero, resulting in $C_{33} = I$ and $C_{13} = C_{23} = 0$. Therefore, in view of equations (6.22), (6.35) and (6.38) as well as the assumption of decoupled in-plane normal and shear deformations, the SEDF for in-plane responses of the HRP-honeycomb core can be written as follows:

$$W(C_{11}, C_{22}) = \frac{1}{4} \sum_{r=1}^n \mu_r \left\{ \frac{1}{\alpha_r} \left[\left(C_{11} \frac{1 + (4 \cos^2 \theta - 2)v_1^{(r)} + v_3^{(r)}}{2} + C_{22} \frac{1 + (4 \sin^2 \theta - 2)v_1^{(r)} - v_3^{(r)}}{2} \right)^{\alpha_r} - 1 \right] + \frac{1}{\beta_r} \left[\left(C_{22} \frac{1 + (4 \cos^2 \theta - 2)v_1^{(r)} + v_3^{(r)}}{2} + C_{11} \frac{1 + (4 \sin^2 \theta - 2)v_1^{(r)} - v_3^{(r)}}{2} \right)^{\beta_r} - 1 \right] - \ln(C_{11} C_{22}) \right\} \quad (6.50)$$

$$0 \leq v_1^{(r)}, v_3^{(r)} \leq 1, \quad \mu_r \geq 0, \quad \alpha_r \geq 1, \quad \beta_r \geq 1, \quad r = 1, 2, \dots, n$$

As can be seen in equation (6.50), the hyperelastic SEDF in the subroutine was only adopted for capturing the normal deformations of the core along its principal directions by imposing $C_{12} = 0$ and neglecting the contribution of shear deformation. Consequently, the second *Piola-Kirchhoff* stress and tangent stiffness tensors can be easily calculated by using equations (6.5) and (6.6).

By assigning the initial orientation vectors to the element (for ribbon and transverse directions), which were defined parallel to the analysis coordinate system (X, Y) in the FEA program, as illustrated in Figure 6-9, subroutine computes the material stiffness matrix components and updates the stress components in the local material coordinate system. Based on the deformed state, the orientations of the material directions are also updated during each load increment of the analysis. Not that, in the user-subroutine, $D_{1212} = \bar{G}_{12}$ (effective shear modulus of the core predicted by FEM of the core RVE) is employed which results in a linear in-plane shear stress-strain relation at any stage of deformation.

A three-dimensional model using a solid element can also be obtained by decoupling the in-plane and out-of-plane components of the tangent stiffness tensor, which leads to $D_{1133}=D_{3311}=D_{2233}=D_{3322}=0$. Also, D_{3333} , D_{3131} , and D_{2323} may be calculated using either the out-of-plane elastic constants of the core reported in the literature [1, 3, 4] or the values predicted by the FEM of the core RVE. The process of implementing the user-subroutine and conducting the analysis by MSC Marc FEA program is summarized in the flowchart shown in Figure 6-11. The source code of the subroutine is also presented in Appendix A.

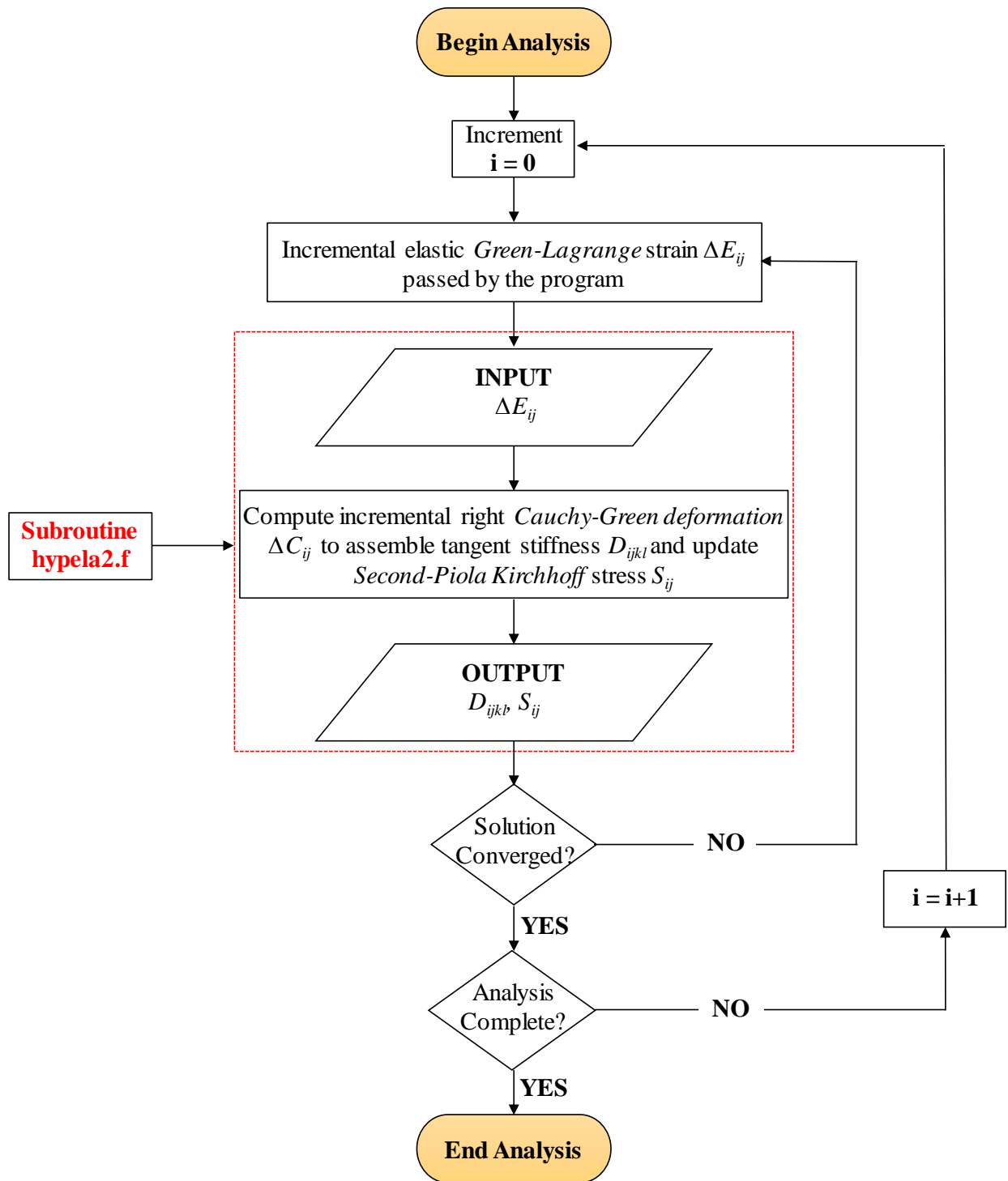


Figure 6-11. Summary of finite element analysis using hyperelastic constitutive model implemented by means of user-subroutine in MSC Marc program.

6.5 Result and Discussion

6.5.1 Single Element Finite Element Analysis

The engineering stress-strain plots obtained from FEA on a single element using the hyperelastic material model for in-plane uniaxial loadings along the ribbon and transverse directions are shown in Figure 6-12. The predictions are compared with the test data for the HRP-fiberglass/phenolic honeycomb core. The Poisson effects and strain energy densities are also compared in the same figure. Based on these figures, a good agreement can be seen between the FEA simulation results and the experimental data.

The material parameters in the hyperelastic model in this research were obtained based on curve fitting the effective stress-strain curves predicted by the FEM of the core RVE. As discussed in chapter 5, due to the overly constrained core RVE in FEA, the softening behavior of the core in the compressive test along the ribbon direction observed in the experiment was not captured by the FEM. This discrepancy can also be seen in the FEA simulation results of the single element shown in Figure 6-12 (a). In order to address this problem, the imperfections leading to shear instability observed in the experiments must be incorporated in the FEM of the core RVE as part of future work.

In order to show the effectiveness of the hyperelastic model to capture the in-plane responses of the HRP-honeycomb core, the results obtained from the single element FEA using the hyperelastic material model are also compared with the single element FEA with orthotropic material model, as presented in Figure 6-12. Note that, the orthotropic elastic constants were determined using the FEM of the core RVE at infinitesimal strain. It is evident that, the linear orthotropic constitutive model cannot capture the in-plane, uniaxial behavior of the honeycomb core at higher strain levels.

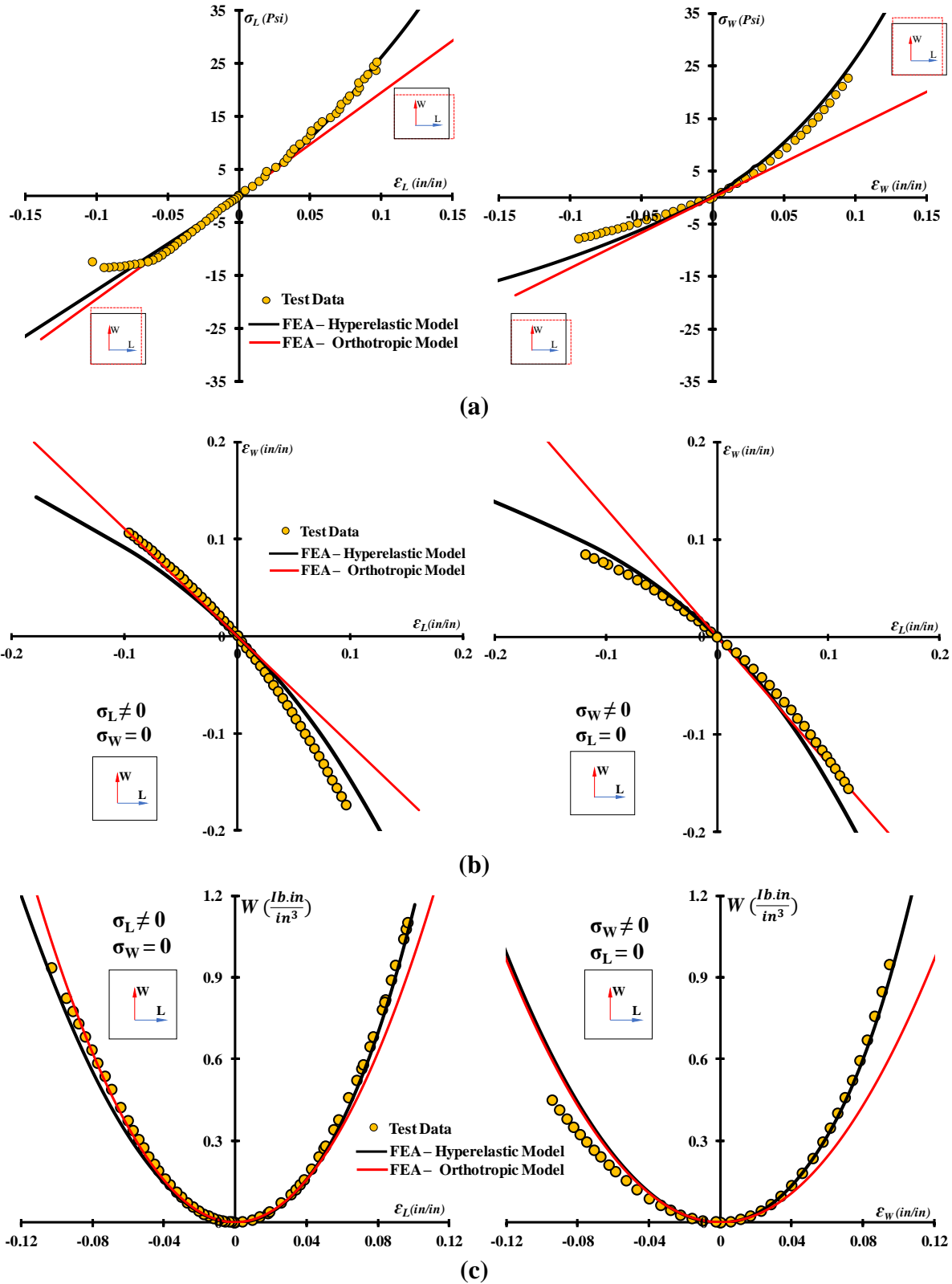


Figure 6-12 (a) Engineering stress-strain curves, (b) Poisson's effects, and (c) strain energy densities predicted by FEM using hyperelastic material model and comparison with test data and FEM using orthotropic material model.

To further strengthen the validation process, the single-element FEM was used for simulations of the core behavior under equi-biaxial tension and compression loading cases under force control boundary conditions. Figure 6-13 shows predictions of the single-element FEM and comparison with the results predicted by the FEM of the core RVE. It can be seen that, the single-element FEM predictions with the hyperelastic material model are in good agreement with results predicted by the micromechanics model.

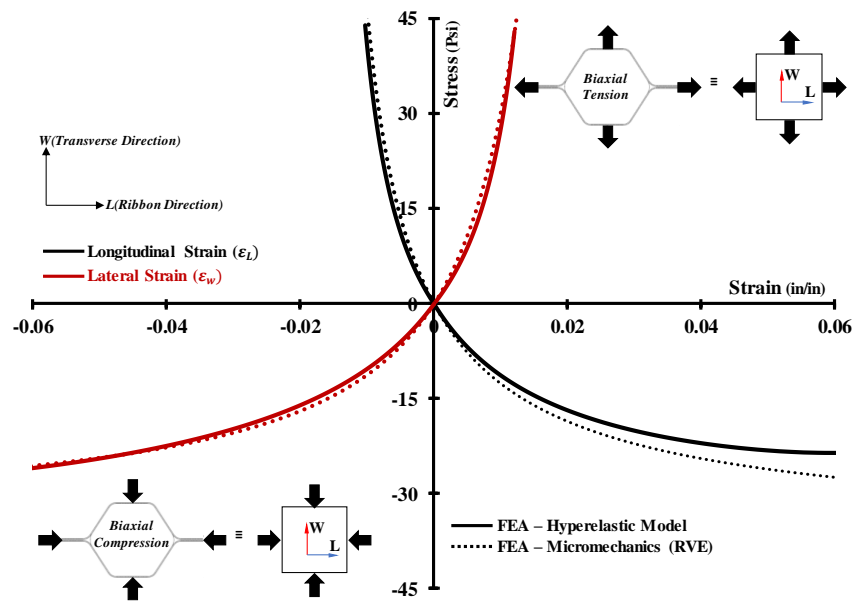


Figure 6-13. Equi-biaxial tension and compression predicted by FEM using hyperelastic material model and comparison with FEM of core RVE.

As observed in this section, the single element FEA was able to capture the mechanical responses of the honeycomb core under simple states of loading. However, for complex loading scenarios such as analysis of the core behavior under general in-plane/transverse flexure, the bulk honeycomb core must be modelled, which will be discussed in the following section.

6.5.2 Full Scale Honeycomb Core Finite Element Analysis

In order to evaluate the effectiveness of the hyperelastic model and further strengthen the validation process, it is necessary to simulate a bulk honeycomb core in a finite element program using solid or planer elements under complex loading and boundary conditions such as simulation of in-plane flexure. For these loading scenarios, the honeycomb core cells will be subjected to a multiaxial state of stress during the deformation process and therefore, the performance of the hyperelastic material model can be assessed.

In this study, the hyperelastic material model is used for nonlinear finite element analysis (FEA) simulations of the bulk HRP-fiberglass/phenolic honeycomb core using planer elements under in-plane pure shear and flexural loadings by simulating the picture-frame pure shear and in-plane cantilever bending tests discussed in chapter 4. The details of the simulations and some key observations are enumerated in the following sections.

6.5.2.1 FEA Simulations of Picture-Frame Pure Shear Tests

As discussed in chapter 4, the picture-frame shear-fixture was used to study the behavior of HRP-fiberglass/phenolic honeycomb core under large pure-shear and biaxial (off-axis pure shear) loadings in (L-W) plane by mounting the honeycomb core specimens in the fixture with two different cell configurations, as illustrated in Figure 4-6 and Figure 4-20, respectively.

Based on the experimental observation using DIC methods for the in-plane pure shear response of the HRP-honeycomb core, it was concluded that the picture-frame pure shear testing of the core should be considered as a structural test and not a material characterization test. Using the FEM of the core RVE, the in-plane shear behavior of the core is predicted to be linear, therefore, the linear effective constitutive model was employed for the HRP-honeycomb core in the homogenization analysis. However, the global response of the picture-frame pure shear test

was observed to be nonlinear particularly at higher load levels which was attributed to the fixture effects and the test set up. In fact, based on the DIC analysis, except the small central area of the core, the state of strain was not pure shear throughout the core specimen.

In this section the pure-shear tests in (L-W) and (X-Y) planes using the picture – frame fixture are simulated to further validate the hyperelastic material model and support the assumption of decoupled and linear in-plane shear constitutive model. For simulations of the above-mentioned tests in a FEA program, both the fixture and honeycomb core were modeled to capture the total response of the test including the fixture effect and honeycomb core behavior. Figure 6-14 shows the schematic of the finite element model of the picture-frame pure shear test performed in the MSC Marc FEA program.

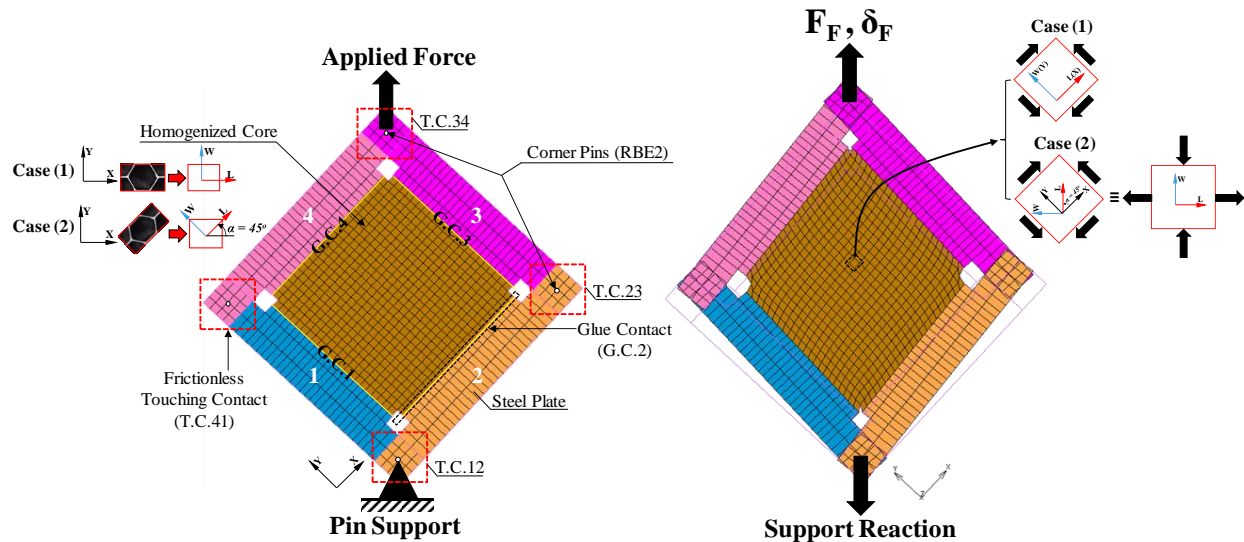


Figure 6-14. Geometry and boundary conditions along with the material orientations setup used for FEA simulations of in-plane (L-W) and off-axis (X-Y) pure shear tests.

The model was assembled using 572 and 384 elements for modeling the honeycomb core specimen and fixture, respectively. The four-node isoparametric arbitrary quadrilateral elements (element 115 in MSC Marc [61]) written for plane strain applications using reduced integration feature were used for this purpose. This element uses an assumed strain formulation written in

natural coordinates which insures good representation of the shear strains in the element [61]. The dimensions of the test specimens and the fixture are the same as those used in the experiments shown in Figure 4-5 and Figure 4-21. For modeling the picture-frame fixture, the four legs of the frame were modeled using the material properties of Steel [74] and the frictionless touching contacts (T.C.) [31] were prescribed between the each two interfacing surfaces, as depicted in Figure 6-14. Then, four pin-joints were assumed at the junction of each two legs by using RBE2 [31] links for simulating the corner pins. The honeycomb core was modeled using the hyperelastic martial model described in the previous section. The segment-to-segment glue contact constrains [31] were then defined between the honeycomb core edges and the frame legs. A nonlinear analysis using the large strain option based on “Total Lagrangian” framework [31] was used. The loadings (displacement control) were applied over 100 equal increments to facilitate the nonlinear analysis.

As illustrated in Figure 6-14, each quadrilateral element of the homogenized honeycomb core in the FEM represents the unit cell of the real core geometry. To simulate the pure shear test in (L-W) plane, the initial orientation vectors for the elements (for ribbon (L) and transverse (W) directions) were defined parallel to the global coordinate system (X,Y) in the FEA program, as shown by Case (1) in the figure. Similarly, for simulation of the pure shear test in (X-Y) plane (off-axis pure shear test), which results in biaxial deformation in (L-W) plane, initial material orientations were defined at 45 degree to the global coordinates, as shown by Case (2) in the same figure. The deformed state of the pure shear test simulation and the expected strain field on a single element of the honeycomb core in the core center are also shown in Figure 6-14.

The force versus displacement plot predicted by the FEM for pure shear simulation in (L-W) plane (Case (1)) is compared with experimental data in Figure 6-15. As shown in the figure, the FEA prediction is in very good agreement with test data. To emphasize the effectiveness of the

hyperelastic constitutive model, FEA prediction with orthotropic material model is also depicted in the same figure. It is evident that the linear orthotropic constitutive model cannot capture the global response of the core with increasing deformations.

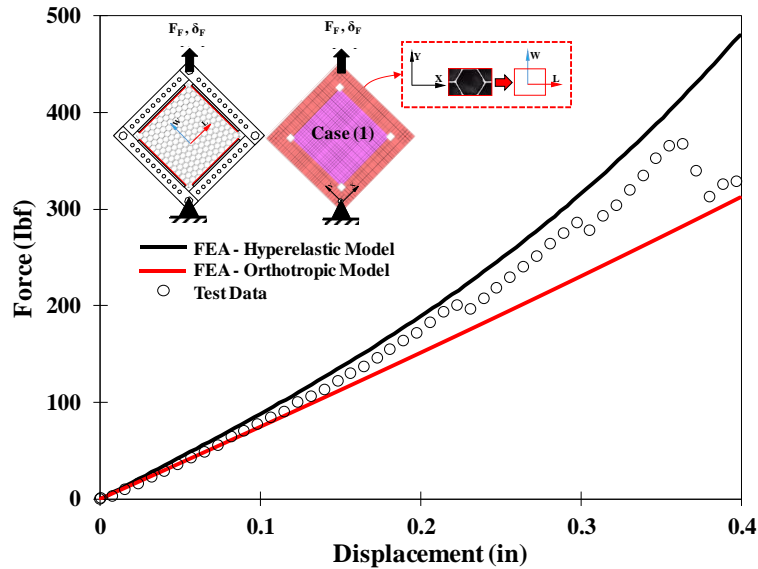


Figure 6-15. Global load-displacement diagrams predicted by FEMs and comparison with test data for pure shear deformation in (L-W) plane.

Figure 6-16 shows the contour plots of in-plane *Green-Lagrange* strains predicted by the FEM using the hyperelastic material model at the onset of the core failure corresponding to the axial load (F_F) of 365 Ibf.

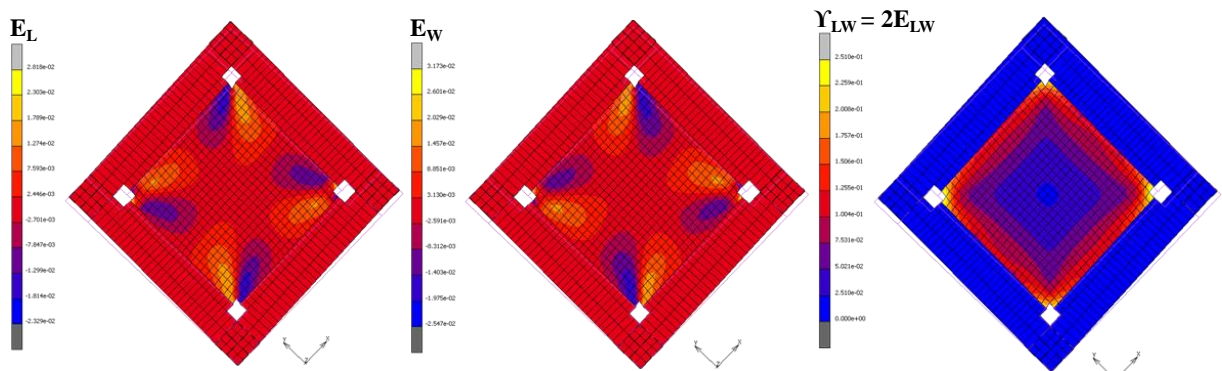


Figure 6-16. In-plane *Green-Lagrange* strains contours predicted by the FEM at the onset of the core failure.

It can be observed that FEM contours shown in Figure 6-16 look qualitatively similar to the DIC contours shown in Figure 4-13. As depicted in the figure, except the central region of the core, the distribution of shear strain is not uniform throughout the core particularly in the immediate vicinity of the edges due to the predefined glue contact constraints. It is evident from the FEM predictions that the magnitude of normal strains are negligible in comparison with the shear strain. However, the regions of large strain concentration at the corners are seen.

Figure 6-17 shows in-plane shear strain profiles along the sketched paths at different load stages predicted by the FEM and comparison with test data (DIC analysis) explained in chapter 4. As can be seen from the figure, except in the immediate vicinity of the edges there is a reasonable agreement between the FEM predictions and test data. The average magnitudes¹ of the longitudinal strains are approximately zero along the paths, as depicted in the same figure.

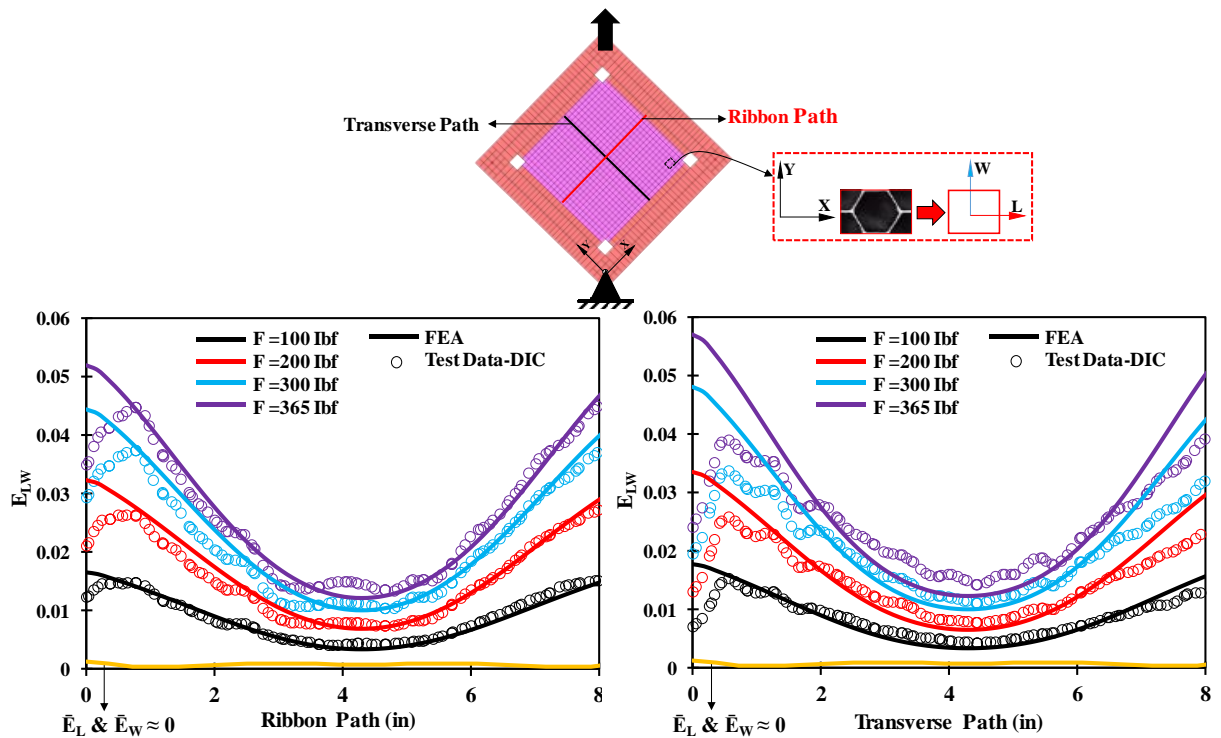


Figure 6-17. Shear strain profiles along the two predefined paths obtained from FEM at different load stages and comparison with test data (DIC).

¹ Average of the four strains predicted by FEA at the four load stages.

The axial force - displacement curve predicted by the FEM for pure shear simulation in (X-Y) plane (Case (2)) or off-axis pure shear simulation is compared with test data in Figure 6-18.

The prediction is in reasonable agreement with test data.

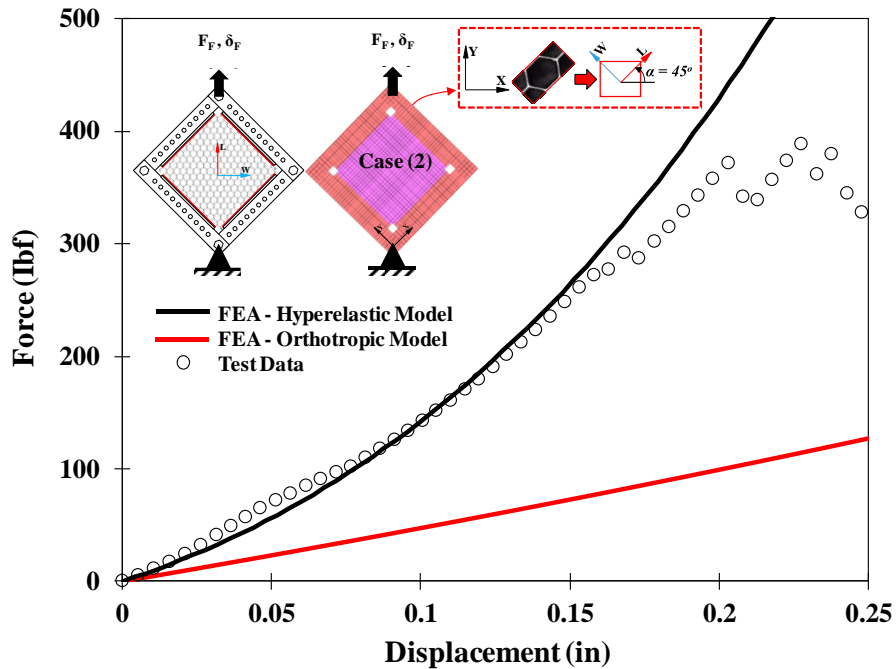


Figure 6-18. Global load-displacement diagrams predicted by FEMs and comparison with test data for pure shear deformation in (X-Y) plane.

As illustrated in Figure 6-18, there is a significant difference between the results obtained from FEMs using the orthotropic and hyperelastic material models. For pure shear in (X-Y) plane, honeycomb core cells (each element in the FEM) experience large deformations along the principle axis L and W, as depicted in Figure 6-14. With increasing deformations, the tangent moduli of the core which depends on the deformed state of the core must be updated which cannot be captured by the orthotropic material model.

The contour plots of in-plane *Green-Lagrange* strains predicted by the FEM using the hyperelastic material model at the onset of the core failure corresponding to the axial load (F_F) of 367 lbf, are illustrated in Figure 6-19. Similar to the DIC contours shown in Figure 4-23, the high strain gradients are seen at the corners and along the glued contact edges. The magnitude of shear strain in the material coordinate system (L-W) is negligible throughout the specimen. The uniform distribution of the longitudinal strains are also observed in the central region of the core.

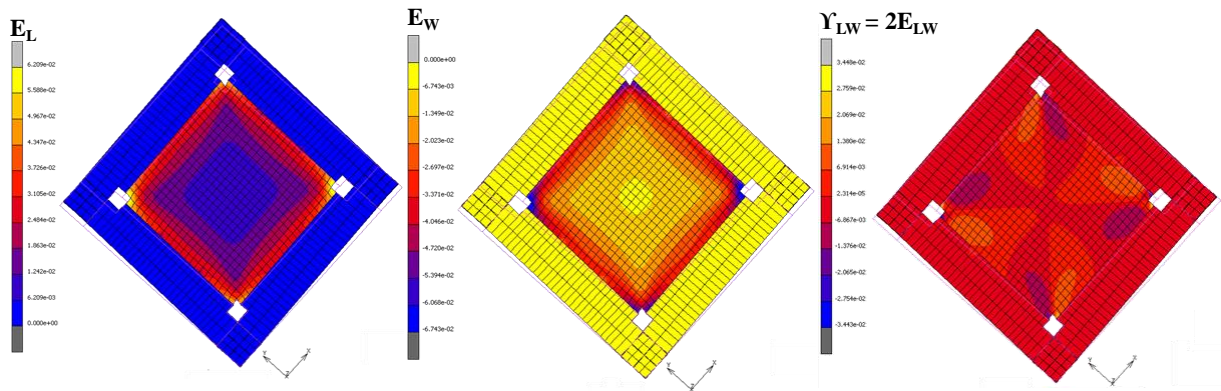


Figure 6-19. In-plane *Green-Lagrange* strains contours predicted by the FEM at the onset of the core failure.

Figure 6-20 shows variation of longitudinal strains (E_L and E_W) along the sketched ribbon and transverse paths at four load levels. It can be observed from the plots that the longitudinal strains are maximum around the corners and then tend to decrease as moving towards honeycomb core center. As presented in the same figure, the average magnitude of shear strain is distributed about zero along both paths. A reasonable agreement between the predicted results by the FEM and the experimental data can be seen. Although discrepancies are seen between the FEM predictions and the test data particularly at the higher load levels, the longitudinal strains distributions from both methods have a similar trend.

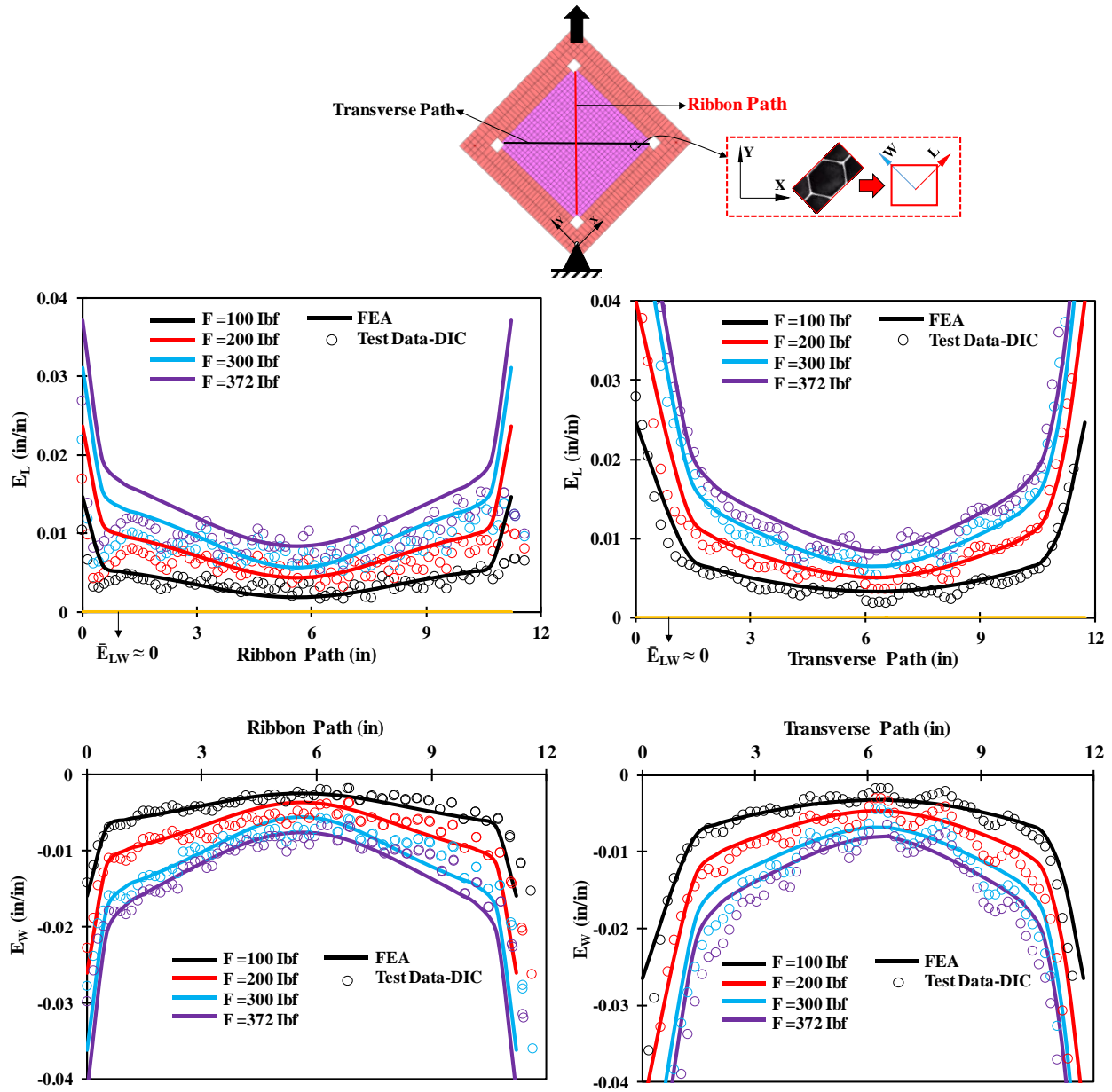


Figure 6-20. Longitudinal strains profiles along the two predefined paths obtained from FEM at different load stages and comparison with test data (DIC).

Based on the FEA predictions for the pure shear test in (L-W) and (X-Y) planes which are in good agreement with test data, not only the developed hyperelastic constitutive model is validated, but also, the assumptions of linear and decoupled constitutive model for in-plane shear response of the HRP-honeycomb core, which have been made for implementing the model in FEA program, are justified. To further strengthen the aforementioned assumptions, the linear expression

for the in-plane shear modulus of the honeycomb core given in equation (4.4) was considered for D_{1212} component of the stiffness tensor in the user subroutine. Therefore, the tangent stiffness for describing the in-plane shear constitutive relation increases linearly as deformation increases. As illustrated in Figure 6-21, for global pure shear response of the HRP-honeycomb core in (L-W) plane, with increasing deformation, a stiffer response (compared to the test data and FEM with constant shear modulus) is predicted by FEM with a variable shear modulus which supports assumption of the constant shear modulus for the HRP-honeycomb core. Moreover, for global pure shear response of the HRP-honeycomb core in (X-Y) plane which is dominated by bi-axial deformation of the cell walls in (L-W) plane, the increased shear stiffness does not have any influence on the global response of the core which justifies the assumption of the decoupled normal and shear constitutive models in (L-W) plane.

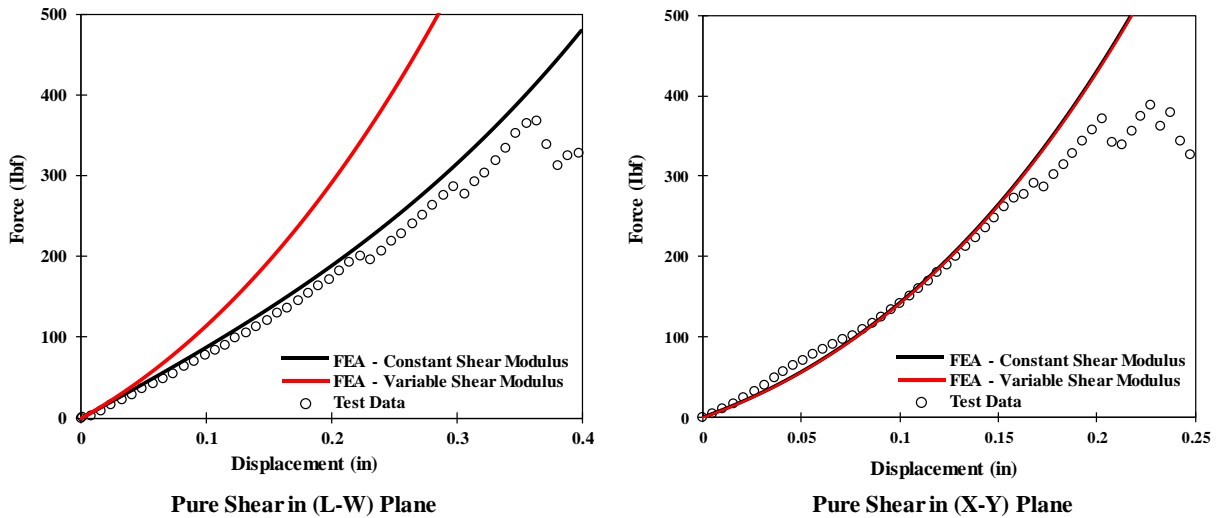


Figure 6-21. FEA predictions with constant and variable shear modulus and comparison with test data for HRP-honeycomb core.

6.5.2.2 FEA Simulations of In-Plane Flexure Tests

The in-plane (L-W) flexure tests conducted using the cantilever HRP-fiberglass/phenolic honeycomb beams were simulated to further validate the hyperelastic material model. Under flexure, the cells on the tension and compression sides deform differently and thus exhibit different elastic behaviors. Therefore, the hyperelastic material model should be able to capture the deformation-dependent elastic properties to simulate the flexure behavior accurately, which will be evaluated in this section.

Figure 6-22 shows the finite element model of the in-plane cantilever-honeycomb beams. The figure also includes the boundary conditions and the coordinate systems used to define the core cell orientations. The dimensions of the test specimens are the same as those used in the experiments shown in Figure 4-27. The specimens were idealized by 4-noded 2D elements under plane strain condition (Marc element 115 [61]). The number of elements used to model the homogenized honeycomb core specimens are also shown in the same figure.

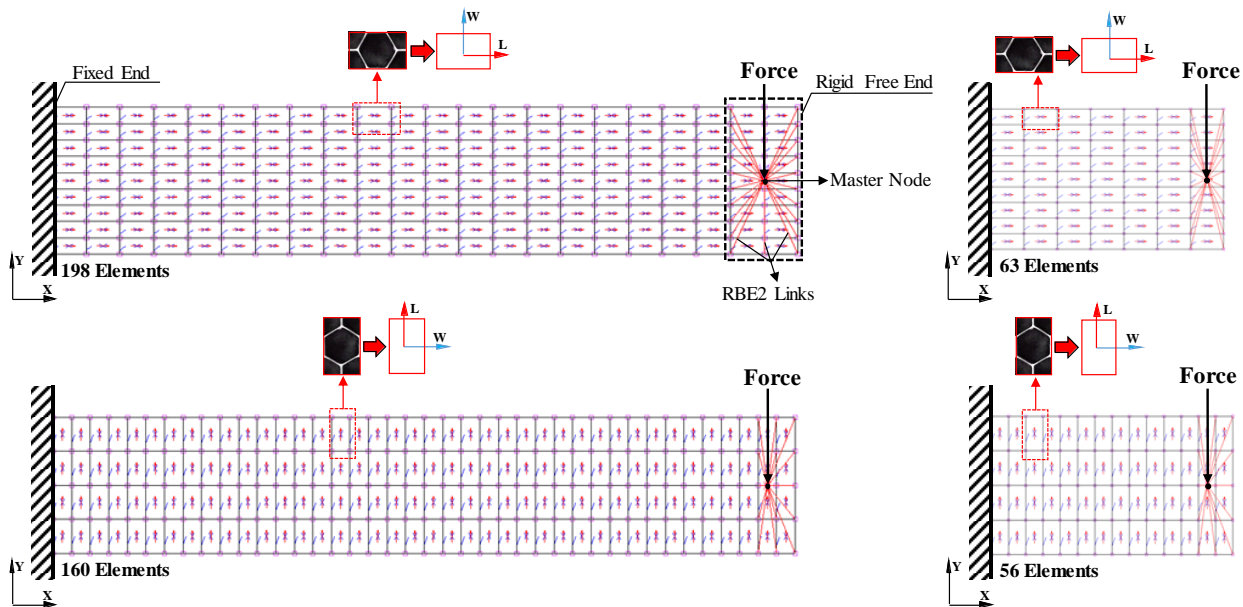


Figure 6-22. Finite element models of the in-plane cantilever-honeycomb beam tests.

As illustrated in Figure 6-22, each element represents a single unit cell of the honeycomb core specimen; the principal material directions (the initial orientation vectors (L, W)) for the elements were defined based on the orientations of the honeycomb core cells (for ribbon and transverse directions) in each test. Similar to the experiment, the flexure deformation was induced by applying an end rotation on a master node at the free end. To create a rigid-free end (resin filled cells in the experiments) and applying an end rotation, the free end edge of the each FEM was forced to rotate as a rigid plane by using RBE2 [31] links between the predefined master node and the nodes forming the free end edge, as depicted in Figure 6-22.

A large strain, nonlinear (geometric and material nonlinearities) finite element analysis based on “Total Lagrangian” framework [31] was conducted in the MSC Marc program. The loadings (force control) were applied over 100 equal increments to facilitate the nonlinear analysis.

Figure 6-23 shows the deformed configuration of the honeycomb core beams (short and long beams with different cell orientations) undergoing flexure in the (L-W).

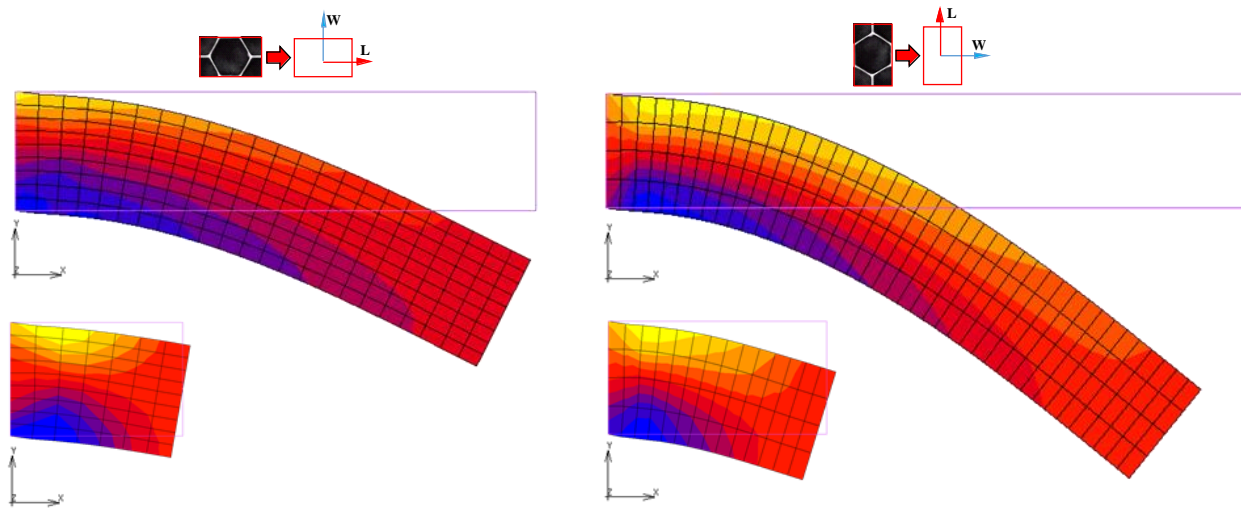


Figure 6-23. Deformed configuration of the honeycomb core beams under flexure in (L-W) plane with different cell orientation vectors for ribbon (L) and transverse (W) directions.

Under flexure, the material orientations change with deformations and the tangent stiffness must be defined in the rotated coordinate system. The orientation of the ribbon (L) and transverse (W) directions in the initial and deformed states are illustrated in Figure 6-24. The deformation produces changes in material orientations which are captured by the hyperelastic model.

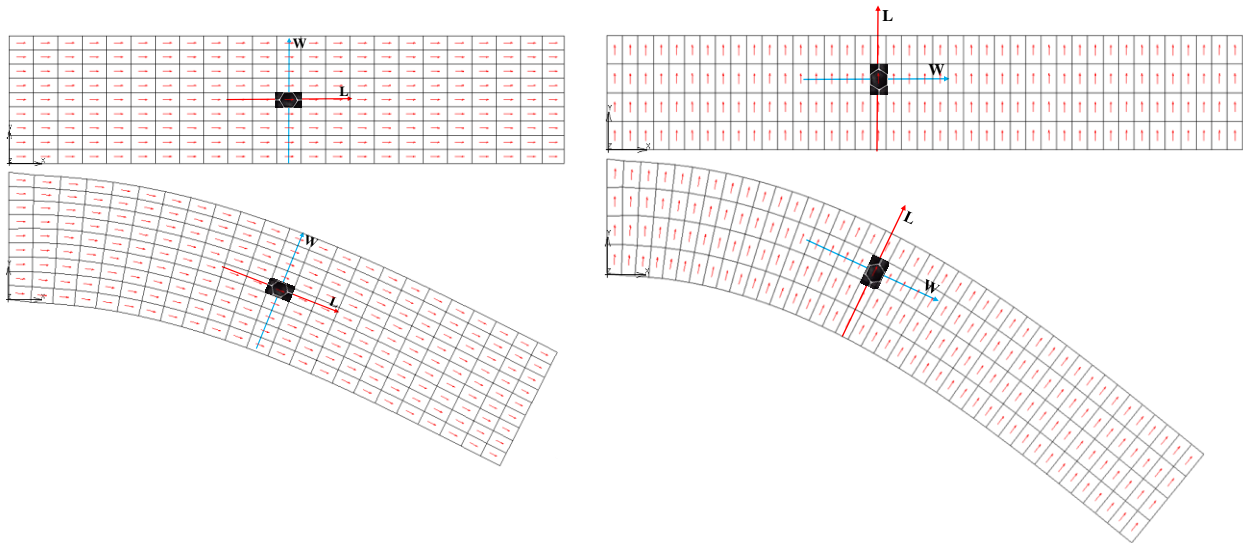
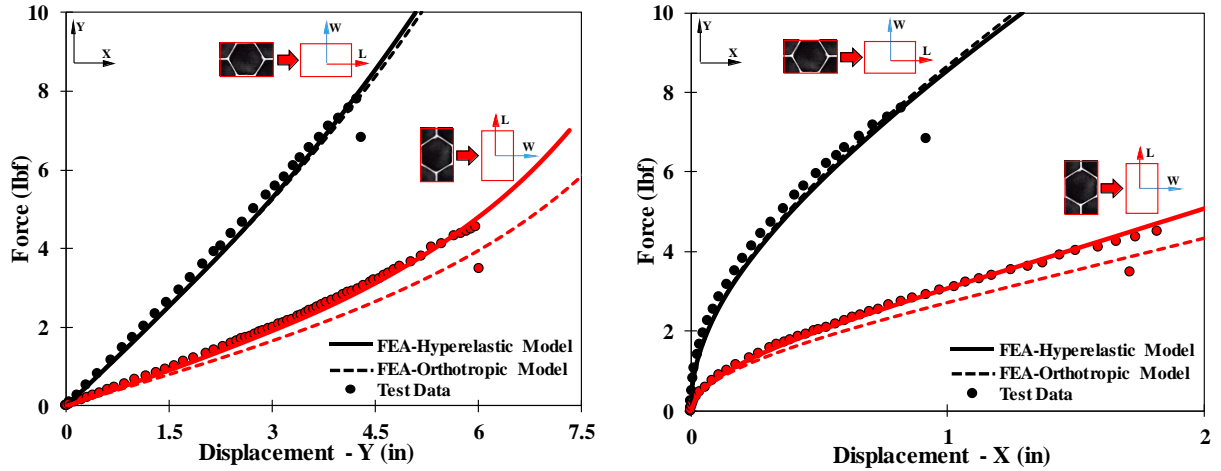
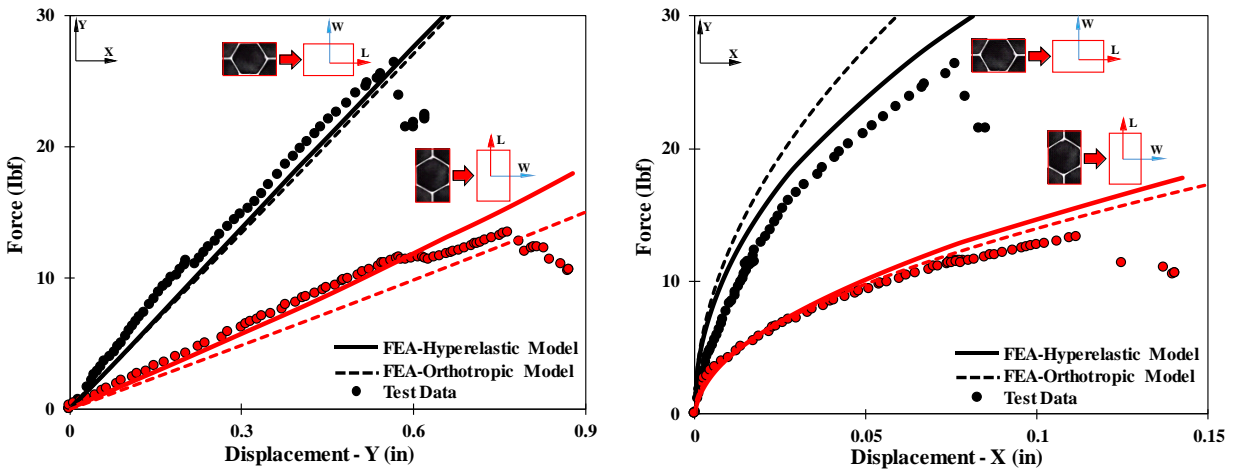


Figure 6-24. Principal material (L, W) orientations for the initial and deformed configurations of cantilever honeycomb beams.

The force -displacement diagrams predicted by the FEM for cantilever bending simulations in (L-W) plane and comparison with the test data for HRP-fiberglass/phenolic honeycomb cores, described in chapter 4, are shown in Figure 6-25. As shown in the figure, the FEA predictions show very good agreement with test data. The flexural responses are much stiffer for the cores with the material orientation vectors (L, W) parallel to the global coordinates (X,Y); this is due to the stiffer response of the HRP-honeycomb core in the ribbon direction which was observed in the uniaxial tests. As illustrated in Figure 6-25, at higher strain levels, the FEM with the orthotropic material model deviates from the test data, particularly for the honeycomb beams with (W(X)-L(Y)) orientation.



(a) Long cantilever honeycomb beams



(b) Short cantilever honeycomb beams

Figure 6-25. Comparison of load-displacement curves predicted by FEMs of cantilever HRP-fiberglass/phenolic honeycomb beam with test data.

It is evident from Figure 6-25 the horizontal displacements (X) are not negligible and they were captured properly by the FEMs because of the nonlinear analysis chosen to account for the geometric and material nonlinearities associated with large rotation of the honeycomb beams and hyperelastic material model, respectively.

The distributions of in-plane *Green-Lagrange* strains across the width of the long and short honeycomb beams with different cell orientations at various cross sections (C.S) are compared with test data obtained from DIC methods in Figure 6-26 to Figure 6-29. The results are shown for different load levels. A good agreement can be seen between the simulation results and the experimental data. The discrepancy between the results, particularly at cross section (1), can be attributed to distorted images captured by ARAMIS system in the vicinity of the fixed-end of the beams due to fixity of the honeycomb core cells and facet size.

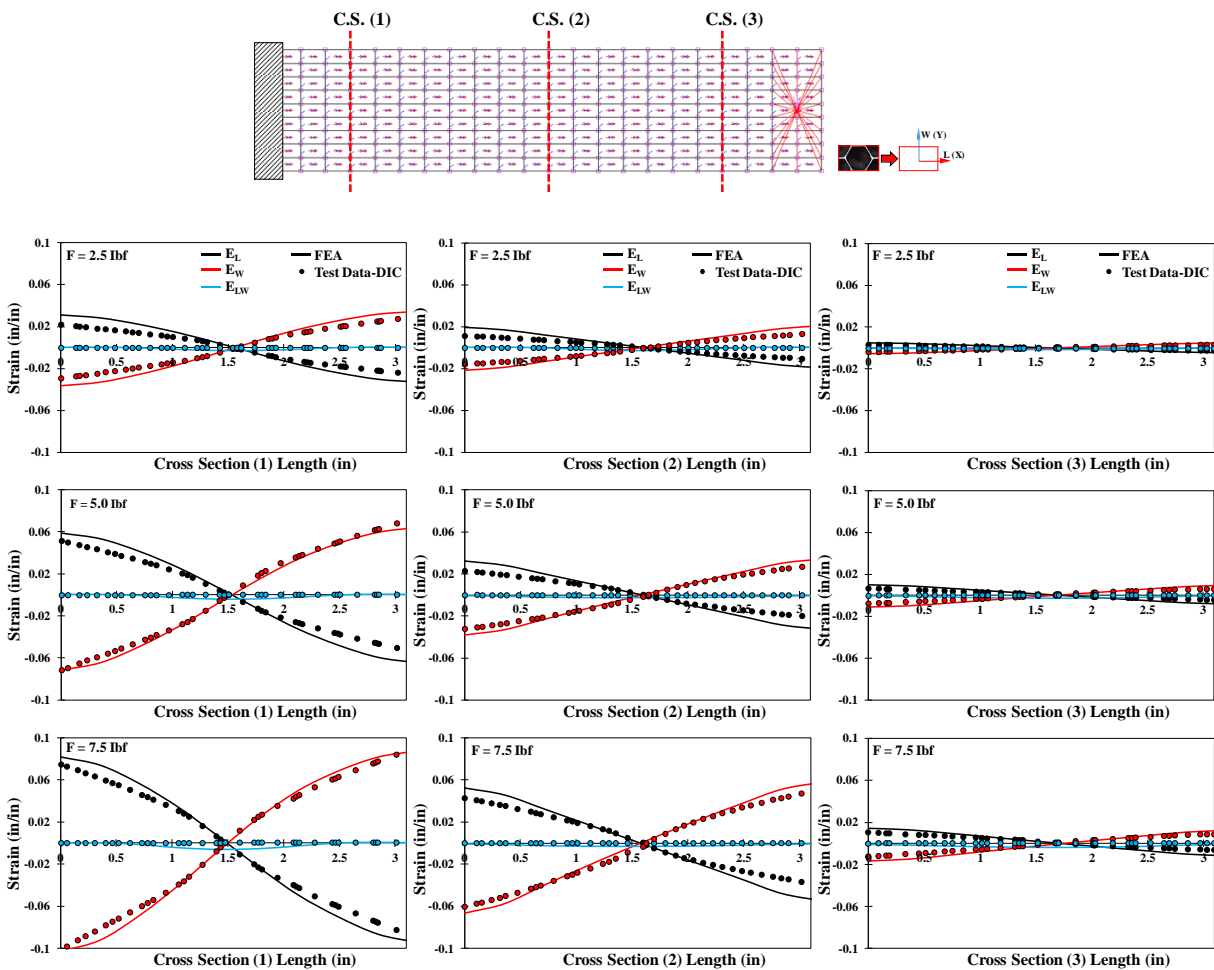


Figure 6-26. Profiles of in-plane strains across the width of the long honeycomb beam with (L(X)-W(Y)) orientation.

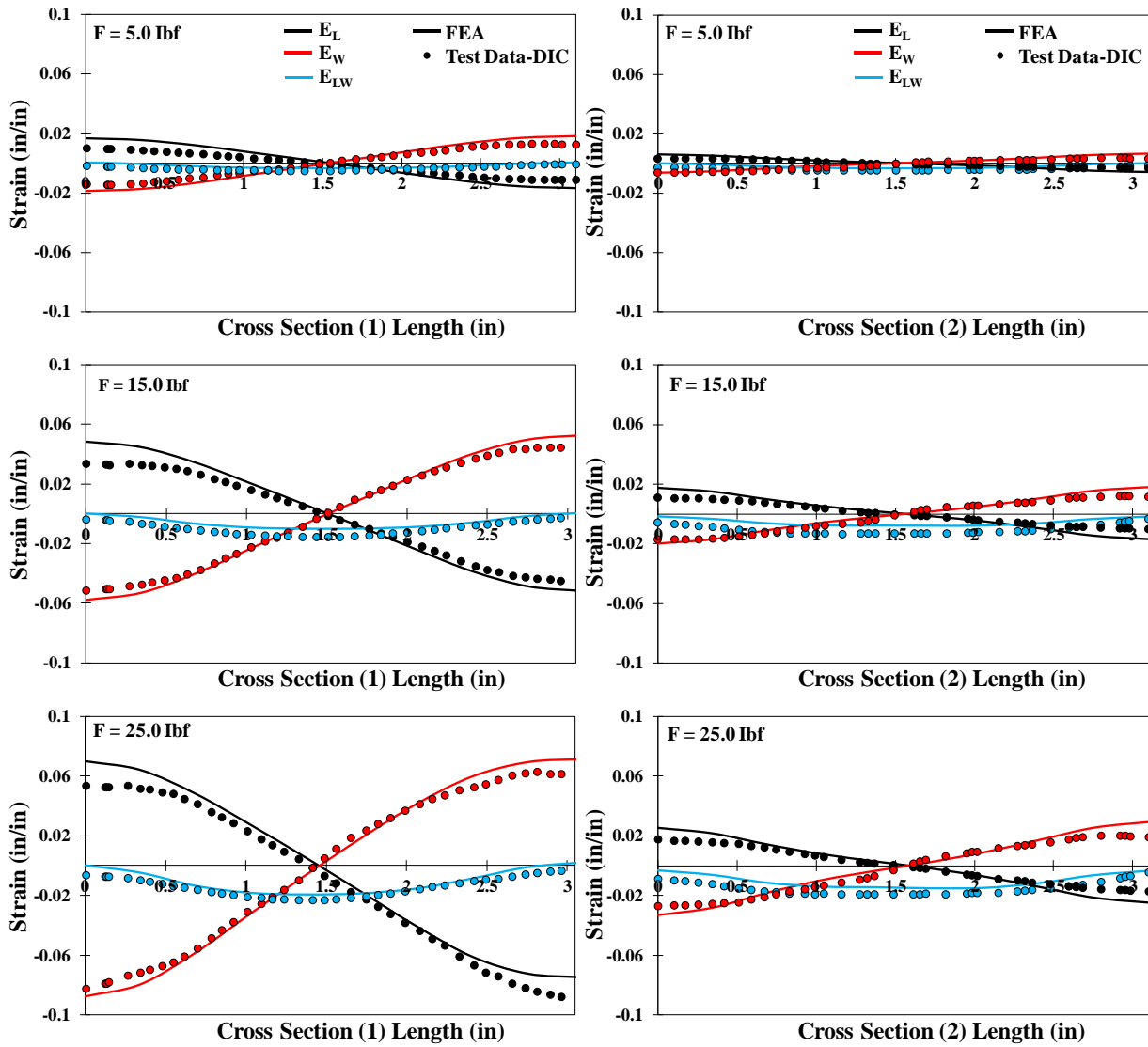
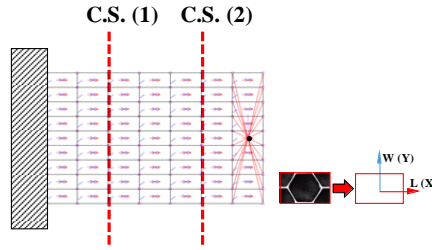


Figure 6-27. Profiles of in-plane strains across the width of the short honeycomb beam with (L (X)-W(Y)) orientation.

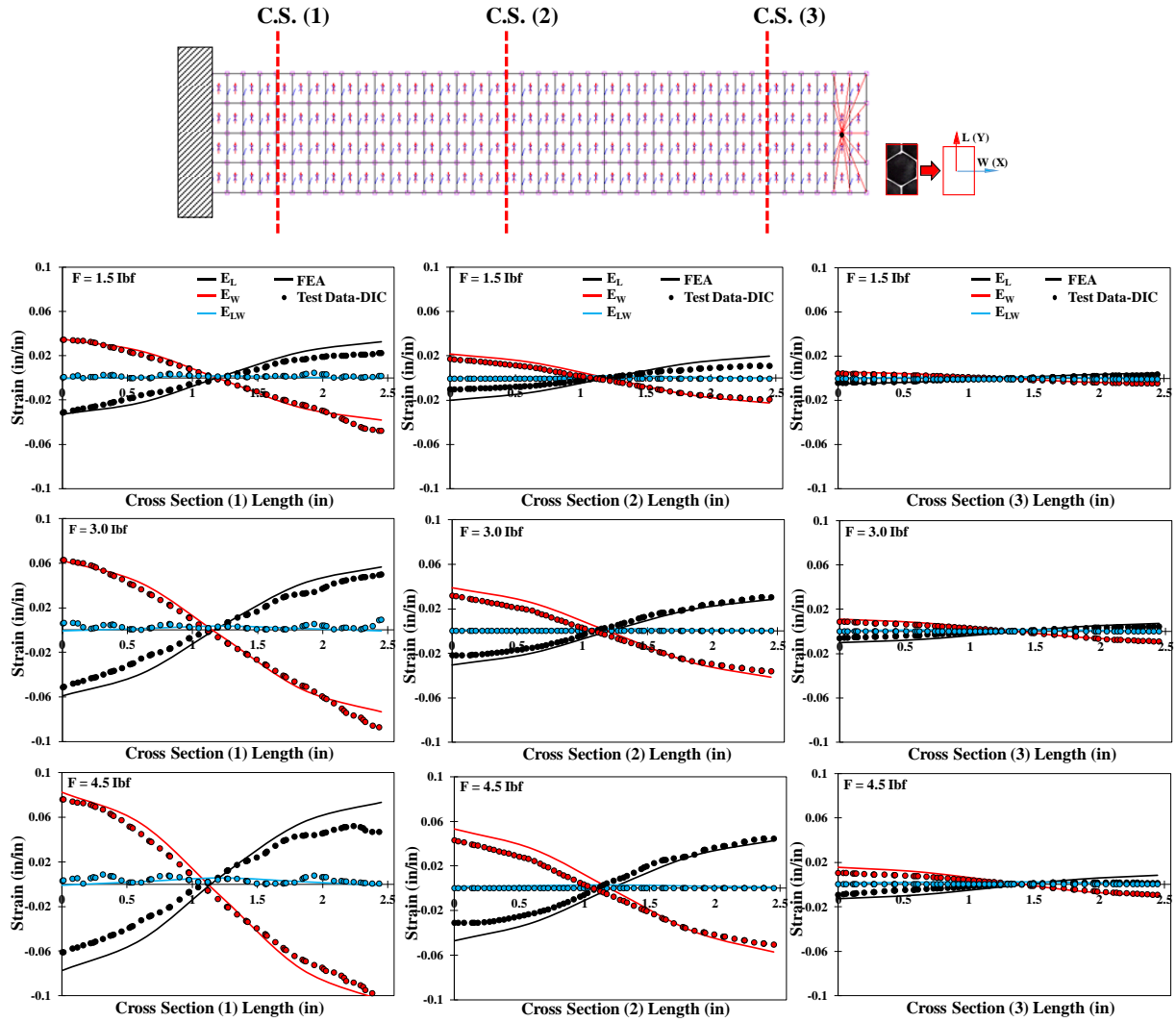


Figure 6-28. Profiles of in-plane strains across the width of the long honeycomb beam with $(W(X)-L(Y))$ orientation.

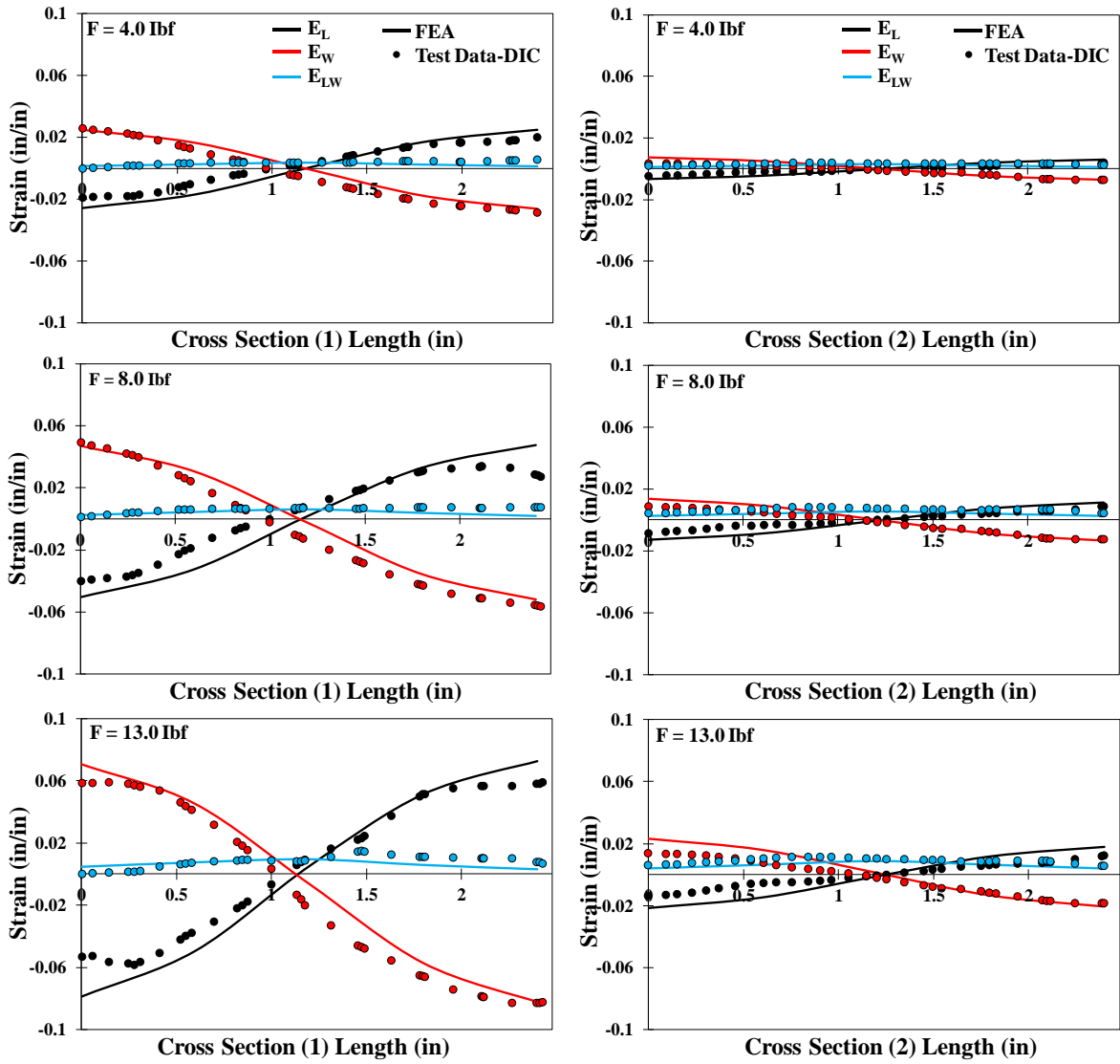
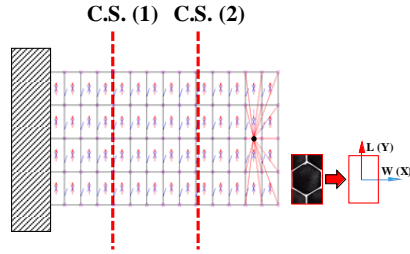


Figure 6-29. Profiles of in-plane strains across the width of the short honeycomb beam with (W (X)-L(Y)) orientation.

As is evident from Figure 6-26 to Figure 6-29, similar to the experimental data, the FEA predictions of the in-plane strains are nonlinear and asymmetric in nature. For example, the normal strains in transverse direction (E_w) on the tension side (top) of the specimen are lower than the compression side (bottom) owing to the lower stiffness under compression, as illustrated in Figure 6-28 and Figure 6-29. The deviation from the test data is more pronounced for compressive strains in ribbon directions (E_L) at higher load levels due to the development of the hyperelastic constitutive model which is not able to capture the softening behavior observed in compressive test in ribbon direction at higher strains.

Based on the results obtained from nonlinear FEA simulations of the homogenized HRP-fiberglass/phenolic honeycomb core using the hyperelastic material model under flexural and pure shear loadings, which compared satisfactorily with test data, it can be concluded the hyperelastic constitutive model and the assumptions which have been made to develop the model are suitable for describing the in-plane nonlinear behavior of the HRP-honeycomb core under large deformations.

The material model can also be employed for FEA simulations of a honeycomb core under transverse flexure such as simulation of four-point-bending test where in a 3D model must be used. As discussed previously, 3D simulations can be easily performed by decoupling the in-plane and out-of-plane constitutive model for the loading scenarios in which the in-plane deformations are dominant. This can be considered for further investigation of this research and showing the capability of the material model.

CHAPTER 7

SUMMARY, CONCLUSIONS AND FUTURE WORK

In this research, a numerical homogenization approach for characterizing the in-plane mechanical responses of nonmetallic honeycomb cores under large deformations has been presented. For this purpose, a commercial adhesively bonded HRP-fiberglass/phenolic hexagonal cell honeycomb core was employed to generate basic material properties and bench mark data required to support and validate the numerical models.

The finite strain in-plane behaviors of the HRP-honeycomb core were characterized by conducting the uniaxial in-plane tension and compression as well as the pure shear tests on the core using custom built fixtures. It was shown that finite deformation, in-plane, uniaxial responses of the core are nonlinear, anisotropic, and fully recoverable (elastic). The nonlinear behavior is attributed to the geometric nonlinearity associated with the large bending-induced deflection of the cell walls. Another unique behavior of the core was its asymmetric response resulted from a stiffening response under tensile-dominated loads and a softening response under compressive-dominated loads.

The in-plane mechanical response of the HRP- honeycomb core subjected to large pure shear deformation was characterized using a custom-built picture-frame shear fixture. Based on the results calculated from kinematic of the fixture, the pure shear response of the core was linear initially with calculation of the relatively high shear modulus. The test data at higher strains was observed to be nonlinear. However, the nonlinearity of the test data was attributed to the shear fixture effects not the honeycomb core behavior. Therefore, the picture-frame pure shear test was considered as a structural test not a material characterization test and it was used for validation of the finite element model of the homogenized core using the developed effective constitutive model by simulating the fixture and bulk core. Digital image correlation (DIC) using ARAMIS system was

also performed to measure in-plane strain and displacement fields throughout the core specimen during the deformation process for evaluation of the FEA simulations of homogenized core using the developed effective constitutive model.

The picture-frame shear fixture was also used to study the behavior of the honeycomb core under bi-axial loading by loading the honeycomb core in shear at $\alpha = 45^\circ$ to the principal material directions which resulted in induced tensile and compressive strains along the ribbon and transverse directions, respectively, as demonstrated by DIC analysis.

Flexure testing using a custom-built fixture were conducted on the cantilever HRP-honeycomb beam specimens to understand core behavior due to combined effects of material non-linearity and asymmetry (different tension and compression stiffness). The load-displacement curves and the in-plane strain distributions across the width of the beams at various load stages were measured by the DIC system for validation process.

A 3D FEM of the core representative volume element (RVE) was developed by using the geometry based on optical measurements of the HRP- honeycomb core unit cell. The detailed geometric characteristics of the honeycomb core cell were captured by the FEM. The FEM was employed to generate the effective stress-strain curves of the in-plane and out-of-plane mechanical responses of the core. The FEA simulations indicated that the stress-strain responses depend significantly on the geometry of the node-bond fillet. The predicted stress-strain curves were consistent with the uniaxial test data of HRP-honeycomb core, particularly under tensile loading, and much stiffer than the FEA model in which the effects of node-bond fillets were ignored. The FEA prediction for compressive load in ribbon direction was stiffer than test data at high strain levels owing to the symmetry boundary conditions used in the FEM and the fact that, in the compression test, any imperfections tend to be magnified, and a buckling analysis needs to be

performed. In order to address this problem, the imperfections leading to shear instability observed in the experiments must be incorporated in the FEM of the core RVE as part of future work.

Despite the good agreement between the FEM predictions and test data for the core under uniaxial loadings, discrepancy was observed between the test data (linear-nonlinear) and linear prediction of the FEM at higher strains for the honeycomb core under pure shear loading. The value of the shear modulus predicted by the FEM was close to the shear modulus of the core calculated from the test data at infinitesimal strain.

The FEA predictions of the out-of-plane behaviors of the HRP-honeycomb core were linear and much stiffer than the in-plane predictions. The FEA results showed that the out-of-plane responses are dominated by the axial stiffness of the ribbon material. It was also demonstrated that under in-plane loadings, out-of-plane (W-T, W-L) Poisson's contraction effects are negligible.

It was shown that using the FEM of the core RVE and test data that hexagonal honeycomb cores must be considered as compressible materials in the homogenization process, particularly under large deformations.

Based on the experimental and numerical observations for the in-plane uniaxial responses of HRP-fiberglass/phenolic honeycomb core which are nonlinear-elastic, anisotropic and asymmetric and also compressibility of the honeycomb core particularly at finite strains, the adaptation of an orthotropic, compressible hyperelastic constitutive model using a polyconvex strain energy density function (SEDF) and its implementation in a commercial finite element program (MSC Marc) has been presented. The model was only used to capture the normal in-plane deformations of the core and the effect of the shear invariant in the SEDF was considered to be negligible owing to the linear shear response and high shear modulus of the core. Since the out-of-plane moduli of the core are orders of magnitude higher than the in-plane moduli, for the loading

scenarios wherein the in-plane deformations dominate the overall deformation of the core such as a honeycomb core under in-plane flexure, the out-of-plane (W-T, W-L) Poisson's contraction effects are negligible, therefore it was assumed that the in-plane and out-of-plane constitutive models are decoupled.

The hyperelastic model was assembled using the in-plane uniaxial effective stress-strain curves obtained from the experimentally validated FEM of the HRP-honeycomb core RVE by curve-fitting the results employing the generalized reduced gradient (GRG) algorithm in the Microsoft Excel solver. It was then implemented in the finite element program (MSC Marc) employing user-subroutine codes. The model was evaluated using a single element model on which simple states of loading were imposed; a good agreement was observed between the model predictions and the test data for uniaxial responses of the fiberglass/phenolic honeycomb core including stress-strain behavior, Poisson effects, and strain energy densities. It was also shown that the single-element model is able to predict the behavior of the core under in-plane equi-biaxial loading, which are in reasonable agreement with results obtained from the FEM of the core RVE.

To show the importance of using the hyperelastic material model for capturing the in-plane uniaxial responses of the HRP-honeycomb core in the homogenized model, the FEA predictions of the model were compared with the single-element FEM with a linear orthotropic constitutive model. It was shown that the orthotropic simulations are consistent with the test data at low strain levels which justifies the suitability of the linear orthotropic constitutive model for simulations of the honeycomb core in sandwich structures wherein the core deformations are constrained by the high stiffness facesheets and consequently, the honeycomb core in-plane deformations are restricted to a small strain regime.

In order to show the effectiveness of the hyperelastic model for nonlinear FEA simulations of the bulk honeycomb core using simple continuum elements under complex loading scenarios, several loading cases including the pure shear in (L-W) and (X-Y) plane (off-axis shear) and in-plane flexure were simulated in MSC Marc program. The simulations were conducted using 2D elements under plane strain condition. Good agreement was observed between the model predictions and the test data. The FEA simulations of the pure-shear tests were also used to support the assumption of decoupled and linear in-plane shear constitutive model used in this research.

The homogenization approach in this research can be used for FEA simulations of in-plane behavior of nonmetallic honeycomb cores irrespective of their cell configuration owing to the inherent orthotropic behavior of the cores. The proposed model was elaborated for the geometry configuration of the hexagonal unit cell to provide a physical meaning for the material constants in the model. The developed model satisfactorily captured the exact nonlinear behavior of the HRP-fiberglass/phenolic hexagonal cell honeycomb under large macroscopic strains resulting from microscopic deformation of the cell walls. Ideally, in some sense, this model should be able to incorporate the geometric features of core cell geometry, ribbon, and adhesive material properties as the controlling parameters and should form the scope for future work. Additional work on different core cell geometries and also 3D simulations such a honeycomb core under flexure resulting from the out-of-plane loading such as simulation of 4-point bending test must be done to further refine the proposed model and make it more robust. Moreover, the model can be used for finite element simulations of honeycomb core thermoforming to provide design guidelines and to form processing limits to prevent node bond failures during processing. However, the proposed model needs to be modified by including the effect of temperature on the mechanical response of the core and other factors that might affect the hyperelastic constitutive model.

REFERENCES

REFERENCES

- [1] Bitzer T. Honeycomb technology: Materials, Design, Manufacturing, Applications and Testing: Springer Science & Business Media, 2012.
- [2] Carlsson LA, Kardomateas GA. Structural and failure mechanics of sandwich composites: Springer Science & Business Media, 2011.
- [3] Gibson LJ, Ashby MF. Cellular Solids: Structure and Properties: Cambridge university press, 1999.
- [4] Composites H. HexWeb honeycomb attributes and properties. Duxford, Cambridge, CB24QD, UK. 1999.
- [5] Balawi S, Abot J. A refined model for the effective in-plane elastic moduli of hexagonal honeycombs. Composite Structures. 2008;84:147-58.
- [6] Burton W, Noor A. Assessment of continuum models for sandwich panel honeycomb cores. Computer methods in applied mechanics and engineering. 1997;145:341-60.
- [7] Masters I, Evans K. Models for the elastic deformation of honeycombs. Composite Structures. 1996;35:403-22.
- [8] Mukhopadhyay T, Adhikari S. Equivalent in-plane elastic properties of irregular honeycombs: An analytical approach. International Journal of Solids and Structures. 2016;91:169-84.
- [9] Penado FE. Effective Elastic Properties of Honeycomb Core with Fiber-Reinforced Composite Cells. Open Journal of Composite Materials. 2013;3:89.
- [10] Sorohan S, Constantinescu DM, Sandu M, Sandu AG. In-plane homogenization of commercial hexagonal honeycombs considering the cell wall curvature and adhesive layer influence. International Journal of Solids and Structures. 2018.

REFERENCES (continued)

- [11] Soliman HE, Kapania RK. Assessment of Existing Models for Honeycomb Homogenized Properties. 2nd AIAA Spacecraft Structures Conference 2015. p. 1162.
- [12] Karakoç A, Freund J. Experimental studies on mechanical properties of cellular structures using Nomex® honeycomb cores. *Composite Structures*. 2012;94:2017-24.
- [13] Keshavanarayana SR, Shahverdi H, Kothare A, Yang C, Bingenheimer J. The effect of node bond adhesive fillet on uniaxial in-plane responses of hexagonal honeycomb core. *Composite Structures*. 2017;175:111-22.
- [14] Janus-Michalska M. Hyperelastic behaviour of auxetic material in tension and compression tests. *Czasopismo Techniczne*. 2018; 2018:61-70.
- [15] Shahverdi, H., Keshavanarayana, S., Kothare, A., Yang, C., Horner, A.L. “Experimental and Numerical Study on the Mechanical Response of Fiberglass/Phenolic Honeycomb Core under Uniaxial In-Plane Loading,” in SAMPE Conference Proceedings, Seattle, WA, United States, 2017.
- [16] Moheimani R, Sarayloo R, Dalir H. Failure study of fiber/epoxy composite laminate interface using cohesive multiscale model. *Advanced Composites Letters*. 2020;29:2633366X20910157.
- [17] Kermani NN, Simacek P, Advani SG. Porosity predictions during co-cure of honeycomb core prepreg sandwich structures. *Composites Part A: Applied Science and Manufacturing*. 2020;132:105824.
- [18] Shahverdi Moghaddam H, Keshavanarayana S, Yang C, Horner A. A Numerical and Experimental Approach to Characterize the Failure Modes of Hexagonal Cell Honeycomb Core Under In-Plane Loading. in *Proceedings of the American Society for Composites - Thirty-second Technical Conference*, 2017.
- [19] Shahverdi H, Keshavanarayana S, Kothare A, Teoh P, Yang C, Horner A. In-Plane Thermal Characterization of Fiberglass/Phenolic Honeycomb Core through an Experimental-Numerical Approach. in *Proceedings of the American Society for Composites—Thirty-third Technical Conference*, 2018.

REFERENCES (continued)

- [20] Papka SD, Kyriakides S. In-plane compressive response and crushing of honeycomb. *Journal of the Mechanics and Physics of Solids*. 1994; 42:1499-532.
- [21] Zhu H, Mills N, Knott J. Analysis of the high strain compression of open-cell foams. *Journal of the Mechanics and Physics of Solids*. 1997; 45:1875-904.
- [22] Zhu HX, Mills N. The in-plane non-linear compression of regular honeycombs. *International Journal of Solids and Structures*. 2000; 37:1931-49.
- [23] Chen Y, Das R, Battley M. Response of honeycombs subjected to in-plane shear. *Journal of Applied Mechanics*. 2016; 83:061004.
- [24] Lan L-H, Fu M-H. Nonlinear constitutive relations of cellular materials. *AIAA journal*. 2009;47:264-70.
- [25] Timoshenko SP, Gere JM. *Theory of elastic stability*. McGraw-Hill, New York; 1961.
- [26] Itskov M. *Tensor algebra and tensor analysis for engineers*: Springer, 2007.
- [27] Demiray S, Becker W, Hohe J. Analysis of two-and three-dimensional hyperelastic model foams under complex loading conditions. *Mechanics of Materials*. 2006;38:985-1000.
- [28] Janus-Michalska M. Hyperelastic behavior of cellular structures based on micromechanical modeling at small strain. *Archives of Mechanics*. 2011;63:3-23.
- [29] Mihai LA, Wyatt H, Goriely A. A microstructure-based hyperelastic model for open-cell solids. *SIAM Journal on Applied Mathematics*. 2017;77:1397-416.
- [30] Ju J, Summers JD. Hyperelastic constitutive modeling of hexagonal honeycombs subjected to in-plane shear loading. *Journal of Engineering Materials and Technology*. 2011;133:011005.

REFERENCES (continued)

- [31] Marc M, Volume A. Theory and user information. MSC Corp. 2010;8.
- [32] ARAMIS G. User Manual–Software. 2009.
- [33] Liu Y, Hu H. A review on auxetic structures and polymeric materials. *Scientific Research and Essays*. 2010;5:1052-63.
- [34] Daniel IM, Ishai O, Daniel IM, Daniel I. *Engineering mechanics of composite materials*: Oxford university press New York, 1994.
- [35] Bauchau O, Craig J. Euler-Bernoulli beam theory. *Structural analysis*: Springer; 2009. p. 173-221.
- [36] Ali I, Jun YJ. Mathematical Models for in-Plane Moduli of Honeycomb Structures-A Review. *Research Journal of Applied Sciences, Engineering and Technology*. 2014;7:581-92.
- [37] Becker W. Closed-form analysis of the thickness effect of regular honeycomb core material. *Composite Structures*. 2000; 48:67-70.
- [38] Balawi S, Abot J. The effect of honeycomb relative density on its effective in-plane elastic moduli: An experimental study. *Composite Structures*. 2008; 84:293-9.
- [39] Malek S, Gibson L. Effective elastic properties of periodic hexagonal honeycombs. *Mechanics of Materials*. 2015; 91:226-40.
- [40] Harkati A, Boutagouga D, Harkati E, Bezazi A, Scarpa F, Ouisse M. In-plane elastic constants of a new curved cell walls honeycomb concept. *Thin-Walled Structures*. 2020;149:106613.
- [41] Grediac M. A finite element study of the transverse shear in honeycomb cores. *International Journal of Solids and Structures*. 1993; 30:1777-88.

REFERENCES (continued)

- [42] Aydinçak İ, Kayran A. An approach for the evaluation of effective elastic properties of honeycomb cores by finite element analysis of sandwich panels. *Journal of Sandwich Structures & Materials*. 2009;11:385-408.
- [43] Catapano A, Montemurro M. A multi-scale approach for the optimum design of sandwich plates with honeycomb core. Part I: homogenisation of core properties. *Composite Structures*. 2014;118:664-76.
- [44] Qiu C, Guan Z, Jiang S, Li Z. A method of determining effective elastic properties of honeycomb cores based on equal strain energy. *Chinese Journal of Aeronautics*. 2017; 30:766-79.
- [45] Chen D. Bending deformation of honeycomb consisting of regular hexagonal cells. *Composite Structures*. 2011; 93:736-46.
- [46] Yang C, Moghaddam HS, Keshavanarayana SR, Horner AL. An analytical approach to characterize uniaxial in-plane responses of commercial hexagonal honeycomb core under large deformations. *Composite Structures*. 2019; 211:100-11.
- [47] Hohe J, Becker W. Effective mechanical behavior of hyperelastic honeycombs and two-dimensional model foams at finite strain. *International Journal of Mechanical Sciences*. 2003; 45:891-913.
- [48] Hohe J, Becker W. Geometrically nonlinear stress–strain behavior of hyperelastic solid foams. *Computational materials science*. 2003; 28:443-53.
- [49] Shahverdi Moghaddam H, Yang C, Keshavanarayana S, Horner A. Analysis of In-Plane Mechanical Response of Hexagonal Honeycomb Core: Effect of Node Bond Adhesive and Proposed Analytical Method. in *Proceedings of the American Society for Composites-Thirty-second Technical Conference*, 2017.
- [50] Hackett RM. *Finite Elasticity. Hyperelasticity Primer*: Springer; 2016. p. 1-3.

REFERENCES (continued)

- [51] Keshavanarayana SR, Shahverdi H, Yang C, Karuppiyah A, Kothare A, DaVolt J. Node Bond Failures and Cell Distortion in Honeycomb Cores. Wichita State University, Department of Aerospace Engineering: Program Sponsor: Spirit AeroSystems; 2017.
- [52] HexWeb™ Honeycomb Attributes and Properties. Stamford, CT: Hexcel Corporation; 1999.
- [53] Soykasap Ö. Micromechanical models for bending behavior of woven composites. *Journal of spacecraft and rockets*. 2006;43:1093-100.
- [54] Redjel B. Mechanical properties and fracture toughness of phenolic resin. *Plastics, Rubber & Composites Processing and Appl*. 1995;4:221-8.
- [55] Shafizadeh J, Seferis J. Characterization of phenolic resins for composite honeycomb applications: Society of Manufacturing Engineers, 2000.
- [56] Kazem H, Rizkalla S, Kobayashi A. Shear strengthening of steel plates using small-diameter CFRP strands. *Composite Structures*. 2018;184:78-91.
- [57] Shahverdi H, Keshavanarayana S, Ivanov D, Yang C, Horner A. Anisotropic Hyperelastic Constitutive Modeling of Fiberglass/Phenolic Hexagonal Honeycomb Core Subjected to Large In-plane Deformations. in *Proceedings of the American Society for Composites-Thirty-fourth Technical Conference*, 2019.
- [58] Pickerd V. Optimisation and Validation of the ARAMIS Digital Image Correlation System for use in Large-scale High-strain-rate Events. Defense Science and Technology Organization Victoria (Australia) Maritime ...; 2013.
- [59] Farley GL, Baker DJ. In-plane shear test of thin panels. *Experimental Mechanics*. 1983; 23:81-8.

REFERENCES (continued)

- [60] Becker W. The in-plane stiffnesses of a honeycomb core including the thickness effect. *Archive of Applied Mechanics*. 1998; 68:334-41.

- [61] Marc M. Volume B: Element Library. MSC Software Corporation. 2017:113-661.

- [62] Moheimani R, Sarayloo R, Dalir H. Symmetrical and antisymmetrical sequenced fibers with epoxy resin on rectangular reinforced structures under axial loading. *Proceedings of the American Society for Composites-Thirty-third Technical Conference 2018*.

- [63] Itskov M, Aksel N. A class of orthotropic and transversely isotropic hyperelastic constitutive models based on a polyconvex strain energy function. *International Journal of Solids and Structures*. 2004; 41:3833-48.

- [64] Ehret AE, Itskov M. A polyconvex hyperelastic model for fiber-reinforced materials in application to soft tissues. *Journal of Materials Science*. 2007;42:8853-63.

- [65] Boehler JP. A simple derivation of representations for non-polynomial constitutive equations in some cases of anisotropy. *ZAMM-Journal of Applied Mathematics and Mechanics/Zeitschrift für Angewandte Mathematik und Mechanik*. 1979;59:157-67.

- [66] Itskov M, Ehret A, Mavrilas D. A polyconvex anisotropic strain–energy function for soft collagenous tissues. *Biomechanics and modeling in mechanobiology*. 2006;5:17-26.

- [67] Tanaka M, Noguchi H, Fujikawa M, Sato M, Oi S, Kobayashi T, et al. Development of large strain shell elements for woven fabrics with application to clothing pressure distribution problem. *Computer Modeling in Engineering & Sciences(CMES)*. 2010;62:265-90.

- [68] Itskov M. A generalized orthotropic hyperelastic material model with application to incompressible shells. *International Journal for Numerical Methods in Engineering*. 2001;50:1777-99.

REFERENCES (continued)

- [69] Ebbing V. Design of polyconvex energy functions for all anisotropy classes: Inst. für Mechanik, Abt. Bauwissenschaften, 2010.
- [70] Ball JM. Convexity conditions and existence theorems in nonlinear elasticity. *Archive for rational mechanics and Analysis*. 1976;63:337-403.
- [71] Schröder J, Neff P. On the construction of polyconvex anisotropic free energy functions. *IUTAM Symposium on Computational Mechanics of Solid Materials at Large Strains*: Springer; 2003. p. 171-80.
- [72] Kemmer G, Keller S. Nonlinear least-squares data fitting in Excel spreadsheets. *Nature protocols*. 2010;5:267.
- [73] Marc M. Volume D: User subroutines and special routines. Santa Ana, California; 2005.
- [74] Hibbeler RC. *Mechanics of materials*. *Mechanical Engineering*. 2005;2:0904472.

APPENDIX

APPENDIX A

USER SUBROUTINE CODES FOR IMPLEMENTATION OF THE HYPERELASTIC CONSTITUTIVE MODEL IN MSC MARC FEA PROGRAM

```
subroutine hypela2(d,g,e,de,s,t,dt,ngens,m,nn,kcus,matus,ndi,
  2   nshear,disp,dispt,coord,ffn,frotn,strechn,eigvn,ffn1,
  3   frotn1,strechn1,eigvn1,ncrd,itel,ndeg,ndm,
  4   nnode,jtype,lclass,ifr,ifu)
c
c
c ***** user subroutine for defining material behavior *****
c
c
c
c IMPORTANT NOTES :
c
c (1) F,R,U are only available for continuum and membrane elements (not for
c shells and beams).
c
c (2) For total Lagrangian formulation use the -> 'Elasticity,1' card(=
c total Lagrange with large disp) in the parameter section of input deck.
c For updated Lagrangian formulation use the -> 'Plasticity,3' card(=
c update+finite+large disp+constant d) in the parameter section of
c input deck.
c
c
c d      stress strain law to be formed
c g      change in stress due to temperature effects
c e      total elastic strain
c de     increment of strain
c s      stress - should be updated by user
c t      state variables (comes in at t=n, must be updated
c        to have state variables at t=n+1)
c dt     increment of state variables
c ngens  size of stress - strain law
c m(1)   external (user) element number
c m(2)   internal (marc) element storage number
c nn     integration point number
c kcus(1) layer number
c kcus(2) internal layer number
c matus(1) user material identification number
c matus(2) internal material identification number
c ndi    number of direct components
c nshear number of shear components
c disp   incremental displacements
c dispt  displacements at t=n (at assembly, lovl=4) and
c        displacements at t=n+1 (at stress recovery, lovl=6)
c coord  coordinates
c ncrd   number of coordinates
c ndeg   number of degrees of freedom
c itel   dimension of F and R, either 2 or 3
c nnode  number of nodes per element
c jtype  element type
c lclass(1) element class
c lclass(2) Herrmann element flag (1)-lower order, (2)- higher order
c ifr    set to 1 if R has been calculated
c ifu    set to 1 if stretch has been calculated
c
c at t=n :
c
c ffn    deformation gradient
c frotn  rotation tensor
c strechn square of principal stretch ratios, lambda(i)
c eigvn(i,j) i principal direction components for j eigenvalues
```

```

c
c at t=n+1 :
c
c ffn1    deformation gradient
c frotn1  rotation tensor
c strechn1 square of principal stretch ratios, lambda(i)
c eigvn1(i,j) i principal direction components for j eigenvalues
c
c The following operation obtains U (stretch tensor) at t=n+1 :
c
c call scla(un1,0.d0,itel,itel,1)
c do 3 k=1,3
c do 2 i=1,3
c do 1 j=1,3
c un1(i,j)=un1(i,j)+sqrt(strechn1(k))*eigvn1(i,k)*eigvn1(j,k)
c1 continue
c2 continue
c3 continue
c
c
c #ifdef _IMPLICITNONE
c implicit none
c #else
c implicit logical (a-z)
c #endif
c include'creeps'
c include'concom'
c ** Start of generated type statements **
c real*8 coord, d, de, disp, dispt, dt, e, eigvn, eigvn1, ffn, ffn1
c real*8 frotn, frotn1, g
c integer ifr, ifu, itel, jtype, kcus, lclass, matus, m, ncrd, ndeg
c integer ndi, ndm, ngens, nn, nnode, nshear
c real*8 s, strechn, strechn1, t, un1
c real*8, save:: theta,mu,al,bt,v1,v3
c real*8 c11,c22,c12,sum11,sum22,sum12
c integer k,i,j
c
c dimension e(*),de(*),t(*),dt(*),g(*),d(ngens,*),s(*)
c dimension m(2),coord(ncrd,*),disp(ndeg*),matus(2),
c * dispt(ndeg*),ffn(itel*),frotn(itel*),
c * strechn(itel),eigvn(itel*),ffn1(itel*),
c * frotn1(itel*),strechn1(itel),eigvn1(itel*),
c * kcus(2),lclass(2),mu(10),al(10),bt(10),
c * v1(10),v3(10)
c
c=====
c===== Material Parameters Defining the Hyperelastic Strain Energy Density Function in Equation (6.50)=====
c=====
c***** Reading the input data for material parameters from external INPUT.DAT file*****
c
c NAMELIST /INPUT_DATA/ theta,mu,al,bt,v1,v3 ! Theta is in radian
c
c if (inc.eq.0 .and. incsub.eq.0) then
c OPEN (10,FILE='INPUT.DAT')
c READ (10,INPUT_DATA)
c CLOSE (10)
c endif
c
c=====
c=====Computation of Right Cauchy Green Deformation tensor Components C11 and C22 using Equation (6.47)=====
c=====
c
c11=2.d0*(e(1)+de(1))+1.d0
c22=2.d0*(e(2)+de(2))+1.d0
c12=0.d0 ! Applying the assumption included in Equation (6.50)
c
c=====
c=====Computation of Tangent Stiffness Tensor Using Equation (6.6)=====
c=====

```

```

sum11=0.d0
sum22=0.d0
sum12=0.d0

```

```

do 10 i=1,7 ! Number of Terms

```

```

sum11=sum11+((bt(i)-1.)*(v1(i)*(c11-c22)*cos(theta)**2+((0.5)*
1 v1(i)-(0.25)*v3(i)+0.25)*c22-(0.5)*c11*(v1(i)-(0.5)*
1 v3(i)-0.5))**2*(c11*c22-c12**2)**2*(v1(i)*cos(theta)**2-(0.5)*
1 v1(i)+(0.25)*v3(i)-0.25)**2*(-2.*v1(i)*(c11-c22)*cos(theta)**2+
1 (0.5*(2.*v1(i)-v3(i)+1))*c11-c22*(v1(i)-(0.5)*v3(i)-0.5))**bt(i
1 )+((c11*c22-c12**2)**2*(al(i)-1)*(v1(i)*cos(theta)**2-(0.5)*v1(i
1 )+(0.25)*v3(i)+0.25)**2*(2.*v1(i)*(c11-c22)*cos(theta)**2+(0.5*(
1 -2.*v1(i)+v3(i)+1))*c11+c22*(v1(i)-(0.5)*v3(i)+0.5))**al(i)+
1 (v1(i)*(c11-c22)*cos(theta)**2+((0.5)*v1(i)-(0.25)*v3(i)+0.25)*
1 c22-(0.5)*c11*(v1(i)-(0.5)*v3(i)-0.5))**2*c22**2)*(v1(i)*
1 (c11-c22)*cos(theta)**2+((0.5)*v1(i)-(0.25)*v3(i)-0.25)*
1 c22-(0.5)*c11*(v1(i)-(0.5)*v3(i)+0.5))**2)*mu(i)/
1 ((v1(i)*(c11-c22)*cos(theta)**2+((0.5)*v1(i)-(0.25)*v3(i)+0.25)
1 *c22-(0.5)*c11*(v1(i)-(0.5)*v3(i)-0.5))**2*(c11*c22-c12**2)**2
1 *(v1(i)*(c11-c22)*cos(theta)**2+((0.5)*v1(i)-(0.25)*v3(i)-0.25)
1 *c22-(0.5)*c11*(v1(i)-(0.5)*v3(i)+0.5))**2)

```

```

sum22=sum22+((bt(i)-1.)*(v1(i)*cos(theta)**2-(0.5)*v1(i)+(0.25)
1 *v3(i)+0.25)**2*(c11*c22-c12**2)**2*(v1(i)*(c11-c22)*cos(theta)**2
1 +(-(0.5)*v1(i)+(0.25)*v3(i)+0.25)*c11+(0.5)*c22*(v1(i)-(0.5)
1 *v3(i)+0.5))**2*(-2.*v1(i)*(c11-c22)*cos(theta)**2+(0.5*(2.*v1(i)
1 -v3(i)+1.))*c11-c22*(v1(i)-(0.5)*v3(i)-0.5))**bt(i)+((c11*c22
1 -c12**2)**2*(al(i)-1.)*(v1(i)*cos(theta)**2-(0.5)*v1(i)+(0.25)
1 *v3(i)-0.25)**2*(2.*v1(i)*(c11-c22)*cos(theta)**2+(0.5*(-2.*v1(i)
1 +v3(i)+1.))*c11+c22*(v1(i)-(0.5)*v3(i)+0.5))**al(i)+c11**2*(v1(i)
1 *(c11-c22)*cos(theta)**2+(-(0.5)*v1(i)+(0.25)*v3(i)+0.25)*c11+
1 (0.5)*c22*(v1(i)-(0.5)*v3(i)+0.5))**2*(v1(i)*(c11-c22)*
1 cos(theta)**2+(-(0.5)*v1(i)+(0.25)*v3(i)-0.25)*c11+(0.5)*c22*
1 (v1(i)-(0.5)*v3(i)-0.5))**2)*mu(i)/((c11*c22-c12**2)**2*(v1(i)*
1 (c11-c22)*cos(theta)**2+(-(0.5)*v1(i)+(0.25)*v3(i)+0.25)*c11+
1 (0.5)*c22*(v1(i)-(0.5)*v3(i)+0.5))**2*(v1(i)*(c11-c22)
1 *cos(theta)**2+(-(0.5)*v1(i)+(0.25)*v3(i)-0.25)*c11+(0.5)
1 *c22*(v1(i)-(0.5)*v3(i)-0.5))**2)

```

```

sum12=sum12+(-(bt(i)-1.)*(v1(i)*cos(theta)**2-(0.5)*v1(i)+
1 (0.25)*v3(i)+0.25)*(c11*c22-c12**2)**2*(v1(i)*cos(theta)**2
1 -(0.5)*v1(i)+(0.25)*v3(i)-0.25)*(v1(i)*(c11-c22)*cos(theta)**2
1 +(-(0.5)*v1(i)+(0.25)*v3(i)+0.25)*c11+(0.5)*c22*(v1(i)-(0.5)
1 *v3(i)+0.5))**2*(-2.*v1(i)*(c11-c22)*cos(theta)**2+(0.5*
1 (2.*v1(i)-v3(i)+1.))*c11-c22*(v1(i)-(0.5)*v3(i)-0.5))**
1 bt(i)+((v1(i)*cos(theta)**2-(0.5)*v1(i)+(0.25)*v3(i)+0.25)*
1 (c11*c22-c12**2)**2*(al(i)-1.)*(v1(i)*cos(theta)**2-(0.5)*v1(i)
1 +(0.25)*v3(i)-0.25)*(2.*v1(i)*(c11-c22)*cos(theta)**2+
1 (0.5*(-2.*v1(i)+v3(i)+1))*c11+c22*(v1(i)-(0.5)*v3(i)+0.5))
1 **al(i)-c12**2*(v1(i)*(c11-c22)*cos(theta)**2+(-(0.5)*v1(i)+
1 (0.25)*v3(i)+0.25)*c11+(0.5)*c22*(v1(i)-(0.5)*v3(i)+0.5))**2)*
1 (v1(i)*(c11-c22)*cos(theta)**2+(-(0.5)*v1(i)+(0.25)*v3(i)-0.25)
1 *c11+(0.5)*c22*(v1(i)-(0.5)*v3(i)-0.5))**2)*mu(i)/
1 ((c11*c22-c12**2)**2*(v1(i)*(c11-c22)*cos(theta)**2
1 +(-(0.5)*v1(i)+(0.25)*v3(i)+0.25)*c11+(0.5)*c22*
1 (v1(i)-(0.5)*v3(i)+0.5))**2*(v1(i)*(c11-c22)*cos(theta)**2+
1 -(0.5)*v1(i)+(0.25)*v3(i)-0.25)*c11+(0.5)*c22*
1 (v1(i)-(0.5)*v3(i)-0.5))**2))

```

```

10 continue

```

```

c***** Tangent Stiffness Matrix Components*****

```

```

do i=1,6
do k=1,6
d(i,k)=0.d0
end do
end do

```

```

d(1,1)=sum11
d(2,2)=sum22
d(3,3)=105620.d0 !Out-of-Plane Effective Young's Modulus
d(1,2)=sum12
d(1,3)=0.d0
d(2,3)=0.d0
d(2,1)=d(1,2)
d(3,1)=d(1,3)
d(3,2)=d(2,3)
d(4,4)=170.d0 !In-Plane Effective Shear Modulus
d(5,5)=9345.d0 !Out-of-Plane Effective Shear Modulus
d(6,6)=16046.d0 !Out-of-Plane Effective Shear Modulus

c=====
c=====Computation of 2nd Piola-Kirchhoff Stress Tensor Using Equation (6.5)=====
c=====

s(1)=s(1)+d(1,1)*de(1)+d(1,2)*de(2)+d(1,3)*de(3)
s(2)=s(2)+d(2,1)*de(1)+d(2,2)*de(2)+d(2,3)*de(3)
s(3)=s(3)+d(3,1)*de(1)+d(3,2)*de(2)+d(3,3)*de(3)
s(4)=s(4)+d(4,4)*de(4)
s(5)=s(5)+d(5,5)*de(5)
s(6)=s(6)+d(6,6)*de(6)

c=====
return
end

```